

N71-232015
N71-23206
NASA CR-117893

NATIONAL AERONAUTICS AND SPACE ADMINISTRATION

Technical Report 32-1526

Volume II

The Deep Space Network

Progress Report

For January and February 1971

**CASE FILE
COPY**

JET PROPULSION LABORATORY
CALIFORNIA INSTITUTE OF TECHNOLOGY
PASADENA, CALIFORNIA

April 15, 1971

NATIONAL AERONAUTICS AND SPACE ADMINISTRATION

Technical Report 32-1526

Volume II

The Deep Space Network

Progress Report

For January and February 1971

JET PROPULSION LABORATORY
CALIFORNIA INSTITUTE OF TECHNOLOGY
PASADENA, CALIFORNIA

April 15, 1971

Prepared Under Contract No. NAS 7-100
National Aeronautics and Space Administration

Preface

This report series presents progress on DSN supporting research and technology, advanced development and engineering, and implementation, and DSN operations which pertain to mission-independent or multiple-mission development as well as to support of flight projects. Each issue presents material in some, but not all, of the following categories in the order indicated.

Description of the DSN

Mission Support

- Interplanetary Flight Projects
- Planetary Flight Projects
- Manned Space Flight Project
- Advanced Flight Projects

Advanced Engineering

- Tracking and Navigational Accuracy Analysis
- Communications Systems Research
- Communications Elements Research
- Supporting Research and Technology

Development and Implementation

- Space Flight Operations Facility Development
- Ground Communications Facility Development
- Deep Space Instrumentation Facility Development
- DSN Project and System Development

Operations and Facilities

- DSN Operations
- Space Flight Operations Facility Operations
- Ground Communications Facility Operations
- Deep Space Instrumentation Facility Operations
- Facility Engineering

In each issue, the part entitled "Description of the DSN" describes the functions and facilities of the DSN and may report the current configuration of one of the six DSN systems (tracking, telemetry, command, monitoring, simulation, and operations control).

The work described in this report series is either performed or managed by the Tracking and Data Acquisition organization of JPL for NASA.

Contents

DESCRIPTION OF THE DSN

DSN Functions and Facilities	1
<i>N. A. Renzetti</i>	
DSN Operations Control System	4
<i>J. E. Maclay</i>	

MISSION SUPPORT

Interplanetary Flight Projects

Pioneer Mission Support	6
<i>A. J. Siegmeth</i>	
Helios Mission Support	18
<i>P. S. Goodwin</i>	

Planetary Flight Projects

Viking Mission Support	28
<i>D. J. Mudgway</i>	

Manned Space Flight Project

Apollo Mission Support	33
<i>R. B. Hartley</i>	

ADVANCED ENGINEERING

Tracking and Navigational Accuracy Analysis

Second Order Charged Particle Effects on Electromagnetic Waves in the Interplanetary Medium	42
<i>O. H. von Roos</i>	

Communications Systems Research

Information Systems: Hardware Version of an Optimal Convolutional Decoder	49
<i>W. Lushbaugh</i>	
Improved Frequency Dividers	56
<i>G. Lutes</i>	
The Limits of Minimum Distance Decoding	59
<i>R. J. McEliece</i>	
Symmetrically Decodable Codes	62
<i>R. J. McEliece and J. E. Savage</i>	

Contents (contd)

Boolean Difference Calculus and Fault Finding	65
<i>I. S. Reed</i>	
New Developments in the Hydrogen Maser Frequency Standard	72
<i>A. Sward</i>	
Sequential Ranging With the Viterbi Algorithm	75
<i>U. Timor</i>	

Communications Elements Research

A Study of Microwave Transmission Through Perforated Flat Plates	80
<i>T. Y. Otoshi</i>	
Design of Hydrogen Maser Cavity Tuning Servo	86
<i>C. Finnie</i>	
Improved RF Calibration Techniques: System Operating Noise Temperature Calibrations	89
<i>M. S. Reid</i>	

Supporting Research and Technology

Photon Energies of a Cathode-Ray Tube System	92
<i>J. J. Volkoff</i>	
Mark IIIA Simulation Center Interactive Alphanumeric Television System	100
<i>C. F. Leahey</i>	
A Reanalysis Program for Antenna Member Size Changes	108
<i>R. Levy</i>	
Antenna Structures: Evaluation of Field Measurements of Reflector Distortions	113
<i>B. Marcus and M. S. Katow</i>	

DEVELOPMENT AND IMPLEMENTATION

SFOF Development

SFOF Cable Control	122
<i>R. A. Paine</i>	
Diagnostics for the SFOF Mark IIIA Central Processing System: Pre-Mission CPS/Facility Checkout Procedures	125
<i>R. A. Wells</i>	

Contents (contd)

GCF Development

GCF Reconfiguration of the Goldstone DSCC Microwave Terminals for 50-kbit Data Transmission	129
<i>R. G. Hanselman</i>	

DSIF Development

Coherent Reference Generator for DSN Mark III Data System	133
<i>R. B. Crow</i>	
Tracking and Data System Near-Earth Telemetry Automatic Switching Unit	136
<i>L. Butcher</i>	

DSN Projects and Systems Development

DSN Discrepancy Reporting Subsystem	140
<i>D. G. Tustin</i>	
Optimal Frame Synchronization	141
<i>W. Kizner</i>	

OPERATIONS AND FACILITIES

DSN Operations

DSN Traceability and Reporting Program	145
<i>J. A. Miccio</i>	

GCF Operations

The Teletype Discipline of Data Transfer Designed for Support of Mariner Mars 1971 Missions	148
<i>F. E. Bond, Jr.</i>	

DSIF Operations

DSIF Uplink Amplitude Instability Measurement	165
<i>A. Bryan and G. Osborn</i>	
Processed Data Combination for Telemetry Improvement—DSS 62	169
<i>J. M. Urech</i>	

Facility Engineering

Overseas DSIF 64-m Antenna Project Status	177
<i>F. D. McLaughlin</i>	

DSN Functions and Facilities

N. A. Renzetti
Mission Support Office

The objectives, functions, and organization of the Deep Space Network are summarized. The Deep Space Instrumentation Facility, the Ground Communications Facility, and the Space Flight Operations Facility are described.

The Deep Space Network (DSN), established by the NASA Office of Tracking and Data Acquisition under the system management and technical direction of JPL, is designed for two-way communications with unmanned spacecraft traveling approximately 16,000 km (10,000 mi) from earth to planetary distances. It supports, or has supported, the following NASA deep space exploration projects: *Ranger*, *Surveyor*, *Mariner Venus 1962*, *Mariner Mars 1964*, *Mariner Venus 67*, *Mariner Mars 1969*, *Mariner Mars 1971* (JPL); *Lunar Orbiter* and *Viking* (Langley Research Center); *Pioneer* (Ames Research Center); *Helios* (West Germany); and *Apollo* (Manned Spacecraft Center), to supplement the Manned Space Flight Network (MSFN).

The DSN is distinct from other NASA networks such as the MSFN, which has primary responsibility for tracking the manned spacecraft of the *Apollo* Project, and the Space Tracking and Data Acquisition Network (STADAN), which tracks earth-orbiting scientific and

communications satellites. With no future unmanned lunar spacecraft presently planned, the primary objective of the DSN is to continue its support of planetary and interplanetary flight projects.

To support flight projects, the DSN simultaneously performs advanced engineering on components and systems, integrates proven equipment and methods into the network,¹ and provides direct support of each project through that project's Tracking and Data System. This management element and the project's Mission Operations personnel are responsible for the design and operation of the data, software, and operations systems required for the conduct of flight operations. The organization and procedures necessary to carry out these activities are described in Ref. 1.

¹When a new piece of equipment or new method has been accepted for integration into the network, it is classed as Goldstone duplicate standard (GSDS), thus standardizing the design and operation of identical items throughout the network.

By tracking the spacecraft, the DSN is involved in the following data types:

- (1) *Radio Metric*: generate angles, one- and two-way doppler, and range.
- (2) *Telemetry*: receive, record, and retransmit engineering and scientific data.
- (3) *Command*: send coded signals to the spacecraft to activate equipment to initiate spacecraft functions.

The DSN operation is characterized by six DSN systems: (1) tracking, (2) telemetry, (3) command, (4) monitoring, (5) simulation, and (6) operations control.

The DSN can be characterized as being comprised of three facilities: the Deep Space Instrumentation Facility (DSIF), the Ground Communications Facility (GCF), and the Space Flight Operations Facility (SFOF).

I. Deep Space Instrumentation Facility

A. Tracking and Data Acquisition Facilities

A world-wide set of deep space stations (DSSs) with large antennas, low-noise phase-lock receiving systems, and high-power transmitters provide radio communications with spacecraft. The DSSs and the deep space com-

munications complexes (DSCCs) they comprise are given in Table 1.

Radio contact with a spacecraft usually begins when the spacecraft is on the launch vehicle at Cape Kennedy, and it is maintained throughout the mission. The early part of the trajectory is covered by selected network stations of the Air Force Eastern Test Range (AFETR) and the MSFN of the Goddard Space Flight Center.² Normally, two-way communications are established between the spacecraft and the DSN within 30 min after the spacecraft has been injected into lunar, planetary, or interplanetary flight. A compatibility test station at Cape Kennedy (discussed later) monitors the spacecraft continuously during the launch phase until it passes over the local horizon. The deep space phase begins with acquisition by either DSS 51, 41, or 42. These and the remaining DSSs given in Table 1 provide radio communications to the end of the flight.

To enable continuous radio contact with spacecraft, the DSSs are located approximately 120 deg apart in longitude; thus, a spacecraft in deep space flight is always

²The 9-m (30-ft) diam antenna station established by the DSN on Ascension Island during 1965 to act in conjunction with the MSFN orbital support 9-m (30-ft) diam antenna station was transferred to the MSFN in July 1968.

Table 1. Tracking and data acquisition stations of the DSN

DSCC	Location	DSS	DSS serial designation	Antenna		Year of initial operation
				Diameter, m (ft)	Type of mounting	
Goldstone	California	Pioneer	11	26 (85)	Polar	1958
		Echo	12	26 (85)	Polar	1962
		(Venus) ^a	13	26 (85)	Az-El	1962
		Mars	14	64 (210)	Az-El	1966
—	Australia	Woomera ^b	41	26 (85)	Polar	1960
Tidbinbilla	Australia	Weemala (formerly Tidbinbilla) ^b	42	26 (85)	Polar	1965
		Ballima ^b (formerly Booroomba)	43	64 (210)	Az-El	Under construction
—	South Africa	Johannesburg ^b	51	26 (85)	Polar	1961
Madrid	Spain	Robledo ^b	61	26 (85)	Polar	1965
		Cebreros ^b	62	26 (85)	Polar	1967
		Robledo	63	64 (210)	Az-El	Under construction

^aA research-and-development facility used to demonstrate the feasibility of new equipment and methods to be integrated into the operational network. Besides the 26-m (85-ft) diam az-el-mounted antenna, DSS 13 has a 9-m (30-ft) diam az-el-mounted antenna that is used for testing the design of new equipment and support of ground-based radio science.

^bNormally staffed and operated by government agencies of the respective countries (except for a temporary staff of the Madrid DSCC), with some assistance of U.S. support personnel.

within the field-of-view of at least one DSS, and for several hours each day may be seen by two DSSs. Furthermore, since most spacecraft on deep space missions travel within 30 deg of the equatorial plane, the DSSs are located within latitudes of 45 deg north or south of the equator. All DSSs operate at S-band frequencies: 2110–2120 MHz for earth-to-spacecraft transmission and 2290–2300 MHz for spacecraft-to-earth transmission.

To provide sufficient tracking capability to enable useful data returns from around the planets and from the edge of the solar system, a 64-m (210-ft) diam antenna network will be required. Two additional 64-m (210-ft) diam antenna DSSs are under construction at Madrid and Canberra, which will operate in conjunction with DSS 14 to provide this capability. These stations are scheduled to be operational by the middle of 1973.

B. Compatibility Test Facilities

In 1959, a mobile L-band compatibility test station was established at Cape Kennedy to verify flight-spacecraft-DSN compatibility prior to the launch of the *Ranger* and *Mariner* Venus 1962 spacecraft. Experience revealed the need for a permanent facility at Cape Kennedy for this function. An S-band compatibility test station with a 1.2-m (4-ft) diam antenna became operational in 1965. In addition to supporting the preflight compatibility tests, this station monitors the spacecraft continuously during the launch phase until it passes over the local horizon.

Spacecraft telecommunications compatibility in the design and prototype development phases was formerly verified by tests at the Goldstone DSCC. To provide a more economical means for conducting such work and because of the increasing use of multiple-mission telemetry and command equipment by the DSN, a compatibility test area (CTA) was established at JPL in 1968. In all essential characteristics, the configuration of this facility is identical to that of the 26-m (85-ft) and 64-m (210-ft) diam antenna stations.

The JPL CTA is used during spacecraft system tests to establish the compatibility with the DSN of the proof test

model and development models of spacecraft, and the Cape Kennedy compatibility test station is used for final flight spacecraft compatibility validation testing prior to launch.

II. Ground Communications Facility

The GCF provides voice, high-speed data, wideband data, and teletype communications between the SFOF and the DSSs. In providing these capabilities, the GCF uses the facilities of the worldwide NASA Communications Network (NASCOM)³ for all long distance circuits, except those between the SFOF and the Goldstone DSCC. Communications between the Goldstone DSCC and the SFOF are provided by a microwave link directly leased by the DSN from a common carrier.

Early missions were supported by voice and teletype circuits only, but increased data rates necessitated the use of high-speed circuits for all DSSs, plus wideband circuits for some stations.

III. Space Flight Operations Facility

Network and mission control functions are performed at the SFOF at JPL. The SFOF receives data from all DSSs and processes that information required by the flight project to conduct mission operations. The following functions are carried out: (1) real-time processing and display of radio metric data; (2) real-time and non-real-time processing and display of telemetry data; (3) simulation of flight operations; (4) near-real-time evaluation of DSN performance; (5) operations control, and status and operational data display; and (6) general support such as internal communications by telephone, intercom, public address, closed-circuit TV, documentation, and reproduction of data packages. Master data records of science data received from spacecraft are generated. Technical areas are provided for flight project personnel who analyze spacecraft performance, trajectories, and generation of commands.

³Managed and directed by the Goddard Space Flight Center.

Reference

1. *The Deep Space Network*, Space Programs Summary 37-50, Vol. II, pp. 15–17. Jet Propulsion Laboratory, Pasadena, Calif., Mar. 31, 1968.

DSN Operations Control System

J. E. Maclay

DSN Engineering and Operations Office

A new network capability for high-speed transfer of operational control information has been implemented. The increase in speed is attributable to two things: use of high-speed data line instead of teletype yields a 24-fold increase, and source data is input in machine language instead of manually, yielding an additional increase.

A new DSN operations control system capability to send operational traffic from the SFOF to the DSSs by high-speed data (HSD) line has been implemented. There are currently three types of traffic that go by this mechanization: tracking predicts, DSN sequence of events, and DSN 7-day schedule.

The implementation uses the standard GCF HSD system, but required new designs in SFOF and DSIF. The encoding, formatting, and outputting is done in the SFOF by the operations control output router, a software part of the DSN monitor and operations control real-time processor. Reception and decoding are done at the DSS as part of the DSIF monitor program in the digital instrumentation subsystem Phase II (DIS II), with printout on the DIS line printer (and also a Magpak recording of tracking predicts).

To have a backup, and because not all DSSs have a DIS II, the output router can also output in Baudot code over teletype (TTY) lines for printout on a TTY machine, although any line of printing over 69 characters long is truncated (as opposed to a 132-character line on the DIS line printer).

For the two reasons given, tracking predicts and DSN 7-day schedules are constrained to a maximum of 69 characters per line, even when sent via HSD to the DIS line printer. The DSN sequence of events uses all 132 characters of a line printer, and thus cannot be sent by TTY. This is not considered to be a problem, as voice can be used as backup until reception capability is restored. (Prior to *Pioneer F* support, the remaining DSSs will also have this reception capability.)

The Mark II DSN had an output capability, but it was limited to transmitting tracking predicts by TTY; predicts generated on the 7094 were converted to Baudot code in the 7044 and sent to the GCF comm processor without personnel handling during the process. The DSN 7-day schedule and the sequence of events were handwritten for keyboard entry into the comm processor. The new output router can accept any type of traffic which is in machine language, does a code conversion (to XDS 6-bit BCD for DIS page prints, XDS floating point for Magpak recordings, and Baudot code for TTY transmission), reformats if required, adds the blanks and carriage functions needed in the page print output format, and meters the output onto GCF lines. Currently, "machine

language" means EBCDIC¹ coding on either magnetic tape or computer files, but may later be expanded to include the Univac 36-bit coding utilized in an available RF predicts program.

Comparison of the HSD medium and the TTY medium is straightforward. One line of print is put in each HSD block, and since the DIS line printer is capable of printing faster than the 4 HSD block per second rate of GCF, the network-wide speed is 4 printed lines per second via HSD line. TTY requires 6 s per printed line, so

¹Extended binary-coded decimal interchange code.

transmission by HSD is 24 times as fast as by TTY. Thus, predicts for initial acquisition, which require 14 min by TTY, will go in 35 s by HSD. For other traffic, the ratio is much higher when one considers that in the new system, a sequence of events (for example, one 200 items long) file is read and output and printed in less than a minute, whereas in the Mark II era it required several man-hours to condense a sequence to TTY page size, and then it was manually put onto TTY lines.

This capability clearly will help the DSN to give better support to missions with high activity, and to reduce station turnaround times.

Pioneer Mission Support

A. J. Siegmeth
Mission Support Office

This article describes the design profile of the Pioneer F and G missions. The characteristics of these flights that interface with Deep Space Network tracking and data acquisition support are depicted. A delineation of the mission description and a summary of spacecraft systems and subsystems are given.

I. Introduction

Reference 1 contains a summary of the tracking and data system planning activities for the *Pioneer F* and *G* missions. This article begins the description of *Pioneer F* and *G* missions, with special emphasis on characteristics that interface with the tracking and data acquisition functions. DSN planning efforts during the design phase of the spacecraft hardware were centered around the assurance of a functional compatibility between the spacecraft design and the configuration of the DSN Mark III system.

In this article, *Pioneer F* and *G* mission profiles are presented. Spacecraft systems are briefly described and the following subsystems are outlined: electrical power supply, electrical power conditioning, structure, thermal control, propulsion, and attitude control. Future articles will contain: (1) a description of the telecommunications and antenna subsystems; (2) a summary of launch and space flight trajectories, giving tracking and data acquisition constraints; (3) the configuration of the six DSN systems; and (4) the planning activities related to navigational requirements.

II. Pioneer F and G Mission Profile

The mission objectives of the *Pioneer F* and *G* spacecraft are to conduct, during the 1972-73 Jovian opportunities, exploratory investigation beyond the orbit of Mars of the interplanetary medium, the nature of the asteroid belt, and the environmental and atmospheric characteristics of the planet Jupiter.

As the earth and Jupiter orbit around the sun, their relative position permits a spacecraft to be launched every 13 months into a Jupiter-bound trajectory with a minimum of launch energy. During optimum conditions, injection velocities of approximately 14 km/s will suffice; a favorable launch period can cover several weeks. During the remainder of the 13-month interval, the velocity requirements will rise to prohibitive values. Among the available launch vehicle configurations, the *Atlas/Centaur*/TE 364 vehicle was chosen for *Pioneer F* and *G* missions. The launch energy generated by this vehicle will make possible the launch of *Pioneer F* during late February or early March 1972, and *Pioneer G* during April 1973. These missions will make possible the initial direct exploration of vast regions of the solar system from 1 to 6 AU from the sun, including the vicinity of

the planet Jupiter. The asteroid belt is located in this region between 2 and 3.6 AU from the sun. *Pioneer F* will be the first NASA spacecraft to explore the outer planet environment beyond the orbit of Mars. It will take between 600 and 800 days to travel from the earth to the vicinity of Jupiter, using trajectories compatible with the favorable launch opportunities.

The spacecraft are equipped with field-and-particles and optical-type instruments. Nearly all the time during travel between the earth and Jupiter will be spent in the interplanetary solar-wind environment. The influences of the earth's magnetosphere will cease several hours after launch. The spacecraft will fly through the high-density Jovian magnetosphere to explore the trapped radiation particles of the solar system's largest planet. The general relationship of a typical *Pioneer F* trajectory to the sun, earth asteroid belt, and Jupiter is depicted in Fig. 1.

A simplified mission profile of *Pioneer F* is shown in Fig. 2. The telecommunications range at Jupiter encounter will be approximately $5\frac{1}{2}$ AU and, after the encounter of Jupiter, *Pioneer F* will move toward the outer planets and eventually leave the solar system. In contrast, the *Pioneer G* trajectory profile is such that this spacecraft, after the Jupiter encounter, will stay within the solar system as a solar orbiter.

The *Pioneer F* and *G* missions will require continuous tracking and data acquisition coverage by the 26-m antenna network from liftoff to Jupiter encounter plus 6 months. The flight project also expects that during critical mission events the 64-m antenna stations will be continuously available to accomplish mission objectives. In addition, the project plans to obtain from the 64-m antenna stations at least one horizon-to-horizon tracking pass per week from liftoff to encounter plus 6 months.

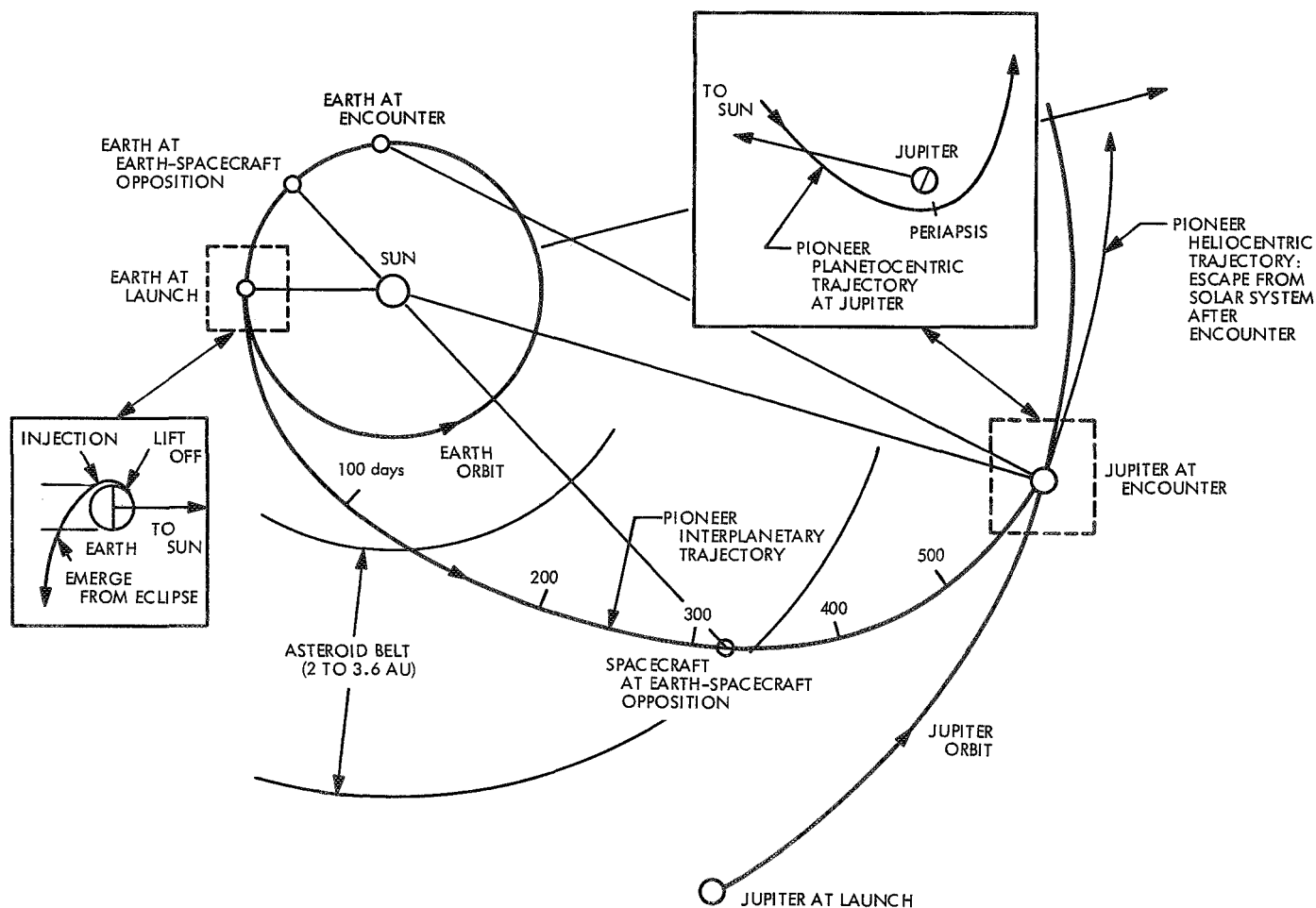


Fig. 1. Ecliptic projection of a typical *Pioneer F* trajectory

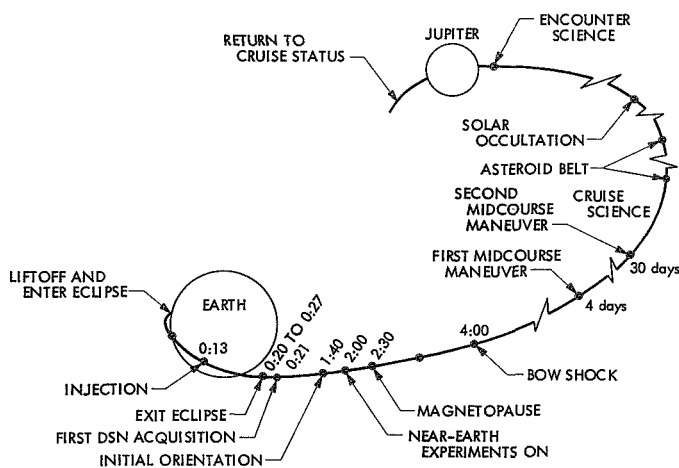


Fig. 2. Pioneer F mission profile

After the Jovian encounter plus 6 months, the tracking and data system should furnish, as a minimum, daily coverage for both missions until the limit of the receipt of downlink data signal.

It will be a continuous challenge for the DSN to acquire and collect the data stream transmitted by the Jovian missions. Variations of the solar activities will naturally have a continuous impact on the measurements made by the field-and-particles instruments relating to the solar wind and the interplanetary magnetic field.

Pioneer F and *G* spacecraft will reach the asteroid belt approximately 6 months after launch and will stay in this belt for more than 6 months. Some astronomers hypothesize that the asteroid belt might be composed of the remnant of a planet which was circling the sun at 2.8 AU. Seventy-five thousand bodies of the asteroid belt are larger than magnitude 20; the largest is Ceres with a diameter of 768 km. The exploration of the asteroid belt can lead to the understanding of the origin and evolution of the solar system; therefore, the data collected by the DSN can have a high scientific significance.

To give a better idea of the challenge of a Jupiter flyby, a few of the important characteristics of the largest solar planet are given: Jupiter's average distance from the sun is 5 AU, which is equivalent to approximately 75×10^7 km. Its mass is equivalent to 318 times the earth's mass and comprises 70% of all planetary mass. Jupiter's diameter (approximately 71,387 km) is 11 times the earth's diameter. It is remarkable that Jupiter's density is only approximately one-fourth of the earth's density and its fastest rotation period is 9 h and 50 min. In other

words, one Jupiter day is almost 10 h long. Jupiter has 12 satellites, 4 of them having a magnitude equivalent to the earth's moon. The four Jupiter moons are called IO, Europa, Ganymede, and Callisto. Jupiter has many varying striped surface features. The red spot is about three times the size of earth. It is assumed that Jupiter's upper atmosphere is composed of hydrogen, helium, ammonia, and methane. It is an intense radio noise source at decametric frequencies. Fortunately, this noise drops considerably toward the S-band frequency range. The typical cold sky system noise temperature of the Goldstone 64-m antenna station is 25°K . If one moves this antenna to the direction of Jupiter, the system noise temperature will increase to approximately 30°K . This increase of 5°K can cause a telemetry signal-to-noise degradation of around 0.5 dB. The dense magnetosphere of this large planet is caused by an extremely high magnetic field, which can be as high as 5×10^{-4} T (5 gauss).

To place the spacecraft on a trajectory to the desired target point in the vicinity of Jupiter, one or more mid-course corrections have to be made to compensate for launch vehicle injection velocity vector errors. Flight project plans to perform the first maneuver within the first ten days and the second, if necessary, about 30 days after launch.

The medium and the 2.75-m-diameter high-gain antenna of the *Pioneer F* and *G* spacecraft have to continuously point toward the earth during the entire flight to assure effective data return (Fig. 3). Therefore, precession maneuvers will be conducted throughout the mission as required to maintain an earth-pointing cruise attitude. These maneuvers, homing into the uplink signal transmitted by the DSN toward the spacecraft, will take place only once every 2 or 3 days during the early phase of each mission, and will decrease in frequency to once in 1 or 2 weeks by the time of Jupiter encounter.

Approximately 315 days after launch, the relative position of the spacecraft and earth will place the spacecraft in a superior conjunction configuration versus the sun and the earth. Because the spacecraft is somewhat out of the ecliptic plane, the spacecraft/earth line will not intercept the sun but will come within a few solar radii. In this configuration, the radio beam will be intercepted through the high-density part of the solar corona and will be influenced significantly by the plasma. Because of the closeness of the spacecraft to the sun, DSN antennas will pick up, together with the spacecraft signal, solar high-frequency noise, which will degrade the

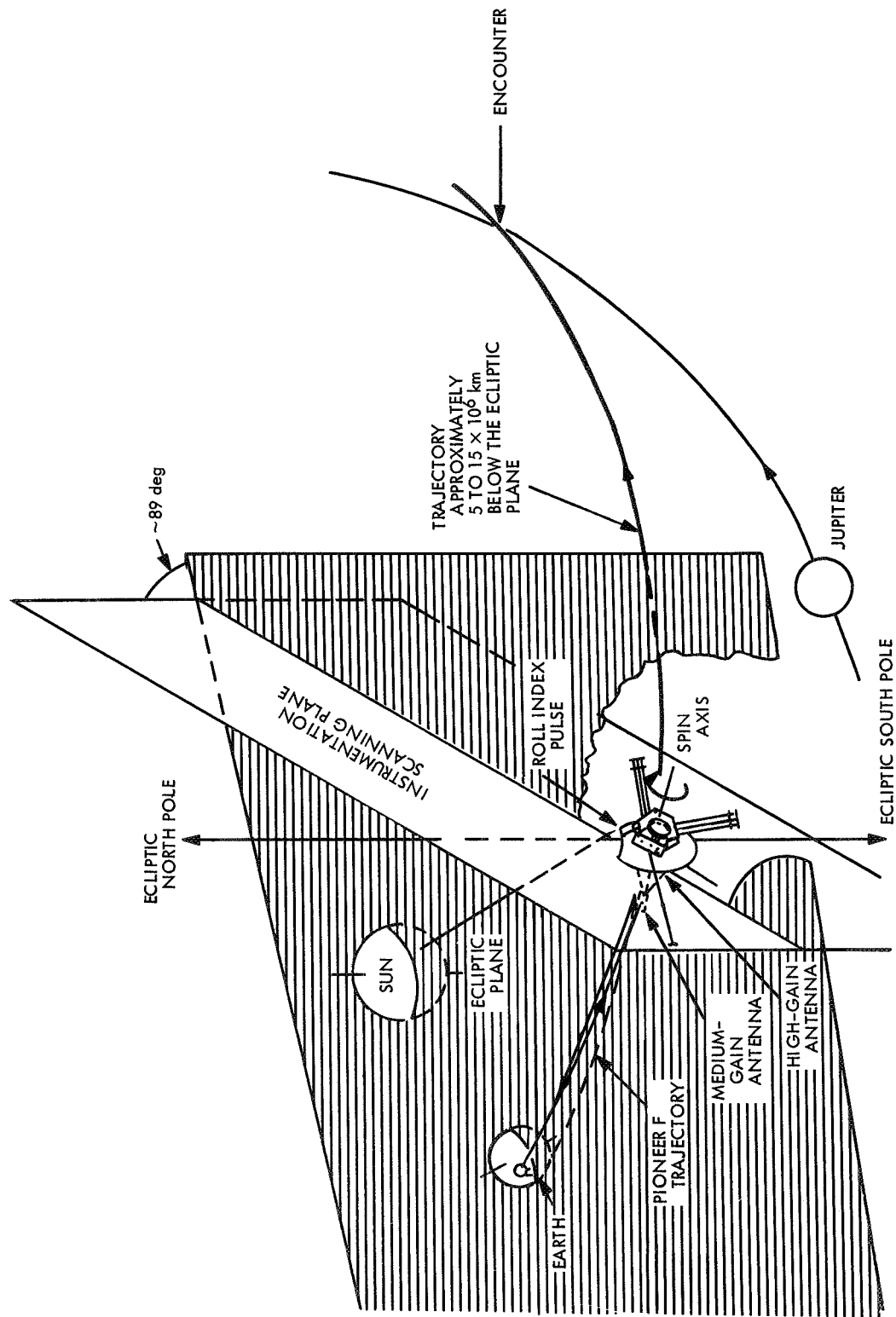


Fig. 3. Pioneer F earth/Jupiter transfer trajectory

received signal-to-noise ratio and can cut down considerably the quality and usefulness of the spacecraft/earth telecommunication link. This condition will exist for approximately 1 or 2 weeks.

To optimize the scientific value of the data return during the Jovian encounter, the flight project has selected specific flyby trajectories. The objectives of the encounter trajectory for *Pioneer F* are:

- (1) To penetrate the Jupiter radiation belt.
- (2) To provide good viewing conditions for Jupiter before periapsis.
- (3) To obtain a short occultation for the spacecraft by Jupiter (less than 1 h).
- (4) To provide a radius of closest approach to the center of Jupiter between 2 and 3 Jupiter radii.

The typical trajectories will approach Jupiter in a counterclockwise direction, as viewed from the celestial North Pole, will meet the planet slightly south of the ecliptic, pass around the planet in a counterclockwise direction to an attitude between $1\frac{1}{2}$ and 2 Jupiter radii above the surface of the planet, and will exit slightly north of the planet. The postencounter trajectory will have an inclination to an ecliptic of less than 5 deg and the spacecraft will slowly escape the solar system. An additional 3 years will be required to cross Saturn's solar orbit.

The *Pioneer G* trajectory and sequence of events up to Jupiter encounter will be similar to that of *Pioneer F*.

During the voyage from earth to Jupiter, the spacecraft has to travel through a hostile environment, which can directly or indirectly affect the flight hardware and the operational characteristics of the spacecraft transponder/antenna system and can also constrain data acquisition and collection by the DSN. Special efforts will be made to study and analyze all possible constraints and to plan a configuration that will operate properly with these constraints and assure the best data return. A brief summary of some of the space hazards the spacecraft can be exposed to follows:

- (1) As the spacecraft rushes through the earth's Van Allen belt, the instruments will detect vast

intensity variations of high-energy protons and electrons. During this early deep space phase, the DSN must assist the Mission Operations Team in transmission of numerous commands and must collect all telemetry data.

- (2) As the spacecraft travels through the asteroid belt, onboard sensors will attempt to detect meteoroids. During this phase, there is a very small probability that the spacecraft may collide with one of the meteoroids. This can cause an abrupt change in the spacecraft attitude and a loss of the spacecraft high-gain antenna radio link. In this event, the DSN must attempt to acquire spacecraft signals radiated by the medium-gain or omni-antennas.
- (3) The electrons, protons, and magnetic field in the Jovian belt have a much higher intensity and flux density than in the Van Allen belt. It is possible that the crystal oscillators of the spacecraft transponder will slightly detune as the spacecraft traverses the Jovian belt. The high-intensity Jovian magnetosphere can also change the polarization ellipticity of the spacecraft signal radiated toward earth. In addition, the spacecraft flying in the close vicinity of Jupiter undergoes an abrupt velocity change which causes, within 2 or 3 h, a considerable change in the doppler shift; this shift has to be tracked by the spacecraft receiver and by the DSN.

III. Spacecraft Systems

The *Pioneer F* and *G* spacecraft are carrying, as primary electrical power sources, radioisotope thermoelectric generators (RTGs) provided by a contractor of the Atomic Energy Commission. The spacecraft has been designed by the TRW Systems Group on contract with the NASA/Ames Research Center. The production and testing of the spacecraft will also be performed by the same vendor. The basic design requirements of the *Pioneer F* and *G* spacecraft can be summarized as follows:

- (1) Be compatible with the *Atlas* SLV3C/*Centaur*/PE-364-4 launch vehicle.
- (2) Be compatible with the Mark III DSN system.
- (3) Provide a thermally controlled compartment to house the scientific instruments.

- (4) Provide a telecommunications data system to sample readings from the instrumentation and transmit the information to earth.
- (5) Provide a system to permit changes in operating modes of onboard equipment on command from earth.
- (6) Provide a magnetically clean and an electromagnetic interference-free spacecraft.
- (7) Operate in space for more than 2 years and for distances beyond the orbit of Jupiter.

To make the telecommunications subsystem of the spacecraft compatible with the Mark III DSN system, specific capabilities must exist. The spacecraft transponder must operate at predetermined DSN S-band frequencies and should have the capability to operate in a coherent two-way mode having a fixed ratio between the uplink and downlink frequencies. This capability is necessary to extract at the deep space stations accurate doppler measurements to determine the accurate spacecraft velocity relative to earth. These measurements are necessary for trajectory determination and for the generation of predictions required by the deep space stations to make an effective acquisition of the data link possible. The spacecraft must also be equipped with an auxiliary onboard oscillator to provide a downlink during times when the deep space stations have not established a two-way uplink/downlink telecommunications configuration.

The *Pioneer* Project Office of NASA/Ames Research Center plans to control every element of the mission system by a project documentation system. *Pioneer F* and *G* Project Specification PC-210, Spacecraft and Related Requirements, describes the functional requirements that the space vehicles must meet to achieve the primary and secondary mission objectives. This key document describes the expected environment through which the spacecraft will pass, and the required characteristics and performance of the spacecraft systems and subsystems. In addition, it specifies the reliability, quality assurance, and test programs to be conducted at the subsystem and system levels and the requirements for the activities at the launch complex to prepare the spacecraft and scientific instruments for launch. This document references the *Pioneer F* and *G* specification PC-222, Spacecraft/DSIF Interface Specification. A subset of this document is PC-222.02, which defines the characteristics of the equipment of the deep space stations pertinent to the spacecraft and the requirements imposed on the

spacecraft by the DSN. The contents of this document were collected by the Project office from the DSN Standard Practice, 810-5, Revision A, Change 1, Deep Space Network/Flight Project Interface Design Handbook. DSN developed this handbook for use by all flight projects as a standard source of advanced technical information that describes the DSN interfaces with the Project office in the fields of telecommunications, data processing, and simulation. Since the *Pioneer* project uses the contents of this interface design handbook, assurance can be made that, on a functional level, the project interfaces will be compatible with the DSN configuration. To validate the functional compatibility between spacecraft design and the Mark III DSN system, plans are underway to make RF and data system compatibility tests between *Pioneer F* and *G* flight hardware at the Compatibility Test Area located at JPL. A verification of this compatibility will be made a few days prior to launch at DSS 71, located at Cape Kennedy, during the final checkout of the spacecraft and launch vehicle.

Based on the contractual functional design requirements of the spacecraft and its telecommunications subsystem, the spacecraft contractor, under the guidance of the *Pioneer* Project office, has developed the flight hardware.

The basic geometry of the *Pioneer F* and *G* spacecraft is shown in Figs. 4 and 5, and a perspective view is given in Fig. 6. The spacecraft essentially has two thermally controlled equipment compartments, one hexagonally shaped and containing spacecraft equipment and the other an appendage containing scientific instruments. Forward of the equipment compartments is a 2.75-m-diameter parabolic reflector, which is a basic component of the spacecraft high-gain antenna. Mounted on three struts forward of the reflector are the medium-gain antenna and the feed for the high-gain parabolic reflector. Electric power is supplied by four RTGs mounted in pairs on two radially deployable trusses. The generators are in a stowed position for launch, next to the equipment compartment and under the reflector of the high-gain antenna. The angle between the support trusses for the generators is 120 deg. In the deployed position, the generators extend well beyond the perimeter of the reflector to reduce the radiation environment within the equipment compartments and to reduce their magnetic influence on the magnetometer. This latter instrument is located on the end of a long folding boom, which, in the deployed condition, extends radially from the instrument side of the equipment compartment.

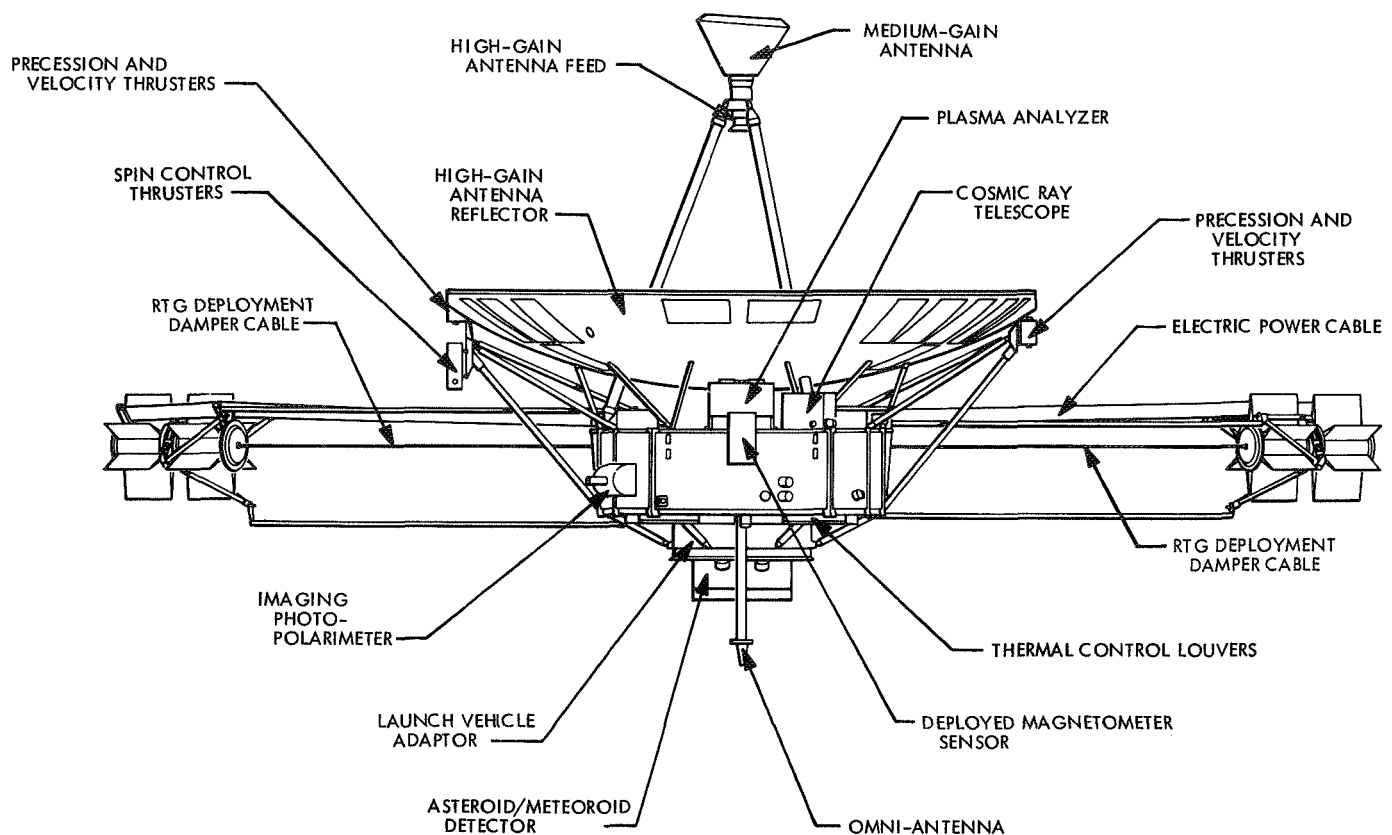


Fig. 4. Pioneer F and G spacecraft (side view)

Numerous viewing apertures are provided in the equipment compartments, as required by the scientific instruments. Mounts, external to the equipment compartment, have been provided for the meteoroid and asteroid instrumentation.

The spacecraft is spin-stabilized with a spin rate somewhat below 5 rpm. The launch vehicle's spin-up system brings the spacecraft, together with the third stage of the launch vehicle, up to a rotational speed of around 60 rpm. After the third-stage burnout and separation, the spin rate will be slowed down from 60 to 20 rpm by the use of automatically fired thrusters. Finally, deployment of the RTGs and the magnetometer will further de-spin the spacecraft to a nominal spin rate of 4.8 rpm. The objective of this spin stabilization is to stabilize spacecraft attitude. Spin-axis precession maneuvers will be applied during the mission to orient the spin axis of the spacecraft to the earth and thus illuminate the earth with the directional beams of the medium-gain and high-gain antennas.

Because the geocentric longitude of the spacecraft varies over a wide range during the mission, the space-

craft has a monopropellant attitude-control system which is capable of precessing the spin axis and maintaining the earth-pointing attitude on command. The initial re-orientation to point the spacecraft spin axis toward the earth will occur within a few hours after launch. The spacecraft is equipped with a complete telemetry and data handling system which will generate a data stream containing the output of the scientific instruments and spacecraft equipment measurements. A system for receiving the modulating and distributing command instructions received from earth will provide flexibility in operation of the scientific instruments and the spacecraft. Spacecraft equipment will deliver conditioned power to the scientific instruments and also supply the instruments with appropriate timing and orientation indexing signals for control of measurements and data accumulation.

IV. Spacecraft Subsystems

A. Electrical Power Supply

The primary electrical power source consists of four Snap-19 radioisotope thermoelectric generators (RTGs).

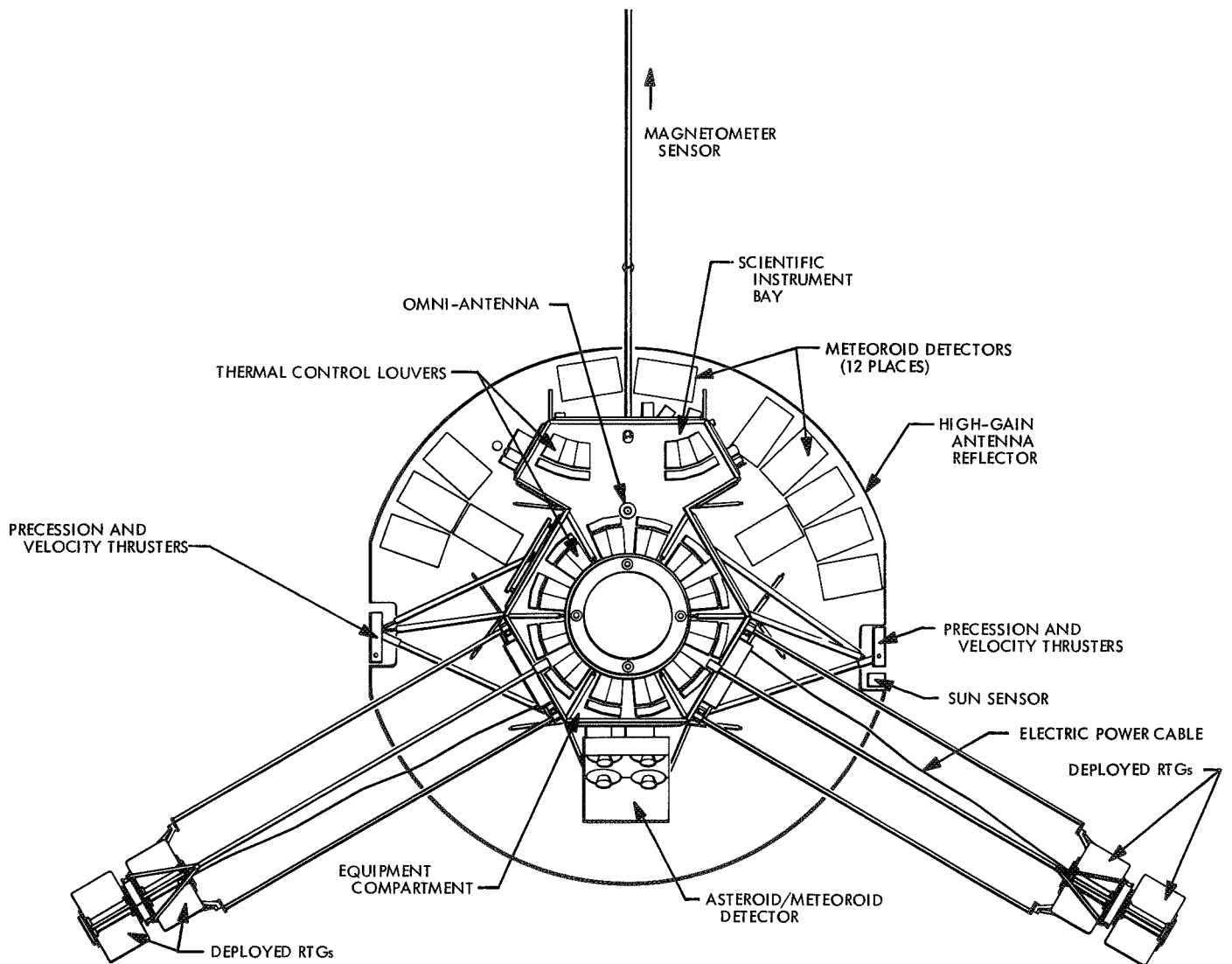


Fig. 5. Pioneer F and G spacecraft (bottom view)

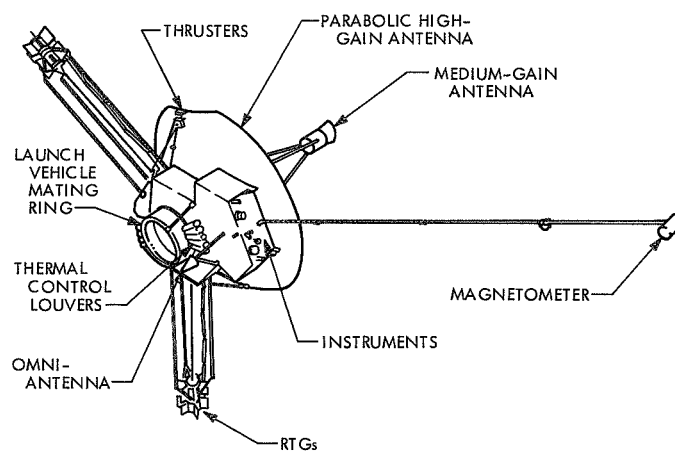


Fig. 6. Pioneer F and G spacecraft (perspective view)

The four units are in pairs in a tandem arrangement on the end of two supporting trusses. Provisions are made for retracting the RTGs to fit within the nose fairing of the launch vehicle for launch and for deploying them radially to the extended position after separation from the launch vehicle. Figure 7 shows the spacecraft mounted in the nose fairing and as assembled for the launch phase of the mission.

Each RTG unit will provide almost 40 W of electrical power during the early part of the mission and about 30 W 5 years after launch. It is expected that the power requirements of the spacecraft and scientific instruments will not exceed the capability of three of the RTG units at the time of Jupiter encounter. Therefore, the probability of having adequate power available at encounter is very high. The net weight of each RTG is around 13.6 kg.

B. Electrical Power Conditioning

The objective of the electrical power subsystem is to distribute and condition the power received from the RTGs to the spacecraft equipment and the scientific instruments. To meet the requirements of the power loads, the dc output of each RTG goes into a separate inverter. The 2.5-kHz squarewave output of the four inverters is fed into an ac bus. Most of the ac power is rectified and filtered to supply the main dc bus, which is shunt-regulated to 28 V $\pm 1\%$ by dumping excess power through an external shunt radiator. The regulation of the 28-V dc bus is reflected back through the ac bus and through the fixed-ratio inverters, fixing the RTGs

operating voltage at 4.2 V. A battery automatically carries any temporary overloads and is recharged automatically when excess power is available. The scientific instruments and the traveling-wave-tube power amplifier of the transmitter section of the transponder receive power from the main dc bus. Most of the other spacecraft loads are supplied from the central transformer-rectifier-filter unit, which receives power from the ac bus and provides various dc output voltages.

C. Structure

The hexagonal equipment compartment is the basic structural element of the spacecraft. It supports the high-gain antenna on its forward end, attaches the launch vehicle by the launch-vehicle mating ring at its aft end, supports the scientific instrument compartment, accommodates the major portion of other subsystem assemblies, and provides for mounting of various external components, including the RTGs and the magnetometer boom. Rigid tubular truss work attached to the framework of the equipment compartment supports the parabolic reflector of the high-gain antenna, the high-gain antenna feed, the medium-gain antenna, the three thruster clusters, the attachment for the deployable booms for the RTGs, and the launch-vehicle mating ring. The reflector of the high-gain antenna is made from an aluminum honeycomb sandwich.

D. Thermal Control

The thermal control subsystem provides the required thermal environment for the spacecraft components and scientific instruments during all phases of the flight. The objective of the thermal control subsystem is to maintain, in the vicinity of the scientific instruments, temperatures between -18 and $+38$ C and to keep the spacecraft equipment at temperatures required for satisfactory operation. Heating effects caused by the RTGs (stowed within the nose fairing), the third-stage motor casing, and the jet plume must be accommodated. The large variations in solar intensity and relative direction during interplanetary flight, and the loss of heat from the equipment compartments through sensor apertures, are compensated through louvers and special installation.

E. Propulsion and Attitude Control

During the major portion of the flight, earth-pointing attitude is necessary for the narrow beam of the high-gain antenna of the spacecraft to illuminate the earth and to maintain effective communications. Figure 8 depicts

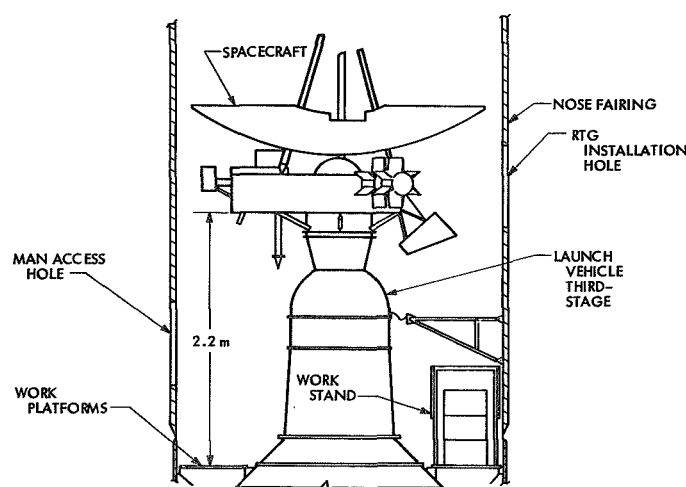


Fig. 7. Folded Pioneer F and G spacecraft mounted on launch vehicle within nose fairing

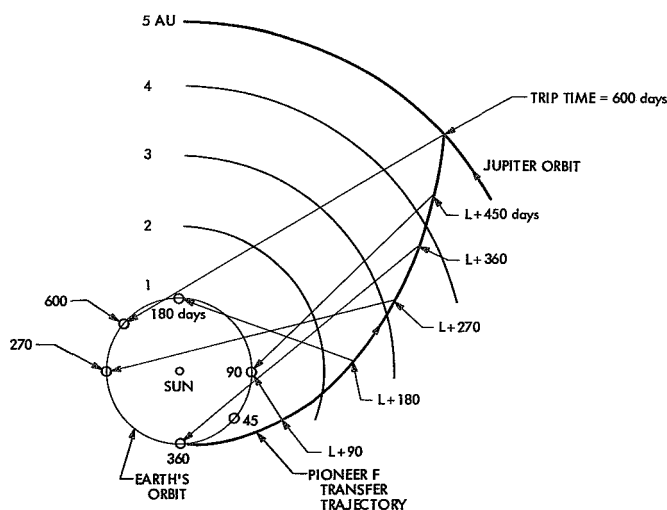


Fig. 8. Relative position of Pioneer F spacecraft spin and antenna axis toward earth

the relative position of the spacecraft's spin and antenna axis versus the earth. It can be seen that the geocentric longitude of the spacecraft varies continuously throughout the mission and, therefore, it is necessary to make numerous attitude adjustments. Since the spacecraft high-gain antenna has a half-power beamwidth of approximately 3.5 deg, it is anticipated that more than 200 spin-axis orientation maneuvers will be necessary to compensate for the relative movement of the spacecraft versus earth, and also for the precession caused by solar pressure, which is 0.2 deg per day during the early part of the mission. In addition, to provide the planned encounter trajectory at Jupiter, some adjustments of the velocity vector may be required during the interplanetary flight. To make the velocity vector adjustments possible, thrust must be generated in a particular direction; therefore, with thrusters in a fixed relationship to the spacecraft, reorientations of the spacecraft will also be necessary.

Changes in the spin rate will also be required. After injection, the rate will be on the order of 60 rpm and must be reduced to about 20 rpm before the deployment of the magnetometer and RTGs. As a result of the deployment, the spin rate is reduced to between 4 and 5 rpm (nominal: 4.8 rpm). In addition, to make possible attitude and velocity changes, small changes in the spin rate have to be corrected to maintain the rate of spin within the required limits.

Changes in attitude, velocity, and spin rate during the interplanetary flight will be accomplished by monopropellant hydrazine thrusters. Thrust will be provided by exothermic decomposition of the hydrazine in a catalyst

bed and extension of the gas through a nozzle. Figure 9 depicts the location of the attitude-control spin control, velocity, and precession thrusters at the edge of the parabolic high-gain antenna structure. These thrusters can be operated in pairs. Each cluster contains a forward-facing nozzle and a rearward-facing nozzle. Two forward or two rearward nozzles will be used for velocity adjustment and opposite-facing nozzles will be fired for attitude changes, causing precession of the spin axis. Spin-rate changes will be accomplished by tangentially aligned nozzles thrusting with and against the spin.

A sun or star sensor (Fig. 10) provides reference signals necessary to time the thrust pulses for precession of the spin axis in a desired direction (Fig. 11). Attitude changes can be accomplished "open loop" by ground command, or "closed loop" by homing the spacecraft on the S-band uplink signal radiated by a deep space station toward the spacecraft. The duration of thrust for velocity and spin-rate changes is established by ground calculations. This information is transmitted to the spacecraft, where it is stored for execution on command. Similarly, for an "open loop" reorientation, the direction and amount of precession desired can be transmitted to the spacecraft via the command link and stored for execution on command. This storage information can be combined to perform a precession-velocity change-precession sequence with suitable time intervals in the sequence and to provide a completely automated velocity vector adjustment with return to a selected spacecraft orientation.

A closed-loop decision maneuver will be used regularly for accurate realignment of the spin axis of the spacecraft toward earth. A medium-gain and a high-gain spacecraft antenna will be used, respectively, for course and fine homing on the uplink and telecommunications signal. For the closed-loop maneuver, the axis of the medium-gain antenna and the feed of the high-gain antenna are offset from the spin axis and provide an amplitude-modulated signal when the spin axis is not aligned with the earth. The so-called CONSCAN subsystem processes this signal and fires the precession thrusters to establish the required precession and orient the spin axis toward earth.

The hydrazine will be supplied to the thrusters through appropriate lines and valves from a single, spherical pressurized bladder-tank, which is located in the center of the spacecraft equipment compartment. Electrical and small radioisotope heaters will be used to keep the plumbing of the hydrazine system above 2°C, which temperature keeps the fuel in a liquid state.

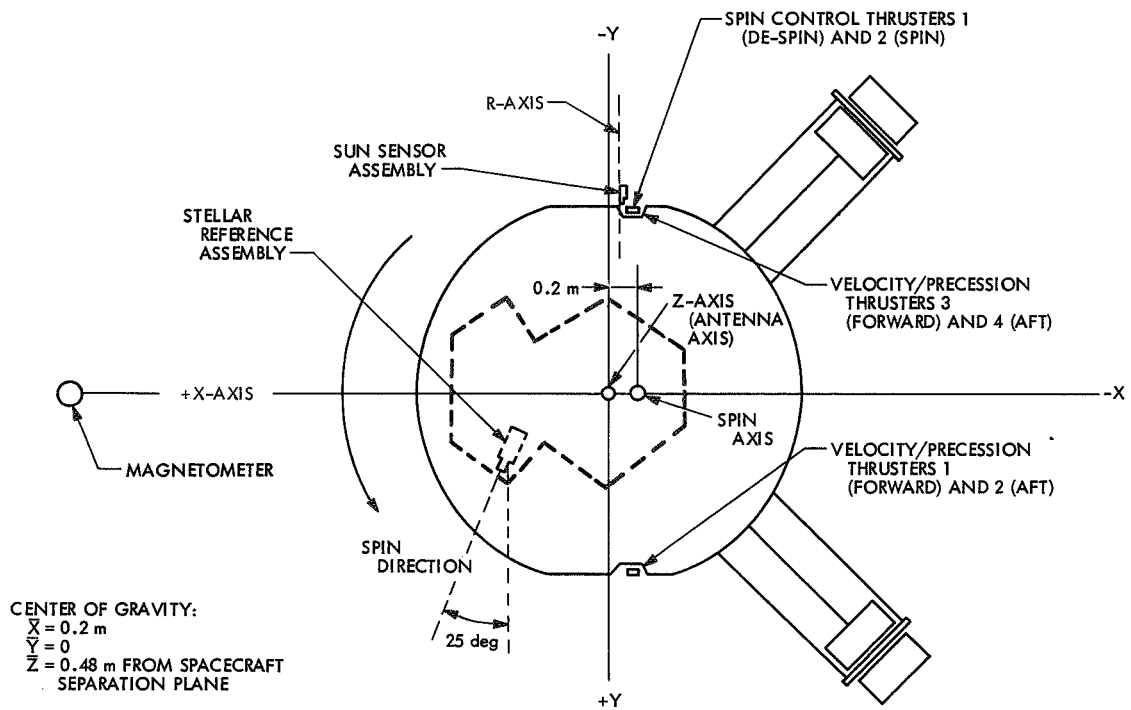


Fig. 9. Attitude-control equipment locations (view looking aft, from spacecraft to booster)

CHANNEL	FIELD OF VIEW FROM X-Z PLANE, deg	FIELD OF VIEW FROM Z-AXIS, deg	FIELD OF VIEW, deg 30 x 0.2
1	—	±12	
2	0.5	12 - 90	
3	0.5	90 - 170	

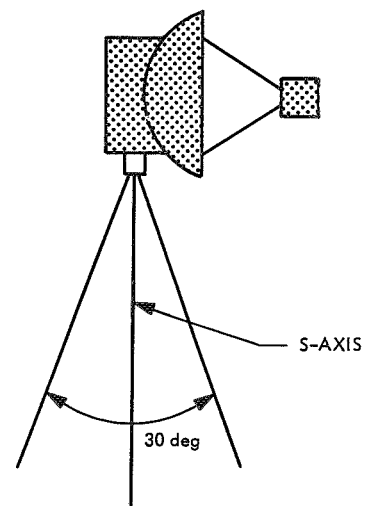
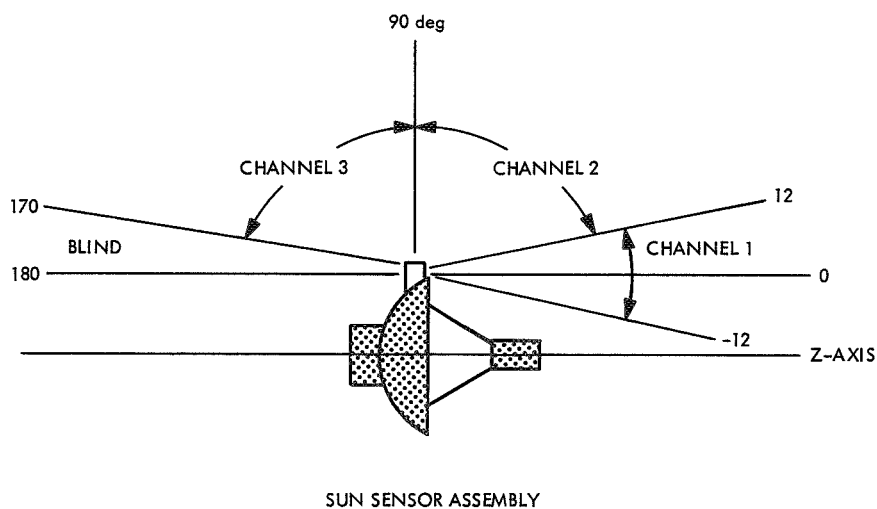
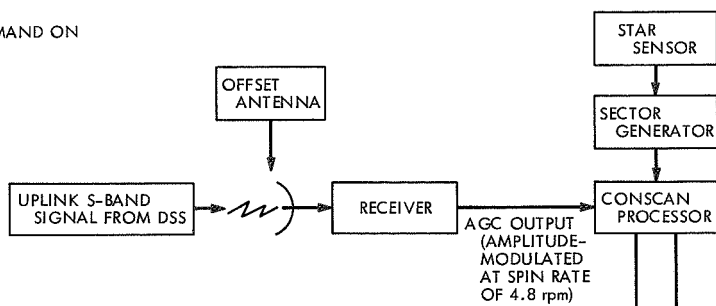


Fig. 10. Sun and star sensors

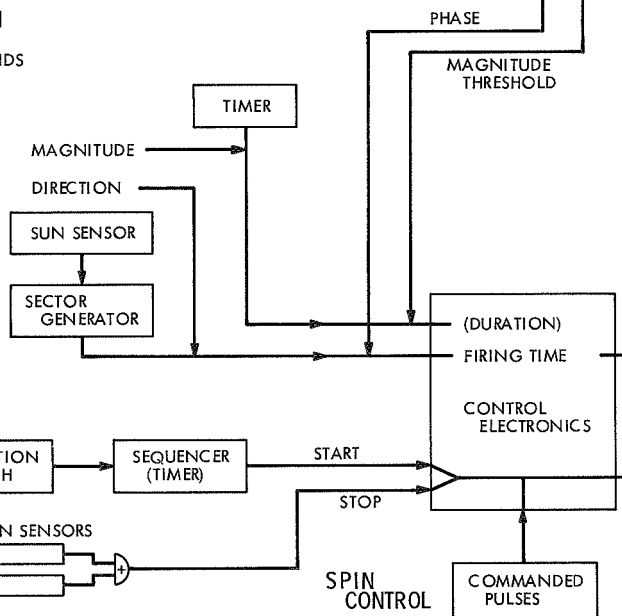
CLOSED-LOOP EARTH TRACKING

COMMAND ON

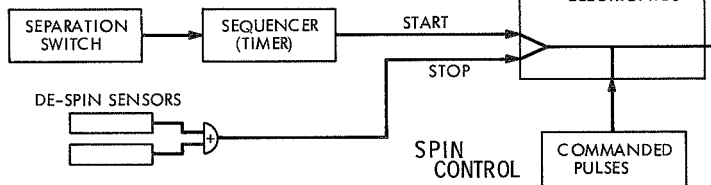


OPEN-LOOP PRECESSION

STORED COMMANDS



DE-SPIN



PERFORMANCE

PROPELLANT
~ 27.2 kg HYDRAZINE

CAPABILITY
200 m/s + 1250-deg PRECESSION
+ 14 rpm + DE-SPIN

PRESSURE
BLOWDOWN: 369 - 93 N/cm² (535 - 135 psi)

THRUST (ONE THRUSTER)
0.52 - 0.24 kg

SPECIFIC IMPULSE
215 s (CONTINUOUS)
140 s (PULSED)

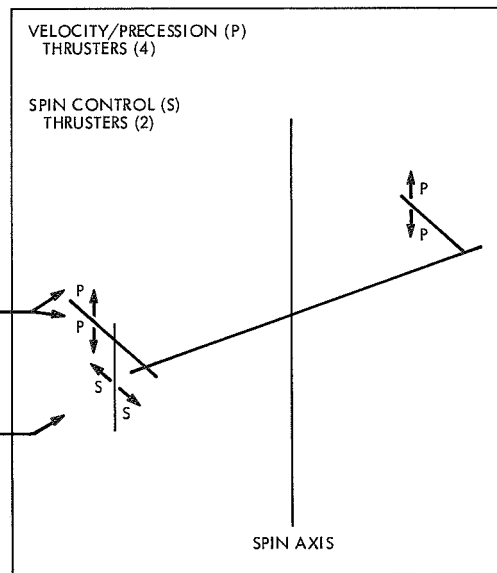


Fig. 11. Attitude, velocity, and spin control (attitude-control subsystem)

Reference

1. Siegmeth, A. J., "Pioneer Mission Support," in *The Deep Space Network*, Space Programs Summary 37-66, Vol. II, pp. 4-11. Jet Propulsion Laboratory, Pasadena, Calif., Nov. 30, 1970.

Helios Mission Support

P. S. Goodwin
Mission Support Office

This article relates the historical factors that led to the establishment of Project Helios; describes the project management relationships between the United States and the Federal Republic of West Germany, and the role of the Deep Space Network; and gives a brief description of the spacecraft and its telecommunications subsystem.

I. Background

The Space Act of 1958 authorized the National Aeronautics and Space Administration (NASA) to conduct programs of international cooperation with other nations in the peaceful exploration of space. To implement this article in the NASA Charter, the U.S. National Academy of Science, in behalf of NASA, introduced an offer of international space cooperation to the Committee on Space Research of the International Council of Scientific Unions. This, in turn, led to discussions between United States and Federal Republic of West Germany officials on the subject of a possible advanced cooperative project in space. An agreement in principle was made between the German Minister for Scientific Research, Gerhard Stoltenberg, and NASA Administrator James E. Webb in September of 1966 to carry out a cooperative solar probe project—provided that a mission of mutual interest could be defined. This decision was made official during Chancellor Erhard's visit with President Johnson in November 1966. This project was subsequently named *Helios* after the ancient Greek goddess of the sun.

To implement this agreement, NASA and the West German Minister for Science established a *Helios* Mission Definition Working Group in July 1968. This group's

effort culminated in the publishing of the *Helios* Program "Mission Definition Group Report," dated April 1969. This report recommended that two solar probes be launched toward the sun—one each in calendar years 1974 and 1975—to achieve a perihelion distance from the sun of approximately 0.3 AU. Each spacecraft would carry ten experiments to perform fields and particle measurements in the region between the earth and the sun. The target perihelion distance of 0.3 AU was selected because it was a heretofore unexplored region of interplanetary space and was within the estimated extrapolation of the state-of-the-art for the high-temperature solar cells necessary to generate spacecraft power. The size and weight of the proposed *Helios* spacecraft was recommended to be compatible with the *Atlas/Centaur* launch vehicle, with the addition of a TE-364-4 solid propellant third-stage.

The publication of the *Helios* Mission Definition Report was followed by a "Memorandum of Understanding" between NASA Administrator Thomas Paine and German Science Minister Gerhard Stoltenberg in June 1969, and by joint statements by President Nixon and Chancellor Kiesinger in August 1969. These documents ratified the activities to date and established the basis

for the future relationships between the two participating countries. The *Helios* Project would be managed jointly by both countries, with each co-manager being responsible for those elements of the cooperative project that were assigned to his particular country. In brief, the West German Project Manager would be responsible for the design, development, and fabrication of the spacecraft and the mission design and operations, while the U.S. Project Manager would be responsible for the launch vehicle, the launch facilities, and the tracking and data system. Of the ten onboard scientific experiments, seven were to be of German origin, and three of U.S. origin—however, the integration of all ten experiments into the spacecraft would be the responsibility of the West Germans. Each country would be responsible for providing the funding necessary to accomplish its portion of the program. Coordination of the effort was to be achieved via semiannual Joint Working Group Meetings to be held alternately in each country. The first *Helios* Joint Working Group Meeting was held in September 1969 in Bonn, West Germany. Subsequently, two additional Joint Working Group Meetings have been held: the second in April 1970 at Goddard Space Flight Center, Greenbelt, Maryland; and the third in October 1970 in Bonn. The next *Helios* Joint Working Group Meeting is scheduled for late April 1971 at Goddard Space Flight Center.

II. *Helios* Project Management Organization

In addition to the scientific objectives mentioned above, a second and very important objective of the *Helios* Project is to develop a broad governmental-educational-industrial technological base within the Federal Republic of Germany to conduct space research. Therefore, the West German participation in the *Helios* Project is not solely restricted to the development of the spacecraft and the mission design, but also includes the development of German tracking facilities, a German Control Center, and a full mission operations organization to conduct the mission. In addition, the international agreement provides for the cross-training of a significant number of West German specialists at various NASA installations to learn U. S. techniques pertaining to space exploration. These factors, together with the international character of the project, account for the "committee-like" structure of the *Helios* Project Management Organization (Fig. 1).

The upper lefthand quadrant of Fig. 1 depicts the familiar NASA flight project organizational structure wherein NASA Headquarters assigns the project management responsibility to one of its field centers, with

functional support in specific areas being provided by other NASA field centers. The significant difference here is that only a portion of the elements comprising a total flight project are represented. The missing elements appear on the West German side of the interface in the upper righthand quadrant of Fig. 1—along with some new elements due to the factors mentioned above. The West German *Helios* Project management is seen to parallel and complement the U.S. *Helios* Project organization so that, in total, the top half of Fig. 1 represents the formal international project organization for Project *Helios*. An important advantage of this formal structure is that it provides a clear and distinct division of responsibility between the two countries in the administration, technical supervision, and financial management of the *Helios* Program.

As mentioned above, the technical coordination of the two countries' efforts is accomplished via the *Helios* Joint Working Group activities. The *Helios* Joint Working Group organizational structure is depicted in the bottom half of Fig. 1. In accordance with the international agreement, the Joint Working Group Meetings are co-chaired by the U. S. and West German *Helios* Project managers, respectively. Reporting to them are the chairmen of the various technical subgroups that support the project. These subgroup chairmen are the same individuals who have been assigned the equivalent functional responsibility in the formal project organization depicted in the top half of Fig. 1. However, the subgroup panel membership within each of these technical subgroups is fairly evenly divided between the U. S. and West German representatives in order to achieve internationally optimum solutions to problems facing the project. During the semiannual *Helios* Joint Working Group sessions, these subgroups meet both individually to resolve problems within their own areas of specialization, and jointly to resolve problems associated with the interface between the areas of technical responsibility. When necessary, the activities of the subgroups are augmented by special task or study groups assigned to investigate in detail a particular aspect of the program. A recent and successful example of the latter was the establishment of a special study group to develop a typical near-earth phase sequence of events following launch in order to determine that the spacecraft design as currently contemplated will fulfill all operational constraints upon the mission. This study group was chaired by the Mission Analysis and Operations Subgroup and its membership was comprised of representatives from each of the other subgroups. Once it has accomplished this initial task, the Near-Earth Phase Study Group will probably become

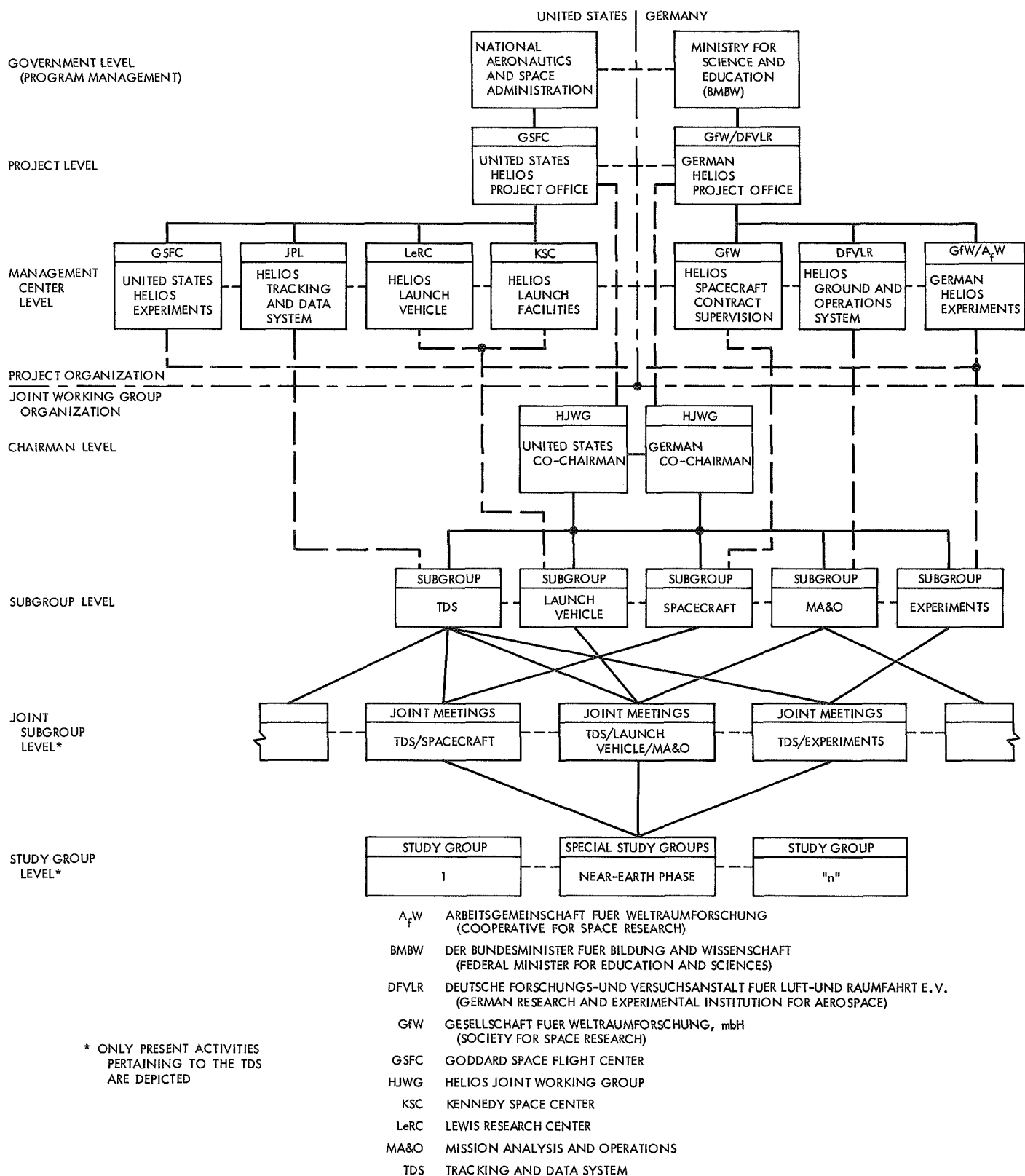


Fig. 1. Helios Project Management Organization

dormant until the final launch trajectories are developed. At that time, the group is expected to reconvene to prepare the final near-earth phase sequence of events.

The technical decisions reached during the *Helios* Joint Working Group Meetings are reviewed by the co-chairmen. Upon their approval, these decisions are routed via the respective project office to the formal organization (top portion of Fig. 1) for implementation. In the case of decisions affecting the U. S. Tracking and Data System (TDS), these are routed to the Jet Propulsion Laboratory as the cognizant NASA field center for *Helios* TDS management. The NASA TDS function for *Helios* has two major subdivisions: (1) support from the near-earth phase facilities, and (2) support from the Deep Space Network (DSN). The near-earth phase facilities have TDS responsibility from launch up to that portion of the trajectory wherein the DSN has continuous visibility of the spacecraft, at which time the DSN assumes responsibility for the TDS function. The near-earth phase facilities are composed of selected stations from the NASA MSFN and STADAN Networks and from the Air Force Eastern Test Range (AFETR). The selection of stations from these facilities is a function of the particular trajectory flown and the individual project's data requirements. The selection is individually negotiated by the JPL Cape Kennedy Field Station for each flight project, but in general is composed of both tracking stations (including radars) and telemetry reception stations. The near-earth phase facilities may or may not have a requirement to send commands to the spacecraft—depending upon the criticality of the flight sequence during the near-earth phase of the particular mission. However, the AFETR at all times retains responsibility for range safety. Data from the near-earth phase stations are fed via a combination of NASCOM and/or AFETR communications circuits back to Cape Kennedy, Florida, where flight operations are conducted for the near-earth phase of the mission. During this period, radiometric data are fed to the Cape Kennedy Real-Time Computer Complex, where early trajectory computations are performed. Near-earth phase telemetry data are displayed at the Mission Control Center at Cape Kennedy and are also routed to the DSN's Space Flight Operations Facility (SFOF) in Pasadena, California. When the spacecraft reaches the pre-determined point in the trajectory, the TDS responsibility is transferred to the DSN. By this time, mission operations responsibility has been transferred from Cape Kennedy to the SFOF.

The other part of the NASA Tracking and Data System is the Deep Space Network. Its function in supporting

Helios is to provide near-continuous tracking, telemetry, and command support from initial acquisition through the end of the primary mission. In accomplishing these objectives, the DSN will request and receive TDS support from the stations being implemented in West Germany. Also, as noted before, the West Germans have responsibility for mission operations. During Phase I, the period from launch through 2 to 4 weeks following launch, the West German Mission Operations Team will reside in the SFOF. At the conclusion of Phase I, *Helios* mission operations will be transferred from the SFOF to the German Control Center in Oberpfaffenhofen (near Munich), West Germany. This will initiate Phase II, which will conclude at the end of the primary mission. During Phase II, the German Control Center will act as a remote terminal to the SFOF for the conduct of mission operations; however, network operations will continue to be conducted from the SFOF since the DSN retains TDS responsibility through the end of Phase II. Because of these additional operational interfaces, the DSN has representative membership in the TDS and MA&O Subgroups (center portion of the lower half of Fig. 1). In addition, the DSN has been assigned the responsibility for training over a dozen West German specialists. These factors explain why the DSN's support to the *Helios* Project is slightly more complicated organizationally than the support provided to a typical U. S. flight project. However, the organizational structure depicted in Fig. 1 has been functioning very satisfactorily to date and there is no anticipation of the need for a significant change to occur during the lifetime of the project.

III. Spacecraft Description

A. Physical Concept

A description of the current configuration of the spin-stabilized *Helios* spacecraft is helpful in understanding the support requirements that the spacecraft design places upon the Deep Space Network. The present *Helios* spacecraft concept differs only slightly in appearance from one of the two proposed configurations in the Mission Definition Report. The report had assumed that the spacecraft would be launched by an *Atlas/Centaur/TE-364-4* launch vehicle combination. By the time of the second *Helios* Joint Working Group Meeting (April 1970), it became possible for the *Helios* Project to consider employing a *Titan-IIID/Centaur/TE-364-4* launch vehicle combination. Since this was a possibility rather than a firm commitment, the *Helios* project managers decided that instead of permitting the spacecraft design to in-

crease significantly in either size or weight, they would target the *Helios* mission profile to have a perihelion closer to the sun—i.e., 0.25 AU instead of 0.3 AU. This decision markedly altered the thermal design of the spacecraft (which now must withstand 16 solar constants¹ at perihelion instead of the previous 11 solar constants—due to the inverse square law effect), but would not preclude flying the new configuration to the original 0.3-AU perihelion in the event it was necessary to return to the *Atlas/Centaur/TE-364-4* launch vehicle. As a result, the alternate cylindrical shape for the main body of the spacecraft recommended in the Mission Definition Report was discarded in favor of the spool shape shown in Fig. 2. The conical sections of the spacecraft body in the current design reflect unwanted solar energy away from the spacecraft structure while at the same time provide for a reasonable angle of incidence between the sun rays and the solar cells that are mounted on these conical surfaces. Also, because of the greater solar energy, a fewer number of solar cells were required.

¹A solar constant is defined as the average solar energy received at earth distance from the sun, i.e., the solar flux at 1.0 AU.

Therefore, the current design contains a mixture of 50% solar cells and 50% second surface (i.e., front surface) mirrors to reflect excess solar energy from the conical surfaces. The cylindrical midsection, containing no solar cells but all of the spacecraft electronics and the bulk of the onboard scientific experiments, remains basically unchanged from that depicted in the Mission Definition Report. The maximum spacecraft design weight of 280 kg (570 lb) is compatible with either a *Titan* or *Atlas* for the first stage of the launch vehicle combination. The overall clearance dimensions of the spool-shape spacecraft configuration can be accommodated by using either of the more recently designed *Viking-Mars* or *Intelsat IV* shroud systems (depending upon launch vehicle selection) rather than an extended version of the *Surveyor*-type spacecraft shroud contemplated during the Mission Definition Group's studies. Therefore, the present *Helios* spacecraft design configuration meets the objectives set forth in the Mission Definition Report when using the *Atlas/Centaur*, while at the same time permits trajectories to be flown closer to the sun—i.e., 0.25 AU and possibly 0.2 AU—when launched aboard a *Titan/Centaur* launch vehicle combination. For the present, planning is pro-

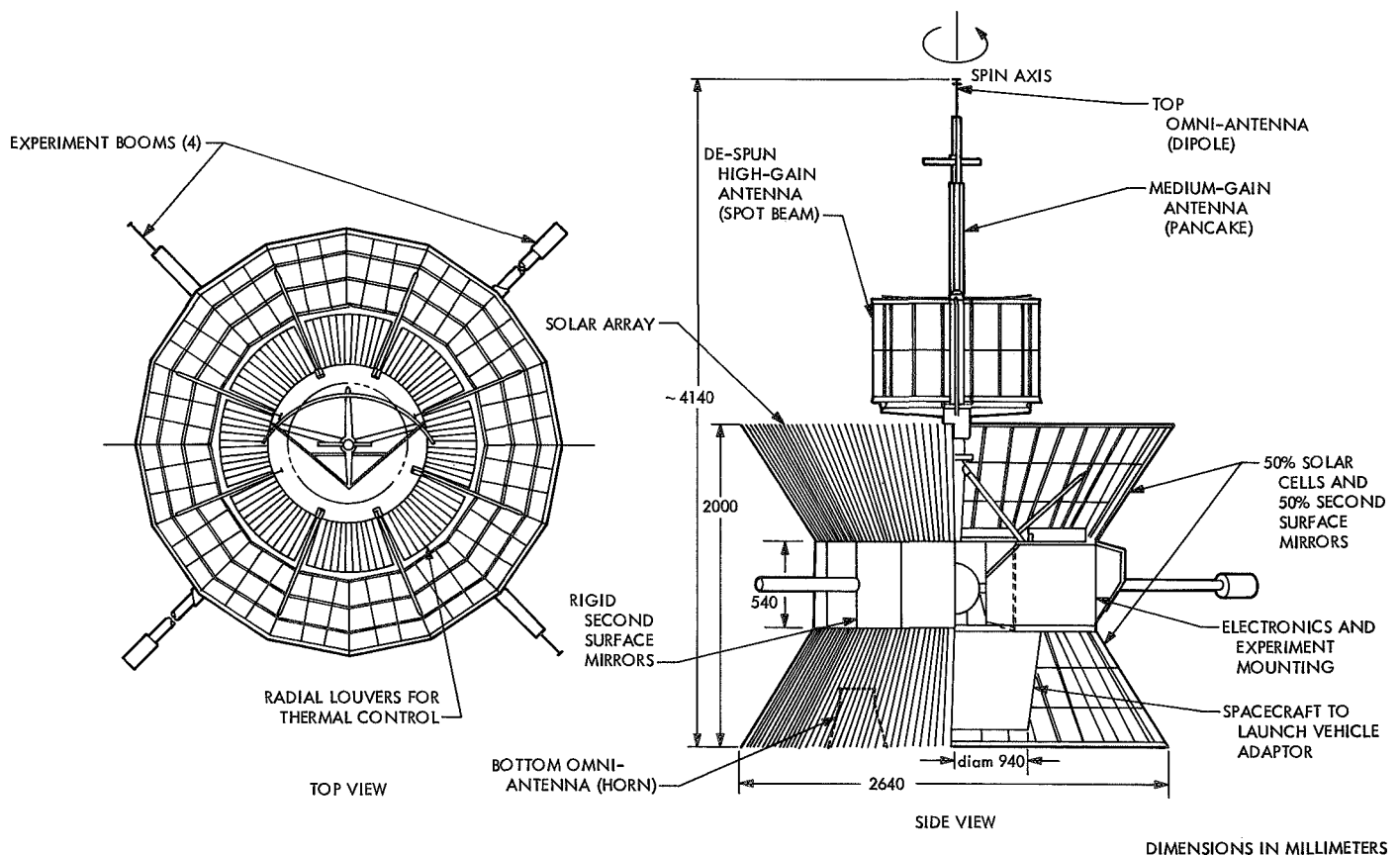


Fig. 2. *Helios* spacecraft

ceeding on the assumption that the *Titan/Centaur* launch vehicle will be used; however, these plans are constrained to always maintain compatibility to use the *Atlas/Centaur* vehicle. As might be expected, these launch vehicle constraints impact the thermal and structural design of the spacecraft much more significantly than they do the telecommunications system design.

B. Antenna System

Following injection of the spacecraft into its heliocentric orbit, and DSN acquisition, the spacecraft is positioned by command such that its spin axis (Fig. 2) is pointing to the pole of the ecliptic. This maneuver provides proper illumination of the solar cells and positions the spacecraft's antennas such that their patterns will intercept the earth throughout the trajectory of the spacecraft. There are three parts to the *Helios* spacecraft antenna system: (1) a two-antenna, quasi-omni-directional system; (2) a medium-gain antenna system whose "pancake" pattern lies in the plane of the ecliptic; and (3) a high-gain or "spot-beam" antenna that is mechanically oriented to point directly at the earth throughout the spacecraft's heliocentric orbit. These antennas are individually described below.

The omni-directional antenna system is composed of a linearly polarized dipole antenna atop the central mast (Fig. 2), and a circularly polarized horn antenna pointing downward and mounted inside of the bottom solar cell conical skirt. These two antennas are hard-wired to a fixed ratio power splitter, thence to one of the two onboard transponders (Fig. 3). The division ratio of the power splitter is adjusted such that the combination will provide a nearly uniform combined antenna pattern almost completely surrounding the spacecraft. The omni-antenna system finds its primary use during the period from shroud ejection following launch up through the completion of the orientation maneuver that positions the spin axis of the spacecraft toward the pole of the ecliptic. Since the latter maneuver is completed by the time the spacecraft reaches a distance from earth equivalent to the moon's orbit, the omni-directional antenna system might be considered the "near-earth" antenna system. However, this is not to imply that the omni-directional antenna system will not be used during later phases of the mission when signal margins permit.

The medium-gain antenna consists of a single longitudinal helix antenna mounted on the mast beneath the omni-antenna but above the high-gain antenna. This antenna produces a linearly polarized, pancake-like pat-

tern which, following the above-mentioned maneuver, directs its maximum radiation in all directions within the plane of the ecliptic while minimizing its radiation toward the poles of the ecliptic. It is approximately 15 deg wide in the direction perpendicular to the ecliptic and has a downlink gain of 8 dB. It is the prior knowledge of this pattern that enables the final positioning of the spacecraft spin axis toward the pole of the ecliptic. The medium-gain antenna is connected through a second diplexer to the second transponder aboard the spacecraft. However, the transmitter portion of the second transponder is shared between the medium-gain antenna and the high-gain antenna described below.

The *Helios* spacecraft high-gain antenna is a cylindrical, parabolic-shaped reflector that is mechanically despun to counter the spacecraft body's spin-rate of 60 rpm. The de-spin angular velocity is adjusted to exactly counter-match the spacecraft body's spin velocity in order to achieve a fixed beam direction in space. The direction that the spot-beam points within the plane of the ecliptic is a phase angle adjustment with respect to the pulses received from the onboard sun sensor that clocks the speed of the spool-shaped main body of the spacecraft. Since the angle between the sun and the earth changes as the spacecraft traverses its elliptical heliocentric orbit, the phase angle for the high-gain antenna must be updated by earth command during the mission. The high-gain antenna beam is again linearly polarized with a beamwidth of 5½ deg within the plane of the ecliptic, and 14 deg normal to the plane of the ecliptic. The downlink gain of this antenna is 23 dB. It is used to transmit high-rate telemetry from the spacecraft to the earth, and operates in conjunction with the spacecraft receiving on the medium-gain antenna, using the second transponder mentioned above. Since the second transponder contains a turnaround ranging loop, it is possible to employ either the DSN lunar or planetary ranging system in conjunction with the spacecraft medium-gain antenna system. However, at perihelion distances and beyond, the spacecraft's radio system configuration will be such that it will receive ranging signals via the medium-gain antenna and return them to earth via the high-gain antenna.

C. Radio System

The foregoing *Helios* spacecraft antennas are connected to the onboard radio system, as depicted in Fig. 3. As mentioned previously, the spacecraft contains two complete transponders. Despite the fact that these transponders operate on the same frequencies (both uplink and downlink), they are not completely redundant

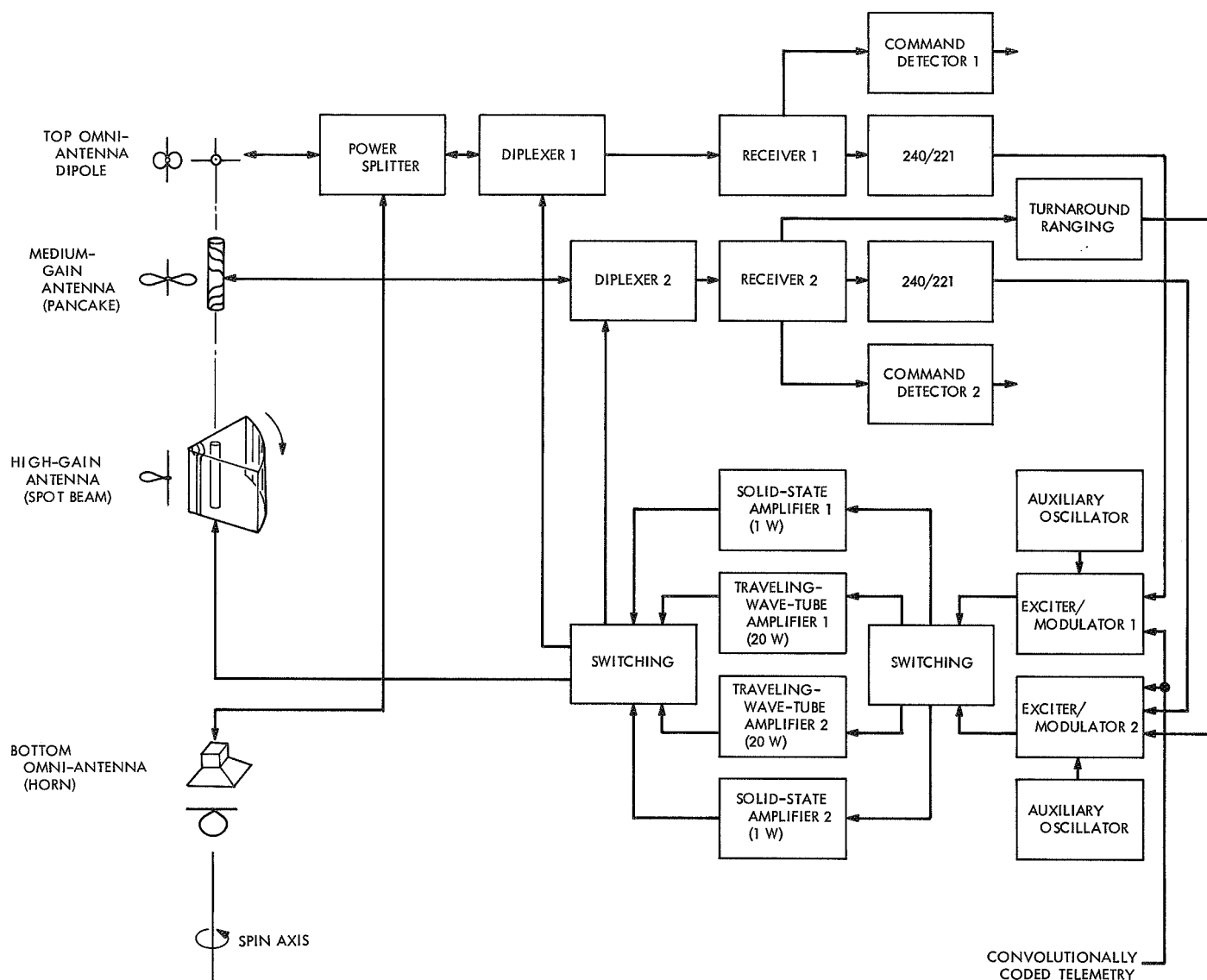


Fig. 3. Helios spacecraft radio system

in that the transponders are partially hard-wired and partially switchable. To explain the degree of redundancy provided by the present *Helios* spacecraft radio system design, it is best to describe the signal flow under various mission conditions.

From launch through the completion of the maneuver that orients the spin axis to the pole of the ecliptic, the spacecraft is operating with the omni-directional antenna system and with transponder 1. Prior to separation of the spacecraft from the TE-364-4 third-stage, uplink and downlink communication is via the top omni-antenna (since the bottom omni-horn-antenna is masked by the third-stage rocket motor). At separation, the spacecraft

is spinning with the spin axis oriented along the velocity vector of the outgoing trajectory, which lies in the plane of the ecliptic. Since, under these circumstances, the medium-gain antenna pattern intercepts but a small segment of the earth, the omni-antenna system is used for initial DSN acquisition. The two-antenna omni-system provides nearly spherical antenna pattern coverage except for a null directly ahead of the spacecraft. Since the "look-angle" from the spacecraft to an earth station will traverse this forward null very rapidly as the spacecraft departs the vicinity of the earth, the existence of this forward null does not impose a serious initial acquisition constraint. Following separation, onboard sun sensors cause the spacecraft's attitude control system to

perform the first of two orientation maneuvers—namely, to position the spacecraft's spin axis such that the spacecraft's solar cells receive maximum energy from the sun. During this (step I) maneuver, the spacecraft's spin axis remains basically in the plane of the ecliptic. Since, depending upon the trajectory, the initial DSN acquisition of the injected spacecraft can occur prior to, during, or subsequent to the completion of the step I maneuver, a nearly uniform spacecraft omni-directional system is needed. Following completion of the step I maneuver, the spacecraft's attitude remains fixed while the *Helios* Mission Operations Team in the SFOF evaluates the condition of the various onboard systems, using spacecraft telemetry. Following this, selected scientific experiments aboard the spacecraft are activated in the near-earth science mode. The near-earth science phase is complete by the time the spacecraft reaches lunar distance from the earth. At this time, the science instruments are deactivated and the spacecraft is readied for the second orientation maneuver (step II). During the step II maneuver, the spin axis is commanded to precess in a direction that will orient it to the pole of the ecliptic. As this is done, the medium-gain antenna's pancake-like pattern will slowly begin to intercept the earth. At this time, the spacecraft is commanded to operate with transponder 2 in the diplex mode via the medium-gain antenna. Using the received signal strength at the DSS as an indicator, the spacecraft is commanded to continue precessing its spin axis until the pancake antenna pattern causes a maximum signal strength indication to be achieved on earth. The maximum is determined by causing the spacecraft to precess beyond its optimum orientation and then return to the optimum position—at which time the spin axis will be oriented toward the pole of the ecliptic. Following completion of the step II maneuver, the de-spin velocity and phase angle of the high-gain antenna are adjusted by command to direct the "spot beam" toward earth. Since the spinning spacecraft will be self-stabilized (gyroscopically) in this position (unless unexpectedly perturbed), no further orientation maneuvers should be necessary. All ten onboard scientific instruments are then activated and commanded to return data via the high-gain antenna at the maximum information rate permitted by the telecommunications system capability through the remainder of the mission. The foregoing orientation maneuver considerations explain in part the rationale behind the radio system block diagram shown in Fig. 3. Other aspects will be discussed in the paragraphs that follow.

The benefits achieved by having redundant components aboard the spacecraft must be traded off against

the reliability of the switching circuits necessary to utilize the redundant component. Since these studies are still in process, the *Helios* Project spacecraft radio system depicted in Fig. 3 is subject to change with time. Nevertheless, an understanding of the basic design philosophy of the *Helios* spacecraft radio system as presently conceived is helpful in assessing its operational impact upon the DSN. For instance, it is interesting to note that the redundant components associated with the uplink from the DSN to the spacecraft have separate, hard-wired paths, while the redundant components in that portion of the transponder associated with the downlink are connected to switching matrices which permit the use of a number of alternate paths or operating modes in the event of a failure along one of the downlink paths.

Let us consider first the uplink portion of the spacecraft radio system. As mentioned previously, both transponder loops operate on the same center frequency. Also, both receiver 1 and receiver 2 are continuously energized in order to ensure an uplink command capability to the spacecraft. Since these receivers are hard-wired to separate antennas, the selection of the uplink transponder path is determined by spacecraft logic circuits that select the stronger of the two signals from the receiver automatic gain control values. Prior to the completion of the step II orientation maneuver, it is anticipated that the stronger signal will be via the omni-directional antenna and receiver 1 since the medium-gain antenna pattern will not have yet been oriented toward earth. Following the step II maneuver, the reverse should be true since the medium-gain antenna has an uplink advantage of approximately 6 dB over the omni-directional system. The transition characteristics between these two antenna/receiver paths are dependent upon both the actual trajectory being flown and the sequences employed in the orientation maneuvers. For these reasons, it is quite possible that future studies will show the need for some kind of mode control within the spacecraft receiver loops during the orientation maneuvers in order to prevent the interruption of two-way lock due to unwanted antenna switching. However, with respect to commands, the following precautions have already been taken: (1) The subcarrier frequency for command detector 2 has been made intentionally different from that for command detector 1; and (2) since the command bit rates for the two channels are submultiples of their subcarrier frequency, the bit rates to the two command detectors are different. These two features ensure that commands will be executed only via the pre-selected channel. The last major distinction

between the two uplink channels aboard the spacecraft is that the turnaround ranging loop components are connected only to receiver 2. This is because uplink signal-to-noise ratio considerations via the omni-antenna system very rapidly diminish the usefulness of that path once the spacecraft has been injected into heliocentric orbit. Since the *Helios* spacecraft reaches a distance from earth equal to the moon's orbit approximately 9 h after launch, it was felt that the additional complexity and weight associated with a ranging loop via the omni-antenna was not justified.

Next, let us consider the downlink portion of the *Helios* spacecraft radio system. In contrast to the uplink portion of the system, the active downlink path through the radio system is under ground-commandable mode-control. As implied by Fig. 3, a considerable number of paths or modes are possible in the downlink portion of the radio system. For the moment, only the more significant modes or combinations will be discussed. First, the downlink portion of the radio system may be operated in either the non-coherent or the coherent mode in association with one of the uplink receivers. The non-coherent mode utilizes onboard auxiliary crystal oscillators to derive the transmitter's frequency. This mode is used principally prior to the initial DSN acquisition and again during solar occultation periods. The coherent mode employs the uplink frequency (as received aboard the spacecraft) multiplied by the ratio of 240/221 in order to translate it to the nominal downlink frequency. The coherent mode is required for two-way doppler tracking and for ranging.

The coherent mode is the primary mode of operation during the cruise phase of the mission. Regardless of whether the non-coherent or coherent mode is selected, only one exciter/modulator is activated at one time. The active exciter/modulator feeds one of four possible amplifier circuits, only one of which is active at a given time. The four power amplifier circuits are composed of redundant modules of two classes of amplifiers: (1) 1-W solid-state amplifiers whose primary service is during the near-earth phase of the mission, and (2) 20-W traveling-

wave-tube amplifiers used during the main phase of the mission. Following the spacecraft power amplifiers is a switching matrix circuit which will permit the downlink to be sent to earth via any one of the three antenna systems described in *Section III, Part B*. Modulated onto this downlink carrier signal is the spacecraft's single-channel, convolutionally coded telemetry—which contains a preprogrammed commutation of both science and engineering data. Also on the downlink carrier signal is the turnaround ranging modulation from receiver 2, which is sent to exciter/modulator 2 to be returned to earth via either the medium-gain or the high-gain antenna system. This completes, for the moment, the basic functional description of the *Helios* spacecraft radio system.

IV. Conclusion

This article has attempted to provide the reader with a basic understanding of the international character of the *Helios* project—how it became established and how it is organized. In addition, the reader has been given an overview of the spacecraft configuration and a brief description of its onboard radio system. The next article will discuss the launch windows and probable launch dates for the two proposed *Helios* spacecraft missions, the nominal post-injection trajectories and attitude maneuvers of the spacecraft as they relate to the support to be provided by the DSN, and a discussion of the DSN tracking load imposed by support to other flight projects during the *Helios* time-period. These two articles will then form the baseline for detailed descriptions of the various subsystems within the *Helios* spacecraft radio system and their interfaces with the DSN, starting with the third article. However, since the *Helios* spacecraft configuration and mission profile design are subject to evolutionary improvement between the present time and the launch of the first spacecraft in the summer of 1974, future articles will also include any evolutionary design changes that affect the spacecraft/DSN telecommunications link, or the interface between the DSN and the *Helios* Project's Mission Operations Team.

Bibliography

These documents are on file in The *Helios* Project Office, Goddard Space Flight Center, Greenbelt, Md., and in The *Helios* Project Office, Gesellschaft fuer Weltraumforschung, mbH, Bonn-Bad Godesberg, West Germany.

Helios Program Mission Definition Report. National Aeronautics and Space Administration—Der Bundesminister fuer Bildung und Wissenschaft, Washington, D.C. (Bonn-Bad Godesberg, West Germany), Apr. 1969.

Project Plan for Helios A and B. Goddard Space Flight Center, Greenbelt, Md., Nov. 1970.

Helios Spacecraft Requirements Document, GfW TN 70/14. Gesellschaft fuer Weltraumforschung, mbH, Bonn-Bad Godesberg, West Germany, Jul. 1970.

Preliminary Support Instrumentation Requirements Document. Gesellschaft fuer Weltraumforschung, mbH, Bonn-Bad Godesberg, West Germany, Sep. 1970.

Preliminary Experiments Command and Data Handling Requirements Document. Gesellschaft fuer Weltraumforschung, mbH, Bonn-Bad Godesberg, West Germany, May 1970.

Project Helios Minutes for First Joint Working Group Meeting at Bonn-Bad Godesberg, Sep. 23–26, 1969. Gesellschaft fuer Weltraumforschung, mbH, Bonn-Bad Godesberg, West Germany.

Project Helios Minutes for Second Joint Working Group Meeting at Goddard Space Flight Center, Greenbelt, Maryland, Apr. 27–30, 1970. Goddard Space Flight Center, Greenbelt, Md.

Project Helios Minutes for Third Joint Working Group Meeting at Bonn-Bad Godesberg, West Germany, Oct. 5–8, 1970. Gesellschaft fuer Weltraumforschung, mbH, Bonn-Bad Godesberg, West Germany.

Viking Mission Support

D. J. Mudgway
Mission Support Office

This article discusses the capabilities of the DSN as a significant factor in the radio frequency and data management design and the engineering requirements of the two orbiters and two landers for the Viking missions. Also described is the DSN involvement in the extremely complex lander acquisition sequence in which trade-offs are made between the total lander "on" period of 2 h and competing factors of round-trip light time and telemetry and command lock-up times.

I. Vehicle Descriptions

The Viking 1975 mission to Mars uses two spacecraft, each consisting of an orbiter and a lander, launched up to 10 days apart and arriving at the planet up to 30 days apart about a year later. On arrival, each spacecraft is placed in orbit, and the scientific instruments on board are used to obtain data to aid in the selection of a suitable landing site.

The lander is then separated from the spacecraft and injected into a suitable landing trajectory from which the complex landing sequence depicted in Fig. 1 can be carried out. Each orbiter will then act as a relay station between either of the landers and earth, receiving data from each lander on a UHF relay circuit, recording and retransmitting the same data on an S-band link to the DSSs. A lower rate, direct S-band link from the landers to the DSS can also be used during orbital operations when desired. However, each lander can support this latter link only for 2 h in each 24-h period.

The stringent requirements for planetary quarantine which apply to the landers preclude the replacement of

lander elements, such as the radio system, after the lander capsule has been sealed prior to launch. This does not apply to the orbiter, however, and a spare orbiter radio system is kept available in case either orbiter should develop a fault in this area.

II. Frequency Selection

From the foregoing brief summary of the Viking 1975 mission, it is apparent that frequency assignments for S-band communications with the DSN must satisfy the following basic requirements:

- (1) Two 2-way channels, one for each of the two orbiters, both to be operated simultaneously from any one DSS.
- (2) One 2-way channel, to be shared between the two landers. Each lander uses it only during the daily 2-h period during which it is in direct contact with earth.
- (3) One 2-way channel, to be assigned to the spare orbiter radio system. This could be used on either orbiter as required.

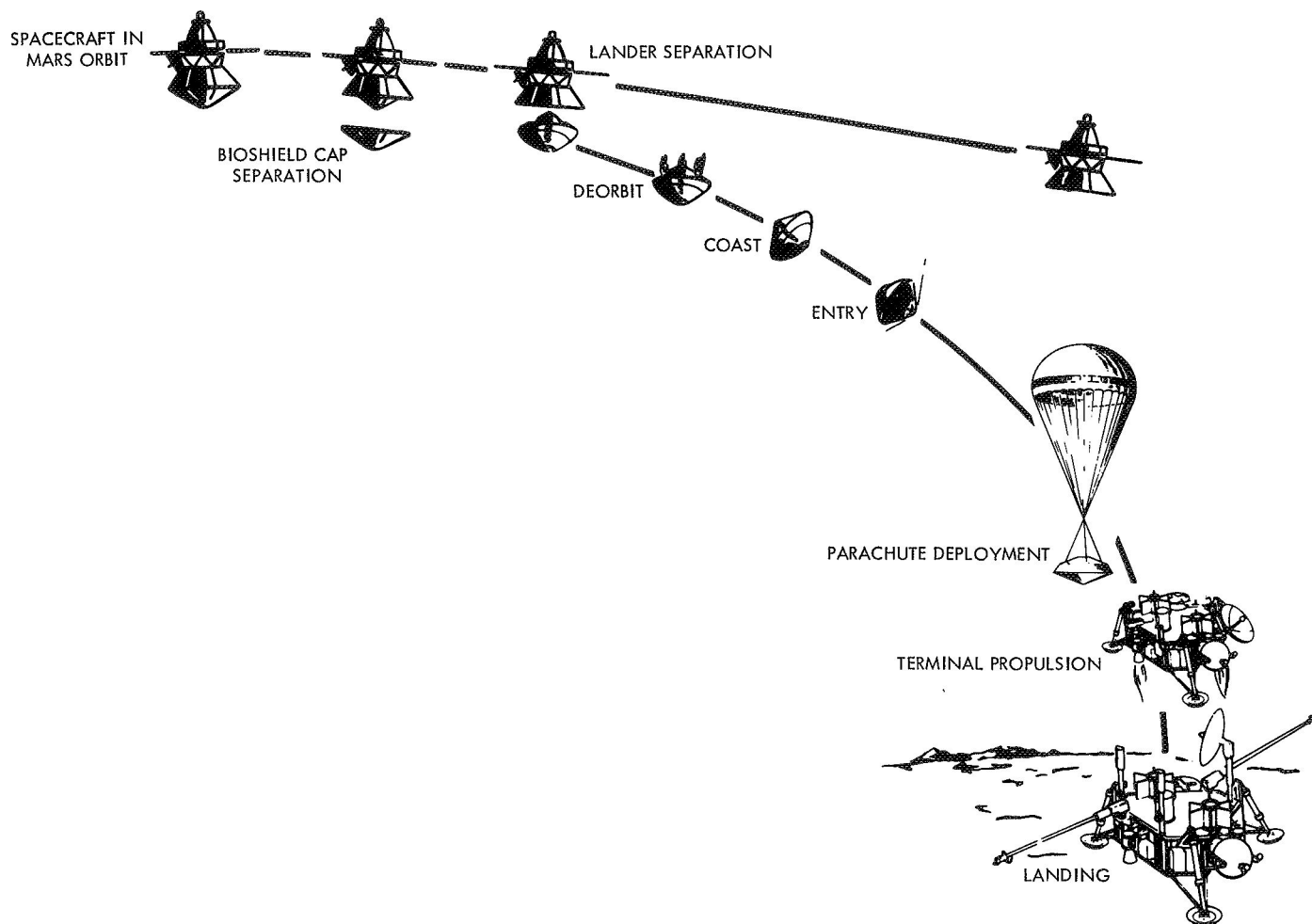


Fig. 1. Typical Viking landing sequence

In making these four frequency assignments, many other factors were also involved. These included the capability of the DSSs to support simultaneous multiple up and down links, bandwidth requirements for ranging, command, and telemetry, doppler offsets, and existing channels already assigned to current flight projects.

The 64-m-antenna DSSs will have the capability to support two simultaneous uplinks and four simultaneous downlinks. However, the high-power Klystron amplifiers used for transmitting the uplink are known to produce intermodulation products under certain conditions of nonlinear operation. Therefore, it was necessary to select frequencies for which these undesirable products would be minimized, and would not appear in the band pass of adjoining receive channels. In the case of the channels selected, there are no first-degree intermodulation products of order less than 700 lying within the chosen receive band.

Excluding the doppler effects, the RF bandwidths required on each channel are:

Ranging	3.6 MHz
Telemetry (high rate)	4.1 MHz
Command	4.0 kHz

Therefore, to prevent spectral components falling outside the designated space bands, the lowest uplink transmit frequency must be at least 1.8 MHz from the lower transmit band edge (2110 MHz) and the highest downlink receive frequency must be 2.05 MHz from the higher band edge (2300 MHz). Therefore, the frequencies chosen must lie between channels 9 and 21.

The frequency offset due to two-way doppler effects can become appreciable in missions of this type, and

must also be taken into consideration in assigning frequencies to avoid interference between adjacent channels. A two-way doppler plot for a typical *Viking* trajectory is shown in Fig. 2 for the period from launch to encounter. A cyclic variation of ± 8.0 kHz due to earth rotation is superimposed on the steady-state offset throughout the mission.

It can be seen from these plots that, during the cruise periods of the mission, the two-way doppler offset may exceed 300 kHz. Furthermore, the specified tuning range of a DSIF receiver is 9 parts in 10^5 (which is equivalent to about 207 kHz), and the bandwidth of adjacent deep space frequency channels is approximately ± 185 kHz.

To all of these effects must be added an uncertainty in the actual orbiter or lander carrier frequency of $\pm 3 \times 10^{-5}$.

Finally, although the space band contains some 29 channels spaced approximately 270 kHz apart, these are not all available to a new flight project. Channels 14, 17, and 23 are assigned to *Mariner* Mars 1971, channels 15 and 21 to the Helios Project, and channels 6 and 7 to *Pioneer*.

The DSN has taken all these factors into consideration in making the tentative frequency assignments in Table 1.

Table 1. Tentative frequency assignments for *Viking* spacecraft

Channel	Frequency, MHz	Recommended use
10A	2293.518519	Orbiter 1
10B	2111.948303	
13A	2294.629630	
13B	2112.971451	Orbiter spare
16A	2295.740741	Landers 1 and 2
16B	2113.994599	
19A	2296.851852	Orbiter 2
19B	2115.017747	

III. Orbital Doppler

Typical one-way doppler frequency shift due to orbital motion for the orbiter is shown in Fig. 3, as a function of time from periapsis. The corresponding doppler rates are shown in Fig. 4.

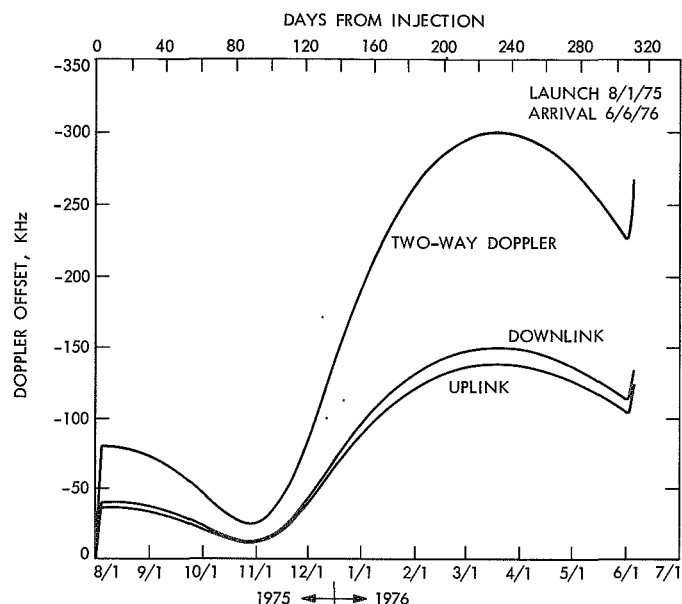


Fig. 2. Doppler offset for typical *Viking* trajectory

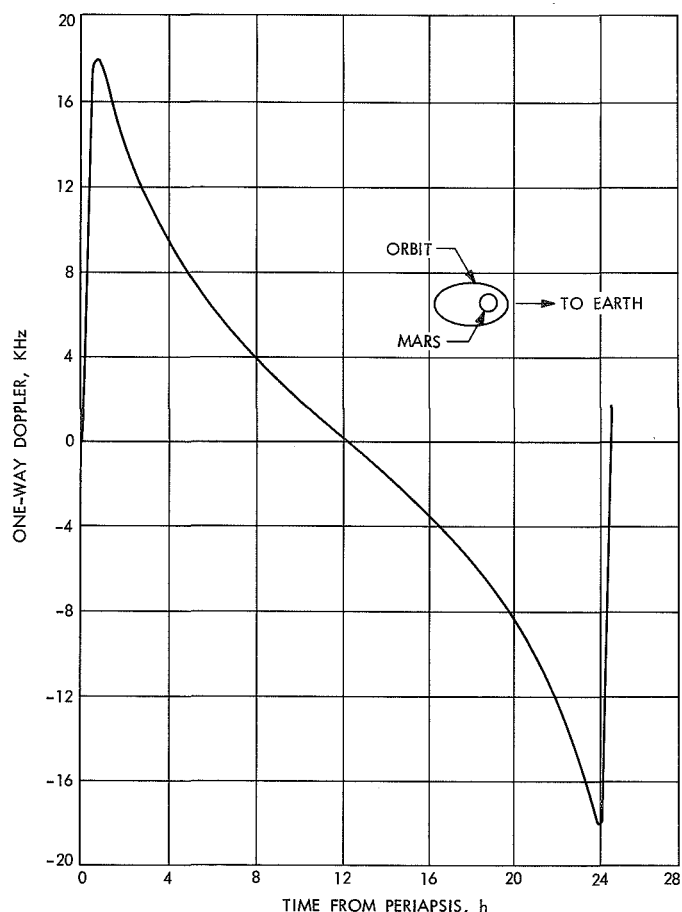


Fig. 3. Typical *Viking* orbiter one-way doppler shift (look angle parallel to line of apsides)

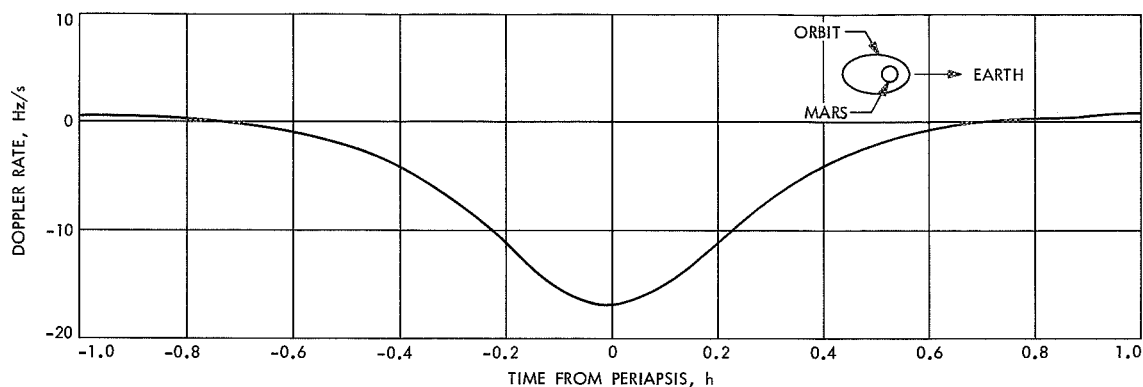


Fig. 4. Typical Viking orbiter one-way doppler rate (look angle parallel to line of apsides)

In order to continuously maintain a coherent two-way link with the DSS, the orbiter transponder must be able to accommodate doppler excursions of about -40 kHz peak-to-peak and doppler rates of about 20 Hz/s, while the ground receiver at the DSS must accommodate approximately twice these amounts. In both the uplink and downlink doppler, an additional allowance must be made for an earth-Mars separation rate equivalent to about -70 kHz at the beginning of orbital operations, changing to about $+20$ kHz at the end of the mission.

Although the ground receiver can accommodate a tuning range of 207 kHz at S-band, with RF tracking rates in excess of 50 Hz/s, it is imperative that the ability of the *Viking* orbiter to track under these conditions be carefully examined, and a determination made as to the need for a programmed local oscillator on the DSS ground transmitter.

The doppler offset seen by the *Viking* lander due to Mars rotation will exceed ± 1.7 kHz, together with ± 3.28 kHz due to earth rotation and the effect due to earth-Mars separation. In this case, the rate of change of doppler is much lower and unlikely to exceed the lander RF loop capability.

The capabilities of orbiter, lander, and DSS to track the orbital doppler are dependent on the signal-to-noise ratio and allowable phase error. Careful analysis of the trade-offs must be made to ensure the required capability of the telecommunication link during orbital operations.

IV. Lander Acquisition

As mentioned previously, each lander is constrained by power and thermal considerations to a daily "on"

period of about 2 h. With an earth-Mars round-trip light time of 40 min, it becomes apparent that a carefully planned lander acquisition sequence is necessary if the maximum time for ground commanding and telemetry data transmission is to be realized.

The lander transmitter is turned on at a specified time each day by a beacon signal from the orbiter passing overhead, and is turned off at the expiration of the 2 -h transmitting period. The lander receiver is turned on about 1 h prior to the transmitter.

The lander acquisition procedure takes advantage of this information to turn on the ground transmitter about 1 h prior to the expected lander on period, sweeping the ground carrier right across the lander receiver pass-band and returning to the expected best lock frequency of the lander receiver.

Thus, when the orbiter beacon activates the lander transmitter, it should come *on* in the two-way coherent mode.

On reaching earth, the DSS receiver, subcarrier demodulator, and bit synchronizer must be locked up, after which a final adjustment to the telemetered static phase error (SPE) can be made prior to starting any command sequences.

Estimates for the time required to accomplish these functions vary from 1 to 5 min, although it is expected that the time will diminish as proficiency improves and uncertainties in the lander carrier and subcarrier frequencies are reduced. The sequence of events described above is shown in Fig. 5.

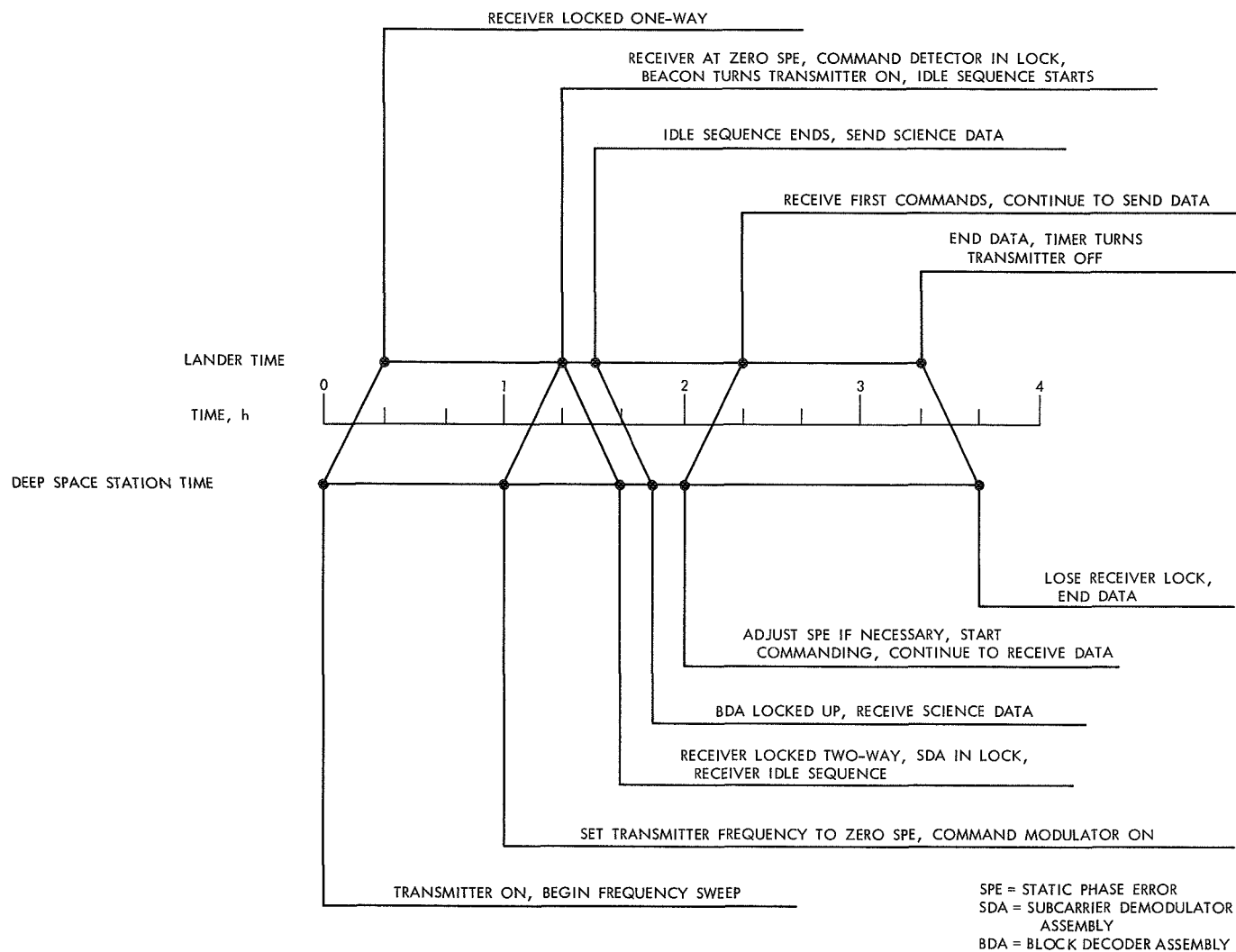


Fig. 5. Typical lander-DSS acquisition sequence

In order to avoid loss of valuable science data during these lock-up activities, it has been proposed that the lander might transmit a few minutes of idle-sequence bit prior to sending the first science data.

A procedure such as this would permit early lock-up of the DSS telemetry equipment in preparation for the arrival of the science data at the conclusion of the idle sequence.

Apollo Mission Support

R. B. Hartley

DSN Engineering and Operations Office

The support provided by the Deep Space Network (DSN) to the Manned Space Flight Network (MSFN) during the Apollo 14 mission is described. Support was provided from the three 26-m (85-ft) DSN/MSFN Wing stations, the Goldstone 64-m (210-ft) antenna, the Ground Communications Facility, and the Space Flight Operations Facility. Permission and mission activities are discussed and a brief mission description is included.

I. Introduction

The DSN support provided to the MSFN for the past *Apollo* lunar missions has been described in Ref. 1 and earlier issues of the Space Programs Summary Volume II series. This article describes the support provided for the *Apollo 14* (AS-509) mission, the third successful manned lunar landing.

II. Mission Description

Apollo 14 was the seventh manned *Apollo* mission flown above the three-stage *Saturn V* launch vehicle and carried astronauts Alan B. Shepard, Jr. (Commander), Stuart Allen Roosa (Command Module Pilot), and Edgar Dean Mitchell (Lunar Module Pilot). The mission goal was to land in the Fra Mauro uplands, the same goal that the abortive *Apollo 13* mission was unable to achieve. The *Apollo 14* mission successfully accomplished

its objectives in spite of a large number of minor problems, which are mentioned in the following discussion.

Launch from Cape Kennedy Pad 39A occurred at 21:03:02.9 GMT on January 31, 1971, at a launch azimuth of 75.56 deg. The launch had originally been scheduled for a 20:23 GMT launch, but a launch hold of some 40 min was required due to the new weather restrictions developed after the lightning strikes of *Apollo 12*. This was the first time a manned *Apollo* mission was not launched on time. Injection into translunar trajectory occurred midway through the second revolution in the Earth parking orbit with a 5-min 49-s burn of the S-IVB-stage engine.

Following translunar injection (TLI), the Command/Service Module (CSM) separated from the booster and attempted to dock with the unattended Lunar Module (LM). For the first time on *Apollo*, this docking proce-

ture was unsuccessful, with the capture latches of the docking probe failing to seize the Lunar Module drogue. Without a successful docking there would be no lunar landing, although the crew was in no danger. The docking had to be accomplished within several hours before the S-IVB attitude-control system became inoperative and the S-IVB and Lunar Module started to tumble. Under direction from Mission Control Center in Houston, the astronauts made five additional docking attempts in various configurations. On the sixth attempt, docking was successful.

After docking, the probe was removed from the Command Module/Lunar Module tunnel for examination. No abnormal behavior or contamination could be detected, and the mission was given the "go-ahead" for lunar landing. After separation from the spacecraft, the S-IVB (the launch vehicle third stage) was directed toward a crash on the Moon as a calibration of the seismometer left there during the *Apollo 12* mission. The impact occurred at 07:40:55 GMT on February 4, 1971, at lunar coordinates 8 deg 03 min S, 26 deg 03 min W, approximately 174 km southwest of the seismometer which showed vibrations for some 2 h.

Midcourse correction 1 was deleted due to the accuracy of the translunar injection maneuver. Midcourse correction 2 was executed at 03:39 GMT on February 2, 1971, removing the spacecraft from its "free-return" trajectory to save fuel for the lunar landing sequence. The remainder of the translunar cruise was nominal except for an observed dip from 37.0 to 36.7 V in one of the Lunar Module ascent stage batteries. This dip, first noticed during the Lunar Module checkout at 10:56 GMT on February 3, caused some concern and a test was executed at 02:38 GMT, February 4, which confirmed that the battery would properly support a load.

Other minor problems during translunar coast included difficulty in maintaining correct pointing of the spacecraft high-gain antenna and a high rate of pressure decrease during a cabin leak check. The latter problem was caused by a urine vent valve being accidentally left open. Midcourse correction 3 was deleted but a small midcourse correction 4 was executed at 02:01 GMT, February 4, with the burn lasting less than 1 s.

A successful lunar orbit insertion (LOI) burn put the spacecraft in a 315- by 110-km (169.6- by 58.9-nmi) elliptical orbit. Two orbits later a descent orbit insertion (DOI) burn changed these dimensions to 110 by 17.2 km (59.0 by 9.3 nmi). During lunar orbit, additional pointing

problems with the high-gain Command/Service Module antenna were experienced.

During lunar orbit 12, the Command/Service Module and Lunar Module separated with astronauts Shepard and Mitchell in the Lunar Module preparing for descent to the lunar surface on orbit 14. Difficulty was experienced maintaining lock on the Lunar Module high-gain antenna, but behavior was normal on the next orbit. An abort pushbutton sent erroneous inputs to the Lunar Module guidance computer on four occasions. The button may have been defective or contaminated since tapping on the switch panel cleared up the problem. The computer was reprogrammed to ignore these abort inputs.

During the descent phase, the landing radar came on in the "near" mode [1066.8 m (3500 ft) maximum] instead of the "far" mode. This problem was first noticed when the radar failed to acquire lock when passing through 9.15 km (30,000 ft). The radar was turned off and on, and lock was acquired.

The landing was normal and was within 20 m of the intended landing site. After more than 5 h of preparation, the two astronauts began their first excursion during which surface samples were collected, the ALSEP¹ and TV camera were deployed, and the "thumper" was activated. The "thumper" is a hand-held rod which taps the lunar surface as a small explosive charge within it is detonated. This device proved to be especially unreliable, and the astronaut was able to detonate only 13 of the 21 charges. Due to this problem and several others including difficulty unfolding the S-band erectable antenna, a twisted urine tube in the Commander's suit, a broken wrist cable in the Lunar Module Pilot's suit, and an EVA (extra-vehicular activity) radio problem, the astronauts fell behind their planned timeline and were unable to complete all assigned tasks.

During the ensuing rest period, an S-band bistatic radar experiment was conducted between the orbiting Command/Service Module and DSS 14. This experiment is discussed below. Also during the rest period, the Lunar Module astronauts conducted a pressure check of the space suits to confirm that an abnormally high leak rate on the Lunar Module Pilot's suit had not increased to the danger level. All was in order and the astronauts began the second excursion 2 h and 28 min ahead of schedule. This excursion was to take the astronauts 1000 m to the edge of Rim crater. Although this goal was not

¹*Apollo* lunar surface experiments package.

quite reached, many rock samples of new and different types were collected.

Lunar liftoff, rendezvous, and docking were normal with none of the problems of the earlier docking. Following transfer of the lunar samples to the Command/Service Module, the LM was jettisoned and directed toward a crash on the Moon near the ALSEP seismometer. One orbit later, on orbit number 35, the crew executed the trans-Earth injection burn to start the return trip to Earth.

Apollo 14 landed at approximately 172 deg W, 27 deg S, midway between Samoa and New Zealand.

Table 1 shows the mission event times and Table 2 gives the television coverage. Care must be exercised when using ground elapsed time (GET), which on previous missions recorded the time from launch. With *Apollo 14's* launch slip (the first on *Apollo*), the clock carries a different meaning. In order to make the sun angles upon lunar landing identical to the premission plans, the translunar trajectory was made 40 min faster than planned. The GET clock was then set forward 40 min and 3 s at 03:38:03 GMT on February 3. A new clock, actual elapsed time (AET), records the time from launch, and the GET clock is merely a convenient reference time which corresponds very closely to the planned mission timeline.

Table 1. *Apollo 14* sequence of major events

Event	Ground elapsed time, h:min:s	Actual elapsed time, h:min:s	Greenwich Mean Time, h:min:s	Event	Ground elapsed time, h:min:s	Actual elapsed time, h:min:s	Greenwich Mean Time, h:min:s
Launch	00:00:00	00:00:00	Jan 31/21:03:03	Undock	104:28:03	103:48:00	Feb 05/04:51:03
TLI ignition	02:28:30	02:28:30	Jan 31/23:31:33	CSM circularization	105:46:48	105:06:45	Feb 05/06:09:48
TLI cutoff	02:34:19	02:34:19	Jan 31/23:37:22	Powered descent initiation	108:42:01	108:01:58	Feb 05/09:05:01
First midcourse (TLI + 9 h)	Deleted			Touchdown	108:55:14	108:15:11	Feb 05/09:18:14
Second midcourse (to hybrid) (TLI + 28 h)	30:36:07	30:36:07	Feb 02/03:39:10	Begin EVA-1	114:20:00	113:39:57	Feb 05/14:43:00
Begin bistatic frequency measurement	52:20:00	52:20:00	Feb 03/01:23:03	ALSEP activated	117:05:00	116:24:57	Feb 05/17:28:00
End bistatic frequency measurement	52:25:00	52:25:00	Feb 03/01:28:03	ALSEP high-bit rate on	117:36:00	116:55:57	Feb 05/17:59:00
Change ground elapsed time	55:15:03	54:35:00	Feb 03/03:38:03	ALSEP high-bit rate off	118:14:00	117:33:57	Feb 05/18:37:00
Begin LM inspection	60:59:00	60:18:57	Feb 03/09:22:00	End EVA-1	119:04:00	118:23:57	Feb 05/19:27:00
Third midcourse (LOI - 22 h)	Deleted			Begin bistatic radar	130:05:00	129:24:57	Feb 06/06:28:00
Fourth midcourse (LOI - 5 h)	77:38:13	76:58:10	Feb 04/02:01:13	End bistatic radar	131:04:00	130:23:57	Feb 06/07:27:00
Second LM inspection (30 min)	78:14:58	77:34:55	Feb 04/02:37:58	Begin EVA-2	131:48:14	131:08:11	Feb 06/08:11:14
CSM first occultation	82:23:03	81:43:00	Feb 04/06:46:03	End EVA-2	136:19:00	135:38:57	Feb 06/12:42:00
Lunar orbit insertion	82:36:43	81:56:40	Feb 04/06:59:43	LM ascent	142:25:43	141:45:40	Feb 06/18:48:43
S-IVB impact	83:17:55	82:37:52	Feb 04/07:40:55	CSM/LM docking	144:12:00	143:31:57	Feb 06/20:35:00
Descent orbit insertion	86:50:55	86:10:52	Feb 04/11:13:55	LM separation	146:25:00	145:44:57	Feb 06/22:48:00
				LM deorbit burn	147:54:00	147:13:57	Feb 07/00:17:00
				LM crash	148:22:25	147:42:23	Feb 07/00:45:25
				Trans-Earth injection	149:16:04	148:36:01	Feb 07/01:39:04
				Fifth midcourse	166:14:00	165:33:57	Feb 07/18:37:00
				Splashdown	216:42:01	216:01:58	Feb 09/21:05:01

Table 2. *Apollo 14* television

GMT, h:min	GET, h:min	AET, h:min	Duration, h:min	Subject	Vehicle	Station ^a
Feb 1/00:07	03:04	03:04	01:55	Transportation and docking	CSM	GDS
Feb 1/08:09	11:06	11:06	01:06	Inspection of docking probe	CSM	GDS
Feb 3/09:04	60:41	60:01	00:41	Interior of spacecraft	CSM	HSK
Feb 5/14:56	114:33	113:53	06:30	EVA-1	LM	HSK/MAD
Feb 6/07:34	131:11	130:31	05:20	EVA-2	LM	GDS/HSK
Feb 6/20:12	143:49	143:09	00:09	Rendezvous	CSM	MAD
Feb 6/20:27	144:04	143:24	00:10	Docking	CSM	MAD
Feb 8/01:21	171:58	171:18	00:51	Inflight demonstrations	CSM	GDS
Feb 8/23:31	195:08	194:28	00:25	Press briefing	CSM	GDS

^aGDS = Goldstone MSFN station
 HSK = Honeysuckle MSFN station, Australia
 MAD = Madrid MSFN station, Spain

III. Requirements for DSN Support of *Apollo 14*

A. DSN/MSFN Wing Stations

As was done during previous *Apollo* lunar missions, DSSs 11, 42, and 61 were committed to support *Apollo 14* under direct MSFN/MSC control starting at launch minus 2 wk through the end of the mission.

B. DSS 14

The Mars station, DSS 14, was required to receive voice, telemetry, biomedical, and TV and relay the data to the Goldstone Prime MSFN station (GDS). Specific requirements existed for lunar landing, EVA television, and LM crash. Coverage was also desired for television during translunar coast.

C. Precision Doppler Data

As part of a continuing study of lunar potential anomalies (mascons), DSS 14 was required to provide precision doppler recordings of the Command/Service Module during several low lunar orbits and of the Lunar Module during the descent phase and later during the crash. An additional internal DSN requirement was levied for more doppler data during all low Command/Service Module orbits and several adjoining high orbits in support of a JPL study of mascons (with the same principal investigator who originated the formal requirement). As one can see from the timeline (Fig. 1), one pass from DSS 62 was necessary to provide almost complete coverage of

this requirement. A related requirement was for high-speed strip-chart recordings of DSS 14 received signal level during orbit 3 of the Command/Service Module, descent and touchdown of the Lunar Module, and the crash of the Lunar Module.

D. Bistatic Radar Experiment

On April 14, 1969, Stanford University submitted a formal proposal to NASA to conduct an experiment, *Downlink Bistatic Radar Study of the Moon*, using DSS 14. The specific goals of this experiment are:

- (1) To determine the Brewster angle of the lunar crust at S-band.
- (2) To measure the spectral properties of bistatic radar echoes from low-altitude orbit.
- (3) To gain operational experience with *Apollo* systems and operations as an aid in the design of future bistatic radar experiments.

The experiment should reveal fundamental new scientific information on the upper few centimeters of the lunar crust through a short wavelength determination of the Brewster angle of the lunar surface, and should provide engineering data necessary for optimizing the design of future bistatic radar experiments from low lunar orbits (approximately 100-km altitude). Furthermore, the results should provide a lunar S-band, bistatic radar calibration which would have considerable utility in the

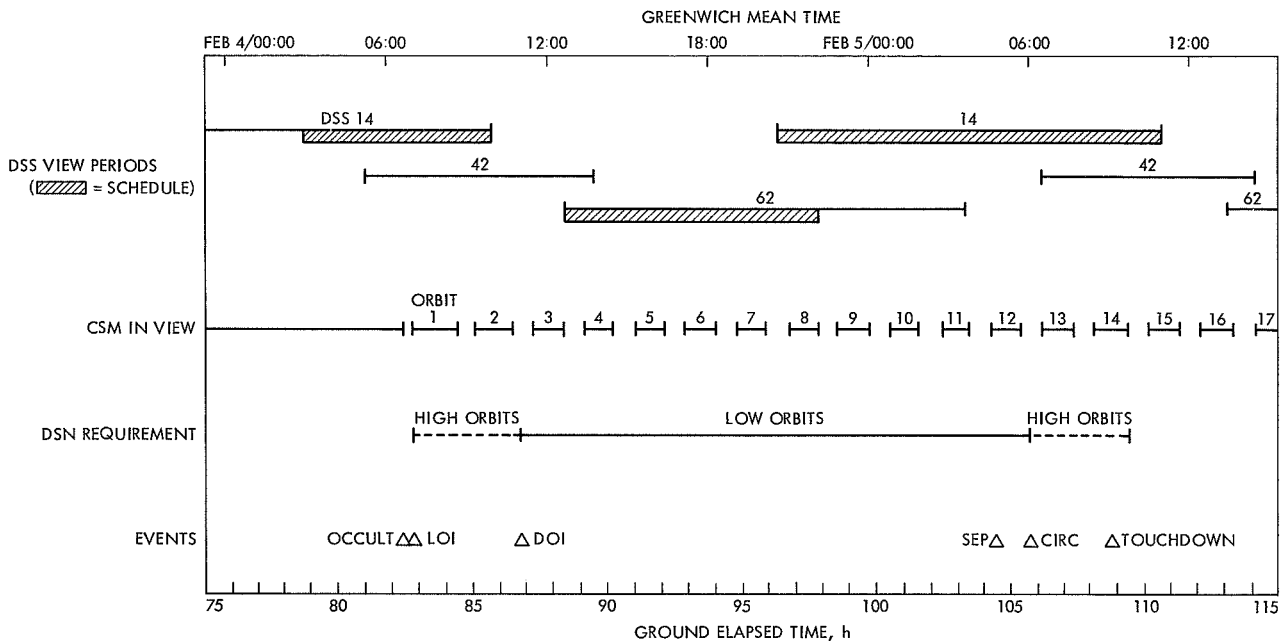


Fig. 1. DSN internal mascon study requirement

interpretation of similar experiments conducted in the future at the planets.

It was proposed that the downlink CSM S-band signal would be directed toward the lunar surface. At DSS 14 the reflected signal (and a portion of the direct signal) would be received in two polarizations simultaneously using the polarization diversity S-band cone. The outputs of the two receiver chains would be recorded on FR 1400 recorders.

E. Goldstone Timing Synchronization

An obsolete time sync agreement in effect since *Apollo 11*, which provided for routine measurements with a DSIF portable cesium clock at all Goldstone/*Apollo* support sites, was amended on June 9, 1970. The new agreement, which will be valid for all future *Apollo* missions, is as follows:

A one pulse-per-second tick is distributed via DSN microwave to DSS 14. The pulse originates in the DSIF Standards Laboratory, arrives at the sites with known offsets, and is accurate to better than 5 μ s. This signal is made available to the MSFN at the MSFN microwave interface at DSS 14. The portable cesium clock will be used only to calibrate the microwave delays when changes have occurred to the microwave system. Routine support of the portable

clock will be discontinued. In the case of a bona fide timing emergency, the portable cesium clock will be available with a delay of 2 h during the normal working day and 48 h otherwise. Following any clock trip a TWX giving the results with respect to the National Bureau of Standards and the expected National Bureau of Standards-U.S. Naval Observatory offset will be sent out to interested parties.

F. Twenty-Kilowatt Uplink

Original plans for the operation of the Wing stations were for two simultaneous 10-kW radiated uplink signals. This was accomplished using two 20-kW transmitters fed into a combiner which introduced a 3-dB loss. Thus, 10 kW of power from each transmitter was radiated from the antenna. The other 10 kW from each transmitter, which was lost in the combiner, was dissipated in a 20-kW water load. When transmitting a single uplink, there was no longer a need for the combiner and its accompanying 3-dB loss, and a nonstandard configuration was entered at some Wing sites which bypassed the combiner, allowing a single 20-kW radiated power uplink. Unfortunately, since this was not a standard configuration, the combiner water load interlock was not disabled; that is, any failure in the water load would shut down the transmitter, even though the water load was not in use. No changes could be authorized because the radiation of a single 20-kW uplink had never been requested or committed.

On June 12, 1970, GSFC levied an official requirement upon the DSN for the 20-kW capability. An Engineering Change Order was issued to disable the water load interlock when in the 20-kW configuration. The modifications were completed in November 1970. Certain operational limitations remain:

- (1) There exists no backup 20-kW capability since the installed microwave switching gear allows only one transmitter (the DSN transmitter) to be switched around the combiner.
- (2) All uplinks must be turned off before any microwave switching can occur.

G. Wing Site Support of ALSEP

ALSEP communications are usually accomplished using the 30-ft antennas of the MSFN. In September 1969, the DSN received a requirement for the Wing sites to track ALSEP during the Active Seismic Experiment on ALSEP No. 4 during the *Apollo 14* mission period. During this new experiment, the ALSEP transmits at 10.6 kbits/s, a higher rate than past ALSEPs and beyond the capability of the 30-ft stations. The experiment is dubbed the "thumper" because of a series of small charges which are actuated by the astronauts to generate artificial seismic waves.

IV. Apollo Interface Team

Between *Apollo 13* and *14*, the DSIF was reorganized to eliminate the separate positions of Operations Engineering, Operations Planning, and System Data Analysis (SDA) for *Apollo*. Instead the DSIF planning efforts are represented by a single DSIF Operations Project Engineer for *Apollo*, and some of the operations functions, such as predict generation, have been assumed by the DSN mission independent operations organization.

V. Prepermission Preparations and Testing

A. DSN/MSFN Wing Stations

DSSs 11, 42, and 61 were placed under configuration control for the *Apollo 14* mission as of 00:01 GMT on January 17, 1971, and subsequently placed on mission status by the MSFN as of 00:01 GMT on January 21, 1971. Prior to January 21, each Wing site conducted extensive maintenance and testing of the equipment common to the DSN and MSFN. The new requirement for Wing support of the ALSEP indicated a need for

ALSEP premission testing. The downlink tests pose no problem, but the ALSEP uplink frequency (2119 MHz) is at the extreme end of the normally used band (MSFN: 2100–2110 MHz; DSN: 2110–2118 MHz). Some tuning of the klystron power amplifier is therefore needed. Unfortunately, the klystrons may be retuned only a finite number of times before the cavity adjustment screws will bind up, requiring costly and time-consuming repair. In order to maintain these klystrons in good condition for the mission, the DSN limited the MSFN to one ALSEP uplink test at each Wing site. These tests, conducted on January 11 and 12, failed at all three Wing sites due to identical intersite microwave problems unrelated to the klystrons. It is unfortunate that the results of the first test were not applied to the second and third site. Nevertheless, the MSFN requested additional testing and, after management discussions, one additional test at each site (January 23 and 24) was allowed. Later investigation may show that this testing is related to the transmitter problems experienced during the mission.

B. DSS 14

In addition to the bistatic experiment tests and the predict tests mentioned below, DSS 14 conducted two tests before the *Apollo 14* mission (see Table 3). The first was an officially required participation in Day 5 of the MSFN network readiness test. DSS 14's participation turned out to be nothing more than a data transmission test between the DSS 14 communications center and the Goldstone MSFN station. The second test was an internal DSIF configuration verification test on January 19. The third test was an extensive data flow test with a spacecraft simulator used at DSS 14 to generate data which were fed through the entire system ending at the Goldstone MSFN station. Due to delays the test required more than the allotted 24 h on January 21, and the television and Lunar Module tests were rescheduled on January 27. Configuration control was imposed on DSS 14 on January 17.

C. Bistatic Experiment Preparations

A meeting was held at JPL on May 8, 1970 to discuss the feasibility of the proposed experiment. In attendance were representatives of MSC, GSFC, NASA Headquarters, North American Rockwell, Stanford University, and the DSN, DSIF, and GCF. The potential problem areas were identified and a number of action items were assigned. Shortly afterward a support requirement was issued at MSC (May 19, 1970). The final details on the configuration at DSS 14 were discussed at another meet-

Table 3. DSS 14 tests

Date	Time, h:min	Test	Comments
12/21/70	16:00–24:00	Bistatic cable installation	
12/22/70	22:00–02:01	Bistatic equipment checkout	
12/23/70	02:01–06:00	Bistatic track of <i>Pioneer VI</i>	Receivers 3 and 4 not yet installed; no 152.4 cm/s (60 ips) narrow-band frequency modulation FR 1400 modules
01/08/71		Day 5 of network readiness test	Data transmission test
01/08/71	22:30–05:30	Bistatic test	During <i>Pioneer VI</i> track; used <i>Pioneer VI</i> signal; FR 1400 not available
01/19/71		Configuration verification test	
01/21/71	14:20–14:20	Data flow test (24 h)	
01/27/71	14:18–22:17	Data flow test	TV and LM tests
01/28/71	20:00–07:10	Bistatic final calibration	

ing at JPL on November 9, 1970 with approximately the same representation as the May 8 meeting.

A number of installation periods and tests were conducted from late December 1970 until launch on January 31. These tests are included in Table 3.

D. DSN Predicts

Predict data for DSS 14 is generated in two ways. The prime method uses state vectors supplied by Houston MSC or Goddard Space Flight Center, and generates

DSN predicts in the SFOF computers. The backup system involves a 29-point acquisition message generated at MSC, transmitted directly via TTY to DSS 14, and converted at DSS 14 from X-Y to HA-dec coordinates with an atmosphere refraction correction added if necessary.

In November 1970 the DSIF served notice that it would not allow further use of the 29-point conversion program because the software had never been properly certified or documented, even though it had been successfully used on several *Apollo* flights. To make matters worse, the SFOF IBM 7094/7044 computer system was about to be removed to make way for a second IBM 360/75, and it was uncertain if the predict software for the 360 would be ready for *Apollo*.

Several compromises were necessary. The 7044 was removed, but the 7094 was merely moved to a new location in the SFOF. The 7094, however, lacked a high-speed printer (used for checking the predicts), adequate tape drives (to lessen the required tape changes), and a 7044 to transmit the predicts.

The missing 7044 was overcome by the procedure shown in Fig. 2. A state vector received in the SFOF was input to the 7094. The output tape was then carried to the PDP-7 computer in the Media Conversion Center of the SFOF where the predicts were transferred to TTY punched paper tape. This tape was taken to a tape reader in the Communications Center, where a TTY header was added, and the data was transmitted. A test of this system on January 18 was successful except for a bad TTY punch in the Media Conversion Center. The test was repeated on January 19 with complete success. In an effort to obtain clearance to use the 29-point conversion program, a number of tests were conducted starting in December 1970. The last tests on January 12 and 22 resulted in acceptance on an emergency backup, best-effort basis only.

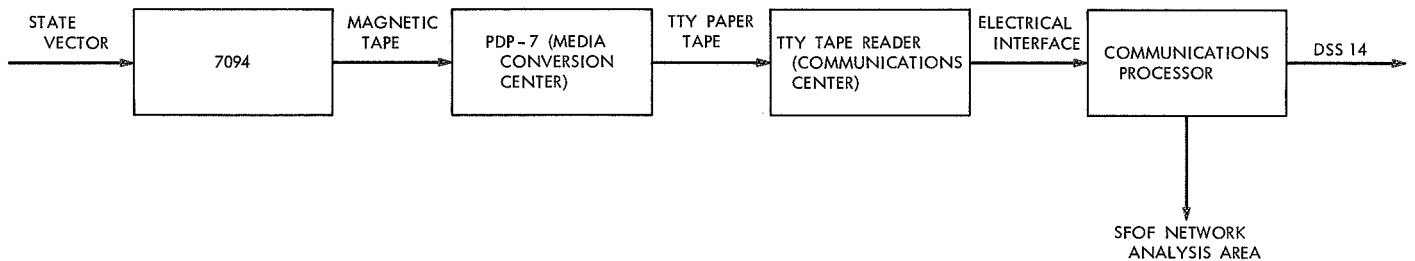


Fig. 2. DSN predict generation for *Apollo 14*

VI. Apollo 14 Operations

A. DSN/MSFN Wing Stations

DSSs 11, 42, and 61 successfully supported all phases of the *Apollo 14* mission. The problems experienced are noted in Table 4. The many transmitter problems are being investigated at this time.

B. DSS 14

Seven passes were tracked as shown in Table 5. The only schedule change occurred on February 4 when DSS 14 was requested to be on track earlier than the scheduled 03:00 GMT in order to observe the second Lunar Module checkout. This second checkout was to investigate the Lunar Module battery problem, and it was thought that low power levels might have resulted in a degraded telemetry signal. Accordingly, DSS 14 was tracking at 00:43 GMT on February 4. DSS 14 experienced no problems that had any effect on *Apollo 14* support.

C. DSS 62

DSS 62 tracked the Command/Service Module as planned on February 4 from 13:32:18 to 22:12:47 GMT. The required doppler data was successfully taken and sent to JPL.

D. Predict Operations

It is apparent that the extraordinary care given to predict generation problem before the mission paid off, because no problems were experienced during the mission (unusual for *Apollo*). The personnel were eagerly cooperative, and it is felt that this spirit is responsible for maintaining and operating the system with so many known weak points.

The 29-point acquisition messages were also used on occasion at DSS 14. Several comparisons were made between the two types of predicts with no significant discrepancies except for the Lunar Module powered descent. This difference was anticipated since the 7094 predict program cannot model a long duration burn with a changing force vector. Thus, the 29-point message was much more accurate and was used for powered descent.

E. SFOF Participation

The SFOF areas and equipment used for *Apollo 14* included the Operations Area, the Network Analysis Area, the displays, the relocated 7094, and the Media Conver-

Table 4. Wing station tracking

DSS	GMT, h:min	Problem
11	Jan 31/22:31-22:34	None
	Jan 31/23:53-07:35	PA 4 (power amplifier) high-voltage rectifier interlock; no apparent reason. PA 3 arc detector trip; no apparent reason
	Feb 01/20:43-08:42	None
	Feb 02/21:10-09:02	Maser 1 exhaust valve frozen; will replace maser
	Feb 03/21:17-08:54	PA 3 arc detector trip at 22:24; switch to PA 4 after 19 seconds
	Feb 04/21:13-10:05	PA 4 high-voltage ac overcurrent trip; no apparent reason
	Feb 05/21:53-10:54	None
	Feb 07/00:01-11:21	None
	Feb 07/23:37-11:32	None
	Feb 08/23:30-12:06	PA 4 high-voltage ac overcurrent trip; no apparent reason; PA was in standby
42	Feb 01/04:45-12:25	Both klystron power supplies tripped on beam overvoltage; transmitters were not radiating
	Feb 02/05:31-13:18	None
	Feb 03/05:41-13:41	None
	Feb 04/05:42-13:57	None
	Feb 05/06:37-14:45	None
	Feb 06/07:33-15:47	None
	Feb 07/08:02-16:11	None
	Feb 08/08:06-16:29	None
	Feb 09/08:24-16:41	None
	Feb 09/17:08-18:48	None (ALSEP track)
61	Feb 01/11:58-02:00	None
	Feb 02/12:33-02:17	None
	Feb 03/12:45-02:26	None
	Feb 04/13:32-03:07	None
	Feb 05/13:50-04:05	PA 2 excessive reflected power trip during pretrack; retuned klystron
	Feb 06/14:43-04:51	None
	Feb 07/15:10-04:54	None
	Feb 08/15:28-04:58	None
	Feb 09/17:56-19:25	None

Table 5. DSS 14 tracking

Date, Feb 1971	GMT, h:min:s
1	01:13:50-06:30:00
2	00:30:52-06:30:00
2	22:59:00-04:30:00
4	00:43:00-09:55:00
4	21:07:15-10:57:40
5	21:42:34-11:51:40
6	22:40:00-06:00:00

sion Center. The SFOF support is limited to predict generation and some off-line monitoring. As mentioned above, the support was excellent.

F. GCF Participation

The DSN GCF provided voice and teletype circuits as required to support the operations mentioned above. In addition, JPL acts as West Coast Switching Center for the NASA Communications Network and handles many non-DSN circuits in support of *Apollo*. The only known GCF problem was a bad set of communications processor log tapes covering parts of the precision doppler data collection. These data were later recovered from DSS 14 and 62 tracking data tapes were sent in by mail.

Reference

1. Hartley, R. B., "Apollo Mission Support," in *The Deep Space Network*, Space Programs Summary 37-64, Vol. II, pp. 7-11. Jet Propulsion Laboratory, Pasadena, Calif., Aug. 31, 1970.

Second Order Charged Particle Effects on Electromagnetic Waves in the Interplanetary Medium

O. H. von Roos

Tracking and Orbit Determination Section

Possible influences on the measurements of the total electron content due to magnetic fields, spatial inhomogeneities, and pulse shape distortions are investigated and found to be negligibly small at Deep Space Network tracking frequencies.

1. Introduction

There are essentially two methods now in use to measure the effect of the interplanetary plasma on the propagation of radio signals used for tracking a spacecraft. One method is the differenced range versus integrated doppler (DRVID) calibration utilizing the difference in phase and group velocity of the electromagnetic waves (Ref. 1). The other method uses two different frequencies (dual frequency method) taking advantage of the frequency dependence of the phase and group velocity (Ref. 2). The effects of the interplanetary plasma on the electromagnetic wave propagation can be theoretically expressed by the fact that the (relative) dielectric constant ϵ is given by

$$\epsilon = 1 - \frac{\omega_p^2}{\omega^2} \quad (1)$$

where

$$\omega_p^2 = \frac{4\pi e^2}{m} N = \text{plasma frequency}$$

ω = angular frequency of the radio wave

and

N = number of electrons per cm^3

The refractive index is then given by

$$n = \sqrt{1 - \frac{\omega_p^2}{\omega^2}} \approx 1 - \frac{\omega_p^2}{2\omega^2} \quad (2)$$

since the plasma frequency is $\omega_p \approx 0.18 \text{ MHz}$ assuming $N = 10 \text{ cm}^{-3}$ and the carrier frequency ω is much larger than ω_p , the former being 400 MHz for the dual frequency experiments and 2000 MHz for the DRVID method. There ensues, then, a first order theory of the effects of the solar plasma on the electromagnetic wave propagation as put forward by Eshleman in comprehensive form (Ref. 3). This first order theory neglects magnetic field influences, influences due to spacial and temporal inhomogeneities in the electron density N , and, finally, pulse shape distortion due to dispersion. We shall address ourselves to these higher order effects and show that they are indeed negligible at the high carrier frequencies involved.

II. Development of the Theory

It can be shown (Ref. 4) that the equation for the electric field of a monochromatic electromagnetic wave in the presence of a constant magnetic field in convenient vector notation is given by

$$\nabla \times \nabla \times \mathbf{E} - \frac{\omega^2}{c^2} \mathbf{E} = \frac{\omega_p^2}{c^2} [A \mathbf{E} + B \hat{\mathbf{h}} \times \mathbf{E} + C \hat{\mathbf{h}} \hat{\mathbf{h}} \cdot \mathbf{E}] \quad (3)$$

where

$$A = \frac{i\omega(\nu - i\omega)}{(\nu - i\omega)^2 + \omega_c^2} \quad (4a)$$

$$B = -i \frac{\omega \omega_c}{(\nu - i\omega)^2 + \omega_c^2} \quad (4b)$$

$$C = \frac{\nu}{\nu - i\omega} - \frac{\nu(\nu - i\omega) + \omega_c^2}{(\nu - i\omega)^2 + \omega_c^2} \quad (4c)$$

and

ω_p = plasma frequency

ω = angular frequency of the wave

ν = effective collision frequency for the electrons

ω_c = cyclotron frequency

$\hat{\mathbf{h}}$ = unit vector in direction of the constant magnetic field

The magnitude of the interplanetary magnetic field is of the order of 10^{-9} tesla (10^{-5} gauss) resulting in a cyclotron frequency of $\omega_c \approx 176 \text{ sec}^{-1}$. The collision frequency is $\nu < 1 \text{ sec}^{-1}$. Therefore, for $\omega \approx 2 \times 10^9 \text{ sec}^{-1}$, the influence of the magnetic field and the influence of collisions are totally negligible as far as the wave propagation is concerned. This is even true for the ionosphere and solar corona where magnetic field strengths are of the order of 10^{-4} tesla (1 gauss) so that $\omega_c \approx 10^6 \text{ sec}^{-1}$. For these cases Eq. (3) reduces readily to

$$\nabla \times \nabla \times \mathbf{E} - \frac{\omega^2}{c^2} \mathbf{E} = \frac{\omega_p^2}{c^2} \left(i \frac{\omega_c}{\omega} \hat{\mathbf{h}} \times \mathbf{E} - \mathbf{E} \right) \quad (5)$$

where the ratio $\omega_c/\omega = 5 \times 10^{-4}$ indicates the smallness of the magnetic field influence. The first term on the right-hand side of Eq. (5) leads to an *observable* Faraday rotation effect, however (Ref. 5). The reason for this is that the

rotation of the polarization is proportional to the *difference* of the two wave vectors:

$$k_{\pm} = \frac{\omega}{c} \left(1 - \frac{\omega_p^2}{2\omega^2} \pm \frac{1}{2} \frac{\omega_p^2}{\omega^2} \frac{\omega_c}{\omega} \right) \quad (6)$$

whereas the electron content measurements, as in the dual frequency and DRVID methods, essentially depend on the wave vectors k_+ and k_- separately, in which case the magnetic field influence is negligibly small.

The field equation (3) reduces, therefore, to

$$\nabla \times \nabla \times \mathbf{E} - \frac{\omega^2}{c^2} \mathbf{E} = - \frac{\omega_p^2}{c^2} \mathbf{E} = - \frac{4\pi e^2}{c^2 m} N \mathbf{E} \quad (7)$$

Turning now to the spacial inhomogeneities of the electron density, it must be realized that the smallest scale of such fluctuations is at worst of the order of kilometers. Measurable changes rather take place over thousands of kilometers. Therefore, considering the small carrier wavelengths involved, a first order Wentzel-Kramers-Brillouin method is quite adequate for the solution of Eq. (7). Suppose that the electron density varies in the direction of propagation of the signal (the x direction). With the ansatz

$$E = A(x) \exp [i(kx - \omega t) + i\phi(x)] \quad (8)$$

where

$$k^2 = \frac{\omega^2}{c^2} - \frac{4\pi e^2}{c^2 m} N_0 \quad (9)$$

with N_0 a reference electron density chosen such as to make the difference $N(x) - N_0$ small, we obtain an expression for the correction in amplitude $A(x)$ and phase $\phi(x)$ from Eq. (7):

$$2i(k + \phi') A' + (i\phi'' - 2k\phi') A - \left[(\phi')^2 - \frac{4\pi e^2}{c^2 m} (N - N_0) \right] A = 0 \quad (10)$$

We neglected the second derivative of the amplitude A'' because of its smallness (see, for instance, Ref. 6). Setting

$$\phi' = \sqrt{\frac{4\pi e^2}{c^2 m} (N - N_0)} \quad (11)$$

we obtain from Eq. (10)

$$\frac{A'}{A} = \frac{i}{2} \frac{i\phi'' - 2k\phi'}{k + \phi'} \quad (12)$$

Noting that ϕ' is of the order of ϕ/L where L is the scale length of changes in the electron density which measures in kilometers and that on the other hand k^{-1} is of the order of centimeters, we see that Eq. (12) can be replaced by

$$\frac{A'}{A} = -i\phi' \quad (13)$$

the error being of the order of 10^{-5} ($\phi/kL \approx 10^{-5}$). But Eq. (13) yields as solution

$$A = e^{-i\phi} \quad (14)$$

disregarding an immaterial integration constant. From Eq. (8) we see immediately that there is no effect in first order.

In second order we obtain from Eq. (12)

$$\frac{A'}{A} = -i\phi' + \frac{i}{2k} [2(\phi')^2 + i\phi''] \quad (15)$$

which when integrated yields

$$A = e^{-i\phi} \exp \left\{ k^{-1} \int^x d\tau \left[i(\phi')^2 - \frac{1}{2} \phi'' \right] \right\} \quad (16)$$

The first term under the integral sign in Eq. (16) is always imaginary (see Eq. 11) and will, therefore, always lead to a phase shift.

If the electron density $N(x)$ is always larger than the reference electron density N_0 throughout the ray path, the signal will always be attenuated. In the opposite case the second term under the integral becomes imaginary and leads to an additional phase shift. However, the effect is extremely small, being of the order $\lambda/L \approx 10^{-5}$ at best.

Turning now to a situation in which the electron density inhomogeneities are transverse (z direction) to the radio beam direction, we put

$$E = A(z) \exp [i(kx - \omega t) + i\phi(z)] \quad (17)$$

and obtain in complete analogy to Eq. (11)

$$\phi' = \sqrt{\frac{4\pi e^2}{c^2 m} [N(z) - N_0]} \quad (18)$$

where of course the prime means differentiation with respect to z . The amplitude turns out to be

$$A(z) = A_0 (\phi')^{-1/2} \quad (19)$$

We assume for convenience that $N(z) > N_0$. It is clear then that a surface of constant phase, the wave front, is given by Eqs. (17) and (18):

$$kx + \int_{z_0}^z \sqrt{\frac{4\pi e^2}{c^2 m} [N(\tau) - N_0]} d\tau = \text{constant} \quad (20)$$

so that

$$\frac{dx}{dz} = -\frac{1}{k} \sqrt{\frac{4\pi e^2}{c^2 m} [N(z) - N_0]} = \tan \alpha \approx \alpha \quad (21)$$

where α is the angle between the direction of propagation and the x coordinate (the undisturbed direction of propagation). To roughly estimate the angle α , let us put $N(z) = N_0(1 + z^2/D^2)$ where D , the scale length, is assumed to be 10^3 km. For a beamwidth B of 26 m, the diameter of the DSN antennas, we obtain from Eq. (21)

$$\alpha = \frac{\omega_P}{\omega} \frac{B}{D} = 1.8 \times 10^{-9} \text{ radians} \quad (22)$$

assuming $N_0 = 10 \text{ cm}^{-3}$ and $\omega = 2 \times 10^9 \text{ sec}^{-1}$.

The apparent change in the range due to such small angles is very small indeed. To estimate its value, it suffices to consider that for a distance of 1 AU, the lateral deviation of the ray path is only about 0.2 km, assuming an angle as given by Eq. (22). The change in the range or length of the ray path is then only fractions of a centimeter.

Solar plasma clouds originating from solar flares are also of concern because of their vastly larger electron density. Typically, their dimensions are of the order of 10^6 km and their electron densities are 10 to 100 times that of the ambient plasma wind. Here we use a ray tracing technique to estimate their possible influence on the deflection of radio beams. A simplified geometry of a plasma cloud is given in Fig. 1.

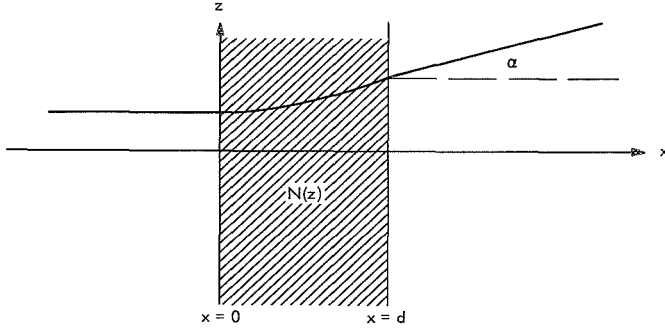


Fig. 1. Simplified geometry of a plasma cloud

A radio signal enters a plasma slab, confined between the planes $x = 0$, and $x = d$, normally to its surface. Due to a lateral electron density inhomogeneity $N(z)$, the beam will be deflected toward a region of *lower* electron concentration and will eventually emerge in a different direction characterized by the angle α in Fig. 1. The refractive index of the plasma is again given by

$$n = \sqrt{1 - \frac{4\pi e^2}{m\omega^2} N(z)} = 1 - \frac{2\pi e^2}{m\omega^2} N(z) \quad (23)$$

since the radar frequency ω is so much larger than the plasma frequency $4\pi e^2 N/m$. In order to obtain an expression for the angle α and to ultimately evaluate the effect of the bending on the ray path, it is quite sufficient to use Fermat's principle

$$\delta \int n ds = 0 \quad (24)$$

If we express the ray in Fig. 1 by $z = z(x)$, the Euler equation for it becomes very simple:

$$\frac{1}{n} \frac{dn}{dz} = \frac{z''}{1 + (z')^2} \quad (25)$$

where a prime means differentiation with respect to x . Integrating Eq. (25) once yields

$$[1 + (z')^2]^{1/2} = \frac{n}{n_0} \quad (26)$$

$n_0 = n$ at the position $x = 0$ (see Fig. 1), and $z' = dz/dx = 0$ at $x = 0$. It follows from Eq. (26) that

$$x = \int_{z_0}^z \frac{dz}{\sqrt{\left(\frac{n}{n_0}\right)^2 - 1}} \quad (27)$$

is the desired relationship between z and x . Since x is by definition real, n must be greater than n_0 . The beam is indeed deflected into regions of a higher refractive index or a lower electron concentration.

According to P. F. MacDoran¹ the time rate of change of the electron content I of a typical solar plasma cloud can be as much as

$$\frac{dI}{dt} = 3 \times 10^{15} \text{ m}^{-2} \text{ sec}^{-1} \quad (28)$$

Assuming a cloud velocity of 300 km-sec⁻¹ and an extension of some 10⁶ km (values which are generally accepted; see, for instance, Ref. 7), we obtain a characteristic value for the electron density gradient of about

$$\frac{dN}{dz} \approx 10 \text{ m}^{-4} \quad (29)$$

To estimate the angle α in Fig. 1, we now use Eq. (23) together with a linear relationship $N = N_0(1 - \gamma z)$. The integral (27) becomes

$$x = \int_{z_0}^z \frac{dz}{\sqrt{\left(1 + \gamma \frac{2\pi e^2}{m\omega^2} N_0 z\right)^2 - 1}} \quad (30)$$

Defining

$$\beta = \gamma \frac{2\pi e^2}{m\omega^2} N_0 \quad (31)$$

and putting $z_0 = 0$ for convenience, we obtain from Eq. (30)

$$\beta x = \ln \{1 + \sqrt{\beta^2 z^2 + 2\beta z} + \beta z\} \quad (32)$$

We also have (see Fig. 1):

$$\tan \alpha = \left(\frac{dz}{dx}\right)_{x=d} = \sqrt{(1 + \beta z_1)^2 - 1} \quad (33)$$

where z is the solution of Eq. (32) with $x = d$.

The solution of Eq. (32) in turn is given by

$$\beta z = \cosh(\beta x) - 1 \quad (34)$$

¹Private communication.

and, finally,

$$\tan \alpha = \sinh(\beta d) \quad (35)$$

Just to see how small the angle α is, we take typical values for the plasma cloud as given by MacDoran. Let $N_0 = 300 \text{ cm}^{-3}$ and $\omega = 4\pi \cdot 10^9 \text{ Hz}$. From Eq. (29) the value of γ turns out to be

$$\gamma = \frac{1}{3} 10^{-7} \text{ m}^{-1} \quad (36)$$

Let $d = 10^9 \text{ m}$, the scale length of a typical plasma cloud, then

$$\tan \alpha = \sinh \beta d = \sinh(10^{-7}) \quad (37)$$

so that α is 10^{-7} rad signifying a lateral deflection of the beam at a distance of 1 AU of about 10 km, somewhat larger than before (Eq. 22) but still totally negligible.

Finally, we address ourselves to the question of pulse degradation by dispersion in the interplanetary plasma. It is clear that a pulse or pulse train may be represented by a Fourier integral. Accordingly the electric field of the radio signal is

$$E \sim I = \int F(\omega) d\omega \exp[i\phi(\omega)] \quad (38)$$

where

$$\phi(\omega) = \frac{x}{c} \left(\omega - \frac{\omega_P^2}{2\omega_0} \right) - \omega t \quad (39)$$

which is a solution of Eq. (7) using the approximation

$$\left(1 - \frac{\omega_P^2}{\omega^2} \right)^{1/2} = 1 - \frac{\omega_P^2}{2\omega^2}$$

The pulse spectrum $F(\omega)$ is sharply peaked at the carrier frequency ω_0 with an inverse bandwidth ω_1 small compared to the carrier. For the DSN transmitter $\omega_1/\omega_P = 2.5 \times 10^{-4}$, surely a small number. Because of these properties of $F(\omega)$, the phase $\phi(\omega)$ can be expanded in a Taylor series about ω_0 and we have

$$\begin{aligned} \phi(\omega) &= \left(\frac{x}{c} - t \right) \omega_0 - \frac{\omega_P^2 x}{2c\omega_0} + \left(\frac{x}{c} - t + \frac{\omega_P^2 x}{2c\omega_0^2} \right) (\omega_0 - \omega) \\ &\quad - \frac{\omega_P^2 x}{2c\omega_0^3} (\omega_0 - \omega)^2 + \dots \end{aligned} \quad (40)$$

With the substitution $\omega_0 - \omega = \omega'$, we obtain from Eqs. (38) and (40)

$$\begin{aligned} I &= \exp \left\{ i \left[\frac{x}{c} \left(\omega_0 - \frac{\omega_P^2}{2\omega_0} \right) - \omega_0 t \right] \right\} \int d\omega' F(\omega') \\ &\quad \times \exp \left\{ i \left[\frac{x}{c} - t + \frac{\omega_P^2 x}{2c\omega_0^2} \right] \omega' - i \frac{\omega_P^2 x}{2c\omega_0^3} (\omega')^2 \right\} \end{aligned} \quad (41)$$

where it is recognized that the first exponential determines the phase velocity and the first term in the second exponential determines the group velocity and the last term represents a distortion of phase and amplitude. For mathematical convenience we take a gaussian pulse

$$F(\omega') = \frac{1}{\sqrt{\pi} \omega_1} \exp \left[- \frac{(\omega')^2}{\omega_1^2} \right] \quad (42)$$

The integral (41) becomes with the pulse spectrum (42)

$$\begin{aligned} I &= \left(1 + i \frac{\omega_P^2 \omega_1^2 x}{2c\omega_0^3} \right)^{-1/2} \exp \left\{ - \frac{\left[\frac{x}{c} - t + \frac{\omega_P^2 x}{2c\omega_0^2} \right]^2}{4 \left(\frac{1}{\omega_1^2} + i \frac{\omega_P^2 x}{2c\omega_0^3} \right)} \right\} \\ &\quad \times \exp \left\{ i \left[\frac{x}{c} \left(\omega_0 - \frac{\omega_P^2}{2\omega_0} \right) - \omega_0 t \right] \right\} \end{aligned} \quad (43)$$

The term $\epsilon = \omega_P^2 \omega_1^2 x / 2c\omega_0^3$ responsible for the pulse degradation can quickly be seen to be ridiculously small even for distances x of the order of 1 AU. For $\omega_1 \approx \frac{1}{2} 10^6 \text{ sec}^{-1}$, $\omega_0 \approx 2 \times 10^9 \text{ sec}^{-1}$, $\omega_P \approx 1.8 \times 10^5 \text{ sec}^{-1}$ (for $N_0 = 10 \text{ cm}^{-3}$), we have

$$\epsilon = 1.6 \times 10^{-12} x$$

where x is measured in kilometers. The influence of dispersion on the pulse shape is negligible. The situation would change drastically if the carrier frequency would be lowered and the modulation frequency (inverse bandwidth) would be enlarged. For instance, a twice as high modulation frequency together with half the carrier frequency would result in a $4 \times 8 = 32$ -fold enhancement of the pulse shape effect.

It must be realized that Eq. (43) is only valid if $\epsilon < 1$. In that case Eq. (43) may be written as:

$$I = \exp \left\{ i \left[\frac{x}{c} \left(\omega_0 - \frac{\omega_p^2}{2\omega_0} \right) - \omega_0 t \right] \right\} \\ \times \exp \left\{ - \frac{\omega_1^2}{4} \left[\frac{x}{c} - t + \frac{\omega_p^2 x}{2c\omega_0^2} \right]^2 \right\} \\ \times \exp \left\{ i \epsilon \left(\frac{\omega_1^2}{4} \left[\frac{x}{c} - t + \frac{\omega_p^2 x}{2c\omega_0^2} \right]^2 - \frac{1}{2} \right) \right\} \quad (44)$$

where of course

$$\epsilon = \frac{\omega_p^2 \omega_1^2}{2\omega_0^3} \frac{x}{c} \quad (45)$$

In case of a slowly varying electron density along the ray path, we have

$$\omega_p^2 x = \frac{4\pi e^2}{m} I \quad (46)$$

where

$$I = \int_0^x N(\tau) d\tau \quad (47)$$

is the electron content in cm^{-2} since we use cgs units throughout.

At the time

$$t' = \frac{x}{c} - t + \frac{\omega_p^2 x}{2c\omega_0^2} \quad (48)$$

the pulse arrives at the receiver. In that case, x is the distance between the spacecraft and the earthbound receiver. If the pulse (44) is beat against a reference

pulse of the same shape (Eq. 42), there results a signal which may be expressed as

$$v = \exp \left[- \frac{\omega_1^2}{4} (t')^2 \right] \cos \left\{ \epsilon \left(\frac{\omega_1^2}{4} (t')^2 - \frac{1}{2} \right) \right\} \\ - \exp \left[- \frac{\omega_1^2}{4} (t' + \delta)^2 \right] \quad (49)$$

In Eq. (49) the high frequency component has been averaged out and δ is the delay time between the received pulse and the reference pulse. If the pulse maxima coincide ($\delta = 0$), there results a net signal

$$v = 2 \exp \left[- \frac{\omega_1^2}{4} (t')^2 \right] \sin^2 \left\{ \epsilon \left(\frac{\omega_1^2}{2} (t')^2 - \frac{1}{2} \right) \right\} \quad (50)$$

and, since ϵ is small, Expression (50) can be written as

$$v = -2\epsilon^2 \left(\frac{\omega_1^2}{2} (t')^2 - \frac{1}{2} \right)^2 \exp \left[- \frac{\omega_1^2}{4} (t')^2 \right] \quad (51)$$

The pulse Eq. (51) is symmetric about its maximum ($t' = 0$). If the delay time δ is not zero, the pulse shape is asymmetric. Therefore, by changing δ , it is possible to measure the group velocity accurately if the quantity ϵ is not too small. For the DSN, however, ϵ is far too small as we have seen previously and therefore a pulse shape analysis is out of the question.

III. Conclusion

In the foregoing, we have shown that higher order effects of the interplanetary plasma on radio signals as utilized in the DSN are negligible as far as a determination of the electron content is concerned. We have also seen that a lateral change in electron concentration engenders very small angular deviations of the ray path. They also lead to a negligible change in the apparent range. The first order theory is therefore completely adequate to deal with the charged particle content.

References

1. MacDoran, P. F., "A First-Principles Derivation of the Differenced Range Versus Integrated Doppler (DRVID) Charged-Particle Calibration Method," in *The Deep Space Network*, Space Programs Summary 37-62, Vol. II, pp. 28-34. Jet Propulsion Laboratory, Pasadena, Calif., Mar. 31, 1970.
2. Koehler, R. L., *Interplanetary Electron Content Measured Between Earth and the Pioneer VI and VII Spacecraft Using Radio Propagation Effects*, Report SEL 67-051. Stanford Electronics Laboratories, Stanford University, Calif., May 1967.
3. Eshleman, R., "Radar Astronomy of Solar System Plasmas," in *Solar System Radio Astronomy*. Edited by J. Aarons. Plenum Press, New York, 1965.
4. Ginzburg, V. L., *Propagation of Electromagnetic Waves in Plasma*. Gordon and Breach, Science Publishers, Inc., New York, 1965.
5. Stelzried, C. T., *Faraday Rotation Measurement of a 13-cm Signal in the Solar Corona*, Technical Report 32-1401. Jet Propulsion Laboratory, Pasadena, Calif., July 15, 1970.
6. Wait, J. R., *Electromagnetic Waves in Stratified Media*, p. 86. The Macmillan Co., New York, 1962.
7. Land, J. A., and Croft, T. A., *J. Geophys. Res.*, Vol. 75, p. 4623, 1970.

Information Systems: Hardware Version of an Optimal Convolutional Decoder

W. Lushbaugh

Communications Systems Research Section

A hardware version of an optimal convolutional decoder is described. This decoder implements the Viterbi Algorithm for maximum-likelihood decoding of short constraint length convolutional codes. It is capable of decoding at data rates up to a megabit for codes of constraint-length 3, 4, or 5 at code rates $\frac{1}{2}$ or $\frac{1}{3}$.

I. Introduction

The simulation results obtained by Heller (Ref. 1) for the decoding of short constraint length convolutional codes using the Viterbi decoding algorithm created considerable interest in the practical application of the algorithm. Layland (Ref. 2) described an all software decoder of this type capable of a 5 kbits/s data rate for a $K = 4$ rate $\frac{1}{3}$ code. This article describes a hardware version of a Viterbi decoder capable of a megabit data rate for constraint lengths 3, 4, or 5, at code rates $\frac{1}{2}$ or $\frac{1}{3}$.

II. Convolutional Codes and the Optimum Convolutional Decoding Algorithm

A convolutional encoder for a code of constraint length K and rate $1/V$ consists, typically, of a shift register of length $K - 1$, coupled with V parity-check adders. For each new bit to be encoded, the V linear combinations

(Mod 2) of the $K - 1$ bits in the shift register, and the new data bit, are computed and transmitted. The new data bit is then shifted into the coder register and the oldest bit therein shifted out. Clearly, the encoder can be viewed as a finite-state machine with 2^{K-1} states. For each of the 2^{K-1} states that the encoder can assume, there are only two predecessor states possible e.g., if $K = 4$ and the present state is 001, the two possible predecessors are 010 and 011. Thus each state has a possible *zero* or *one* predecessor, the *zero* or *one* being associated with the least significant bit of the state number.

The optimum convolutional decoder contains information pertaining to all possible states of the encoder i.e., there are 2^{K-1} sets of likelihoods or metrics, and 2^{K-1} most-likely bit streams (called survivors) leading to each of the states. At each step in the algorithm, a computation element associated with each state examines the two possible predecessors, adds the correlation between the branch

symbols from each predecessor and the new V received symbols, and chooses the higher likelihood as the new metric for that state. The survivor associated with the winner is also copied as next state survivor and the *zero* or *one* associated with the winner is added as the newest bit in this survivor stream. It has been shown experimentally (see Ref. 2), that oldest bits of the 2^{K-1} survivors converge to each other and to the maximum likelihood decoded answer.

III. Design Philosophy

Two main systems designs were originally considered for the Viterbi decoder. These were the serial computation of the 2^{K-1} states which would use parallel operations on each of the state metrics, and the finally adopted design of parallel computations of the states with a computing unit associated with each of states using serial arithmetic. This design was adopted because the design aim of completing one branch (bit) calculation in $1\ \mu\text{s}$ could easily be met, and because the hardware for one state calculation could be put on a printed circuit board and enable the design to be expanded to larger constraint lengths. A picture of the state board is shown in Fig. 1. Sixteen of these boards were used in the present design, and in general 2^{K-1} are needed for a constraint length K machine.

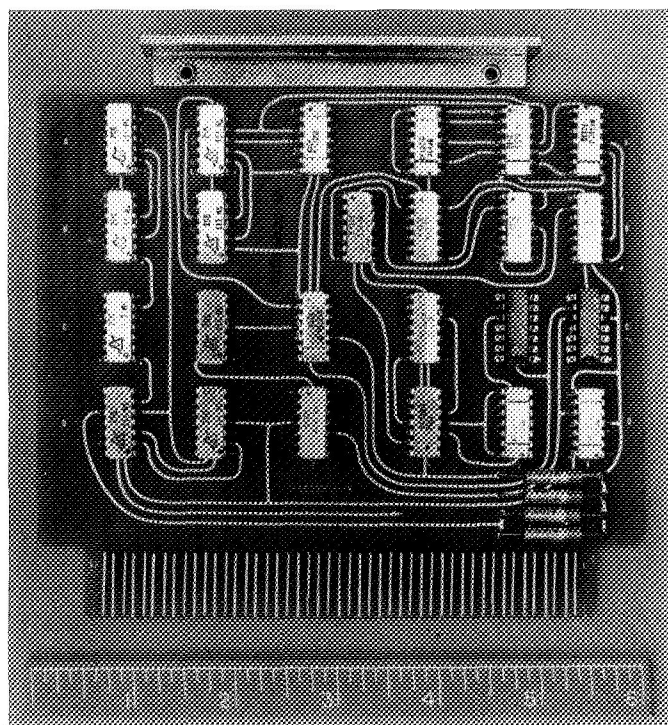


Fig. 1. Viterbi decoder state board

IV. Operation of the State Board

The logic diagram of the state board is shown in Fig. 2. The state board consists mainly of shift register memory, 10 bits for the metric of that state, 32 bits for the survivor stream associated with that state and some serial adders. To increase the speed of the system, two 10-bit registers are actually used to hold metrics, one for each of the two candidates for the new state metric. The metrics are shifted at a 10-MHz rate to be consistent with the $1\ \mu\text{s}$ per node. Since the two candidates are serially introduced to a state board, and the correlation with the received symbols is opposite for each, the received metric from a *zero* predecessor state has the branch metric (for that state) added to it while the metric from the *one* predecessor state has it subtracted. The larger of these two values then becomes the new metric for the state in question. Both of these values have to be saved, since the larger of the two is not known until the sign bits of each arrive at the end of the cycle. A comparison of the two possibilities is made serially as the branch metric is added and the result is stored into the x flipflop at the end of the cycle. This x decision then steers the correct metric out of the board on the next cycle and is used to copy the correct survivor stream into the state board in question. This x value also becomes the most recent member of the survivor stream.

The length of the survivor stream is 32 bits broken into two 16-bit portions, so that a 16-MHz shift rate is necessary to copy the survivors in $1\ \mu\text{s}$. The decoded bit is taken from the oldest survivor of the all *one's* state board. As is shown in Ref. 2, little degradation is suffered by choosing this answer rather than the survivor associated with the maximum likelihood state at each step.

A. Special Boards

In addition to the 2^{K-1} state boards in the system, four special-purpose boards were needed to complete the system. These were the timing board, which develops the various timing signals needed, the metric calculator, a metric select board, and a node sync board.

1. Metric calculator. For a rate $\frac{1}{2}$ code there are only eight possible received sets of 3 symbols for each transmitted bit. Moreover, each state unit of the decoder always expects to see the same set of received symbols. Thus the eight possible values of sums and differences of the three received symbols can be computed in one central location and fed to the appropriate state boards. The states that receive each branch metric are determined by the code, and to change codes, only these eight signals

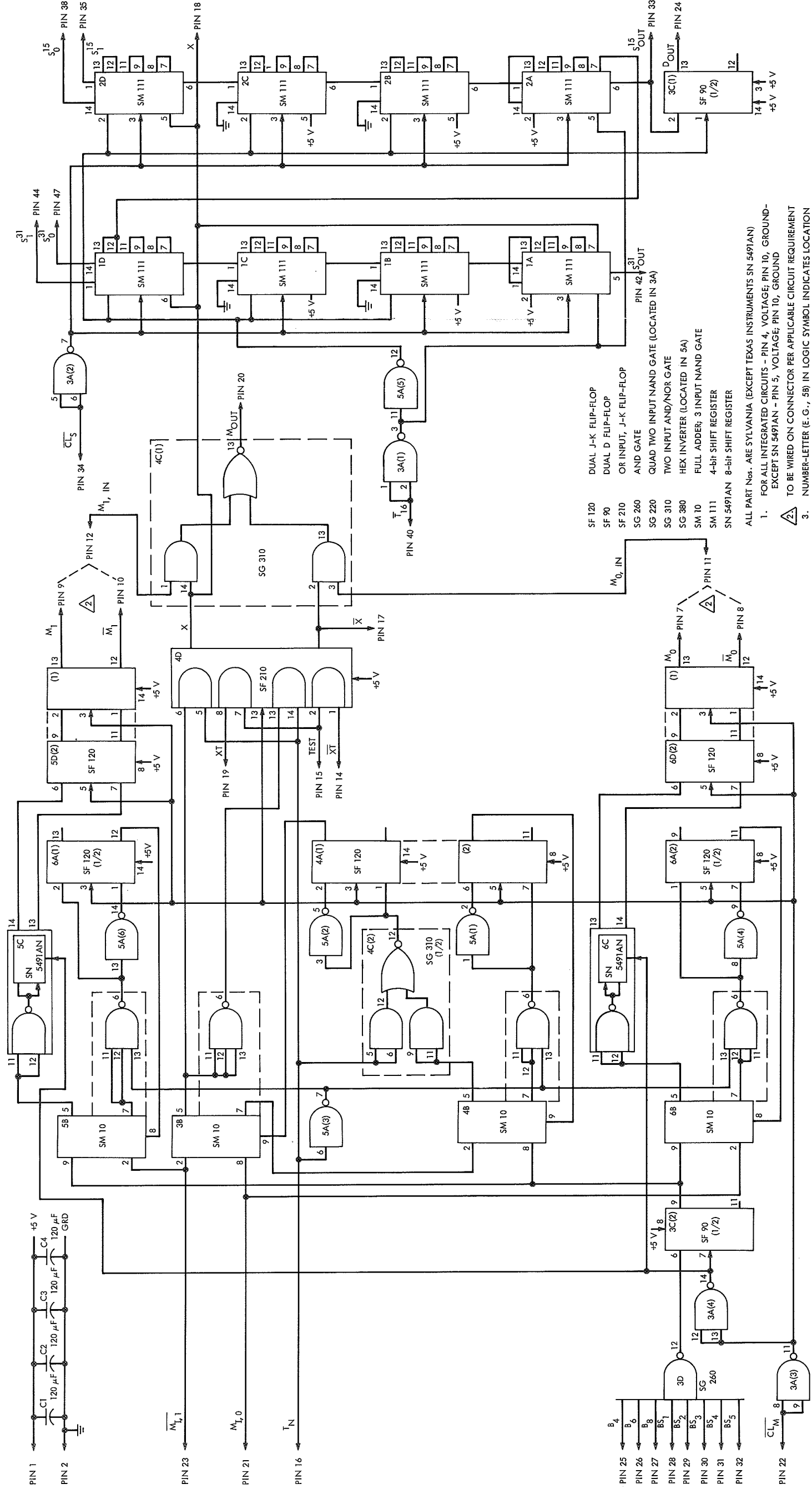


Fig. 2. Logic diagram Viterbi decoder main board

need to be rerouted. This selection and distribution of the branch metrics is performed by the code select board which consists of 16 four-way select gates, one for each state board in the system, allowing up to four codes to be hard-wired into the system and selectable with a four-position switch.

The metric calculator has been designed to accept symbols quantized up to four bits each. When these symbols are properly scaled and three are added together the range of branch metrics for a rate $\frac{1}{2}$ code is -45 to $+45$.

Changing the code rate to rate $\frac{1}{2}$ is accomplished by setting one of the symbols to zero on the metric calculator and using the four significant results that remain as the branch metrics.

To change the constraint length of the code, state boards are associated in groups of $16/2^{K'-1}$ where K' is one of the other possible values of constraint length i.e., either 4 or 3. Each of the groups of states now corresponds to a superstate with each state unit within it receiving the same branch metrics. It can be shown that all states within a superstate perform identically after a transient of $16/2^{K'-1}$ steps in the algorithm.

2. Node sync. Layland has shown in Ref. 3 that node synchronization of a Viterbi decoder can be obtained using the decoder state likelihoods integrated over several hundred code branches assuming only that the data source is sufficiently random. The design finally adopted, however, does not use integration over a fixed number of nodes but instead compares the uphill climb of the metrics to the sum of the absolute values of the received symbols

$$\sum_1^v |r_j|$$

Figures 3 and 4 show the experimental densities of the state likelihoods minus

$$\sum_1^v |r_j|$$

for a $K = 4$ and $K = 5$ code. It was observed from these curves that if $+4$ is added to both curves, then the in-sync version would be shifted positive while the out-of-sync curve would remain negative. Thus an in-sync indication is the positive drift of the quantity

$$M_k - M_0 - \sum_{n=1}^k \sum_{j=1}^v |r_{j,n}| + 4k$$

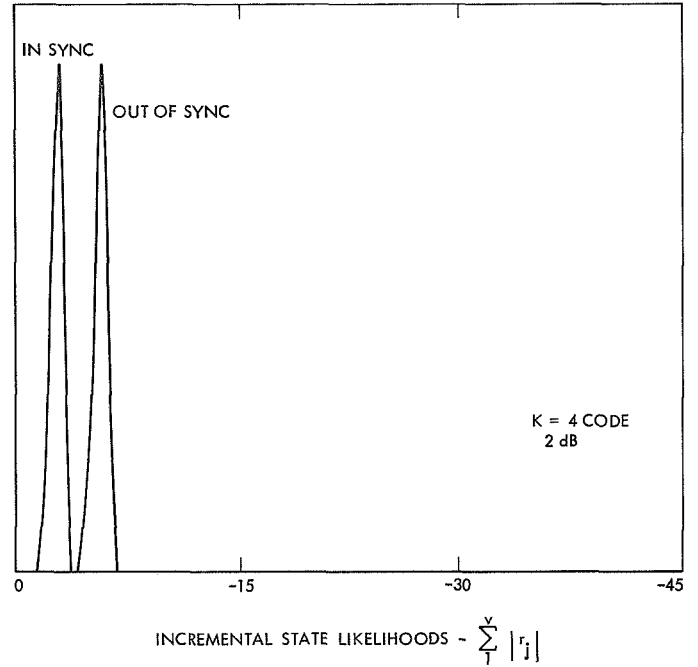


Fig. 3. Experimental densities of incremental state likelihoods minus $\sum_1^v |r_j|$ for a $k = 4$, rate $\frac{1}{2}$ code

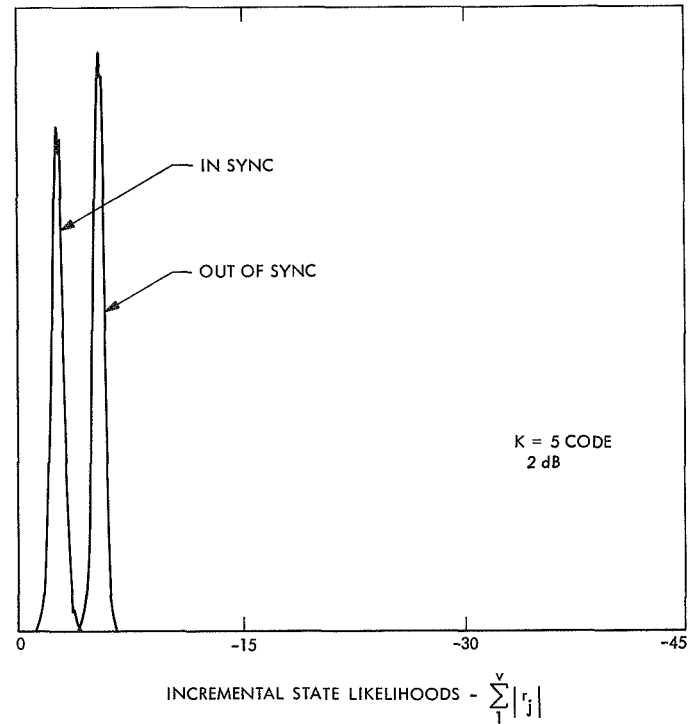


Fig. 4. Experimental densities of incremental state likelihoods minus $\sum_1^v |r_j|$ for a $k = 5$, rate $\frac{1}{2}$ code

where M_k is the k th metric and M_0 is the metric at some starting point. In the actual design, 10 bit numbers are used for this quantity which is initially loaded with some $M_0 + 256$ and the sign bit is monitored for positive or negative overflow. These overflows are in turn divided by three to increase the integration time to the order of magnitude suggested by Layland.

B. Code Conventions

For each $V - 3$ code there are 6 different permutations of sending the three symbols as well as a twofold symmetric way of interpreting the order of the taps on the encoder. For this reason a standard way of interpreting each code is desirable. The present decoder has been wired according to the conventions defined by the following algorithm:

- (1) Write the code in binary on V lines and write the weight of each term below, e.g., for a $K = 6$ and $V = 3$ code

$$\begin{array}{r} 1\ 0\ 1\ 1\ 1\ 1 \\ 1\ 0\ 1\ 1\ 0\ 1 \\ 1\ 1\ 0\ 0\ 1\ 1 \\ \text{Weight of each tap: } 3\ 1\ 2\ 2\ 2\ 3 \end{array}$$

- (2) Take the K digit number that results and its reverse e.g., in this case,

3 1 2 2 2 3 and 3 2 2 2 1 3

and choose the larger of the two as the standard order for writing the code. The newest bit of the encoder will now be associated with the most significant bit of this number.

- (3) Rewrite the code as in step 1 but in the standard order e.g.,

$$\begin{array}{r} 1\ 1\ 1\ 1\ 0\ 1 \\ 1\ 0\ 1\ 1\ 0\ 1 \\ 1\ 1\ 0\ 0\ 1\ 1 \end{array}$$

- (4) Now interpret each row as a binary number, most significant bit on the left, and reorder them by mag-

nitude. The smallest of these will be S_1 , the next S_2 , etc., e.g.,

$$\begin{array}{l} S_1 = 1\ 0\ 1\ 1\ 0\ 1 \\ S_2 = 1\ 1\ 0\ 0\ 1\ 1 \\ S_3 = 1\ 1\ 1\ 1\ 0\ 1 \end{array}$$

This is the uniquely defined standard form for the code and the encoder is to be wired to transmit these 3 symbols in the order S_1, S_2, S_3 . Table 1 shows the standard form of the three codes presently wired into the machine.

Table 1. Standard form of present three codes

Code	S_1	S_2	S_3
$K = 3, V = 2$	101	111	—
$K = 4, V = 3$	1011	1101	1111
$K = 5, V = 3$	10101	11011	11111

V. Conclusions

Figure 5 shows a picture of the completed system. The 16-state board and four special boards, which occupy two slots each, just fills a standard chassis with 25 slots. A single 5-V power supply is used and the system draws 12 A. System debugging has been completed and simulation has shown that the system operates in agreement with error rate predictions from previous software simulation.

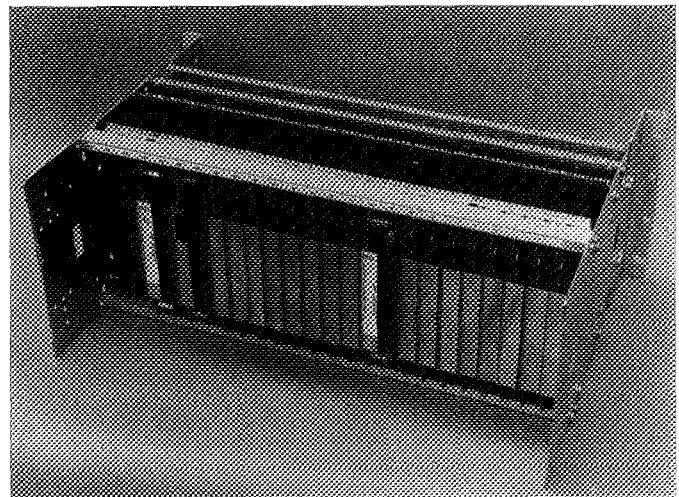


Fig. 5. Completed decoder

References

1. Heller, J. A., "Sequential Decoding: Short Constraint Length Convolutional Codes," in *Supporting Research and Development*, Space Programs Summary 37-54, Vol. III, pp. 171-177. Jet Propulsion Laboratory, Pasadena, Calif., Dec. 31, 1968.
2. Layland, J. W., "Information Systems: Capabilities of an All-Software Optimum Convolutional Decoder," in *The Deep Space Network*, Space Programs Summaries 37-62, Vol. II, pp. 64-66. Jet Propulsion Laboratory, Pasadena, Calif., March 31, 1970.
3. Layland, J. W., "Information Systems: Synchronizability of Convolutional Codes," in *The Deep Space Network*, Space Programs Summary 37-64, Vol. II, pp. 44-50. Jet Propulsion Laboratory, Pasadena, Calif., August 31, 1970.

Improved Frequency Dividers

G. Lutes

Communications Systems Research Section

Frequency dividers with improved phase stability were recently developed for use in the hydrogen maser frequency standard. The commonly used methods of frequency division were found to have excessive phase noise and long-term drift and would seriously degrade the inherent stability of the frequency standard.

I. Introduction

Frequency dividers with improved phase stability were recently developed for use in the hydrogen maser frequency standard. The commonly used methods of frequency division were found to have excessive phase noise and long-term drift and would seriously degrade the inherent stability of the frequency standard.

The improved frequency dividers consist of a digital divider in parallel with an analog gate. The analog gate is opened by the digital divider allowing the input fre-

quency to pass through the gate at the exact time and interval to achieve the desired division.

II. Configuration

A block diagram of the improved frequency divider is shown in Fig. 1.

The first amplifier, A1, is an isolation amplifier which provides a constant 50- Ω input impedance and a voltage gain of approximately seven. The output of A1 is im-

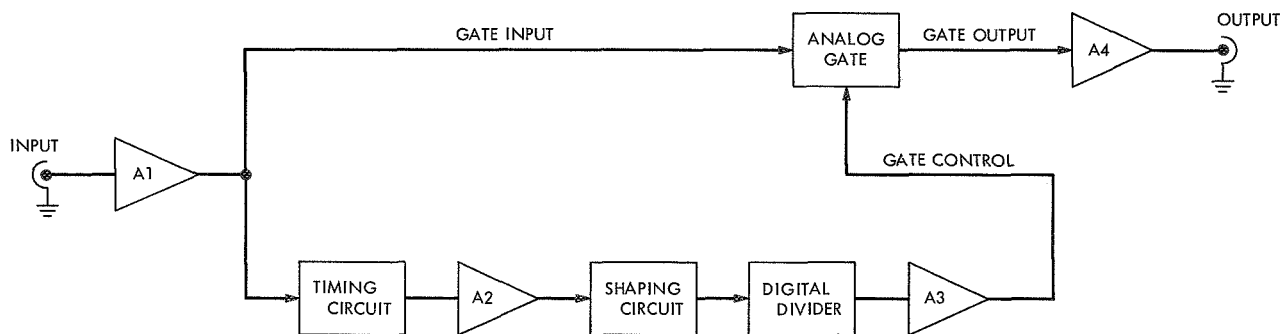


Fig. 1. Frequency divider block diagram

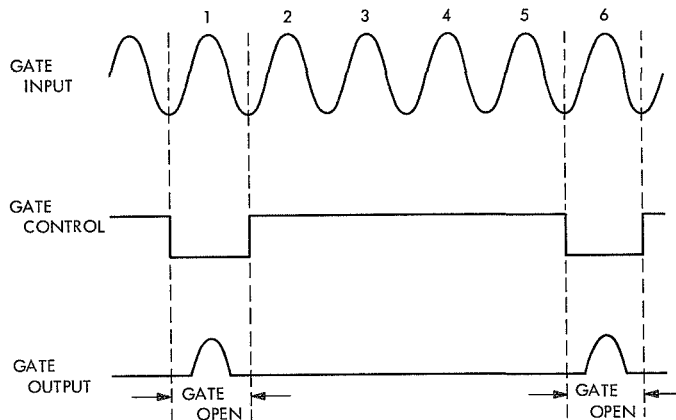


Fig. 2. Divide-by-5 analog gate waveforms

pressed on an analog gate which is opened by a digital signal to allow one half cycle of the signal from A1 to pass through the gate every n th cycle, where n is the division ratio.

The clock for the digital divider is taken from the output of A1 and goes through a timing circuit which is used to set the time relationship between the analog signal and the digital signal at the analog gate (Fig. 2). The signal is then amplified by A2 and shaped properly to drive the digital divider. The output of the digital divider is one pulse every n th cycle of the input frequency and has a pulse width of one cycle, as shown in Fig. 2.

The output pulse from the digital divider goes through an inverting amplifier, A3, which drives the analog gate. The gate is opened and allows the positive part of the input signal to pass through. This results in a signal at the input of the tuned amplifier, A4, which is the positive half sine wave every n th cycle of the input signal (Fig. 2). The output of the tuned amplifier drives a distribution amplifier which is not shown.

III. Operation

The phase noise of the improved frequency dividers was compared to several other modules presently in use. An improvement in phase noise of nearly two orders of magnitude over a typical frequency divider now in use is indicated by the graph of Fig. 3. This graph shows the single sideband phase noise density relative to the carrier as a function of frequency for the modules which were compared. The measurement method is described in Ref. 1.

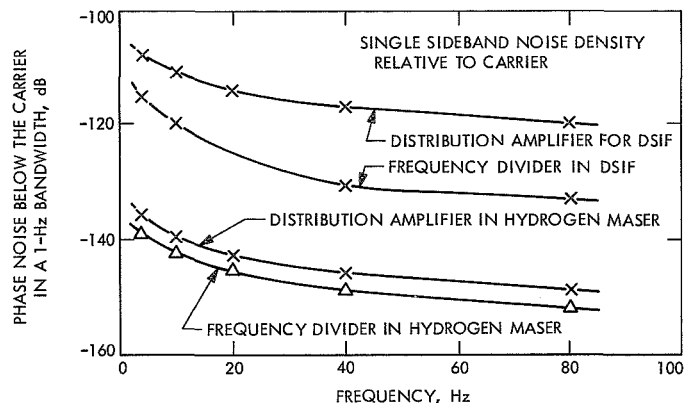


Fig. 3. Comparison of phase noise

The bandwidth of the prototype is approximately 10%. Much wider bandwidths could be achieved since it is limited only by the timing circuit and the tank circuit of the tuned amplifier, A4. Other test results are shown in Table 1.

This type of divider does not have the problems associated with more commonly used designs, such as spurious modes of operation, unreliability, sensitivity to power supply variations and temperature effects.

This design utilizes the reliability of a digital divider but eliminates the phase noise inherent in digital circuitry. A considerable improvement in frequency dividers is indicated by the test results, which show substantially better phase stability, reliability, temperature stability, reproducibility, bandwidth capability, and insensitivity to power supply variations.

Table 1. Test results

Measurement	Nominal	Measured
Input Z	50 Ω	<1.1:1 VSWR
Output Z	50 Ω	<1.1:1 VSWR
Bandwidth	See text	10%
Phase shift with temperature	—	± 10 from 0 to 50°C
Amplitude variation with temperature	—	<0.5 dB from 0° to 50°C
Distortion	<5% THD	<3% THD
Power supply	± 15 and $+5$ V	
THD = total harmonic distortion.		

Reference

1. Meyer, R., and Sward, A., "Frequency Generation and Control: The Measurement of Phase Jitter," in *The Deep Space Network*, Space Programs Summary 37-64, Vol. II, pp. 55-58. Jet Propulsion Laboratory, Pasadena, Calif., Aug. 31, 1970.

The Limits of Minimum Distance Decoding

R. J. McEliece

Communications Systems Research Section

We point out that decoding algorithms which are based on the minimum distance of a block code cannot be used to achieve channel capacity. This degradation is compared with the similar degradation caused by sequential decoding.

I. Introduction

It is well-known that block coding-decoding schemes suffer several disadvantages relative to convolution coding-sequential decoding schemes. The main disadvantages are: (1) the nonexistence of a known sequence of good block codes with relatively simple decoding algorithms, and (2) the inability of good binary block-decoding algorithms to perform well when hard decisions are not used (the famous 2-dB loss on the white gaussian channel).

On the other hand, sequential decoding has a disappointing flaw: it cannot be practically used to achieve reliable communication at all rates below capacity, as R_{comp} limits performance. I wish to point out in this note that a large class of block-decoding schemes suffer from a similar handicap. The class of decoding algorithms I will consider I call *minimum distance* (MD) algorithms. An MD algorithm is one which is based on the minimum distance d of the code; i.e., it corrects up to $(d - 1)/2$ errors, but no more. We shall see that on a binary symmetric channel

with transition probability p , if $p > 0.075^+$, that $R_{\text{comp}}(p)$ exceeds $R_{\text{MD}}(p)$, the largest rate at which reliable communication can be achieved by an MD algorithm. For binary antipodal signalling over a white gaussian channel, with binary detector quantization, the situation is more complicated for MD algorithm: there exists a dimensionless rate $R = 0.5377^+$ at which the minimum E_b/N_0 required for reliable communication is minimum, 2.547⁺. In order to surpass this with sequential decoding—again with binary quantization—one must use convolutional codes of rates < 0.3196 .

II. An Unproved Assumption

Now before giving the details of this calculation, let us admit that these results depend upon an unproved hypothesis. That hypothesis is that for a fixed rate R , the largest possible value for the minimum distance of a block code of length n is asymptotically equal to $n \cdot H_2^{-1}(1 - R)$, where H_2 is the binary entropy function. We really only

know that the best minimum distance is at least this good. However, this hypothesis is widely believed to be true; and if it should turn out to be false, the results of this note can easily be modified and will not be qualitatively changed.

III. The Details

The details of the calculation are quite easy. For the BSC¹ with error probability p , capacity is $1 - H_2(p)$, and R_{comp} is

$$1 - \log_2(1 + 2\sqrt{p(1-p)})$$

By our above assumption, for large n an MD algorithm will correct $\frac{1}{2}n \cdot H_2^{-1}(1-R)$ errors, and so by the law of large numbers if $p < \frac{1}{2}H_2^{-1}(1-R)$ reliable communication can be achieved. Thus we define $R_{\text{MD}}(p) = 1 - H_2(2p)$; this is the supremum of the set of rates at which MD algorithms will succeed in driving the error probabilities to zero. Figure 1 is a plot of $R_{\text{comp}}(p)/\text{Cap}(p)$ and $R_{\text{MD}}(p)/\text{Cap}(p)$ for $0 \leq p \leq 0.25$. For $p \geq 0.25$ $R_{\text{MD}} = 0$, while

$$\frac{R_{\text{comp}}(p)}{\text{Cap}(p)} \downarrow \frac{1}{2}$$

As stated above, the two curves cross at $p = 0.075355^+$.

For the white gaussian channel, with binary antipodal signalling and binary detector quantization, the calculations are only slightly more difficult. If the energy of one binary symbol is E_s , then the probability of detector error is

$$p = Q \sqrt{\frac{2E_s}{N_0}}$$

where

$$Q(x) = \frac{1}{\sqrt{2\pi}} \int_x^\infty \exp\left(-\frac{t^2}{2}\right) dt$$

¹BSC = binary symmetric channel.

and $\frac{1}{2}N_0$ is the spectral density of the noise process. Instead of dealing with capacities, we wish to know the smallest E_b/N_0 for which the probability of error can be made arbitrarily small. With block (or convolutional) codes of rate R the energy available per channel symbol is $E_s = E_b \cdot R$. Thus with maximum likelihood decoding, reliable communication can be achieved if $R \leq 1 - H_2(p)$; thus the minimum E_b/N_0 is

$$\left(\frac{E_b}{N_0}\right)_{\min} = \frac{1}{2R} (Q^{-1}[H_2^{-1}(1-R)])^2 \quad (\text{capacity})$$

For R_{comp} the equation is

$$R \leq 1 - \log_2(1 + 2\sqrt{p(1-p)})$$

i.e.,

$$\left(\frac{E_b}{N_0}\right)_{\min} = \frac{1}{2R} \left(Q^{-1} \left[\frac{1 - 2^{1-R} (2^R - 1)^{1/2}}{2} \right] \right)^2 \quad (R_{\text{comp}})$$

Finally, for MD decoding, we need

$$p = Q \left(\left[\frac{2E_b R}{N_0} \right]^{1/2} \right) \leq \frac{1}{2} H_2^{-1}(1-R);$$

$$\left(\frac{E_b}{N_0}\right)_{\min} = \frac{1}{2R} \left(Q^{-1} \left[\frac{1}{2} H_2^{-1}(1-R) \right] \right)^2 \quad (R_{\text{MD}})$$

These values are plotted in Fig. 2. Note that both the R_{comp} and the Cap curves are monotone decreasing with R , reflecting the gains which accrue with increasing bandwidth occupancy. However, the MD curve has its minimum at $R = 0.537724^+$ for which $E_b/N_0 = 2.547^+$. In order to surpass this with R_{comp} , we see that $R \leq 0.3196^+$ is required. It is interesting to compare Fig. 2 with Fig. 6.49 in Wozencraft and Jacobs (Ref. 1, p. 442) where similar behavior was observed in the performance of BCH codes versus convolutional codes.

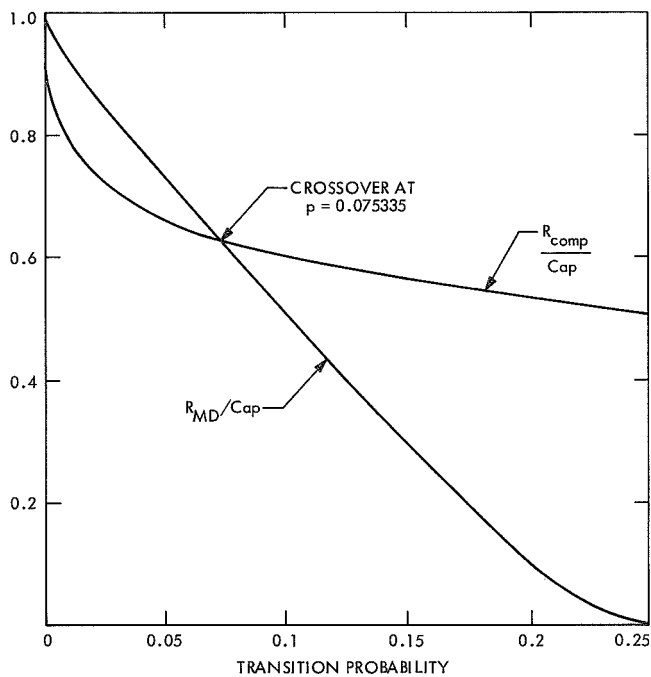


Fig. 1. Comparison of R_{comp} and R_{MD} on a binary symmetric channel

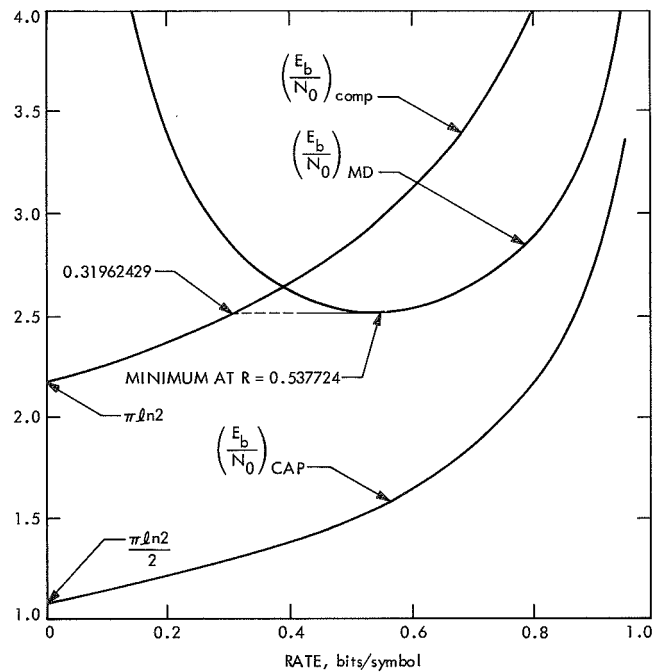


Fig. 2. Comparison of behavior of maximum likelihood sequential, and minimum distance decoding on white gaussian channel with hard limiting

Reference

1. Wozencraft, J., and Jacobs, I., *Principles of Communication Engineering*, John Wiley & Sons, New York, 1965.

Symmetrically Decodable Codes

R. J. McEliece

Communications Systems Research Section

J. E. Savage

Engineering Division, Brown University

With the intention of finding binary block codes which are easily decoded, we examine decoding functions consisting of one level of symmetric functions. We find that all codes so decodable with fixed error correction capability t have rate less than $1/(2t + 1)$ and that this rate is achieved by the repetition code which has two code words and length $2t + 1$. Decoding functions consisting of two or more levels of symmetric functions include all binary functions and can therefore decode arbitrarily good binary codes.

I. Introduction

The design of error control systems often begins with the selection or invention of a code with good error correction capability, and this is followed by the invention of a decoder. Decoders invented in this fashion are often quite complex. This causes one to wonder whether this complexity is the result of an unfortunate choice for the code. In this report we invert the conventional approach to coding by fixing the decoder type and then examining the type, and characteristics of codes decodable with them. We choose to consider decoders for binary, block codes whose decoding function $f = (f_1, f_2, \dots, f_k)$ is a collection of functions, each of which is symmetric on some subset of the components of a received word. We choose to let the code block length be n and denote by M the number of code words in a code.

When the decoding function consists of a single symmetric function ($k = 1$), we show that all codes decodable with it which have minimum distance $d = 2t + 1$ must satisfy

$$M \leq \left\lceil \frac{n+1}{2t+1} \right\rceil = \left\lfloor \frac{n}{2t+1} \right\rfloor + 1 \quad (1)$$

It can also be shown that equality can be achieved. As a consequence of Eq. (1), if d is fixed, then the achievable code rate R decreases with increasing n . This contrasts sharply with the BCH codes, for example, where R approaches 1 with increasing n when d is fixed.

When the decoding function consists of k symmetric functions, we show with a "sphere packing"-like bound

that the maximum code rate is achieved when the domains of definition of f_1, f_2, \dots, f_k are nonoverlapping. This maximum rate is bounded by

$$R \leq \frac{1}{d}$$

and is achievable with a code which consists of the concatenation with itself n/d times of the code containing the $\bar{0}$ word and 1 word of length d . Thus the best symmetrically decodable codes are both repetitious and not very good.

Decoding functions consisting of two or more levels of symmetric functions include the majority—logic decodable codes since the first level can be used to form the syndrome of a linear code using modulo-two sums, which are symmetric functions, followed by one or more levels of majority functions which are also symmetric.

With this report we document a case study of decoders and hope to encourage interest in this unconventional approach to coding.

II. Symmetric Functions

A binary, symmetric function $f(x_1, \dots, x_n)$ of n binary variables has the same value on all n -tuples (x_1, x_2, \dots, x_n) with the same Hamming weight. Thus,

$$f(x_1, x_2, \dots, x_n) = f(y_1, y_2, \dots, y_n)$$

if

$$wt(x_1, \dots, x_n) = wt(y_1, \dots, y_n)$$

Consequently, a binary, symmetric function can assume at most $n + 1$ values, corresponding to the $n + 1$ different weights of binary n -tuples. Also, symmetric functions are rather easy to realize with logic elements. With, at most, n counters, counting to at most n and a few additional logic elements, any symmetric function can be realized.

The symmetric functions form the only known class of functions of low complexity yet rich enough to offer some hope that they can be used to decode codes with good rate and error correction capability.

III. Symmetric Decoders

Consider a binary code C with $|C| = M$ codewords of length n . We suppose that received words R are decoded

by a symmetric function of n variables, $f(x_1, \dots, x_n)$. If the code is to correct t errors, then if E is an error pattern containing $\leq t$ ones, $f(c + E) = f(c)$ for each $c \in C$. But since, as we have seen, the value of a symmetric function depends only on the weight of its argument and since an error pattern of weight t or less can change the weight of c by up to t , we see that the weights of the codewords C_i must satisfy

$$|w(c_i) - w(c_j)| \geq 2t + 1, \quad i \neq j \quad (2)$$

and the maximum number of weights in the range $[0, n]$ which can be chosen to satisfy Eq. (2) is

$$M \leq \left\lceil \frac{n+1}{2t+1} \right\rceil = \left\lfloor \frac{n}{2t+1} \right\rfloor + 1 \quad (3)$$

Equality can be achieved by choosing one word of weight 0, one of weight $2t + 1$, \dots , one of weight $q(2t + 1)$, where

$$q = \left\lfloor \frac{n}{2t+1} \right\rfloor$$

Notice that the rate of such a code is bounded by

$$R \leq \frac{1}{n} \cdot \log_2 \left\lceil \frac{n+1}{2t+1} \right\rceil \leq \frac{1}{2t+1}$$

and we can actually achieve rate $1/(2t + 1)$ with the repetition codes $\{00 \dots 0$ and $11 \dots 1\}$ with decoding function $f =$ majority vote.

IV. Sub-Symmetric Decoders

We now consider a somewhat broader class of decoding functions. The decoder is to consist of k functions f_i , and each f_i is to be a symmetric function of n_i of the variables x_1, x_2, \dots, x_n . We denote the domain of the function f_i by D_i .

If the code C is to correct t errors, then the projection C_i of the code onto each domain D_i will itself correct t errors and must be decodable by f_i . Hence by the results in Section III,

$$M_i \leq \left\lceil \frac{n_i + 1}{2t + 1} \right\rceil$$

Since $M \leq M_1 M_2 \cdots M_k$ (Footnote 1),

$$M \leq \prod_{i=1}^k \left\lceil \frac{n_i + 1}{2t + 1} \right\rceil \quad (4)$$

If the domains D_i are disjoint, this bound can be achieved, since we have seen in *Section III* that it is achievable for $k = 1$, and so we may take $C = C_1 \times C_2 \times \cdots \times C_k$. If however, the D_i are not disjoint the various projections C_i cannot be chosen independently. Nevertheless we argue that nothing can be gained by having the D_i 's overlap, as follows:

Let E be the subset of the variables $\{x_1, \cdots, x_n\}$ which are involved in more than one of the functions f_i , and let C_E be the projection of C onto E . For each word $e \in E$ let C_{ie} be the set of codewords in C_i which are "compatible" with e in the sense that each codeword in C_{ie} agrees with e on $D_i \cap E$. Then the total number of codewords in C compatible with e is $\leq M_{1e} M_{2e} \cdots M_{ke}$ and so

$$M \leq \sum_{e \in E} M_{1e} M_{2e} \cdots M_{ke} \quad (5)$$

Since all codewords in C_{ie} agree in $m_i = |D_i \cap E|$ positions, but their weights must be separated by $2t + 1$, we must have

$$M_{ie} \leq \left\lceil \frac{n_i - m_i + 1}{2t + 1} \right\rceil \quad (6)$$

Also, since $C_i = \cup C_{ie}$ and

$$M_i \leq \left\lceil \frac{n_i + 1}{2t + 1} \right\rceil$$

then

$$\sum M_{ie} \leq \left\lceil \frac{n_i + 1}{2t + 1} \right\rceil \quad (7)$$

Combining Eqs. (5) and (6) we obtain

$$M \leq \sum_e M_{1e} \cdot \left\lceil \frac{n_2 - m_2 + 1}{2t + 1} \right\rceil \cdots \left\lceil \frac{n_k - m_k + 1}{2t + 1} \right\rceil$$

¹Of course, this assumes all variables are used. If some are not, we just connect the unused ones to a symmetric function whose value is constant.

which by Eq. (7) yields

$$M \leq \left\lceil \frac{n_1 + 1}{2t + 1} \right\rceil \cdot \prod_{i=2}^k \left\lceil \frac{n_i - m_i + 1}{2t + 1} \right\rceil$$

This is the same form as Eq. (4), with a total block length of

$$n_1 + \sum_{i=2}^k (n_i - m_i)$$

This is $\leq n$ since for $i \geq 2$ the sets $D_i - D_i \cap E$ are disjoint from each other and from D_1 . Hence if the D_i are allowed to overlap, we can get no more codewords than we could with disjoint D_i at the same (or smaller) block length.

There remains the problem of maximizing Eq. (4) over all values of k and all choices of n_i subject to

$$n_1 + \cdots + n_k = n$$

For each i write $n_i = q_i(2t + 1) + r_i$ with $0 \leq r_i < 2t + 1$. Then we may replace each f_i with q_i functions of $2t + 1$ variables each and obtain

$$\left\lceil \frac{2t + 2}{2t + 1} \right\rceil \times \cdots \times \left\lceil \frac{2t + 2}{2t + 1} \right\rceil = 2^{q_i}$$

possible codewords instead of

$$\left\lceil \frac{n_i + 1}{2t + 1} \right\rceil = q_i + 1$$

Since $2^a \geq a + 1$ for all integers $a \geq 0$, if the product in Eq. (4) is to be maximized no n_i needs to exceed $2t + 1$. So if we write $n = q(2t + 1) + r$, $0 \leq r < 2t + 1$, and take $n_1 = \cdots = n_q = 2t + 1$, $n_{q+1} = r$, we get $M = 2^q$ as the maximum possible number of codewords, and so the rate of the code satisfies

$$R \leq \frac{1}{n} \left\lfloor \frac{n}{2t + 1} \right\rfloor \leq \frac{1}{2t + 1}$$

But since rate $1/(2t + 1)$ can be achieved by a repetition code of length $2t + 1$ and "majority vote" decoding, we see that no code that corrects t errors and is decodable by a sub-symmetric decoder is better than a repetition code. Hence, good symmetrically decodable codes are repetitious.

Boolean Difference Calculus and Fault Finding

I. S. Reed

Electrical Engineering Department, University of Southern California

In this article a method is devised for testing for a possible fault in a gate in a larger switching circuit, that does not require isolating the suspicious gate from the rest of the circuit. The techniques involve a Boolean difference calculus reminiscent of, but not identical to, ordinary difference calculus.

I. Switching Circuits and Gates

A switching circuit $f(x_1, x_2, \dots, x_n)$ is a realization of the mapping $f|2^{(n)} \rightarrow 2$ where 2 is the set of two elements, i.e., $2 = \{0, 1\}$, and $2^{(n)}$ is cartesian products of 2 , taken n times,

$$2^{(n)} = \overbrace{2 \times 2 \times \dots \times 2}^{n \text{ times}}$$

Mapping f is called either a switching or Boolean function. Switching circuits are composed of a number of sub-switching circuits. These elementary switching circuits often occur in modules and are called gates.

A typical switching circuit is illustrated in Fig. 1. It happens that this circuit consists only of *nand* gates. In terms of its gates the circuit of Fig. 1 is the following set of five equations:

$$\left. \begin{aligned} f &= \overline{g_1 g_2} \\ g_1 &= \overline{x_1 g} \\ g_2 &= \overline{x_4 g} \\ g &= \overline{x_1 x_4 u} \\ u &= \overline{x_2 x_3} \end{aligned} \right\} \quad (1)$$

Variables x_1, x_2, x_3, x_4 are called the primary or input variables to the circuit. The outputs of the gates u, g, g_1, g_2 are known as internal or secondary variables, and finally variable f is the output of the circuit. The bars in Eq. (1) denote complementation, i.e., if $u \in 2$, $\bar{u} = 1 \oplus u$ where \oplus is sum, modulo 2.

Suppose f is a switching function of the n binary variables

$$x = (x_1, x_2, \dots, x_n)$$

and u is an internal variable of the circuit. The dependence of f on both x and u is represented functionally as

$$y = f(x, u(x)) \quad (2)$$

where x denotes the binary variables x_1, x_2, \dots, x_n . Necessary and sufficient conditions for f to be a dependent function of u are well known (Ref. 1).

To illustrate the notion of functional dependence, consider again the circuit of Fig. 1. The output

$$y = f(g_1(x), g_2(x)) \quad (3)$$

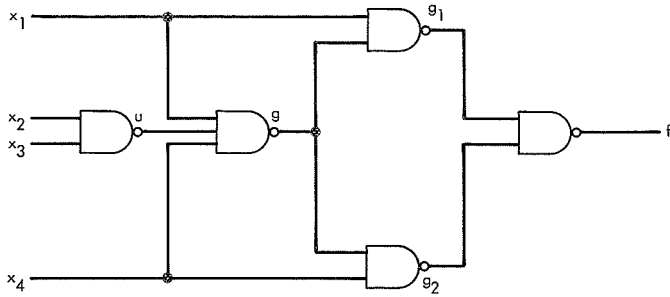


Fig. 1. A typical switching circuit

is a dependent function of both function $g_1(x)$ and function $g_2(x)$ where $x = (x_1, x_2, x_3, x_4)$. Similarly (see Eq. 1),

$$\begin{aligned} y_1 &= g_1(x_1, g(x)) \\ y_2 &= g_2(x_2, g(x)) \end{aligned} \quad (4)$$

are both dependent functions of a primary variable and of the same gate $g(x)$.

Equations (3) and (4) illustrate functionally another important concept. This is circuit fan-in and fan-out. Since $g_1(x)$ and $g_2(x)$ in (3) "feed" the single gate f , the outputs g_1 and g_2 are said to fan-in to f . In Eq. (4) gates g_1 and g_2 are both fed by the same gate g . Schematically Fig. 1 thus requires the output lines of g to fan out from gate g in order to simultaneously feed gates g_1 and g_2 . The generalization of the concept of fan-in and fan-out to n gates is evident.

II. Faults and Their Detection

Let $y = f(x, u(x))$ be a function, dependent on an internal gate variable $u(x)$ where x denotes the set of primary variables x_1, x_2, \dots, x_n . Our purpose is to devise a test for a possible error or fault in the physical realization of gate u .

If a gate such as u can be isolated from the rest of the circuit f , the testing of u would be a straightforward matter. However, today a subcircuit u of a digital integrated circuit usually cannot be disconnected without serious damage to the overall circuit f .

ASSUMPTION A. The only terminals of the circuit f available for testing are the primary input variables x_1, \dots, x_n and the output y .

In order to impress both values 0 and 1, respectively, on u in a reliable manner with test equipment, it is con-

venient to assume there is only one or no fault in the circuit making up f . If u is the gate variable to be tested, one assumes the only possible error in the gates of f resides in the output of gate u . The above single-fault assumption is formalized as follows:

ASSUMPTION B. Let $y = f(x, u(x))$ be a switching function dependent on gate function $u(x)$ where

$$x = (x_1, x_2, \dots, x_n).$$

If gate u is being tested, there is only one possible error or fault in the gates which physically compose f , and that is at the output of gate u .

Now consider the possible errors or faults which can occur at the output of gate u . The types of error possible in u are perhaps best illustrated by the symbol transition diagram of Shannon. Such a diagram is shown in Fig. 2. In Fig. 2 impressed values and received values correspond to transmitted symbols and received symbols, respectively, in the usual Shannon diagram for a binary (or two symbol) channel. $u(x)$ is the desired value or the value which the tester endeavored to impress upon the gate u , whereas $u^R(x)$ is the actual value at the output of gate u as a function of input configuration, $x \in 2^n$. If one could disconnect the output of gate u from the rest of the circuit f and connect the output of gate u to a tester, then $u^R(x)$ would be the actual value received by the tester from gate u .

If the symbol or value k is impressed on gate u , the probability that the same value is received is given by q_k where $k = 0, 1$. The probability is $p_k = 1 - q_k$ that the wrong or opposite symbol is received.

In general, the probabilities in Fig. 2 allow for the possibility of intermittent errors. We are interested for the present only in the static or permanent type of error. These are the probability one type errors. Digital computer designers denote such errors as faults.

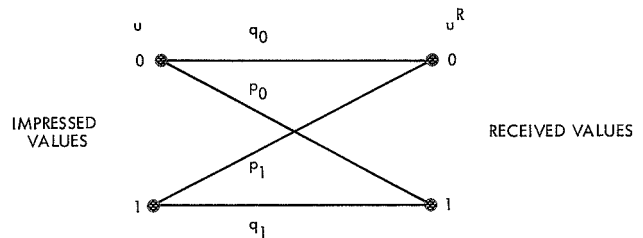


Fig. 2. Shannon error diagram for u

All possible probability one type of errors or faults are illustrated in Fig. 3. The type I fault is u stuck-at-zero. Type II fault is the u stuck-at-one. Finally, the type III error is u complemented.

Type III type errors occur quite frequently in final LSI (large scale integrated) circuit layouts. The bar for complementation is often omitted or inserted erroneously during the final conversion of switching circuit equations to planar circuits. Type I and II faults occur more usually as electronic faults.

We can now prove the following theorem:

THEOREM 1. Let $y = f(x, u(x))$ be a switching function dependent on a gate function $u(x)$ where $x = (x_1, x_2, \dots, x_n)$. Under Assumptions A and B a single fault in u of any of the three types I, II, or III of Fig. 3 can be detected if and only if there exist two input test configurations x^0 and x^1 in 2^n such that

- (1) $u(x^k) = k$
- (2) $f(x^k, u(x^k)) \neq f(x^k, \bar{u}(x^k))$

for both $k = 0$ and $k = 1$.

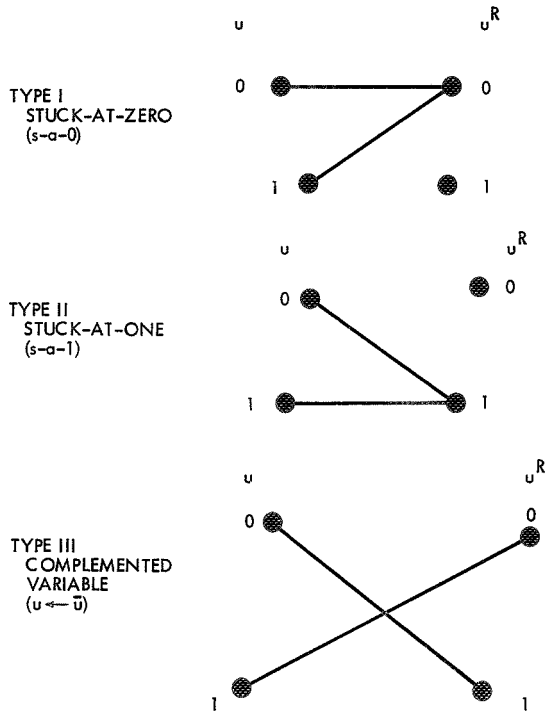


Fig. 3. Three types of faults

Proof: Suppose x^0 and x^1 exist such that (1) and (2) are true and u has a fault, e.g., a type I fault. From Fig. 3 we have

$$u^R(x^0) = u(x^0)$$

$$u^R(x^1) = \bar{u}(x^1)$$

for a type I fault. By Assumptions A and B only the output $y = f$ of the circuit is observable and the observed value of y is

$$y^R(x) = f(x, u^R(x)) \quad (5)$$

for input configuration $x \in 2^n$. If x^0 and x^1 are test configurations, it is apparent that a fault in u can be detected if and only if

$$y^R(x^k) \neq y(x^k) \quad (6)$$

for either $k = 0$ or $k = 1$. Substituting the above value of $u^R(x^1)$ into Eq. (5) yields

$$y^R(x^1) = f(x^1, \bar{u}(x^1))$$

which is not equal to $y(x^1) = f(x^1, u(x^1))$. Thus by Eq. (6) any type I type error can be detected if x^k exist such that (1) and (2) are true for $k = 0$ and 1. In a similar fashion it can be shown that type II and III errors will be detected and sufficiency has been shown.

It is evident that condition (1) is necessary. By Fig. 3 for a type I error in u

$$u^R(x^0) = u(x^0)$$

$$u^R(x^1) = \bar{u}(x^1)$$

and for a type II type error in u

$$u^R(x^0) = \bar{u}(x^0)$$

$$u^R(x^1) = u(x^1)$$

Hence for a type I type error in \bar{u}

$$y^R(x^0) = f(x^0, \bar{u}(x^0))$$

$$y^R(x^1) = f(x^1, u(x^1))$$

and for a type II error

$$y^R(x^0) = f(x^0, \bar{u}(x^0))$$

$$y^R(x^1) = f(x^1, u(x^1))$$

Thus to detect both a type I and II error it is necessary that both

$$f(x^1, \bar{u}(x^1)) \neq f(x^1, u(x^1))$$

and

$$f(x^0, \bar{u}(x^0)) \neq f(x^0, u(x^0))$$

respectively. Thus the necessity for conditions (1) and (2) is established and the theorem is proved.

Condition (2) of the above theorem is true if and only if

$$\Delta_u f(x, u) = f(x^k, \bar{u}(x^k)) \oplus f(x^k, u(x^k)) = 1 \quad (7)$$

where \oplus denotes sum, modulo 2, or what is often called the exclusive *or* operation of Boolean algebra. The left side of Eq. (7), the expression $f(x, \bar{u}(x)) \oplus f(x, u(x))$, is called the partial Boolean difference with respect to u and is denoted by the suggestive notation, $\Delta_u f(x, u)$. The partial Boolean difference was first defined and used by the author (Ref. 2) in analyzing certain error-correcting codes. Aker's in Ref. 1 develops some of the calculus and Boolean functional analysis associated with the partial Boolean difference.

In terms of the partial Boolean difference, Theorem 1 can be restated as follows:

THEOREM 2. *Let $y = f(x, u(x))$ be a switching function dependent on a gate function $u(x)$ where $x = (x_1, x_2, \dots, x_n)$. Under assumptions A and B a single fault u of any of types I, II, or III of Fig. 3 can be detected if and only if there exists two input test configurations x^0 and x^1 in 2^n such that*

$$(1) u(x^k) = k$$

$$(2) \Delta_u f(x^k, u(x^k)) = 1$$

for both $k = 0$ and $k = 1$.

Section III will be devoted to the development of a difference calculus for Boolean algebra which is quite analogous to the classical difference or differential calculus of many real variables. The chain rules of this calculus simplify the computation of the partial difference required in Theorem 2, making possible the automatic generation of test configurations for all gates of a circuit. As stated, Theorem 2 formalizes rather sufficiently a number of related developments by other authors (Refs. 3-5).

III. Boolean Difference Calculus

To develop a calculus for the Boolean difference, recall first the fundamental expansion formula of Boolean algebra. If $x \in 2$ and $f(x)$ is the mapping $f|2 \rightarrow 2$, then

$$\begin{aligned} f(x) &= f(0)\bar{x} \oplus f(1)x \\ &= f(0) \oplus [f(1) \oplus f(0)]x \\ &= f(0) \oplus \Delta f|_{x=0} \cdot x \end{aligned} \quad (8)$$

where $\Delta f|_{x=0}$ denotes the difference with respect to x , evaluated at $x = 0$. The second and third forms of Eq. (8) can be recognized as Newton's interpolation formula over the field of two elements, e.g., Ref. 6, pp. 66-70.

The partial Boolean difference was defined by the left side of Eq. (7) in Section II. We now determine some elementary rules and properties of the Boolean difference. Suppose $f(u)$ and $g(u)$ are mappings of 2 into 2.

$$\text{RULE I. } \Delta_u f(u) = f(1) \oplus f(0)$$

For this rule use definition (7) and formula (8). $\Delta_u f = f(u) \oplus f(\bar{u})$, $f(u) = f(0)u \oplus f(1)\bar{u}$. The rule follows from $u \oplus \bar{u} = 1$.

RULE II. Δ is a "linear" operator.

$$\Delta_u (f \oplus g) = \Delta_u f \oplus \Delta_u g$$

This assertion is immediate by definition and the associativity of addition, modulo 2.

RULE III. If $a \in 2$ is a constant with respect to variable u , $\Delta_u a = 0$.

$$\text{RULE IV. } \Delta_u \bar{f} \cdot g = (\Delta_u f) \cdot g \oplus f \cdot (\Delta_u g) \oplus (\Delta_u f) \cdot (\Delta_u g).$$

Rule III is immediate and Rule IV can be verified directly by calculation. Rule IV can be generalized inductively to a product of n terms.

The following rules of differencing are direct consequences of Rules I through IV.

$$\text{RULE V. } \Delta_u f = \Delta_u f$$

This follows from Rules II and III.

$$\text{RULE VI. } \Delta_u f = \Delta_u f$$

RULE VII. Let u_1, u_2, \dots, u_n be n binary variables, i.e., variables with domain 2, then

$$\Delta_{u_k}(u_1 \cdot u_2 \cdot u_3 \cdot \dots \cdot u_n) = u_1 \cdot u_2 \cdot \dots \cdot u_{k-1} \cdot u_{k+1} \cdot u_{k+2} \cdot \dots \cdot u_n$$

for $k = 1, 2, \dots, n$.

Rules VI and VII are immediate by Rule I.

An important tool for computing the partial differences, needed in Theorem 2, is provided by the partial difference "chain rule" of the next theorem.

THEOREM 3. Let f, g_1, g_2, \dots, g_k and u be Boolean functions of n binary variables x_1, x_2, \dots, x_n . Suppose function f is dependent on functions g_1, g_2, \dots, g_k , and in turn functions g_1, g_2, \dots, g_k are dependent on function u . Then the partial Boolean difference with respect to u satisfies the chain rule,

$$\begin{aligned} \Delta_u f &= \Delta_{g_1} f \cdot \Delta_u g_1 \oplus \Delta_{g_2} f \cdot \Delta_u g_2 \oplus \dots \oplus \Delta_{g_k} f \cdot \Delta_u g_k \\ &\oplus \Delta_{g_1 g_2}^{(2)} f \cdot \Delta_u g_1 \cdot \Delta_u g_2 \oplus \Delta_{g_1 g_3}^{(2)} f \cdot \Delta_u g_1 \cdot \Delta_u g_3 \oplus \dots \\ &\oplus \Delta_{g_{k-1} g_k}^{(2)} f \cdot \Delta_u g_{k-1} \cdot \Delta_u g_k \oplus \dots \\ &\oplus \Delta_{g_1, g_2, \dots, g_k}^{(k)} f \cdot \Delta_u g_1 \cdot \Delta_u g_2 \cdot \dots \cdot \Delta_u g_k \end{aligned}$$

where

$$\Delta_{g_{i_1}, g_{i_2}, \dots, g_{i_m}}^{(m)}$$

denotes the m th partial difference with respect to functions $g_{i_1}, g_{i_2}, \dots, g_{i_m}$.

Proof: A proof for this theorem is provided here only for $k = 2$. A similar proof can be developed for arbitrary k . For more details see Ref. 5.

For this case f is functionally of the form $f = f(g_1(u), g_2(u))$. Use Eq. (8) to expand $f(g_1, g_2)$ with respect to each variable, separately, as follows:

$$\begin{aligned} f(0, g_2) &= f(0, g_2) \oplus [f(1, g_2) \oplus f(0, g_2)] g_1 \\ f(0, g_2) &= f(0, 0) \oplus [f(0, 1) \oplus f(0, 0)] g_2 \\ f(1, g_2) &= f(1, 0) \oplus [f(1, 1) \oplus f(1, 0)] g_2 \end{aligned}$$

Substituting the second and third equations into the first, yields the formula

$$\begin{aligned} f(g_1, g_2) &= f(0, 0) \oplus \Delta_{g_1} f|_{g_2=0} \cdot g_1 \\ &\oplus \Delta_{g_2} f|_{g_1=0} \cdot g_2 \oplus \Delta_{g_1, g_2}^{(2)} f \cdot g_1 g_2 \end{aligned} \quad (9)$$

Formula (9) can evidently be generalized to k variables (Ref. 2).

Take the difference of both sides of Eq. (9) with respect to u , then

$$\Delta_u f = \Delta_{g_1} f|_{g_2=0} \cdot \Delta_u g_1 \oplus \Delta_{g_2} f|_{g_1=0} \cdot \Delta_u g_2 \oplus \Delta_{g_1 g_2}^{(2)} f \cdot \Delta_u (g_1 g_2) \quad (10)$$

since $f(0, 0)$ and the coefficients of g_1, g_2 and $g_1 g_2$ are independent of u . But by Rule IV

$$\Delta_u (g_1 g_2) = (\Delta_u g_1) \cdot g_2 \oplus g_1 \cdot (\Delta_u g_2) \oplus (\Delta_u g_1) (\Delta_u g_2)$$

Substituting this in Eq. (10) and collecting coefficients, we obtain

$$\begin{aligned} \Delta_u f &= (\Delta_{g_1} f|_{g_2=0} \oplus \Delta_{g_1, g_2}^{(2)} f \cdot g_2) \Delta_u g_1 \\ &\oplus (\Delta_{g_2} f|_{g_1=0} \oplus \Delta_{g_1 g_2}^{(2)} f \cdot g_1) \Delta_u g_2 \oplus \Delta_{g_1, g_2}^{(2)} f \cdot \Delta_u g_1 \cdot \Delta_u g_2 \end{aligned}$$

The theorem for $k = 2$ is proved once expansion (8) is used to identify the coefficients of Δ_{g_1} and Δ_{g_2} with $\Delta_{g_1} f$ and $\Delta_{g_2} f$, respectively.

The above theorem and previous rules provide an adequate machinery for calculating partial differences. In the classical difference calculus there are existence theorems associated with certain classes of difference equations and boundary conditions. Similar theorems can be proved for the present difference calculus of Boolean algebra. An example of such a theorem is the next one. This theorem provides a "global" criterion for the existence of test configurations x^0 and x^1 which satisfy both the "boundary" condition

$$(1) \quad u(x^k) = k$$

and the difference equation

$$(2) \quad \Delta_u f(x, u(x)) = 1$$

of Theorem 2.

THEOREM 4. There exist two test configurations x^0 and x^1 , satisfying (1) and (2) of Theorem 2 if and only if functions $u(x)$ and $f(x, u(x))$ are such that

$$(3) \quad \overline{u(x)} \cdot \Delta_u f(x, u) \neq 0$$

$$(4) \quad u(x) \cdot \Delta_u f(x, u) \neq 0.$$

Proof: If (1) and (2) of Theorem 2 are true, then $\overline{u(x^0)} \Delta_u f(x^0, u) = 1$ and $u(x^1) \Delta_u f(x^1, u) = 1$ and (3) and (4)

hold. Conversely if (3) is true, there exists x^0 such that $\overline{u(x^0)} \cdot \Delta_u f(x^0, u) = 1$. But this implies (1) of Theorem 2. Similarly (4) implies (2) of Theorem 2 and theorem is proved.

IV. Example and Remarks

Let f be the switching circuit of Fig. 1. f is a circuit of four primary input variables x_1, x_2, x_3 , and x_4 with circuit equations given by Eq. (1).

As an application of Theorem 2 we will find test configurations $x^k = (x_1^k, x_2^k, x_3^k, x_4^k)$ for $k = 0, 1$ which will test for a fault in gate u . To do this we must compute the partial difference $\Delta_u f$ and set it equal to one. This is done using the chain rule of Theorem 3 and the difference calculus rules of the last section as follows:

$$\begin{aligned}\Delta_u f &= \Delta_u g \cdot \Delta_g f, \\ \Delta_g f &= \Delta_{g_1} f \cdot \Delta_{g_1} g_1 \oplus \Delta_{g_2} f \cdot \Delta_{g_2} g_2 \oplus \Delta_{g_1, g_2}^{(2)} f \cdot \Delta_{g_1, g_2} g_1 \cdot \Delta_{g_2} g_2 \\ \Delta_{g_1} f &= g_2, \quad \Delta_{g_2} f = g_1, \quad \Delta_{g_1, g_2} f = 1 \\ \Delta_{g_1} g_1 &= x_1, \quad \Delta_{g_2} g_2 = x_4 \\ \Delta_u g &= x_1 x_4\end{aligned}$$

Thus we want to find x^k for $x = 0, 1$ such that

$$\begin{aligned}u(x^k) &= k \\ \Delta_u f &= \Delta_u g \cdot \Delta_g f = 1\end{aligned}$$

where

$$\begin{aligned}\Delta_u g &= x_1 x_4 \\ \Delta_g f &= g_2 \cdot x_1 \oplus g_1 x_2 \oplus x_1 x_4\end{aligned}$$

This implies $x^k = (x_1^k, x_2^k, x_3^k, x_4^k)$ must satisfy

$$\begin{aligned}u(x^k) &= k \\ \Delta_u g &= x_1 x_4 = 1 \\ \Delta_g f &= g_2 x_1 \oplus g_1 x_2 \oplus x_1 x_4 = 1\end{aligned} \tag{11}$$

These two configurations are displayed in two rows of the incompletable Table 1. Note that relation $x_1 x_4 = 1$ and $u(x^k) = k$ for $k = 0, 1$ are already satisfied in Table 1. It remains to complete the table, using Eqs. (1), and to show that $\Delta_g f = 1$ can be satisfied.

Table 1. Incompletable table of test configurations for gate u

x_1	x_2	x_3	x_4	u	g	g_1	g_2	f
1			1	0				
1			1	1				

Table 2. Test configurations for gate u ($x_2 x_3 = 0$)

x_1	x_2	x_3	x_4	u	g	g_1	g_2	f
1	1	1	1	0	1	0	0	1
1	—	—	1	1	0	1	1	0

A completed table of test configurations for gate u is shown in Table 2. The two blanks in the table may be filled with elements of the set

$$\{(x_2, x_3) \mid x_2 x_3 = 0\}$$

The solutions of conditions (1) and (2) are not always unique. For this example the test configuration,

$$x^0 = (x_1^0, x_2^0, x_3^0, x_4^0) = (1, 1, 1, 1)$$

is unique and the configuration x^1 is not unique and can be chosen to be

$$x^1 = (x_1^1, x_2^1, x_3^1, x_4^1) = (1, 0, 0, 1)$$

To test for the presence of a fault in any primary input, internal gate, or output one applies Theorem 2 repeatedly, finding test configurations for all such variables. A minimal set of test configurations is obtained by taking minimal union over the set of all test configurations. If n is the number of variables to be tested, the minimal set never exceeds $2n$ test configurations.

References

1. Akers, S. B., Jr., "On the Theory of Boolean Functions," *J. SIAM*, Vol. 2, No. 4, Dec. 1959.
2. Reed, I. S., "A Class of Multiple-Error-Correcting Codes and the Decoding Scheme," *IRE Trans. PGIT-4*, 1954.
3. Armstrong, D. B., "On Finding a Minimal Set of Fault Detection Tests for Combinational Logic Nets," *IEEE Trans. Elec. Comp.*, Vol. IC-15, No. 1, Feb. 1966.
4. Sellers, F. F., Hsiao, M. Y., and Bearnson, L. W., "Analyzing Errors with the Boolean Difference," Annual IEEE Computer Conference, Chicago, Ill., Sept. 1967.
5. Chiang, A. C. L., Reed, I. S., and Banes, A. V., "Data Sensitation, Partial Boolean Difference and Automated Fault Diagnosis," to be published *IEEE Trans. on Elec. Comp.*
6. Van der Waerden, B. L., "Modern Algebra," Vol. I, Frederick Unger Publishing Co., New York, 1949.

New Developments in the Hydrogen Maser Frequency Standard

A. Sward

Communications Systems Research Section

Measurements have been made on the JPL hydrogen masers to determine the average fractional frequency departure versus averaging time. In addition, the receiver section has been modified with a newly developed frequency synthesizer.

I. Introduction

Recently measurements have been made to determine the frequency stability of the new JPL hydrogen masers. In addition, the old receiver-synthesizer section has been modified with a newly developed frequency synthesizer which will not only improve the performance and reliability of the receiver, but also decrease its size and complexity.

This article is a continuation of the articles relating to the hydrogen maser development found in Refs. 1 to 3.

II. Measurement of Frequency Stability

Figure 1 is a plot of the standard deviation of the average fractional frequency departure versus averaging time for two masers. With the power output of the two masers at -85 and -89 dBmW, the measured short-term sta-

bility approaches the theoretical limit predicted by Cutler and Searle (Ref. 4).

III. Receiver-Synthesizer Developments

A new low-drift frequency synthesizer is being built in conjunction with Dana Laboratories which will provide the maser with a frequency settability of 7 parts in 10^{-18} . Its frequency range will be 400 to 510 kHz in steps of 10^{-8} Hz. The synthesizer, when subjected to temperature steps of 25°C , was found to have a maximum drift rate of 0.3×10^{-3} degrees of phase/second at 50 MHz which corresponds to a frequency stability of 1.6 parts in 10^{-14} . This is two orders of magnitude improvement over present units and enables the synthesizer to achieve 10^{-8} Hz resolution. A diagram of the new receiver is shown in Fig. 2. The synthesizer is driven directly from the 100-MHz signal at the output of the 100-MHz distribution amplifier. Output frequencies from the new maser receiver will be 100 MHz, 10 MHz, 5 MHz, 1 MHz, and 100 kHz.

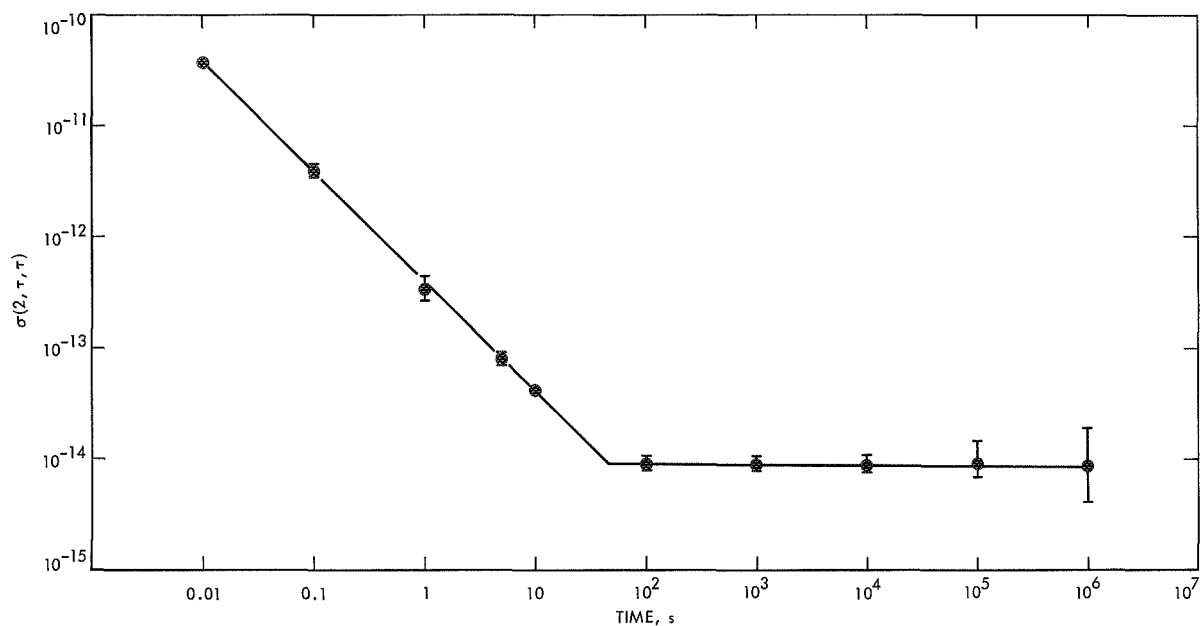


Fig. 1. JPL hydrogen maser frequency stability

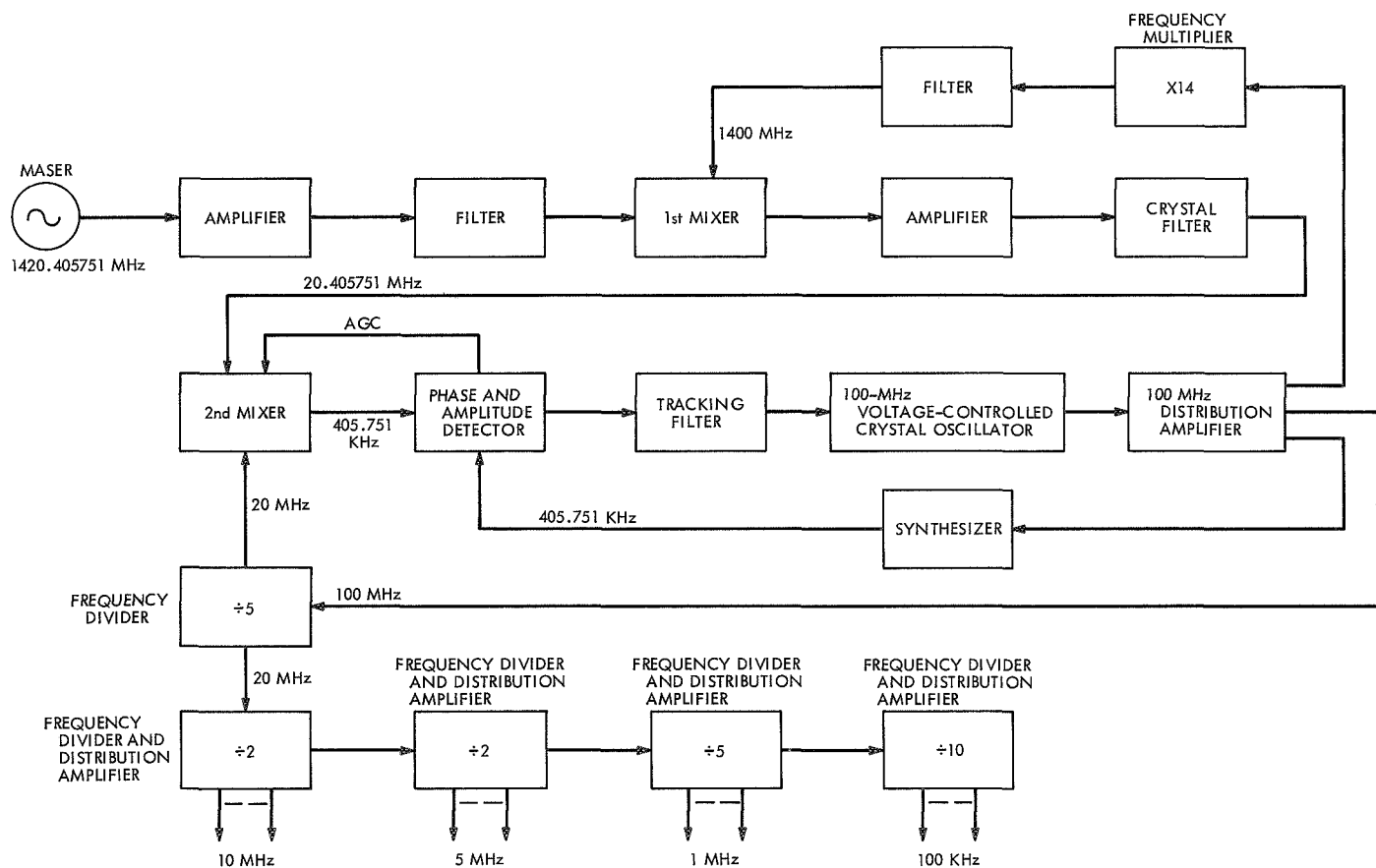


Fig. 2. Hydrogen maser receiver-synthesizer

References

1. Erpenbach, H., Finnie, C., and Petty, S., "Frequency Generation and Control: Atomic Hydrogen Frequency Standard," in *The Deep Space Network*, Space Programs Summary 37-58, Vol. II, pp. 52-55. Jet Propulsion Laboratory, Pasadena, Calif., July 31, 1969.
2. Sward, A., "Frequency Generation and Control: The Hydrogen Maser Frequency Standard," in *The Deep Space Network*, Space Programs Summary 37-59, Vol. II, pp. 40-43. Jet Propulsion Laboratory, Pasadena, Calif., Sept. 30, 1969.
3. Lutes, G., "Frequency Generation and Control: Distribution Amplifiers for the Hydrogen Maser Frequency Standard," in *The Deep Space Network*, Space Programs Summary 37-61, Vol. II, pp. 68-72. Jet Propulsion Laboratory, Pasadena, Calif., Jan. 31, 1970.
4. Cutler, L. S., and Searle, C. L., "Some Aspects of the Theory and Measurement of Frequency Fluctuations in Frequency Standards," *Proc. IEEE*, Vol. 54, February 1966.

Sequential Ranging With the Viterbi Algorithm

U. Timor

Communications Systems Research Section

The performance of the sequential ranging system can be improved by using a maximum likelihood receiver; however, the complexity grows exponentially with the number of components N needed to determine the range unambiguously. A new truncated maximum-likelihood receiver, based on the Viterbi decoder for convolutional codes, is presented and is shown to achieve a maximum-likelihood performance while having a fixed complexity independent of N . The improvement in signal-to-noise ratio, compared to the present receiver, is 1.5 dB for $P_E < 10^{-2}$.

I. Introduction

Ranging systems for deep space applications achieve the required resolution by transmitting, either simultaneously or sequentially, a multi-component signal. Goldstein (Ref. 1) described a sequential ranging system, which transmits $N + 1$ squarewaves of increasing periods $T, 2T, \dots, 2^N T$. The highest frequency component yields the most accurate measurement, but with an added distance of $M \cdot R$, where R is proportional to T and M is an unknown integer. The other N components are used to estimate M and thus remove the ambiguity.

In the above system, the estimation is done sequentially, that is, at each step a binary number a_k is estimated from the signal component which is present at that step. The sequence a_1, \dots, a_N , considered as a binary representation of M , yields an estimate of M .

The performance of the system—that is, the probability of estimating M correctly—can be improved by using a maximum-likelihood estimator, which estimates the whole sequence a_1, \dots, a_N simultaneously. However, the complexity of such a system is proportional to 2^N and is not practical for large N .

We will present a suboptimum estimation procedure, which outperforms the sequential receiver and approaches asymptotically, as the signal-to-noise ratio increases, the performance of the maximum-likelihood receiver. This method is based on the Viterbi algorithm for decoding convolutional codes of short constraint length (ν), and has a complexity of the order of 2^ν , no matter how large N is. The improvement in the signal-to-noise ratio required to achieve a given error probability P_E is 1.5 dB throughout the range of interest ($P_E < 10^{-2}$).

II. The Sequential Receiver

The time-of-flight (TOF) of the signal at t_0 can be represented by

$$\text{TOF} = (M + \epsilon) T \quad (1)$$

where T is the period of the first (highest frequency) squarewave, M is a positive integer and $0 \leq \epsilon < 1$.

Let $\{a_N a_{N-1}, \dots, a_1\}$ be the binary representation of M , that is

$$M = \sum_{k=1}^N a_k 2^{(k-1)} \quad (2)$$

where a_k is 0 or 1.

To measure the TOF, and therefore the range, it is enough to measure ϵ and $\{a_1, \dots, a_N\}$. The present receiver does this sequentially.

We start by transmitting the T -period squarewave to obtain an estimate $\hat{\epsilon}$ of ϵ . The receiver correlates the incoming signal with the receiver coder squarewave and its 90 deg-shift to obtain a pair of outputs x_0, y_0 , from which ϵ is estimated. The correlator is then shifted by $\hat{\epsilon}$ to have a phase of $\hat{\epsilon} - \epsilon$. We will assume that the integration time is long enough to obtain $\epsilon - \hat{\epsilon} = 0$. To estimate a_1, \dots, a_N , squarewaves of periods $2^k T$, $k = 1, \dots, N$ are transmitted sequentially. The outputs of the in-phase and quadrature correlators at the k th step are

$$\begin{aligned} x_k &= s_k + n_k \\ y_k &= r_k + m_k \end{aligned} \quad (3)$$

respectively, where n_k and m_k are independent white gaussian noise samples of zero mean and variance σ^2 ,

$$\begin{aligned} s_k &= \begin{cases} 1 - \alpha_k, & 0 \leq \alpha_k < 2 \\ \alpha_k - 3, & 2 \leq \alpha_k < 4 \end{cases} \\ r_k &= \begin{cases} \alpha_k, & 0 \leq \alpha_k < 1 \\ 2 - \alpha_k, & 1 \leq \alpha_k < 3 \\ \alpha_k - 4, & 3 \leq \alpha_k < 4 \end{cases} \end{aligned} \quad (4)$$

and α_k depends on a_1, \dots, a_k .

It was shown that the probability of error is minimized by shifting the correlator waveform by 90 deg at the k th

step whenever $\hat{a}_{k-1} = 1$, where \hat{a}_{k-1} is the estimate of the previous step. Thus

$$\alpha_k = 2a_k + \sum_{j=1}^{k-1} (a_j - \hat{a}_j) 2^{(j+1-k)} \quad (5)$$

and we estimate

$$\hat{a}_k = \begin{cases} 0 & \text{if } x_k \geq 0 \\ 1 & \text{if } x_k < 0 \end{cases} \quad (6)$$

The procedure is terminated when \hat{a}_N is obtained. The resulting

$$\hat{M} = \sum_{k=1}^N \hat{a}_k 2^{k-1} \quad (7)$$

and $\hat{\epsilon}$ yield the measured TOF.

III. Maximum-Likelihood Estimation

The "estimate-and-shift" sequential method has a strong error propagation property. Suppose the estimate \hat{a}_1 of a_1 is in error, e.g., $a_1 = 0$ but $\hat{a}_1 = 1$. The correlator waveform is shifted by 90 deg at the second step, therefore the no-noise outputs will be A' if $a_2 = 0$ and B' if $a_2 = 1$ instead of A and B , respectively (Fig. 1). Since the receiver estimates $a_2 = 0$ whenever $x_2 \geq 0$, the probability of wrongly estimating a_2 is $1/2$. It can be shown that the error in estimating a_1 will adversely affect the estimation

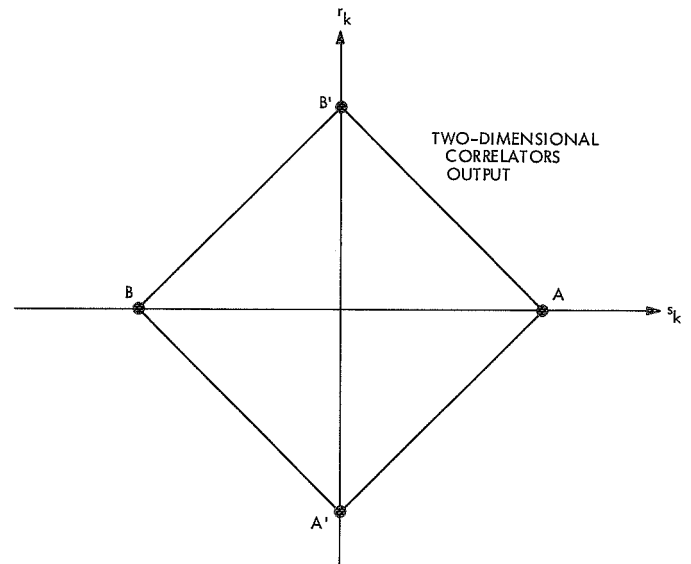


Fig. 1. Correlators output at second step: A or B if $\hat{a}_1 = a_1$ and A' or B' if $\hat{a}_1 \neq a_1$

of a_3, a_4, \dots . However, the effect will diminish as k increases.

This error propagation does not affect the performance of the system, since one wrong estimation is enough to cause an error in the measurement of the TOF. However, since a_k affects all (x_n, y_n) for $n \geq k$, an estimate of a_k based on $\{x_n, y_n; n \geq k\}$ is superior to one which is performed at the k th step, and therefore depends on (x_k, y_k) only.

Assume, as before, that $\hat{\epsilon} \approx \epsilon$ and let

$$\mathbf{x} = (x_1, \dots, x_N)$$

$$\mathbf{y} = (y_1, \dots, y_N)$$

$$\mathbf{a} = (a_1, \dots, a_N)$$

be the correlators output vectors and the TOF binary vector respectively. By Bayes rule we have

$$p(\mathbf{a}|\mathbf{x}, \mathbf{y}) = \frac{p(\mathbf{x}, \mathbf{y}|\mathbf{a})}{p(\mathbf{x}, \mathbf{y})} p(\mathbf{a}) \quad (8)$$

and the maximum-likelihood estimate is the binary vector \mathbf{a}^* which maximizes

$$p(\mathbf{x}, \mathbf{y}|\mathbf{a}) = \frac{1}{(\sqrt{2\pi}\sigma)^{N/2}} \times \exp \left\{ -\frac{1}{2\sigma^2} \sum_{k=1}^N [(x_k - s_k)^2 + (y_k - r_k)^2] \right\} \quad (9)$$

or equivalently minimizes

$$\ell(\mathbf{a}) = \sum_{k=1}^N [(x_k - s_k)^2 + (y_k - r_k)^2] \quad (10)$$

where $s_k, r_k, k = 1, \dots, N$ can be expressed in terms of \mathbf{a} (Eqs. 4 and 5).

Note that the $\hat{a}_j, j = 1, \dots, k-1$ that appear in α_k (and hence in s_k and r_k) are on-the-spot estimates which determine whether the correlator waveforms are shifted in the next step. They depend on the x_j 's alone and not on \mathbf{a} , and are known to the receiver when $\ell(\mathbf{a})$ is evaluated.

Since we have to choose the most likely of 2^N possibilities, the complexity grows as 2^N , and the method is not practical for large N .

IV. Truncated Maximum-Likelihood Estimate and the Viterbi Algorithm

The contribution of a_k to (s_n, r_n) is halved at every successive step, since its coefficient in α_n is proportional to $2^{(k-n)}$ (Eq. 5). In other words, the value of a_k affects the correlator outputs for all $n \geq k$; however, this effect diminishes exponentially as n increases. Thus, there exists some integer ν , which depends on the signal-to-noise ratio, such that the contribution of a_k to (s_n, r_n) for $n > k + \nu$ is negligible. We therefore can approximate Eq. (5) by

$$\alpha_k = 2a_k + \sum_{j=k-\nu}^{k-1} (a_j - \hat{a}_j) 2^{(i+1-k)} \quad (11)$$

for all $k > \nu + 1$.

Thus each (s_k, r_k) depends on a_k and the previous ν components and we have a finite state machine with 2^ν states, corresponding to all possible binary vectors $(a_{k-1}, \dots, a_{k-\nu})$, and two outputs per state depending on a_k . The progress of this machine, during few successive steps can be depicted by its trellis diagram (Fig. 2).

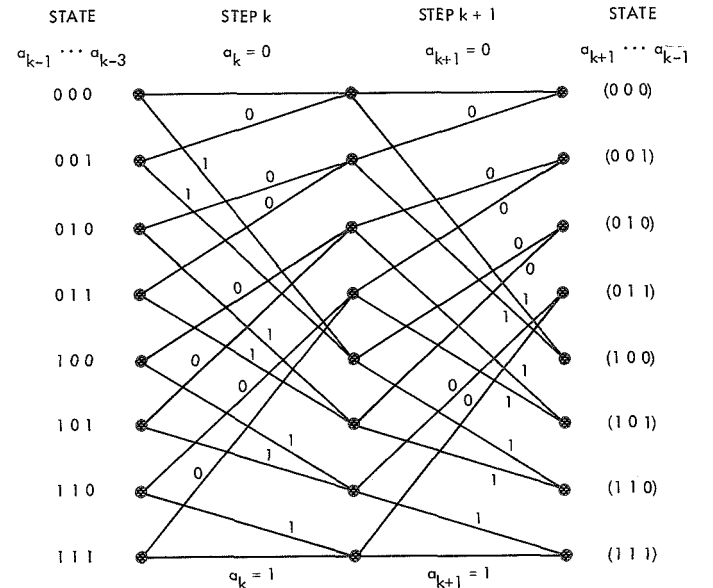


Fig. 2. Trellis diagram for $\nu = 3$ during steps k and $k + 1$

During step k , each state $(a_{k-1}, \dots, a_{k-v})$ can advance to one of two states $(0, a_{k-1}, \dots, a_{k-v+1})$ or $(1, a_{k-1}, \dots, a_{k-v+1})$ depending whether a_k is 0 or 1. The corresponding correlation outputs (s_k, r_k) will depend on the starting state as well as on a_k .

The similarity to convolutional coding with a constraint length of v is immediate. Many decoding procedures have been developed for convolutional codes, however, for short constraint length ($v < 10$) the Viterbi algorithm (Ref. 2) is the most efficient, and is actually a maximum-likelihood estimate of the truncated estimation problem (Ref. 3).

The Viterbi algorithm can be briefly described as follows: With every state we associate a metric (accumulated likelihood function up to this step) and a survivor (the most likely sequence leading to this state). At step k , each state $\hat{S}_k = (a_k, \dots, a_{k-v+1})$ can be reached from two states $S_{k-1}^\delta = (a_{k-1}, \dots, a_{k-v+1}, \delta)$, where δ is 0 or 1. After the received signal is correlated to yield (x_k, y_k) , we compare the two possible ways to reach \hat{S}_k and keep the most likely of them, by properly updating the metric and the survivor of \hat{S}_k . This is done for each one of the 2^v states, and is repeated every step. The final decision is made after the N th (last) step, by comparing the 2^v metrics and selecting the survivor of the largest, to yield the most likely estimate of \mathbf{a} .

Thus a ranging receiver based on the Viterbi algorithm can yield a (truncated) maximum-likelihood performance with a complexity of 2^v , which is independent of the number of components N to be estimated.

V. Error Probabilities

The signal is received in the presence of additive white gaussian noise of zero mean and spectral density N_0 . If the signal power is S and the integration time of each component is $\tau_k = \tau$, $k = 1, 2, \dots, N$ the probability that the sequential receiver will correctly estimate the whole sequence $\{a_1, \dots, a_N\}$, is given by

$$P_c = 1 - \left\{ 1 - \operatorname{erfc} \left[\left(\frac{S\tau}{2N_0} \right)^{1/2} \right] \right\}^N$$

where

$$\operatorname{erfc}(y) = \frac{1}{\sqrt{2\pi}} \int_y^\infty \exp(-x^2/2) dx \quad (12)$$

If $\hat{\epsilon} - \epsilon \neq 0$ the performance is degraded; however, we can assume that the integration time of the highest frequency component is long enough to obtain $\hat{\epsilon} \approx \epsilon$. An analytic expression for the performance of the maximum-likelihood receiver or for the Viterbi algorithm cannot be obtained in closed form. Therefore, the error probabilities for various signal-to-noise ratios were obtained by computer simulations. The noise was generated by a multiplicative congruential generator (Ref. 4), and quantized in steps of $\sigma^2/32$, where σ^2 is the noise-to-signal ratio.

The results for the maximum-likelihood estimate of 10 components ($N = 10$), and a truncation to $v = 5$ are shown in Fig. 3 together with the performance of the sequential receiver. The improvement gained by maximum-likelihood estimation compared to sequential estimation is 1.5 dB for the measured range of error probabilities. This improvement is also achieved by the Viterbi algorithm (with $v = 5$ truncated memory and therefore a

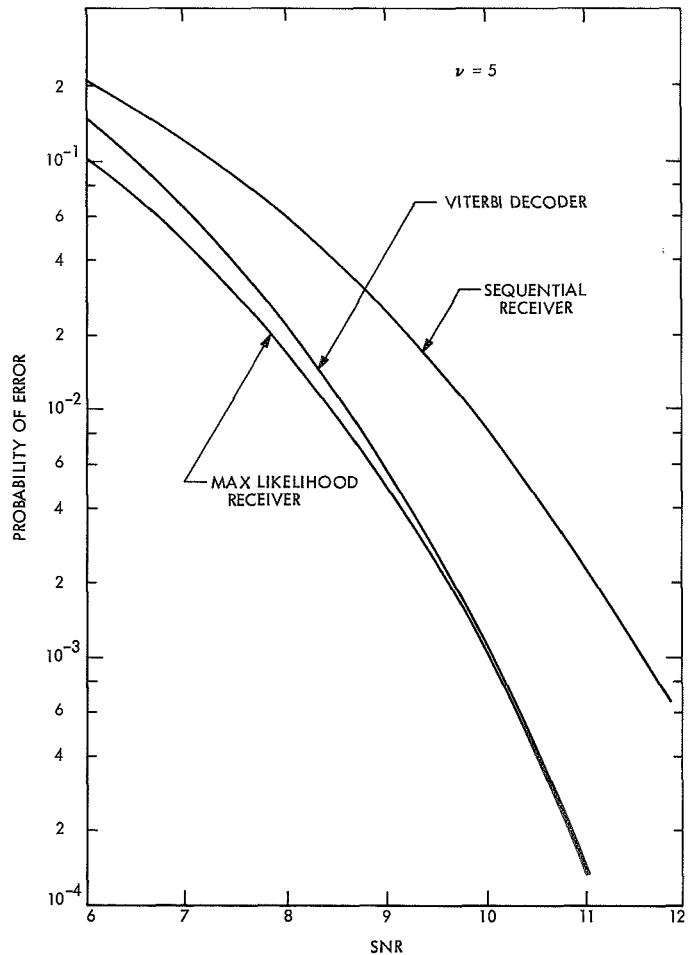


Fig. 3. Performance of various schemes for $N = 10$

smaller complexity), for signal-to-noise ratios which yield $P_E < 10^{-2}$.

V. Conclusions

A truncated maximum likelihood receiver for sequential ranging has been presented. The performance of the sequential ranging system can be improved by using

maximum-likelihood techniques; however, the complexity grows exponentially with the number of components N needed to determine the range unambiguously. The suggested method, which is based on the Viterbi decoder for convolutional codes, performs like the maximum-likelihood receiver while having a finite complexity independent of N . The improvement in signal-to-noise ratio, compared to the present receiver, is 1.5 dB.

References

1. Goldstein, R. M., "Ranging With Sequential Components," in *The Deep Space Network*, Space Programs Summary 37-52, Vol. II, pp. 46-49. Jet Propulsion Laboratory, Pasadena, Calif., July 31, 1968.
2. Viterbi, A. J., "Error Bounds for Convolutional Codes and an Asymptotically Optimum Decoding Algorithm," *IEEE Trans. Infor. Theory*, Vol. IT-13, No. 2, April 1967.
3. Forney, G. D., "Review of Random Tree Codes," Final Report for NASA Ames Research Center under contract NAS2-3637.
4. Chambers, R. P., "Random Number Generation," *IEEE Spectrum*, February 1967.

A Study of Microwave Transmission Through Perforated Flat Plates

T. Y. Otoshi

Communications Elements Research Section

This article presents a simple formula and graph useful for predicting the transmission loss of a circular hole array in a metallic flat plate having either a 60- (staggered) or 90-deg (square) hole pattern. The formula is restricted to the case of an obliquely incident plane wave with the E-field polarized normal to the plane of incidence. The theoretical formula was experimentally verified by testing samples having hole diameters varying from 1.6 to 12.7 mm, porosities varying from 10 to 51%, and plate thicknesses varying from 0.08 to 2.3 mm. The agreement between theory and experiment was typically better than 1 dB at S-band and 2 dB at X-band.

I. Introduction

To those involved with the development of low-noise antennas for deep-space communications and radio astronomy, the subject of leakage through antenna mesh materials is of great interest. This subject is also of interest to those concerned with microwave radiation hazards due to leakage through various types of mesh materials. Meshes have many applications; some examples are reflective surfaces on antennas, Fabry-Perot interferometers, microwave oven doors, RF screen rooms, and RF protective garments.

Meshes are usually of two types: (1) meshes formed by wire grids, and (2) meshes formed by round holes in a flat metallic plate. A significant amount of experimental and theoretical work has been done on the study of microwave transmission properties of wire grid-type

meshes (Refs. 1-5). Using existing experimental data, Mumford (Ref. 4) has derived an empirical formula and nomograph for predicting transmission through wire grid meshes at normal incidence. To this author's knowledge, a similar type summary of experimental results has not been made for transmission through flat plate meshes having round hole perforations. It is the purpose of this article to present a simple theoretical formula applicable to perforated flat plates. This formula is verified by experimental data obtained by both free-space and waveguide measurement techniques.

II. Theoretical Formula and Graph

For the case of a normally incident plane wave, an array of small holes in a metallic sheet behaves as an inductive susceptance in shunt with a TEM (transverse

electromagnetic) transmission line. The normalized susceptance of this array is given as (Ref. 6)

$$\frac{B}{Y_0} = \frac{3ab\lambda_0}{\pi d^3} \quad (1)$$

where

a, b = spacings between holes (see Fig. 1)

d = hole diameter

λ_0 = free-space wavelength

Equation (1) is valid when the hole diameter is small compared to the hole spacings a and b . For the case where a and b approaches d , the corrections described in Ref. 6 can be applied.

Generalizing Eq. (1) to the case of an obliquely incident plane wave with the E-field polarized normal to the

plane of incidence and also accounting for the effect of plate thickness, the approximate expression for transmission loss is

$$T_{dB} = 10 \log_{10} \left[1 + \frac{1}{4} \left(\frac{3ab\lambda_0}{\pi d^3 \cos \theta_i} \right)^2 \right] + \frac{32t}{d} \quad (2)$$

where

θ_i = angle of incidence

t = plate thickness

and $d, a, b \ll \lambda_0$.

The last term of Eq. (2) is the plate thickness correction term given by Marcuvitz (Ref. 7) and was derived by treating the small hole as a circular waveguide beyond cutoff. It should be pointed out that Marcuvitz's transmission loss equation (Ref. 7) for a thick circular aperture in rectangular waveguide and Eq. (2), above, for the array of small holes give results that differ by about 5 dB.

The percent porosity of a mesh is usually known or can be easily calculated for a 60- or 90-deg hole pattern from the expression

$$P_{\%} = \left(\frac{\pi d^2}{4ab} \right) (100) \quad (3)$$

where a and b are the dimensions shown in Fig. 1. Substitution of Eq. (3) into Eq. (2) results in an equation from which a general plot of the type given in Fig. 2 can be made. The curves in Fig. 2 are useful for predicting transmission loss of meshes having either the 60- or 90-deg hole pattern, but are valid only for the case where the E-field is normal to the plane of incidence. Using the mesh on the DSS 14 64-m (210-ft) antenna as an example, at 2295 MHz and 30-deg angle of incidence, the following values are applicable:

$$P_{\%} = 51.0$$

$$\frac{d}{\lambda_0} = 0.0365$$

$$\cos \theta_i = 0.866$$

$$\frac{t}{d} = 0.480$$

Then the intersection of $x = 51 (0.0365) (0.866) = 1.61$ and $t/d = 0.48$ on the graph gives a transmission loss of 43 dB. An estimate of the contribution to zenith antenna

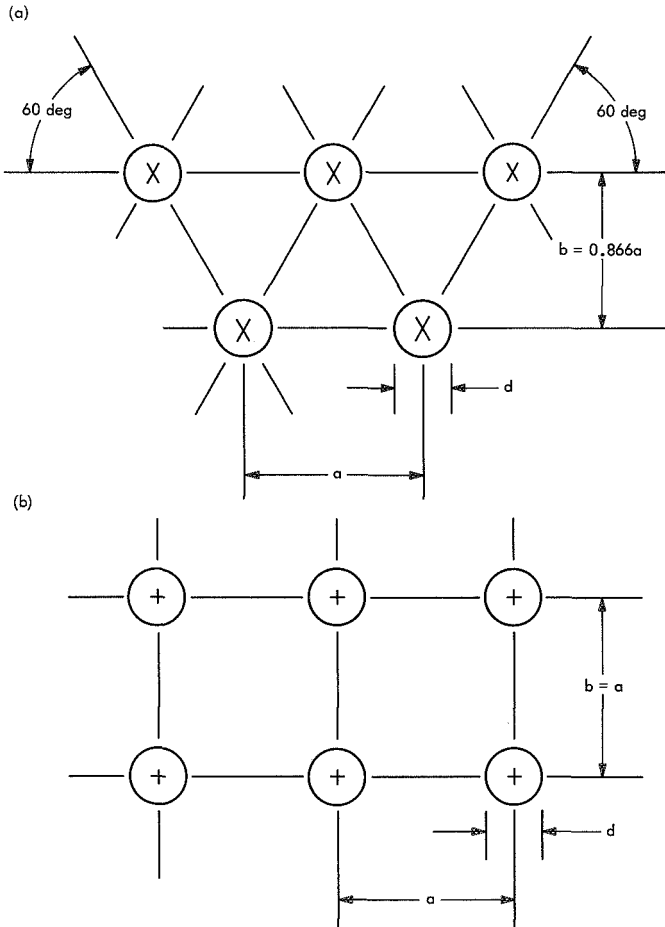


Fig. 1. Hole pattern configurations: (a) 60 deg (staggered) and (b) 90 deg (square)

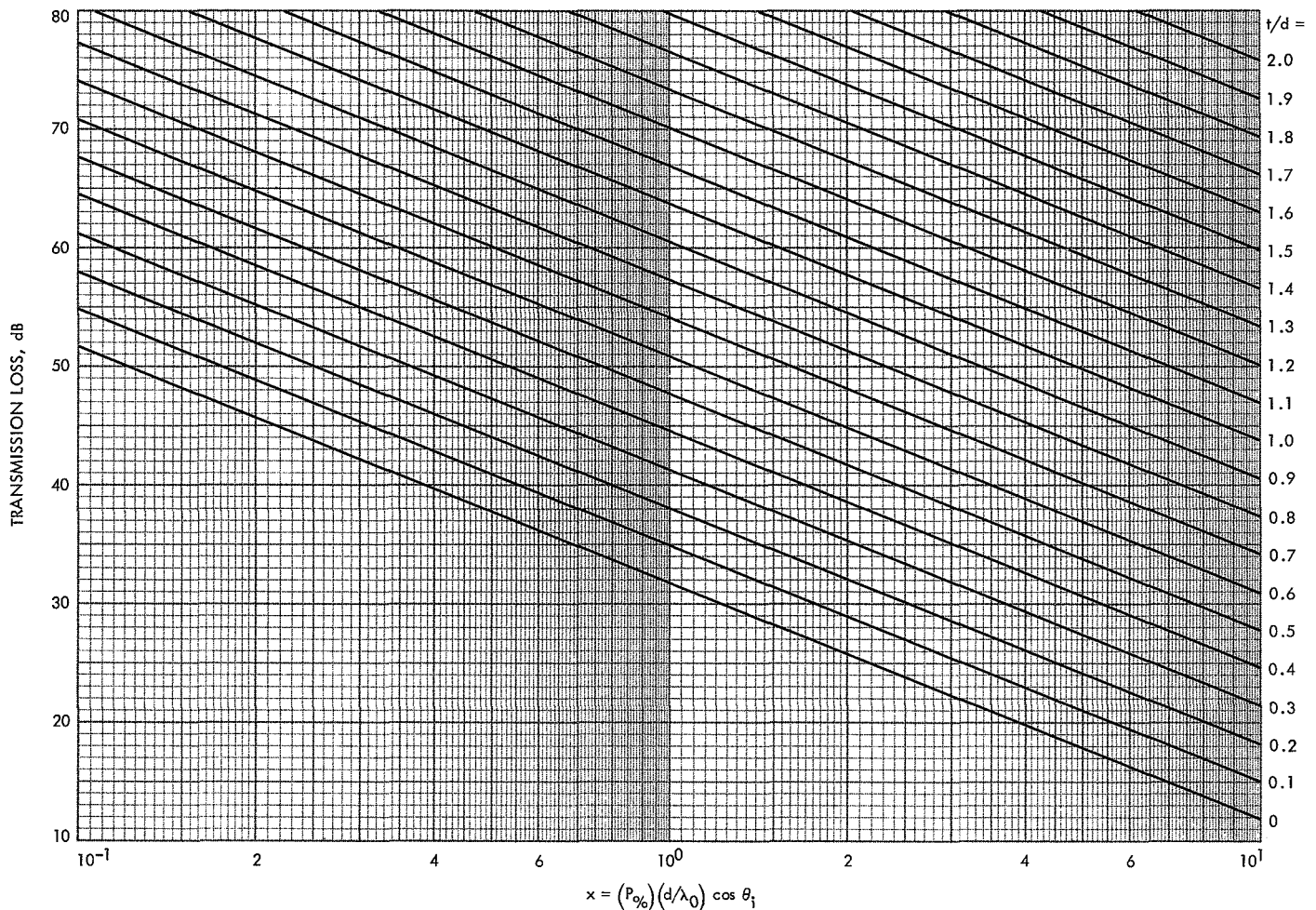


Fig. 2. Transmission loss curves for perforated flat plates having 60- or 90-deg hole pattern (E-field normal to plane of incidence)

noise temperature due to leakage through this mesh would be 0.06 K.

III. Experimental Verification

Table 1 is a summary of experimental results obtained by waveguide and free-space measurement techniques. The mesh test samples were made from flat aluminum plates having 60- and 90-deg hole patterns, hole diameters varying from 1.6 to 12.7 mm, porosities varying from 10 to 51%, and plate thicknesses varying from 0.08 to 2.3 mm.

Waveguide measurements were performed by JPL¹ using a network analyzer and techniques described in

¹Measurements were performed by R. B. Lyon of the JPL Communications Elements Research Section.

Ref. 8. Test samples previously described in Ref. 9 were remeasured. Some of these samples are shown in Fig. 3. The accuracy of the waveguide measurements is estimated to be ± 0.5 dB.

For additional verification, free-space measurement data from a Dalmo Victor Co. report (Ref. 10) are included. The estimated accuracy of the free-space measurements was stated to be about ± 0.5 dB.

Theoretical values for Table 1 were calculated through the use of Eq. (2). It can be seen that the agreement between theoretical and experimental results is typically better than 1 dB at S-band and 2 dB at X-band. Some of the deviations at X-band are attributed to increasing inaccuracy of the waveguide method when the number of basic cells in the waveguide sample becomes small and the sample is not imaged to the waveguide walls.

**Table 1. Comparison of experimental and theoretical transmission data
for flat perforated plates with round holes**

Test frequency, MHz	θ_i , deg	Hole pattern, deg	$\frac{d}{\lambda_0}$	Approximate porosity, %	$\frac{t}{d}$	Theoretical transmission, ^a dB	Measured minus theoretical transmission, dB	Comments
2300	0	60	0.04	10.0	0.345	50.3	-2.3	Daimo Victor data (Ref. 10)
			0.04	22.6	0.345	43.3	-2.5	
			0.07	10.0	0.197	40.8	0	
			0.07	22.6	0.197	33.8	-0.5	
			0.10	10.0	0.138	35.8	-0.9	
			0.10	22.6	0.138	28.8	-1.0	
2388	35.1	60	0.025	30	0.400	48.3	-0.4	DSS 14 64-m antenna
			0.025	33	0.632	54.9	0.1	
			0.025	40	0.496	48.9	-0.8	
			0.025	50	0.632	51.5	-0.8	
			0.038	51	0.085	30.2	-0.9	
			0.038	51	0.480	42.9	-0.7	
			0.051	25	0.316	41.3	-0.4	
			0.051	50	0.316	35.4	-0.5	
			0.076	25	0.211	34.4	-0.5	
			0.076	50	0.211	28.4	-0.1	
			0.076	51	0.227	28.8	0	
			0.101	25	0.158	30.6	-1.3	
			0.101	50	0.158	24.3	-1.0	
2388	35.1	90	0.025	25	0.632	57.5	0.7	
			0.025	50	0.632	51.4	-1.2	
			0.051	25	0.316	41.3	1.0	
			0.051	50	0.316	35.3	0.1	
			0.076	25	0.211	34.5	-0.5	
			0.076	47.3	0.211	28.9	0.4	
			0.101	25	0.158	30.3	-1.3	
			0.101	50	0.158	24.3	-1.1	
8448	38.5	60	0.045	50	0.048	28.1	2.8	DSS 14 64-m antenna
			0.045	50	0.256	34.8	2.8	
			0.089	30	0.400	37.7	-1.7	
			0.089	40	0.496	38.3	-1.0	
			0.134	51	0.085	19.7	-2.0	
			0.134	51	0.480	32.3	-1.3	
^a Based on precise values of hole diameter and spacings.								

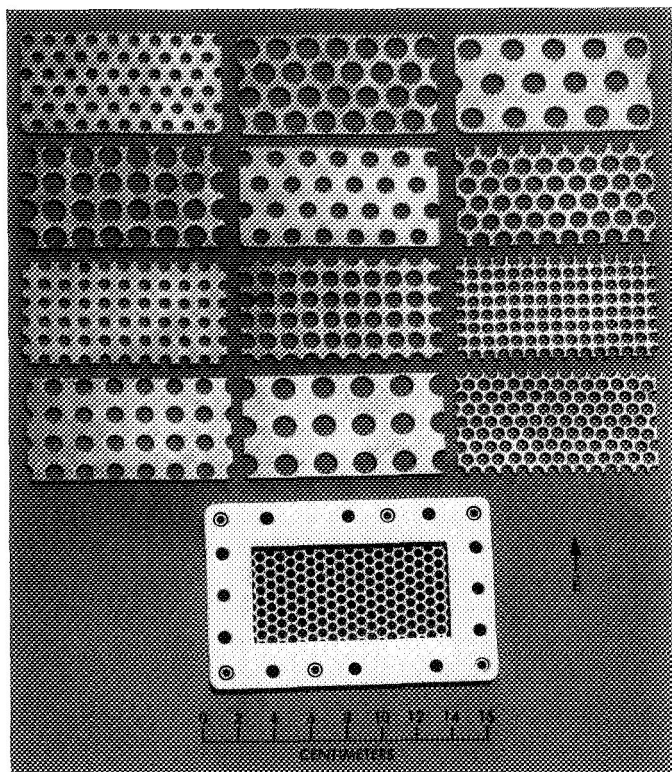


Fig. 3. WR 430 test samples and test sample holder

The waveguide test samples for the data in Table 1 were cut so that the hole pattern would be oriented with respect to the E-field as indicated in Fig. 3. Tests on

some samples at other orientation angles showed that for practical purposes, the transmission loss is independent of the orientation angle (see Ref. 8, p. 56).

It should be re-emphasized that the data presented in this article are applicable to the free-space configuration where the E-field is polarized perpendicular to the plane of incidence. At present, there does not appear to be published experimental or theoretical data on the transmission loss of perforated plates for the parallel polarization case. Based strictly on an equivalent plane sheet theory, however, one would not expect the transmission losses of the perforated plates for the two polarization cases to differ by more than 3 dB when the angles of incidences are less than 30 deg.

IV. Conclusions

Good agreement has been obtained between experimental and theoretical values for transmission losses of perforated flat plates having various hole diameters, porosities, and plate thicknesses. The theoretical formula is restricted to the case of an obliquely incident plane wave where the E-field is polarized normal to the plane of incidence. Even with this stated restriction, the formula and curves presented in this article are useful for predicting leakage through antenna surfaces and RF shields.

References

1. Broek, G. J., and Vooren, J., "On the Reflection Properties of a Periodically Supported Metallic Wire Grating with Rectangular Mesh Showing Small Sag Due To Its Own Weight," *IEEE Trans. Antennas and Propagation*, Jan. 1971 (in press).
2. Kaplun, V. A., et al., "Shielding Properties of Wire Screens at SHF," *Radio Engineering and Electron Physics*, Vol. 9, pp. 1428-1430, 1964.
3. Kontorovich, M. I., et al., "The Coefficient of Reflection of a Plane Electromagnetic Wave from a Plane Wire Mesh," *Radio Engineering and Electron Physics*, pp. 222-231, Feb. 1962.

References (contd)

4. Mumford, W., "Some Technical Aspects of Microwave Radiation Hazards," *Proc. IRE*, p. 445, Feb. 1961.
5. Decker, M. T., "Transmission and Reflection by a Parallel Wire Grid," *J. Res. NBS, Sec. D*, Vol. 63D, No. 1, pp. 87-90, Jul.-Aug. 1959.
6. Culshaw, W., "Reflectors for a Microwave Fabry-Perot Interferometer," *IEEE Trans. Microwave Theory and Techniques*, Vol. MTT-7, p. 226, Apr. 1959.
7. Marcuvitz, N., *Waveguide Handbook*, M. I. T. Radiation Laboratory, Vol. 10, p. 409. McGraw-Hill Book Co., Inc., New York, 1951.
8. Otoshi, T. Y., and Lyon, R. B., "Improved RF Calibration Techniques: A Study of the RF Properties of the 210-ft-diam Antenna Mesh Material," in *The Deep Space Network*, Space Programs Summary 37-66, Vol. II, pp. 52-57. Jet Propulsion Laboratory, Pasadena, Calif., Nov. 30, 1970.
9. Otoshi, T., "RF Porosity Studies," in *Supporting Research and Advanced Development*, Space Programs Summary 37-20, Vol. IV, pp. 135-137. Jet Propulsion Laboratory, Pasadena, Calif., Apr. 30, 1963.
10. Pon, C. Y., *Final Report on Transmission through Perforated Reflectors and Loss Due To Paint for AAS/DSIF Program*. Dalmo Victor Co., Belmont, Calif., Dec. 28, 1961.

Design of Hydrogen Maser Cavity Tuning Servo

C. Finnie

Communications Elements Research Section

Servo design details are described for a prototype hydrogen maser cavity tuner for use with the hydrogen maser frequency standards developed at the Jet Propulsion Laboratory.

This article is a continuation of a tuner design discussion initiated in Ref. 1.

A period counter forms the basis of the tuning system. It has a sampled transfer characteristic given by

$$\tau_{\text{out}} = \frac{1}{s} \left(\tau_0 + \sum_{n=0}^{\infty} \tau_n e^{-s\tau n} \right) \quad (1)$$

where

τ_{out} = output count

τ_n = input variable at sampling time $N\tau$

τ_0 = initial value

The counter will perform a summation of difference measurements if the count direction is reversed after each measurement, and the count is sampled after alternate measurements:

$$\tau_{\text{out}} = \frac{1}{s} \left\{ \tau_0 + \sum_{n=0}^{\infty} (\tau_{2n} - \tau_{2n+1}) \right\} e^{-2s\tau n} \quad (2)$$

Where it is desired to remove a linear temporal change or drift in the input parameter, the count direction may be double switched to give

$$\tau_{\text{out}} = \frac{1}{s} \left\{ \tau_0 + \sum_{n=0}^{\infty} (\tau_{4n+1} - \tau_{4n+2} - \tau_{4n+3} + \tau_{4n+4}) \right\} e^{-2s\tau n} \quad (3)$$

Alternate adjacent samples are subtracted and the differences are accumulated in a buffer which samples the counter at a 2τ sampling rate. A diagram of the complete servo is shown in Fig. 1. The maser section of Fig. 1 represents the cavity pulling relationship described previously (Ref. 1). The output frequency f_o of the maser is modulated by switching between two cavity pulling factors K_1 and K_2 . The switch sequence is that of Eq. (3). Therefore, changes in the maser output frequency will be coherently summed in the up-down counter of the tuner, while static and linear changes in the maser frequency will produce zero and zero-time-average counts in the tuner, respectively.

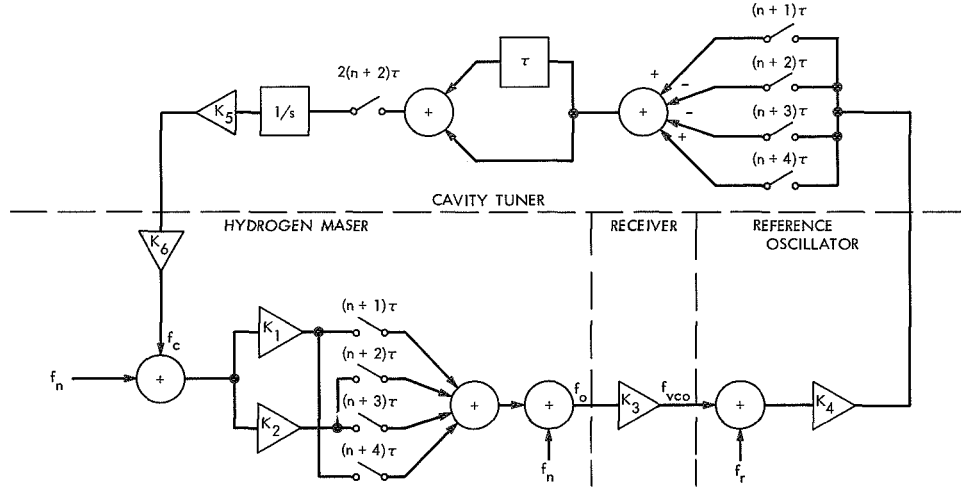


Fig. 1. Cavity tuner servo diagram

The receiver divides the maser frequency, f_o , by the ratio (K_3) between the maser (1420.405 MHz) and the voltage-controlled oscillator (VCO) (100 MHz) of the receiver. The 100-MHz VCO is then mixed with the reference oscillator f_r to produce a nominal 100-s beat period τ_b . This period is measured in the tuner by counting a 1-kHz internal clock for the interval between zero crossings of τ_b . The proportionality constant K_4 between the frequency and period variable is given by

$$K_4 = \frac{\delta \tau_b}{\delta f_b} = \tau_0^2$$

where τ_b average is much greater than modulation or noise produced on τ_b .

In the count sequence, the counter counts up for the first period, allows the dissociator pressure to reach equilibrium for one period, then counts down the next. After completion of the down count, the residual in the counter is transferred to a digital buffer and an analog-to-digital converter. The voltage from the analog-to-digital converter in turn is applied to a varactor which tunes the microwave cavity. The sequence is then inverted with the down count coming first. K_5 is derived from the counter clock rate, the analog amplifier of the digital-to-analog converter, and the position of the counter digits selected for analog conversion. The last gain constant K_6 is the sensitivity of the tuning varactor to its control voltage from the digital-to-analog converter.

The open-loop transfer function for the system becomes

$$\frac{f_c}{f_n} = \frac{(K_1 - K_2) K_3 K_4 K_5 K_6}{s} e^{-2s\tau} = \frac{\alpha e^{-2s\tau}}{s}$$

where α is the loop gain. The closed-loop transfer function (sampled) becomes

$$\frac{f_c}{f_n} = \frac{\alpha e^{-2s\tau}}{1 - (1 - \alpha) e^{-2s\tau}}$$

and the response to the input step (sampled) is

$$f_c = f_{co} \left\{ \sum_{n=0}^{\infty} [1 - (1 - \alpha)^n] e^{-2s\tau(n+1)} \right\}$$

The convergence of the loop is, therefore, a linear decreasing staircase function. Figure 2 is a graph of the loop error as a function of time and loop gain.

A simplified design criteria is given by

$$\sigma_1 \approx \alpha \sigma_2 \geq \epsilon$$

where

σ_1 = allowable variation of maser long-term stability

σ_2 = measurement variation of τ_b

ϵ = change in maser output frequency for the least significant bit of the digital-to-analog converter

The loop gain is approximately equal to the input measurement of τ_b transferred to the output frequency. Hence, if the reference oscillator is one hundred times

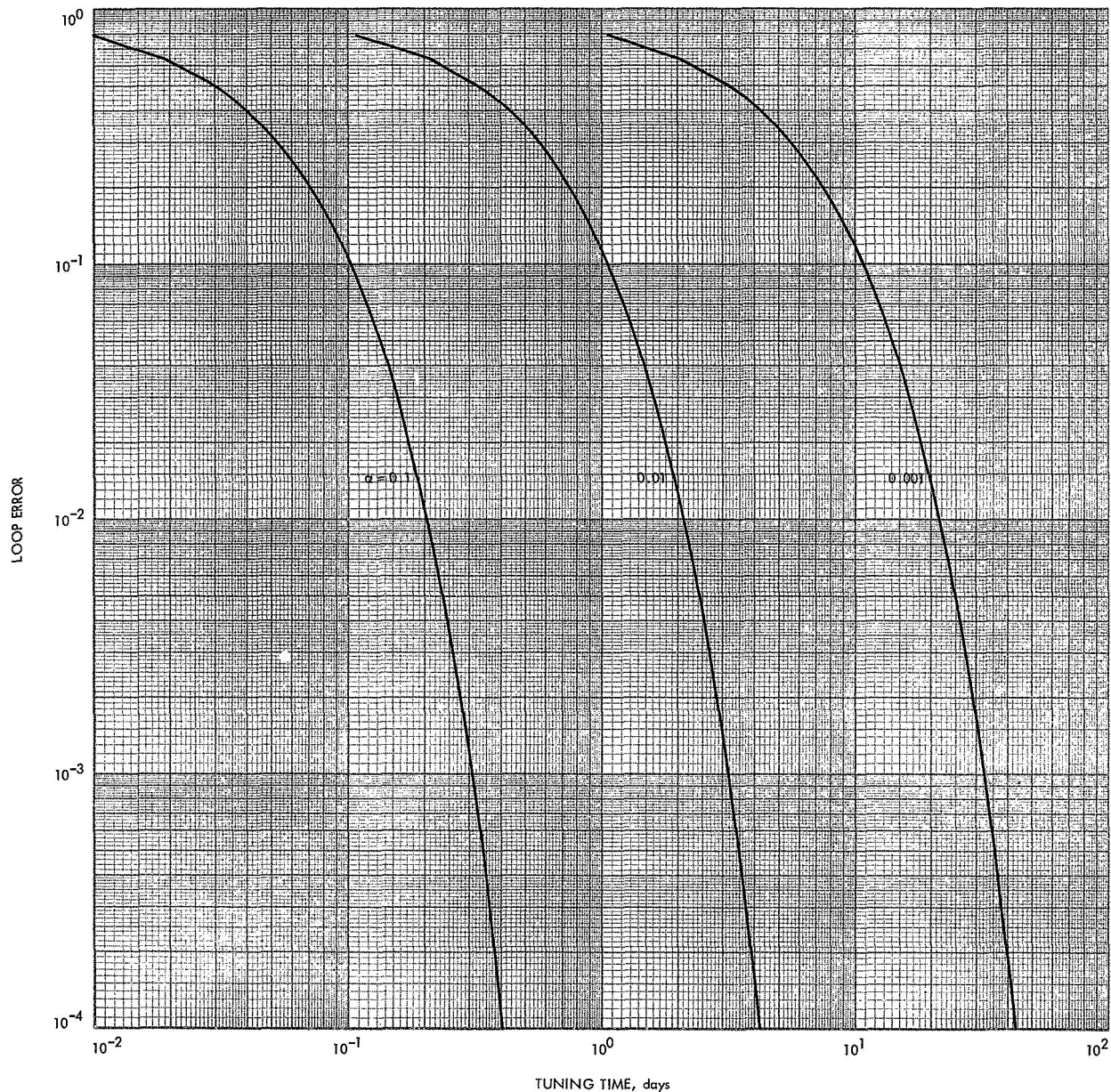


Fig. 2. Tuning error vs tuning time and loop gain

more noisy (σ_f/f) than the hydrogen maser, a degradation in tuning accuracy must be accepted or tuning times on the order of 40 days are required to realize the inherent

accuracy of the maser. The above assumes the noise introduced into the maser output by the tuner to be 10% of the maser 100-s stability.

Reference

1. Finnie, C., "Frequency Generation and Control: Atomic Hydrogen Maser Frequency Standard," in *The Deep Space Network Progress Report*, Technical Report 32-1526, Vol. I, pp. 73-75. Jet Propulsion Laboratory, Pasadena, Calif., Feb. 15, 1971.

Improved RF Calibration Techniques: System Operating Noise Temperature Calibrations

M. S. Reid

Communications Elements Research Section

The system operating noise temperatures of the S-band polarization ultra cone at DSS 11 (Pioneer Deep Space Station), the S-band research operational cone at DSS 13 (Venus DSS), and the polarization diversity S-band and multi-frequency X-band/K-band cones at DSS 14 (Mars DSS) are reported for the period October 1, 1970 through January 31, 1971.

The system operating noise temperature performance of the low noise research cones in the Goldstone Deep Space Communications Complex (GDSCC) is reported. The operating noise temperature calibrations were performed with the ambient termination technique (Ref. 1). The cones on which this technique was used during this reporting period are:

- (1) S-band research operational (SRO) cone at DSS 13.
- (2) S-band polarization ultra (SPU) cone at DSS 11.
- (3) Polarization diversity S-band (PDS) cone at DSS 14.
- (4) Multi-frequency X-band/K-band (MXK) cone at DSS 14.

The averaged operating noise temperature calibrations for the various cones, and other calibration data, are presented in Table 1. The reporting period for the SRO and SPU cones is October 1, 1970 (day 274) through January 31, 1971 (day 31). The reporting period for the PDS cone is from its initial operation on the 64-m antenna, September 15, 1970 through January 31, 1971. The reporting period for the MXK cone is from its initial installation on the 64-m antenna, March 15, 1970 through February 28, 1971.

The calibration data were reduced with JPL computer program number 5841000, CTS20B. Measurement errors of each data point average are recorded under the appropriate number in Table 1. The indicated errors are the standard deviation of the individual measurements and

**Table 1. Averaged operating noise temperature calibrations for the
low noise research cones at GDSCC**

Station	DSS 11	DSS 13		DSS 14		
Cone	SPU	SRO		PDS	MXK	
Configuration	Receive mode			Diplexed		
Frequency, MHz	2295	2295	2388	2295	7840	8448
Maser serial number	9655	9652	9652	9653	150X1	150X1
Maser temperature, K	3.7	5.2	5.2	4	10	7
Maser gain, dB	$55.8 \pm 0.23/0.10$ 6 measurements	$51.0 \pm 0.53/0.17$ 10 measurements	$37.1 \pm 1.18/0.10$ 137 measurements	$53.4 \pm 0.50/0.10$ 5 measurements	$37.0 \pm 1.7/0.55$ 10 measurements	41.3
Follow-up noise temperature con- tribution, K	$0.06 \pm 0.003/0.002$ 6 measurements	$0.11 \pm 0.06/0.02$ 9 measurements	$0.55 \pm 0.09/0.05$ 137 measurements	$0.01 \pm 0.07/0.05$ 4 measurements	$1.7 \pm 0.60/0.20$ 10 measurements	0.58 1 measurement
System operating noise temper- ature, K	$18.3 \pm 0.10/0.06$ 4 measurements	$16.5 \pm 0.37/0.12$ 9 measurements	$16.4 \pm 0.76/0.08$ 137 measurements	$24.1 \pm 0.55/0.05$ 4 measurements	$27.7 \pm 1.3/0.51$ 13 measurements	23.6 ± 0.25 1 measurement

of the means, respectively. They do not include instrumentation systematic errors. The averages were computed using only data with

- (1) Antenna at zenith.
- (2) Clear weather.
- (3) No RF spur in the receiver passband.
- (4) Probable error of computed operating noise temperature due to measurement dispersion less than 0.1 K.

The system operating noise temperatures of the SPU cone at DSS 11 are plotted in Fig. 1 as a function of time in day numbers. Similarly, Figs. 2 and 3 are system operating noise temperatures of the SRO cone at 2295 MHz and 2388 MHz, respectively. Figure 4 shows the PDS cone data and Fig. 5 the MXK cone data.

In all the figures, data that satisfy the four conditions stated above are plotted as asterisks, while data that fail one or more conditions are plotted as circles. The one exception is the single data point at 8448 MHz in Fig. 5 which is plotted as a square; the remainder of the data in the figure is for 7840 MHz. It is expected that

the system operating noise temperatures of the MXK cone at 8427 and 8448 MHz will average approximately 3 K lower than the average temperature at 7840 MHz.

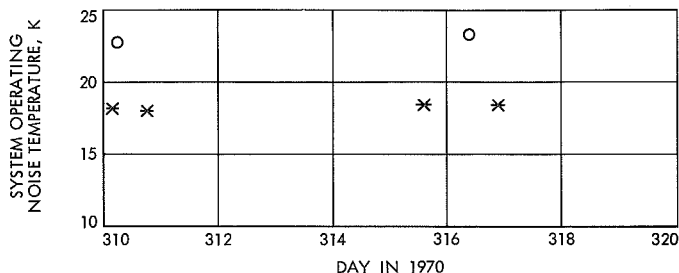


**Fig. 1. System operating noise temperature of
SPU cone at DSS 11**

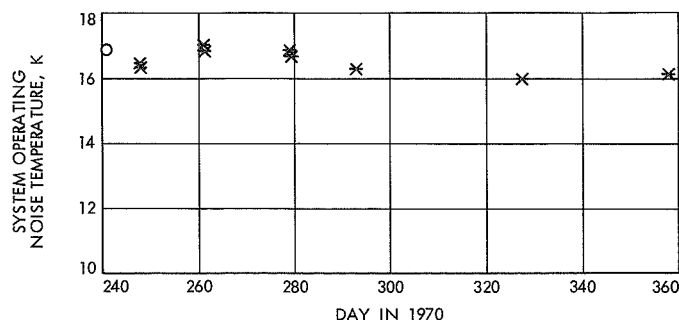


**Fig. 2. System operating noise temperature of
SRO cone at 2295 MHz at DSS 13**

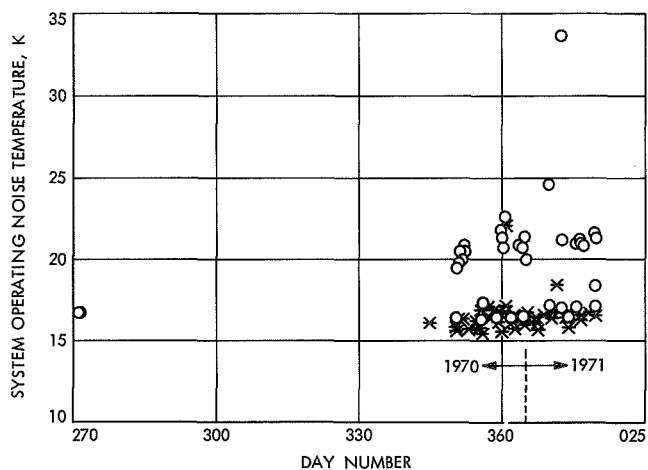


Fig. 3. System operating noise temperature of SRO cone at 2388 MHz at DSS 13

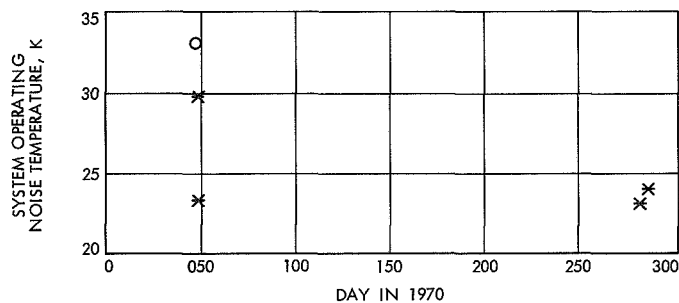


Fig. 4. System operating noise temperature of PDS cone at DSS 14

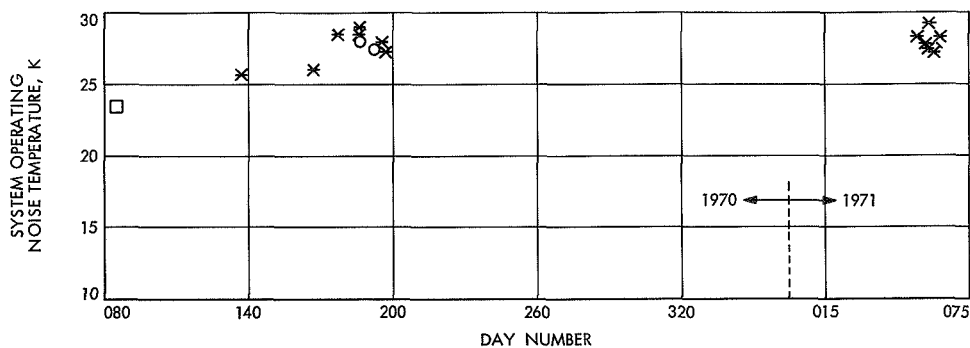


Fig. 5. System operating noise temperature of MXK cone at DSS 14

Reference

1. Stelzried, C. T., "Improved RF Calibration Techniques: Daily System Noise Temperature Measurements," in *The Deep Space Network*, Space Programs Summary 37-42, Vol. III, pp. 25-32. Jet Propulsion Laboratory, Pasadena, Calif., Nov. 30, 1966.

Photon Energies of a Cathode-Ray Tube System

J. J. Volkoff

SFOF/GCF Development Section

Light emitted from a cathode-ray tube (CRT) is comprised of reflected environmental light incident upon the CRT system and light generated at the phosphor screen and transmitted through the CRT system. The total photon energy which leaves the system and those energies which are dissipated in the various elements of the CRT system are derived. An expression for the contrast ratio of the CRT system is also presented and discussed.

I. Introduction

Photons generated by the impingement of electrons upon the phosphorescent material of the phosphor screen pass through the cathode-ray tube (CRT) system as output light. A fraction of the photons from the environment (ambient light) incident upon the CRT system is reflected from the CRT system and contributes light to the generated output light. The combination of these two outputs makes up the total light emitted from the CRT system. A common CRT system is comprised of a phosphor screen, a glass faceplate, and a filter screen which is utilized to enhance the contrast ratio of the CRT system.

When light, either generated at the phosphor screen or entering from the ambient, encounters an element of the CRT system, its energy is partially transformed into heat due to the energy-absorbing nature of the CRT element. The remaining energy is partially transmitted if the element is not opaque, and the residual portion is reflected.

Conservation of the total energy for this process can be expressed by

$$\alpha(\lambda) + \tau(\lambda) + \rho(\lambda) = 1 \quad (1)$$

where $\alpha(\lambda)$, $\tau(\lambda)$, and $\rho(\lambda)$ are, respectively, the absorptivity, transmissivity, and reflectivity coefficients at wavelength λ of the element (Ref. 1).

Since light undergoes an infinite number of reflections in a CRT system, it follows that there occurs an infinite number of sequential events differentiated by absorption, transmission, and reflection mechanics. These series describe the total energy transformations within the CRT system.

The analysis in this article is divided into two sections, the energies resulting from the environmental light inci-

dent upon the system, and the energies resulting from the light generated by the system. In these analyses, all the energies transmitted and reflected from the system, and all the energies dissipated by absorption processes by the phosphor screen, the glass faceplate, and the filter screen elements are considered.

II. Energies From Environmental Light

Consider a coherent beam of light at wavelength λ incident upon the CRT system. The energy $E(\lambda)$ of this light is

$$E(\lambda) = n(\lambda) h \nu \quad (2)$$

where $n(\lambda)$ represents the number of photons at λ , h is Planck's constant, and ν is the frequency of light. The frequency may be expressed as the velocity of light in the medium divided by the wavelength. Using c and λ as representing the velocity and wavelength of light, respectively, under vacuum conditions, the frequency of light may then be written as

$$\nu = \frac{c}{\lambda} \quad (3)$$

Since the velocity of light in standard air is so nearly equal to the velocity of light in vacuum, for practical purposes, the wavelength of light in the two mediums shall be considered equal and shall not be differentiated in this study.

The fraction of the total light energy transmitted through the filter screen and incident upon the faceplate is $\tau_f(\lambda) E(\lambda)$, where $\tau_f(\lambda)$ is the transmissivity coefficient at λ of the screen and the direction of incidence is taken to be normal. The remaining energy $\alpha_f(\lambda) E(\lambda)$ is absorbed by the screen. Since the reflectivity coefficient of a filter screen is negligibly low, the energy absorbed by the screen can be rewritten as $[1 - \tau_f(\lambda)] E(\lambda)$.

Continuing with the light incident upon the glass faceplate, the portion $\rho_g(\lambda) \tau_f(\lambda) E(\lambda)$ is reflected from the outer surface of which $\rho_g(\lambda) \tau_f^2(\lambda) E(\lambda)$ is transmitted back through the screen as the first term of the total light output from the system contributed by the environment

light. While $[1 - \rho_g(\lambda)] \tau_f(\lambda) E(\lambda)$ enters into the faceplate, $[1 - \tau_g(\lambda)] [1 - \rho_g(\lambda)] \tau_f(\lambda) E(\lambda)$ is absorbed by the faceplate and $\tau_g(\lambda) [1 - \rho_g(\lambda)] \tau_f(\lambda) E(\lambda) = E_1$ is incident upon the surface of the inner faceplate (phosphor screen side).

Of E_1 , the portion $\rho_g(\lambda) E_1$ is reflected and $[1 - \rho_g(\lambda)] E_1$ is the energy finally incident upon the phosphorescent material.

The phosphorescent material absorbs and reflects incident energy since its transmissivity coefficient is essentially zero. Thus, for every beam incident upon its surface, a fraction $[1 - \rho_s(\lambda)]$ is absorbed, and $\rho_s(\lambda)$ is reflected. Subsequently, a portion of the reflected beam is re-reflected from the inner surface of the faceplate back for another reflection from the phosphorescent material. Thus, an infinite series of subsequent reflection and absorption energy sequential events occurs. It can be shown that the series of energy reflections and absorptions can be expressed in the form such that the sum total energy of E_1 which is reflected from the faceplate and phosphor screen into the faceplate at the inner side is $F_g(\lambda) E_1$, where

$$F_g(\lambda) = \rho_g(\lambda) + \frac{\rho_s(\lambda) [1 - \rho_g(\lambda)]^2}{1 - \rho_g(\lambda) \rho_s(\lambda)} \quad (4)$$

The total amount of energy E_1 which is absorbed by the phosphorescent material is $F_s(\lambda) E_1$, where

$$F_s(\lambda) = \frac{[1 - \rho_g(\lambda)] [1 - \rho_s(\lambda)]}{1 - \rho_g(\lambda) \rho_s(\lambda)} \quad (5)$$

and $F_g(\lambda) + F_s(\lambda) = 1$.

As the reflected beam $F_g(\lambda) E_1$ passes through the faceplate, $[1 - \tau_g(\lambda)] F_g(\lambda) E_1$ is absorbed by the faceplate, and $[1 - \rho_g(\lambda)] \tau_g(\lambda) F_g(\lambda) E_1$ emerges from the outer surface of the faceplate toward the filter screen. However, $\rho_g(\lambda) \tau_g(\lambda) F_g(\lambda) E_1$ is the portion of energy reflected from the outer surface of the faceplate toward the phosphor screen for another series of reflections and dissipations. By continuing similar arguments for the reflected beam, series expressions for these energies which are dissipated and transmitted in the various elements of the CRT system can be developed. These series are given below for a monochromatic beam of light.

A. Light Energy Output

The total energy $L_0(\lambda)$ emerging from the CRT system is the series of energies formulated from the analysis above, as follows:

$$\begin{aligned} L_0(\lambda) = & \tau_f^2(\lambda) \rho_g(\lambda) E(\lambda) + \tau_f^2(\lambda) [1 - \rho_g(\lambda)]^2 \tau_g^2(\lambda) F_g(\lambda) E(\lambda) \\ & + \rho_g(\lambda) \tau_f^2(\lambda) [1 - \rho_g(\lambda)]^2 \tau_g^4(\lambda) F_g^2(\lambda) E(\lambda) \\ & + \rho_g^2(\lambda) \tau_f^2(\lambda) [1 - \rho_g(\lambda)]^2 \tau_g^6(\lambda) F_g^3(\lambda) E(\lambda) + \dots \end{aligned} \quad (6)$$

which can be written as

$$L_0(\lambda) = \tau_f^2(\lambda) E(\lambda) \left\{ \rho_g(\lambda) + \frac{[1 - \rho_g(\lambda)]^2 \tau_g^2(\lambda) F_g(\lambda)}{1 - \rho_g(\lambda) F_g(\lambda) \tau_g^2(\lambda)} \right\} \quad (7)$$

B. Energy Dissipated Into the Filter Screen

The total energy $L_f(\lambda)$ dissipated into the filter screen in the form of thermal energy is

$$\begin{aligned} L_f(\lambda) = & [1 - \tau_f(\lambda)] E(\lambda) + \rho_g(\lambda) \tau_f(\lambda) [1 - \tau_f(\lambda)] E(\lambda) \\ & + [1 - \rho_g(\lambda)]^2 \tau_g^2(\lambda) F_g(\lambda) [1 - \tau_f(\lambda)] \tau_f(\lambda) E(\lambda) \\ & + [1 - \rho_g(\lambda)]^2 \tau_g^4(\lambda) F_g^2(\lambda) \rho_g(\lambda) [1 - \tau_f(\lambda)] \tau_f(\lambda) E(\lambda) + \dots \end{aligned} \quad (8)$$

resolving to

$$L_f(\lambda) = [1 - \tau_f(\lambda)] E(\lambda) \left\{ 1 + \rho_g(\lambda) \tau_f(\lambda) + \frac{[1 - \rho_g(\lambda)]^2 \tau_g^2(\lambda) F_g(\lambda) \tau_f(\lambda)}{1 - \rho_g(\lambda) F_g(\lambda) \tau_g^2(\lambda)} \right\} \quad (9)$$

C. Energy Absorbed by the Glass Faceplate

The total energy $L_g(\lambda)$ absorbed by the glass faceplate is written as

$$\begin{aligned} L_g(\lambda) = & [1 - \tau_g(\lambda)] [1 - \rho_g(\lambda)] \tau_f(\lambda) E(\lambda) \\ & + [1 - \tau_g(\lambda)] [1 - \rho_g(\lambda)] \tau_f(\lambda) \tau_g^2(\lambda) \rho_g(\lambda) F_g(\lambda) E(\lambda) \\ & + [1 - \tau_g(\lambda)] [1 - \rho_g(\lambda)] \tau_f(\lambda) \tau_g^4(\lambda) \rho_g^2(\lambda) F_g^2(\lambda) E(\lambda) + \dots \\ & + [1 - \tau_g(\lambda)] [1 - \rho_g(\lambda)] \tau_f(\lambda) \tau_g(\lambda) F_g(\lambda) E(\lambda) \\ & + [1 - \tau_g(\lambda)] [1 - \rho_g(\lambda)] \tau_f(\lambda) \tau_g^3(\lambda) \rho_g(\lambda) F_g^2(\lambda) E(\lambda) + \dots \end{aligned} \quad (10)$$

which becomes

$$L_g(\lambda) = \frac{[1 - \tau_g(\lambda)] [1 - \rho_g(\lambda)] [1 + F_g(\lambda) \tau_g(\lambda)] \tau_f(\lambda) E(\lambda)}{1 - \rho_g(\lambda) F_g(\lambda) \tau_g^2(\lambda)} \quad (11)$$

D. Energy Absorbed by the Phosphor Screen

The total energy $L_s(\lambda)$ absorbed by the phosphor screen is similarly a series of energies which, when combined, results in the following equation:

$$L_s(\lambda) = \frac{F_s(\lambda) \tau_g(\lambda) \tau_f(\lambda) [1 - \rho_g(\lambda)] E(\lambda)}{1 - \rho_g(\lambda) F_g(\lambda) \tau_g^2(\lambda)} \quad (12)$$

Energy is conserved since

$$E(\lambda) = L_0(\lambda) + L_f(\lambda) + L_g(\lambda) + L_s(\lambda) \quad (13)$$

III. Energies From Generated Light

Let a coherent beam of light having wavelength λ be generated at the surface of the CRT phosphor screen by the impingement of electrons upon the phosphorescent material. The energy $E_g(\lambda)$ of this beam of light may be expressed by

$$E_g(\lambda) = n_g(\lambda) h \nu \quad (14)$$

where $n_g(\lambda)$ is the number of photons generated.

Of the beam of light which impinges upon the inner surface of the glass faceplate, the portion $\rho_g(\lambda) E_g(\lambda)$ is reflected and the remaining portion $[1 - \rho_g(\lambda)] E_g(\lambda)$ passes into the faceplate. Direction to the faceplate surface is assumed to be normal. The reflected portion incident upon the phosphor screen is partially absorbed by an amount equal to $[1 - \rho_s(\lambda)] \rho_g(\lambda) E_g(\lambda)$ and the other portion $\rho_s(\lambda) \rho_g(\lambda) E_g(\lambda)$ is reflected back upon the inner faceplate surface.

This reflected beam undergoes a similar reflection and absorption sequence between the faceplate and phosphor screen, resulting in an infinite number of sequential events. The combined series of energies passing into the faceplate may be expressed by the form $K_g(\lambda) E(\lambda)$, where

$$K_g(\lambda) = \frac{1 - \rho_g(\lambda)}{1 - \rho_s(\lambda) \rho_g(\lambda)} \quad (15)$$

Similarly, the total energy absorbed by the phosphorescent material by all these primary sequential reflections and absorptions is $K_s(\lambda) E_g(\lambda)$, where

$$K_s(\lambda) = \frac{\rho_g(\lambda) [1 - \rho_s(\lambda)]}{1 - \rho_s(\lambda) \rho_g(\lambda)} \quad (16)$$

Of $K_g(\lambda) E_g(\lambda)$, the portion absorbed by the faceplate is $[1 - \tau_g(\lambda)] K_g(\lambda) E_g(\lambda)$ and the remaining portion $E_r(\lambda) = \tau_g(\lambda) K_g(\lambda) E_g(\lambda)$ becomes incident upon the outer surface of the faceplate. Of $E_r(\lambda)$, the portion $[1 - \rho_g(\lambda)] E_r(\lambda)$ passes onto the filter screen and $\rho_g(\lambda) E_r(\lambda)$ is reflected back toward the inner surfaces of the faceplate. The amount $\tau_g(\lambda) \rho_g(\lambda) E_r(\lambda)$ incident upon the inner surface is then divided into two light beams, one beam passing through the inner surface to the phosphor screen for secondary reflections back through the system, and one beam reflected to the outer surface.

It can be reasoned that the primary light beam $K_g(\lambda) E_g(\lambda)$ entering into the faceplate undergoes an infinite number of reflections from the inner and outer surfaces of the faceplate, and for each sequence of reflections, some fraction of light is passed toward the phosphor screen or toward the filter screen respective of the inner or outer faceplate surface. In the interim of these reflections within the faceplate, a series of energies is absorbed by the faceplate. Thus, three total energies from the primary light beam entering the faceplate from the inner side occur: (1) a total energy reflected from the faceplate toward the phosphor screen $E_{ph}(\lambda)$, (2) a total energy passed from the faceplate toward the filter screen $E_f(\lambda)$, and (3) a total energy absorbed by the glass faceplate $E_a(\lambda)$. These series of energies are combined and formulated as follows:

$$E_{ph}(\lambda) = \frac{[1 - \rho_g(\lambda)] \rho_g(\lambda) \tau_g^2(\lambda) K_g(\lambda) E(\lambda)}{1 - \tau_g^2(\lambda) \rho_g^2(\lambda)} \quad (17)$$

$$E_f(\lambda) = \frac{[1 - \rho_g(\lambda)] \tau_g(\lambda) K_g(\lambda) E(\lambda)}{1 - \tau_g^2(\lambda) \rho_g^2(\lambda)} \quad (18)$$

$$E_a(\lambda) = \frac{[1 - \tau_g(\lambda)] [1 + \rho_g(\lambda) \tau_g(\lambda)] K_g(\lambda) E(\lambda)}{1 - \tau_g^2(\lambda) \rho_g^2(\lambda)} \quad (19)$$

Of the beam $E_f(\lambda)$, the portion $[1 - \tau_f(\lambda)] E_f(\lambda)$ is absorbed by the filter screen, and $\tau_f(\lambda) E(\lambda)$ finally emerges from the CRT system as light.

Continuing back at the inner surface of the faceplate, after $E_{ph}(\lambda)$ impinges upon the phosphor screen, a portion $[1 - \rho_s(\lambda)] E_{ph}(\lambda)$ is absorbed by the phosphorescent material, and the remainder $\rho_s(\lambda) E_{ph}(\lambda)$ is reflected back toward the faceplate. This reflected portion undergoes an infinite number of reflections and absorptions between the faceplate and phosphor screen similar to that undergone by $E_g(\lambda)$, which was described in the above

analysis. Thus, $K_s(\lambda) \rho_s(\lambda) E_{ph}(\lambda)$ is absorbed by the phosphorescent material, and $K_g(\lambda) \rho_s(\lambda) E(\lambda)$ enters into the faceplate, which in turn undergoes interreflections between the inner and outer surface similar to the above analysis (Eqs. 17-19). Again, a portion of this energy entering the faceplate will be divided into three portions: (1) a portion reflected back to the phosphor screen; (2) a portion absorbed by the faceplate; and (3) a portion passing from the outer surface of the faceplate, being partially

absorbed by the filter screen and the remaining energy finally emerging from the CRT system as a term of the series of light output.

Another set of terms can be similarly developed to further the expression of the energy terms evolved from the interreflections of the phosphor and faceplate surfaces. The energy series for each element are given below.

A. Light Energy Output

The total energy $\Gamma_0(\lambda)$ of the light emerging from the CRT system is expressed as

$$\Gamma_0(\lambda) = \frac{[1 - \rho_g(\lambda)] \tau_f(\lambda) \tau_g(\lambda) K_g(\lambda) E_g(\lambda)}{1 - \tau_g^2(\lambda) \rho_g^2(\lambda)} + \frac{[1 - \rho_g(\lambda)]^2 \tau_f(\lambda) \tau_g^3(\lambda) K_g^2(\lambda) \rho_g(\lambda) \rho_s(\lambda) E_g(\lambda)}{[1 - \tau_g^2(\lambda) \rho_g^2(\lambda)]^2} + \dots \quad (20)$$

which becomes

$$\Gamma_0(\lambda) = \frac{[1 - \rho_g(\lambda)] \tau_f(\lambda) \tau_g(\lambda) K_g(\lambda) E_g(\lambda)}{Q(\lambda)} \quad (21)$$

where

$$Q(\lambda) = \frac{1 - \rho_s(\lambda) \rho_g(\lambda) - \rho_g^2(\lambda) \tau_g^2(\lambda) - \rho_s(\lambda) \rho_g(\lambda) \tau_g^2(\lambda) + 2 \rho_g^2(\lambda) \rho_s(\lambda) \tau_g^2(\lambda)}{1 - \rho_s(\lambda) \rho_g(\lambda)} \quad (22)$$

B. Energy Dissipated Into the Filter Screen

The total energy $\Gamma_f(\lambda)$ dissipated into the filter screen is

$$\begin{aligned} \Gamma_f(\lambda) = & \frac{[1 - \tau_f(\lambda)] [1 - \rho_g(\lambda)] \tau_g(\lambda) K_g(\lambda) E_g(\lambda)}{[1 - \tau_g^2(\lambda) \rho_g^2(\lambda)]} \\ & + \frac{[1 - \tau_f(\lambda)] [1 - \rho_g(\lambda)]^2 K_g^2(\lambda) \rho_s(\lambda) \tau_g^3(\lambda) \rho_g(\lambda) E_g(\lambda)}{[1 - \tau_g^2(\lambda) \rho_g^2(\lambda)]^2} \\ & + \frac{[1 - \tau_f(\lambda)] [1 - \rho_g(\lambda)]^3 K_g^3(\lambda) \rho_s^2(\lambda) \tau_g^5(\lambda) \rho_g^2(\lambda) E_g(\lambda)}{[1 - \tau_g^2(\lambda) \rho_g^2(\lambda)]^3} + \dots \end{aligned} \quad (23)$$

which reduces to

$$\Gamma_f(\lambda) = \frac{[1 - \tau_f(\lambda)] [1 - \rho_g(\lambda)] \tau_g(\lambda) K_g(\lambda) E_g(\lambda)}{Q(\lambda)} \quad (24)$$

C. Energy Absorbed by the Glass Faceplate

The total energy $\Gamma_g(\lambda)$ absorbed by the glass faceplate may be formulated in a series of energies as follows:

$$\begin{aligned}\Gamma_g(\lambda) = & \frac{[1 - \tau_g(\lambda)] [1 + \rho_g(\lambda) \tau_g(\lambda)] K_g(\lambda) E_g(\lambda)}{1 - \tau_g^2(\lambda) \rho_g^2(\lambda)} \\ & + \frac{[1 - \tau_g(\lambda)] [1 + \rho_g(\lambda) \tau_g(\lambda)] \rho_s(\lambda) \rho_g(\lambda) \tau_g^2(\lambda) [1 - \rho_g(\lambda)] K_g^2(\lambda) E_g(\lambda)}{[1 - \tau_g^2(\lambda) \rho_g^2(\lambda)]^2} \\ & + \frac{[1 - \tau_g(\lambda)] [1 + \rho_g(\lambda) \tau_g(\lambda)] \rho_s^2(\lambda) \rho_g^2(\lambda) \tau_g^4(\lambda) [1 - \rho_g(\lambda)]^2 K_g^3(\lambda) E_g(\lambda)}{[1 - \tau_g^2(\lambda) \rho_g^2(\lambda)]^3} + \dots\end{aligned}\quad (25)$$

which resolves to

$$\Gamma_g(\lambda) = \frac{[1 - \tau_g(\lambda)] [1 + \rho_g(\lambda) \tau_g(\lambda)] K_g(\lambda) E_g(\lambda)}{Q(\lambda)} \quad (26)$$

D. Energy Absorbed by the Phosphor Screen

The total energy $\Gamma_s(\lambda)$ absorbed by the phosphor screen is similarly reduced from a series to the following form:

$$\Gamma_s(\lambda) = \left[1 + \frac{[1 - \rho_s(\lambda)] \tau_g^2(\lambda) K_g(\lambda)}{Q(\lambda)} \right] \left[\frac{[1 - \rho_s(\lambda)] \rho_g(\lambda) E_g(\lambda)}{1 - \rho_s(\lambda) \rho_g(\lambda)} \right] \quad (27)$$

Again, energy is conserved since

$$E_g(\lambda) = \Gamma_o(\lambda) + \Gamma_f(\lambda) + \Gamma_g(\lambda) + \Gamma_s(\lambda) \quad (28)$$

IV. Total Energies

The total energies produced by both the environmental light incident upon the CRT system and the light generated by the CRT system in the forms of light output and energy absorptions by the CRT elements can be obtained by summing the energies produced for each form. Let $d(E_t)_0$ at λ represent the total light energy output for the considered sample in the wavelength region of λ and $\lambda + d\lambda$. Thus, the incremental energy $d(E_t)_0/d\lambda$ at λ is the sum of the monochromatic energies $L_o(\lambda)$ and $\Gamma_o(\lambda)$ (Sections II-A and III-A). By integrating this result over a given spectrum (λ_1 to λ_2), the total light energy output from the CRT system over that spectrum is obtained. Thus, the total light energy output and total energies absorbed in each element can be written as follows.

A. Total Light Energy Output $(E_t)_0$

$$(E_t)_0 = \int_{\lambda_1}^{\lambda_2} [L_o(\lambda) + \Gamma_o(\lambda)] d\lambda \quad (29)$$

B. Total Energy Dissipated Into the Filter Screen $(E_t)_f$

$$(E_t)_f = \int_{\lambda_1}^{\lambda_2} [L_f(\lambda) + \Gamma_f(\lambda)] d\lambda \quad (30)$$

C. Total Energy Absorbed by the Glass Faceplate $(E_t)_g$

$$(E_t)_g = \int_{\lambda_1}^{\lambda_2} [L_g(\lambda) + \Gamma_g(\lambda)] d\lambda \quad (31)$$

D. Total Energy Absorbed by the Phosphor Screen $(E_t)_s$

$$(E_t)_s = \int_{\lambda_1}^{\lambda_2} [L_s(\lambda) + \Gamma_s(\lambda)] d\lambda \quad (32)$$

V. Contrast Ratio

The contrast ratio of the CRT system is defined as the quotient of the maximum luminance divided by the minimum luminance. Luminance output from a CRT system can be varied by modulating the flux of electrons incident

upon the phosphor screen. By assigning G to represent the maximum degree of photometric modulation or gain of the CRT system, it follows that the maximum and minimum number of photons generated by the electron beam are related by G according to the equivalent

$$[n_g(\lambda)]_{\max} = G [n_g(\lambda)]_{\min} \quad (33)$$

The maximum light energy output can be expressed, from Eq. (29), as

$$[(E_t)_0]_{\max} = \int_{\lambda_1}^{\lambda_2} \{L_0(\lambda) + [\Gamma_0(\lambda)]_{\max}\} d\lambda \quad (34)$$

The minimum light energy output from the CRT system is then

$$[(E_t)_0]_{\min} = \int_{\lambda_1}^{\lambda_2} \left\{ L_0(\lambda) + \frac{[\Gamma_0(\lambda)]_{\max}}{G} \right\} d\lambda \quad (35)$$

Converting these energies to luminance by introducing the luminous efficacy K , the contrast ratio C_r of the CRT system, including environmental light, can now be written as follows:

$$C_r = \frac{\int_{\lambda_1}^{\lambda_2} K(\lambda) \{L_0(\lambda) + [\Gamma_0(\lambda)]_{\max}\} d\lambda}{\int_{\lambda_1}^{\lambda_2} K(\lambda) \left\{ L_0(\lambda) + \frac{[\Gamma_0(\lambda)]_{\max}}{G} \right\} d\lambda} \quad (36)$$

VI. Discussion and Conclusion

It is apparent that Eq. (36) is too involved to be used to practically estimate the contrast ratio performance of a CRT system. For reasons of simplification, it shall be assumed that the distribution of $n(\lambda)$ and $n_g(\lambda)$ with respect to λ is uniform. This permits the assignment of an average value over the considered spectrum for each optical property of the various elements of the CRT system. For example, the average transmissivity coefficient $\bar{\tau}_f$ of the filter screen under this condition can be written as

$$\bar{\tau}_f = \frac{\int_{\lambda_1}^{\lambda_2} \tau_f(\lambda) d\lambda}{\lambda_2 - \lambda_1} \quad (37)$$

Equation (36), under these conditions, can then be modified to the form

$$\bar{C}_r = \frac{\bar{L}_0 + \bar{\Gamma}_0}{\bar{L}_0 + \frac{(\bar{\Gamma}_0)_{\max}}{G}} \quad (38)$$

where the bar over each total energy signifies that average values for the optical properties are used.

By including only the primary reflections (first-order terms) associated with the primary beams of the environmental light and generated light of the CRT system, an expression for the contrast ratio $(\bar{C}_r)'$ which includes only these first-order terms can be derived (Ref. 2). This expression is given as

$$(\bar{C}_r)' = \frac{\bar{\tau}_f k L + \frac{\Gamma_{\max}}{G}}{\bar{\tau}_f k L + \frac{\Gamma_{\max}}{G}} \quad (39)$$

where

$$k = \frac{\bar{\tau}_g^2 \bar{\rho}_s (1 - \bar{\rho}_g) + \bar{\rho}_g}{\bar{\tau}_g} \quad (40)$$

and L and Γ are the luminance levels of the environmental light and generated light, respectively. Also, the spectral distributions of L and Γ are assumed to be equal.

It is of interest to compare the contrast ratio given by Eq. (38), which includes the series of interreflection effects upon the elements, with the contrast ratio given by Eq. (39), which considers only the first-order effects of the primary beam.

Representative values for the optical properties of a typical CRT configuration which utilizes a P4 phosphor is given in Table 1 (Ref. 2).

Assume that the selected CRT has a filter screen with a mean transmissivity $\bar{\tau}_f = 0.50$. By substituting the values for the properties (Table 1) into Eqs. (38) and (39), estimated contrast ratios, including fractional differences, are obtained. These ratios are shown in Table 2 for three different environmental lighting conditions.

It can be seen from Table 2 that the value of contrast ratio using Eq. (39) results in a slightly higher contrast ratio value than that which results from using Eq. (38).

Table 1. Optical property values of a typical CRT

Property	Value
$\bar{\rho}_s$	0.76
$\bar{\tau}_g$	0.63
$\bar{\rho}_g$	0.04
G	33.00

Table 2. Comparative results of contrast ratio

Ratio	Lighting condition		
	Dark	Dim	Bright
Environment-to-generated-light ratio (L/T_{\max})	0	0.10	1.00
\bar{C}_r (Eq. 38)	33.0	17.7	4.16
$(\bar{C}_r)'$ (Eq. 39)	33.0	18.2	4.36
$[\bar{C}_r - (\bar{C}_r)'] / \bar{C}_r$	0	-0.028	-0.048

In the case where a filter screen is not used, the results obtained from the two equations are about double those shown in Table 2. It may be concluded that Eq. (39) may be used to obtain a reasonably accurate estimate of the contrast ratio capability of a CRT system. The results obtained will be slightly optimistic.

For the CRT configuration described in Table 1, the light output and energies dissipated in the various CRT elements may be estimated from Eqs. 28-31. Consider a practical intensity of environmental light to be 10% as great as the light generated by the CRT. Under these conditions, the total photon energy (incident upon and generated by the CRT system) would be porportioned as follows: 32% is transmitted and reflected from the CRT as light output, 36% is dissipated by the filter screen, 40% is absorbed by the glass faceplate, and 2% is absorbed by the phosphorescent material.

For a CRT system which has no filter screen, under the same light conditions given above, the total photon energy would be porportioned as follows: 65% is light output, 42% is absorbed by the glass faceplate, and 3% is absorbed by the phosphorescent material.

References

1. Born, M., and Wolf, E., *Principles of Optics*. Pergamon Press, London, England, 1959.
2. Volkoff, J. J., "Contrast Ratio Determination for the SFOF Video Image Display," in *The Deep Space Network*, Space Programs Summary 37-65, Vol. II, pp. 91-93.

Mark IIIA Simulation Center Interactive Alphanumeric Television System

C. F. Leahey
SFOF/GCF Development Section

The Mark IIIA Simulation Center is capable of simultaneously simulating two spacecraft and three deep space stations using the Univac 1108 and the EMR 6050 computers. The control consoles of the Mark II system were inadequate for controlling a simulation of the size required for the Mark IIIA system. A new control and display system was designed using interactive cathode-ray tube data terminals and high-speed printers. This design upgrades the control and display system for future use in more complex missions. Development, capabilities, and operation of this system are described.

I. Introduction

The purpose of this article is to describe the development, capabilities, and operation of the interactive alphanumeric television (IATV) system. This equipment configuration is an assembly of the DSN Simulation Center (Simcen), designated the Mark IIIA Simcen, which is located in the SFOF.

The installation of the IATV system is part of the current development activity that is taking place in the DSN Simcen in preparation for *Mariner* Mars 1971 and *Pioneer F* support. This activity was described in Ref. 1.

The Mark II Simcen configuration was capable of simulating one spacecraft and one DSS. The Mark IIIA con-

figuration is capable of simultaneously simulating two separate spacecraft and three DSSs.

Since the control consoles which existed in the Mark II system were inadequate for controlling a simulation of the size required for the Mark IIIA system, a new control and display system had to be designed. Originally, the plan was to fabricate the necessary control consoles using discrete components. After doing a preliminary design on these consoles, using the requirements specified by the DSN, it was determined that hardware implementation costs would approach the \$100,000 mark and that the configuration of the consoles could not be easily upgraded for follow-on projects with greater complexity. The use of interactive cathode-ray tube (CRT) display terminals was

decided upon since they would provide the desired flexibility to upgrade the control consoles for more complex missions with few, if any, hardware modifications, and a lesser cost for software changes than if the job were done with discrete components.

II. Description

The IATV display system is functionally diagrammed in Fig. 1. The system contains eight CRT-keyboard display terminals and two printer terminals, and operates from a buffered input/output word channel of the EMR 6050 computer.

The equipment for the IATV system was obtained from an outside source and, with the exception of the channel adapter, is standard off-the-shelf equipment. The channel adapter was designed and built for JPL by the manufacturer.

A. CRT Display Stations

Each of the eight CRT display stations of the IATV display system is comprised of three physically separate units (Fig. 1):

- (1) CRT/TV display unit (14 in.).
- (2) Station controller.
- (3) Keyboard.

Each station controller contains a 1024 byte core memory for storing characters to be displayed on the associated CRT/TV display unit. The station controller is the central control unit of the station and responds directly to the commands and data received either from the keyboard or the computer (through the remote multiplexer). The same type controller is also used as the primary controller for the two hard copy printout stations.

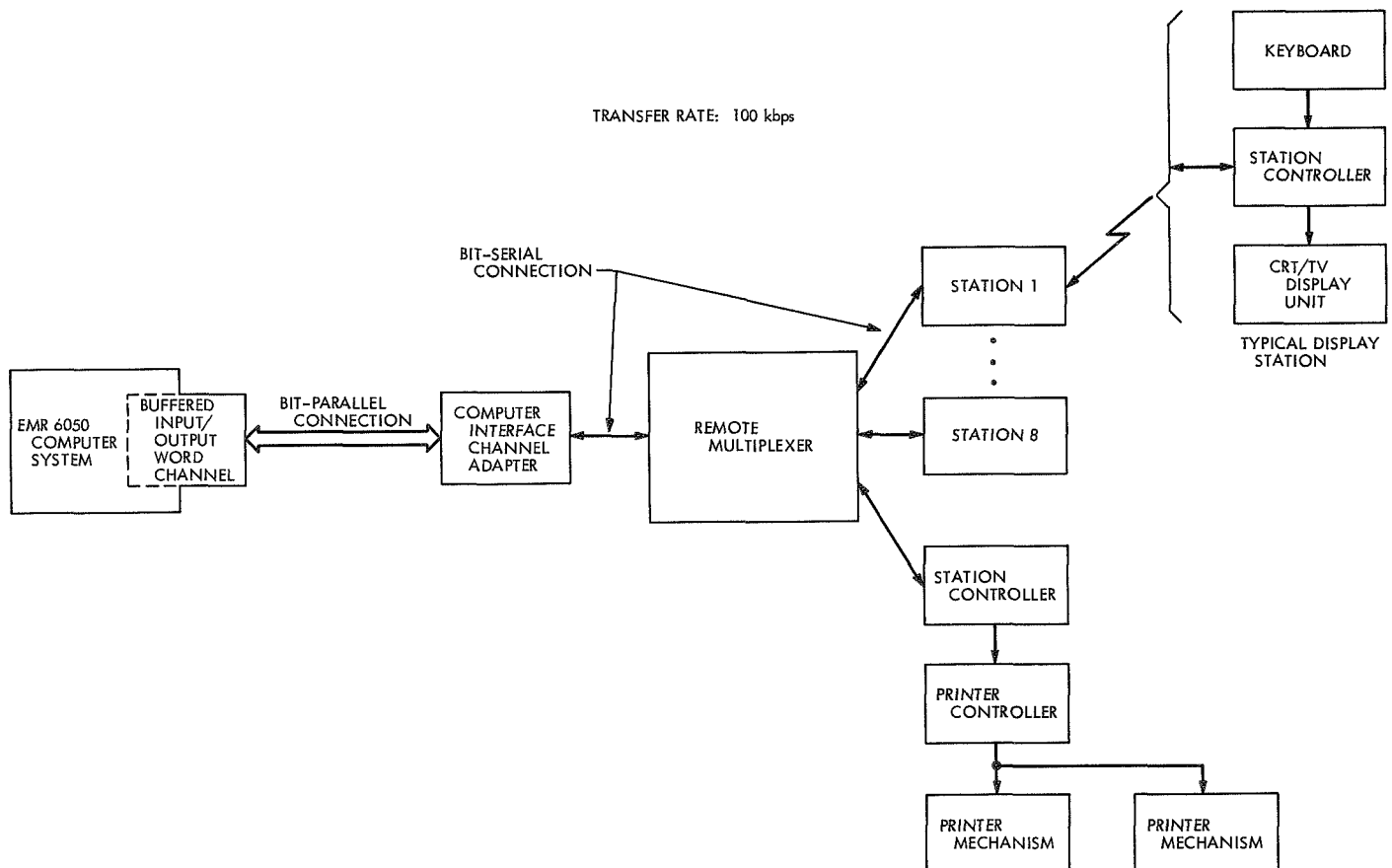


Fig. 1. Functional block diagram of interactive alphanumeric television display system

B. Hard Copy Printout Stations

The two nonimpact, high-speed, hard copy printout stations of the IATV display system are implemented using four physically separate interconnected functional units (Fig. 1):

- (1) Station controller.
- (2) Printer controller.
- (3) Nonimpact printer mechanism (two units).

The station controller and the printer controller are time-shared by the two printer mechanisms.

C. Unit Operations

The operations of each of the five major functional units used in the IATV display system are briefly described in the following subsections. The five major functional units are:

- (1) EMR 6050 computer.
- (2) Computer interface channel adapter.
- (3) Remote multiplexer.
- (4) Display communications station.
- (5) Printout station.

1. EMR 6050 computer. The EMR 6050 computer interface with the display station is by means of a buffered input/output word channel. A number of data, address, and control signals are involved in the interface between the computer and the channel adapter. The data is transferred in parallel between the computer and the channel adapter, 24 bits at a time. Three 8-bit characters are packed into each 24-bit computer word. The characters can be for display or printout or for control of the subsystems of the IATV system.

a. IATV interrupts. The IATV display system is assigned two external device interrupt levels in the computer and is capable of generating four distinct interrupt conditions. Two of these conditions are indicated by bits in the channel adapter status word, which will be discussed later. These conditions are as follows:

- (1) *BM = BL interrupt.* This condition occurs when the channel adapter receives a BM = BL signal on the BM = BL line from the computer, which indicates that the information block in memory has been filled (input) or that the last word is available (output).

- (2) *End of operation interrupt.* This condition occurs when a block read or write operation is terminated by the transfer of all the characters or words, and the channel adapter returns to the not busy condition and has been instructed to return an end-of-operation interrupt.

- (3) *Time out interrupt.* This interrupt provides the channel adapter with the ability to terminate the read operation if a data character is not received from the remote multiplexer within a given time period. This time period is determined by the channel adapter. When a time out occurs, a bit is set in the channel adapter status word.

- (4) *Interrupt character received interrupt.* This condition occurs when the channel adapter receives an interrupt character from a station controller. A bit is set in the channel adapter status word when this occurs.

2. Computer interface channel adapter. The computer interface channel adapter is compatible with the buffered input/output word channel of the EMR 6050 computer and acts as a device controller on this channel. The channel adapter performs four major interrelated functions:

- (1) Transforms the bit-parallel interface to a bit-serial communications channel and conversely.
- (2) Manages the flow of data between the buffered input/output word channel and the devices (stations) serviced by the bit-serial communications line (through the remote multiplexer).
- (3) Responds to the command and control signals generated by the buffered input/output word channel in a functionally and electrically compatible manner.
- (4) Generates the correct transmission format which is compatible with the "line discipline" used on the bit-serial communications line.

a. Commands. The computer can issue the following control commands to the channel adapter:

- (1) *Initiate block write.* This command initiates the transfer of a block of data from the computer to the channel adapter.
- (2) *Initiate block read.* This command initiates the transfer of a block of data from the channel adapter to the computer.

- (3) *Enable interrupt character received interrupt.* This command enables the channel adapter to transmit an interrupt to the computer when an interrupt character is received by the channel adapter from a station controller.
- (4) *Disable interrupt character received interrupt.* This is opposite from command (3).
- (5) *Clear channel adapter.* This command resets the logic and data registers in the channel adapter to a known state.
- (6) *Enable end-of-operation interrupt.* This command enables the channel adapter to return an end-of-operation interrupt, which was previously described.

b. Status conditions. The channel adapter is capable of indicating its status to the computer by means of a status word. Seven status conditions can be indicated and are as follows:

- (1) *Data overrun on input.* Set when a write operation is attempted while the channel adapter has a character waiting to be transferred to the EMR 6050 computer.
- (2) *Input transmission parity error.* Set by the detection of a character parity error during receive operation.
- (3) *Character in read buffer.* Set whenever any character is placed in the channel adapter input data register.
- (4) *Time out interrupt.* Set whenever the time out interrupt (discussed previously) is activated.
- (5) *Interrupt character received interrupt.* Set whenever the interrupt character received interrupt (discussed previously) is activated.
- (6) *Remote multiplexer busy.* Set whenever the remote multiplexer is performing a block read or a block write operation.
- (7) *Data lost.* Set if the channel adapter fails to receive a read command before the channel adapter must begin to assemble the next bit-parallel word.

3. Remote multiplexer. The remote multiplexer functionally performs as an electronic switch controlled by the computer through the computer interface channel adapter. The "address" character transmitted to the remote multiplexer from the computer causes the remote multiplexer to select one of several long line adapter

interfaces, which in turn are connected to the "remote" stations (CRT display or printout stations). The address character always precedes the "text" transmitted to the selection station. The previously selected long line adapter interface and, therefore, the corresponding station is automatically deselected by the SYN character which always precedes the address character.

The remote multiplexer also accepts and responds to control function codes which are effectively addressed to it.

The remote multiplexer functionally consists of a data "shift through" register, control logic, function decode logic, a special character generator, several status registers, and a set of long line adapters. Each long line adapter provides two bit-serial interfaces. One remote type station can be connected to each bit-serial interface. Each long line adapter functionally is an integral part of the remote multiplexer and contains two bit positions of the station acknowledge status (SAS) register, four bit positions of the double rank station interrupt status (SIS) register, and the address/select logic for the two bit-serial interfaces provided by each long line adapter. The shift through register in the basic remote multiplexer is the only storage register provided for data transfer in the remote multiplexer. This register introduces a *one* character delay in data transfer through the remote multiplexer. The SAS and SIS registers contain data relative to the status of the remote stations, which the computer can sample.

a. Operation. The remote multiplexer operates either in the transmit or receive mode. It can either transmit information to the computer or receive from the computer, but not simultaneously. It is a half duplex device and can "turn around" in one bit time period. The data transfer rate through the remote multiplexer is 100 kbps. The remote multiplexer is designed primarily as a hard-wired logic multiplexer for data transfer between the computer and the several terminals (stations) connected to the remote multiplexer. In addition, it can also:

- (1) Execute certain control functions received from the computer.
- (2) Propagate to the computer interrupts generated at any one of the several remote stations connected to the remote multiplexer.
- (3) Present to the computer status word(s) in response to requests from the computer.

4. Display communications station. The display communications station is comprised of the CRT/TV display unit, the station controller, and the keyboard (Fig. 1). The station recognizes and responds to:

- (1) 17 control characters.
- (2) 13 function command characters for the station controller.

USASCII coding is used for all characters. The station can display up to 800 characters (40 characters per line by 20 lines) per display and can display 67 different characters as follows:

- 26 alpha
- 10 numeric
- 28 pictorial
- 3 special pictorial

a. Significant features. Some of the significant features of the display station are as follows:

- (1) Capability to address any displayable location on the CRT screen. This enables the computer to transmit either a full or a partial line and/or screen (split screen capability) or to selectively update any symbol displayed anywhere on the CRT screen without need to send any "space" codes.
- (2) Capability to determine the location of the cursor.
- (3) Ability to send an interrupt code from the display station at any time.
- (4) Computer can enable or disable transmitting from the display station.
- (5) Ability to obtain a STATUS byte from the station informing the computer of the station status.
- (6) Ability to enable or disable refreshing of the information displayed on the CRT screen.

5. Printout station. Two nonimpact-type printout stations are provided in the IATV display system. Each station is connected to the remote multiplexer and receives data for printout from the computer through the remote multiplexer. The printer mechanisms are connected to the

remote multiplexer through one printer controller and one station controller (Fig. 1). The printer controller is connected to the remote multiplexer through a long line cable consisting of three twisted wire pairs. A separate pair is used for data transfer in each direction. The third pair provides bit-serial timing down from the remote multiplexer to the station controller of the printout station.

The station controller provides storage for up to 1,024 characters of data. (To store up to 1,024 characters in the station controller, the program must first set the "cursor" to the first nondisplayable memory location in the station controller. If the cursor is set to memory location 0/0 in the station controller, then up to 960 characters can be stored in the station controller core-memory.)

The printer controller contains the printer control and interface electronics for the printer mechanism. The printer controller also converts each USASCII coded character received from the core memory in the station controller into a 5×7 dot matrix and transmits the dot pattern generated to the printer mechanism. This printer can operate at a rate of 300 characters/s (225 lines/min at up to 80 characters/line, or at 450 lines/min with up to 40 characters/line).

In the system, the computer can select any one of the two printout stations for data printout, and through the remote multiplexer, transfer data for printout by the selected station. Data for printout is first transferred at high speed (100 kbps) to the core memory of the station controller, stored, then transferred, one character at a time, to the printer controller for printout by the printer mechanism at a rate of 300 characters/s.

D. Control and Display

1. Control. All operational control is accomplished through the CRT keyboard. The first 20 positions of line 20 are used exclusively for control input during operations. The last 20 positions of line 20 will be used by the system for response messages, so as not to conflict with other displays or the request portion itself.

Each user of the keyboard must first identify himself before submitting his message. Identification pertains to the various elements of the operating system, such as telemetry, command, etc. Upon receipt of each message, the system will make the necessary identification and route to the applicable processor or program.

2. **Display.** All display will be accomplished on either a CRT or a line printer.

a. **CRT displays.** CRT display capability consists of 8 CRT units (with attached keyboard). All units will have identical functionality, that is, any unit has total control and display capability. Each CRT screen has a display grid of 20 lines of 40 characters each.

The system will initially supply 3 formats which are designed to cover all display needs in an efficient and standard manner. There are two types of format: GRID and ROLL. GRID formats are displays representing current status; ROLL formats show parameter history as well as current status. A synopsis and example of each format used in the system follows.

GRID formats (Figs. 2 and 3)

Format A (24 displays, 4 × 6 MATRIX)

- (1) 8-character DESCRIPTOR
- (2) 8-character VARIABLE

15.48.19 T/M REQUEST S/C 2 FORMAT 123			
AUX BAT	CMD LOCK	RATE	IRR MIRR
ON	OFF	33	NOT STOW
MANACT	CCO	CCONE	GRS2
INHIBIT	INCREASE	88.50	324-01
PYGPEN	DC64S	DC63S	AUPPEN
OFF	POST INS	NT IN EF	FALSE
GES3	SVAC01	TWT10	VBSTCV
764+02	146.5	12345+02	332241
ST A AGC	ST A SPE	SA GTPWR	SA GFREQ
1234-02	77+00	1234-02	4321-05
ST A HA	ST A DEC	ST A RUG	ST A DCC
138.5	35.0	12345678	8570
T,F123\$	THIS HALF FOR REPLY		

Fig. 2. GRID format (format A)

- (3) Fixed point—8 significant digits
- (4) Floating point—5 significant digits, 2-digit exponent
- (5) ALPHANUMERIC—8 characters
- (6) ALL CONVERSIONS (BCD, BINARY, OCTAL, DECIMAL)

Format B (18 displays, 3 × 6 MATRIX)

- (1) 12-character DESCRIPTOR
- (2) 12-character VARIABLE
- (3) Fixed point—12 significant digits
- (4) Floating point—9 significant digits, 2-digit exponent
- (5) ALPHANUMERIC—12 characters
- (6) ALL CONVERSIONS

07.32.16 TRK REQUEST S/C 1 FORMAT 062		
DSS 41 HA	DSS 41 DEC	DSS 41 RNG
4127347	1647236	212476733
S41 1-WY DOP	S41 2-WY DOP	S41 3-WY DOP
1234567890	1234567890	1234567890
S41 RESOLVER	S41 EX VCO C	DSS 41 DCC
862	28987654321	8570
DSS 11 HA	DSS 11 DEC	DSS 11 RNG
1234567	1234567	123456789
S11 1-WY DOP	S11 2-WY DOP	S11 3-WY DOP
1234567890	1234567890	1234567890
S11 RESOLVER	S11 EX VCO C	DSS 11 DCC
123	12345556789	1234
K,F062\$	THIS HALF FOR REPLY	

Fig. 3. GRID format (format B)

ROLL formats (Fig. 4)

Format C (16 line displays)

- (1) 3-column DESCRIPTORS (11 characters each)
- (2) First column always time
- (3) Variable has 11 characters
- (4) Fixed point—11 significant digits
- (5) Floating point—8 significant digits, 2-digit exponent
- (6) ALPHANUMERIC—11 characters
- (7) ALL CONVERSIONS

Display formats are determined at initialization time. This is in the form of format cards entered into the system via the card reader. The user may choose any of the three formats.

b. Line printer displays. Line printer displays are handled in a manner identical to CRT displays. Formats are defined for several lines of print, each line having a separate format description card. Activation of a line printer display is also accomplished via the keyboard.

10.35.59 STA DATA REQUEST FORMAT 001			
GMT	AGC	SPE	14 1-WY DOP
35.42	66.5	77.6	1234567890
35.43	66.5	77.6	1234567890
35.44	66.5	77.6	1234567890
35.45	66.5	77.6	1234567890
35.46	66.5	77.6	1234567890
35.47	66.5	77.6	1234567890
35.48	66.5	77.6	1234567890
35.50	66.5	77.6	1234567890
35.51	66.5	77.6	1234567890
35.52	66.5	77.6	1234567890
35.53	66.5	77.6	1234567890
35.54	66.5	77.6	1234567890
35.55	66.5	77.6	1234567890
35.56	66.5	77.6	1234567890
35.57	66.5	77.6	1234567890
35.58	66.5	77.6	1234567890
S, F1\$			THIS HALF FOR REPLY

Fig. 4. ROLL format (format C)

c. Operation. The execution of all displays is the responsibility of the several display processors, and not the individual programs, which, in general, do not initiate a display. All displays are initiated at the operator's request. Upon receipt of a display request, the keyboard message processor (part of the system) will identify the user, unit, and format number. The format descriptors and map will be retrieved from the drum, the data will be retrieved from the program interface file, and the display will be executed.

III. System Integration

The IATV system integrated fairly easily with the EMR 6050 computer. The main problems encountered were in the checkout of the logic of the channel adapter. Since the channel adapter was a new design, these problems were not unexpected.

After the system was made operable, checkout with user software uncovered a few problems in the printer subsystem of the IATV system. The most significant of the problems uncovered was the lack of an interrupt from the printer subsystem. Since the initial design of the printer subsystem was not capable of generating an interrupt to indicate when a given block of data had been printed, a wait loop was incorporated in the software sufficiently long to insure that the previous block of data had been printed before an attempt was made to print another data block. This proved to be an unsatisfactory solution because of the limited memory space available in the computer for use as a printer data buffer. To solve this problem, the manufacturer changed the station controller used in the printer subsystem to provide an interrupt to the computer whenever a block of data has been completely printed. This proved to be very satisfactory.

Another minor problem with the printers was the lack of paper take-up reels. In this system, the printers are used as data logging devices, and therefore output a large quantity of paper as well as data. Since there were no take-up reels for the paper, the large quantity of paper output was somewhat of a problem. To solve this problem, some surplus teletype reelers were salvaged from some unused printers and were mounted behind the printers.

IV. Summary

The need for a viable user-computer interface is an ever-present requirement. In this case, an interface was needed in which the computer could output data in set

formats and in which the user could enter changes to this data to the computer. This interface could have been implemented with discrete components as the Mark II system had been; but, because of the development of interactive CRT data terminals, a better alternative was available.

The choice of a CRT data terminal system for this interface proved to be satisfactory. In addition to being a satisfactory interface, it is also a flexible interface. It can provide a good base for the development of other information display and control systems for future more complex missions.

Reference

1. Polansky, R. G., "DSN Mark IIIA Simulation Center Development," in *The Deep Space Network*, Space Programs Summary 37-65, Vol. II, pp. 94-96. Jet Propulsion Laboratory, Pasadena, Calif., Sep. 30, 1970.

A Reanalysis Program for Antenna Member Size Changes

R. Levy

DSIF Engineering Section

An efficient procedure is described for reanalysis of space-truss structural frameworks. The procedure has been programmed to operate as a post-processor to determine response changes from sets of displacements developed for the initial structure by an independent structural analysis system. Examples given show substantial savings in computation time when operating in conjunction with the NASTRAN structural analysis system.

I. Introduction

Efficient methods of reanalysis are useful to assess the changes in structural response as a function of modifications to the properties of the individual member components of the structure. The applications encompass all design phases through inception and future alteration, particularly in conjunction with the implementation of the techniques for structural optimization.

Currently, a number of diverse procedures for reanalysis have evolved to operate within the context of prevalent approaches to the overall formulation chosen for analytical solution of the response problem. Some have been designed to be used in conjunction with force method, displacement method, or mixed formulations. Additional alternatives depend for their attractiveness upon whether or not the number of members for which modifications are considered form a relatively large or a relatively small set, or possibly whether or not the modified members can be readily localized to occur within restricted regions of the structure.

Some of the procedures are mathematically exact in the sense that the solutions will be exactly equivalent to solutions that would be obtained from analysis of the modified structure *ab initio*. Other procedures develop approximate solutions for which exact eventual convergence can be demonstrated iteratively. All methods usually appear to fall within either of two classes:

- (1) Given the inverse of the stiffness matrix for the initial structure, the inverse for the modified structure is developed by perturbation.
- (2) The solution for the modified structure is developed as a linear combination of solutions for the initial structure.

II. Proposed Method

In the following, an exact method of solution will be described that develops displacements and member forces for the modified structure from linear combinations of displacement function solutions developed for the initial

structure. Conceptually, the method is based upon a parallel element approach. For each component member to be modified, a hypothetical parallel member is postulated. Cross-sectional properties of the parallel member are taken as exactly equal to the changes in properties of the parent (original) member and the connectivity is duplicated. The final member forces for the modified structure are the sums of the member forces on parent and parallel members. A condition of the solution is to maintain compatibility of the parent and parallel member distortions. Entirely new members can be added by parallel members and original members can be completely removed by assigning duplicate properties of negative magnitude to the parallel member.

Reanalysis is performed by a post-processor computer program that uses input displacement functions developed previously by an independent structural analysis program. Because the only computed data that are input are the displacement functions, the analytical formulation procedure used to process the initial structure and develop these displacements is immaterial. The present implementation of the program is designed to accept input specifically in the format of the NASTRAN analysis system. A present limitation is the restriction to process only changes in the cross-sectional area property for one-dimensional bars. This limitation, however, is compatible with the design requirements of space truss structures, such as the frameworks of antenna reflectors. The advantages of this method are the simplicity of program operation and input requirements, and the efficiency with which parameter studies can be developed for the response as a function of a spectrum of property changes for particular bars.

III. Mathematical Formulation

The displacements of the modified structure U_M are obtained by superposition of displacements of the initial structure U_I and the displacements ΔU caused by the internal forces of the parallel members acting as loads on the initial structure. That is,

$$[U_M] = [U_I] + [\Delta U] \quad (1)$$

The order of the matrices in Eq. (1) is $m \times k$, where m is the number of unconstrained degrees of freedom, and k is the number of external loading vectors.

To evaluate ΔU , it is convenient to express these displacements as the product of the displacements for unit

values U_s of the parallel member forces post-multiplied by the forces R of the parallel members, or

$$[\Delta U] = [U_s] [R] \quad (2)$$

$(m \times k) \quad (m \times b) \quad (b \times k)$

In Eq. (2), the index b is equal to the number of property changes summed over all the members.

To enforce compatibility, let

e_F = final distortions of parent members = distortions of parallel members

e_I = initial distortion of parent member for the external loads

e_s = distortions of parent member for unit values of forces of the parallel members

e_o = distortions of parallel members for unit forces

Therefore, from superposition

$$[e_F] = [e_I] + [e_s] [R] \quad (3)$$

$(b \times k) \quad (b \times k) \quad (b \times b) \quad (b \times k)$

But e_F can be determined directly as the distortions of the parallel members,

$$[e_F] = [e_o] [R] \quad (4)$$

After combining Eqs. (3) and (4) and rearranging, R can be obtained by solving

$$([e_o] - [e_s]) [R] = [e_I] \quad (5)$$

The solution of Eq. (5) for R can be obtained readily in many instances because the order of the coefficient matrix is equal only to the total number of property changes.

Examination of Eq. (5) shows that relatively little additional computational effort is necessary to process more than one property change for a given member. This can be done by saving the e_s and e_I matrices in Eq. (5) and repeating only the relatively minor effort in regenerating new e_o matrices. In this manner, the responses for sequences of property changes for given members can be obtained efficiently.

After solving, and combining Eqs. (1) and (2), the final displacements of the modified structure are obtained from

$$[U_M] = [U_I] + [U_s] [R] \quad (6)$$

$(m \times k) \quad (m \times k) \quad (m \times b) \quad (b \times k)$

The final member forces can be found either by summing forces on parent and parallel bars, or else by expanding

the indices of Eq. (3) to cover all of the members of interest and then applying the internal force-distortion relationship for these members.

In the limited case of one-dimensional bar members, the member distortion is the extension of a bar along its axis and is given by

$$e_i = \frac{S_i L_i}{A_i E_i} \quad (7)$$

where S_i , L_i , A_i , and E_i are, respectively, the member force, length, area, and modulus of elasticity for the i th member. As an alternative to Eq. (7), the present implementation computes the extension from the grid coordinates and displacements associated with the bar as follows:

$$e_i = \sum_{\alpha=1}^3 \frac{q_i^{\alpha} H_i^{\alpha}}{L_i}, \quad i = 1, 2, \dots, b \quad (8)$$

where q_i^{α} is the difference in displacements of the terminal nodes of the bar in the direction of the α th axis of Cartesian coordinates, H_i^{α} is the projection of the bar axis along the α th axis,

and

$$L_i = \left(\sum_{\alpha=1}^3 [H_i^{\alpha}]^2 \right)^{1/2} \quad (9)$$

The computations for Eqs. (8) and (9) are performed by using the member connection cards to define the terminal nodes and the grid cards that give the nodal coordinates. These data can be duplicates of the input for the original structural analysis program. The displacements used to generate the e_i set are the responses to the applied loading. The displacements that generate the e_s set are obtained by applying a pair of unit loads directed towards each other at the terminal nodes associated with each parallel member; each pair of loads forms one loading vector and contributes one column of displacements to the U_s matrix, which is used to compute one column of distortions in the e_s matrix.

The unit loads that produce the e_s set are equilibrated by corresponding unit loads that extend the parallel member. Consequently, the e_0 matrix is a diagonal matrix of

distortions for unit tensile loads, with each diagonal element of the form

$$e_0 = \frac{L_i}{A_i E_i} \quad (10)$$

where A_i is the change in area for the i th member and this can be positive or negative, depending upon whether the area of the i th member is to be increased or decreased.

IV. Program Execution and Conclusions

A flow chart of the reanalysis program described is shown in Fig. 1. The program is developed either to process property changes for individual bars or common property changes to groups of bars.

Table 1 contains a summary of the central processing unit times for program operation (Univac 1108 Exec 8 computer) for two different structures that have been reanalyzed by this program. For both structures, the input displacements were read from a tape which was created by suppressing NASTRAN output punch card images by means of the executive breakpoint feature of the 1108 computer. The central processing unit (CPU) times shown include, in addition to computation time, the time used for data input (card and tape reading) and a substantial amount of printed output.

Two NASTRAN runs were made in each case of Table 1. The first run was made independently of reanalysis requirements. The purpose was to check stability of the analytical model and possibly to provide some

Table 1. CPU times^a for Univac 1108 Exec 8 computer

Parameter	Structure I	Structure II
Matrix order m	48	1350
Total number of bars	60	1492
Number of loading vectors k	2	2
Number of bars in change group b	6	37
NASTRAN CPU times ^a		
Original structure: for U_i	32 s	12 min 44 s
Original structure: for U_i and U_s	45 s (cold start)	11 min 41 s (restart)
Reanalysis program CPU times ^a		
Generate U_M for first area change	2.7 s	37.0 s
Generate U_M for each additional area change	0.3 s	2.3 s
^a CPU times are central processing unit times for all operations of computations plus input/output, exclusive of compilation time.		

SET A SET OF BARS TO BE MODIFIED
 SET B UNION OF SETS OF TERMINAL NODES
 FOR BARS OF SET A

SET C NODES FOR WHICH MODIFIED
 DISPLACEMENTS ARE REQUIRED
 SET D UNION OF SET B AND SET C

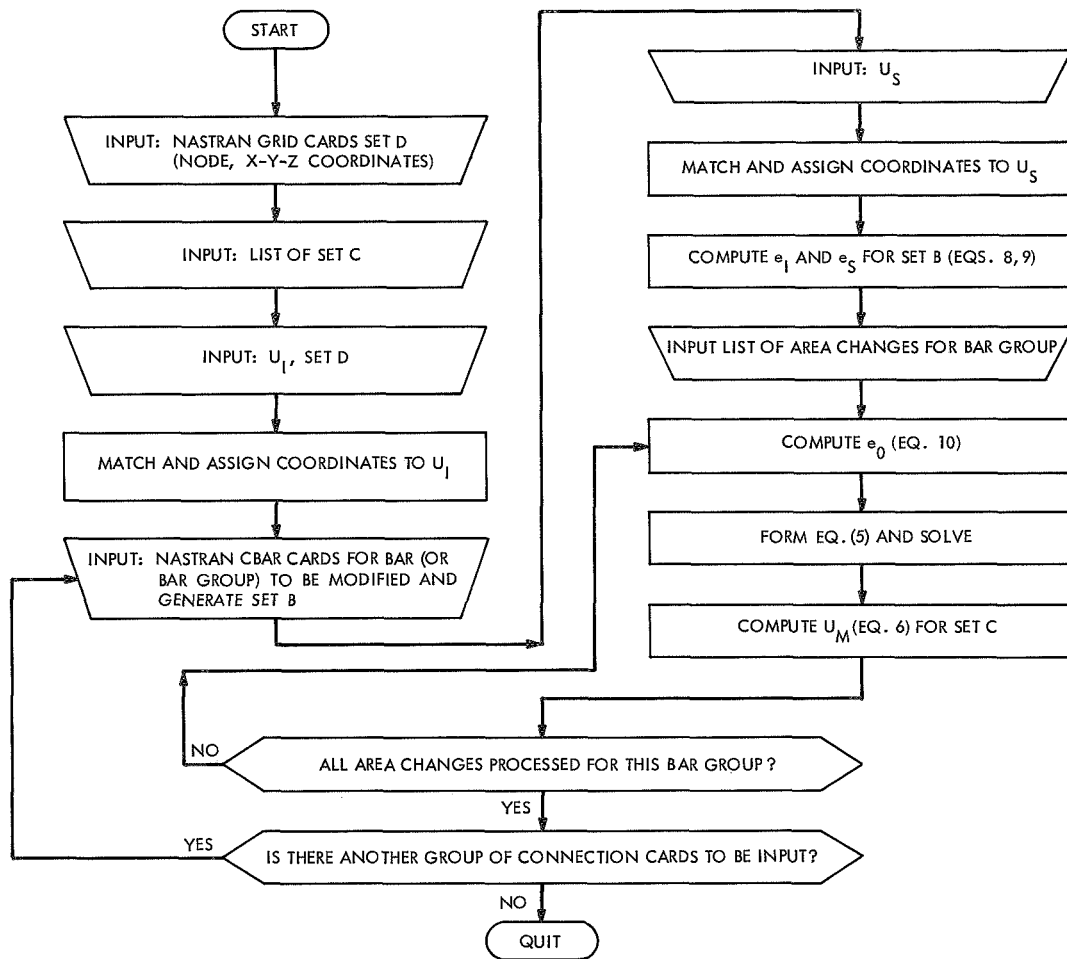


Fig. 1. Flow chart for computations of modified structure displacements (NASTRAN post-processor)

insight into which members were the most desirable candidates for revision. When the checking can be eliminated and the members to be changed are known in advance, reanalysis could start from the second run, which generates all needed information. The time used for the first run, however, gives an indication of the time required to process one additional group change of member properties in lieu of using the reanalysis post-processor program.

Table 2 illustrates the advantages in computation total time that can be obtained by using the reanalysis procedure to process up to four hypothetical property changes for a given bar group for the two structures. The tabulations show the time to analyze each modification as a new structure by using NASTRAN only and the time to

process the modifications by the reanalysis program. The "NASTRAN only" column does not consider program restarts, because experience does not show significant economies in restarting when the basic structure is modified. Although Table 2 shows substantial advantages for reanalysis post-processing when at least two changes are considered, the benefits would be even more pronounced whenever the first NASTRAN run is eliminated and only the second NASTRAN run (Table 1) is used.

Computational time savings are most pronounced when the number of property changes is a relatively small proportion of all of the properties because the number of computations depends upon the number of changes. Whenever a large number of members are jointly to be given a small number of changes, the advantages of re-

Table 2. CPU times^a for reanalysis of multiple property changes of a bar group

Structure	Number of property changes	Time, s	
		NASTRAN only	NASTRAN + post-processor reanalysis
I	1	32	47.7
	2	64	48.0
	3	96	48.3
	4	128	48.6
II	1	768	738
	2	1536	740
	3	2304	743
	4	3072	746
^a CPU times are central processing unit times for all operations of computations plus input/output, exclusive of compilation time.			

analysis would tend to diminish. For example, if all members were to be changed, the time to generate the U_s displacements would be equivalent to the generation of the full flexibility matrix. In such cases, it might be most efficient to analyze the modified structures independently.

In addition to the operations described in the foregoing discussion, it has been found convenient and efficient within the reanalysis program to perform required additional computations in terms of the modified displacements that are developed. For example, the present version of the program contains a subroutine to compute the rms deviations from the best-fitting paraboloid, using the U_M displacements for a set of specified nodes (set C, Fig. 1) on the reflector surface.

Antenna Structures: Evaluation of Field Measurements of Reflector Distortions

B. Marcus and M. S. Katow

DSIF Engineering Section

Field measurements of reflector distortions, using the theodolite angle differences and fixed arc lengths from the vertex of the paraboloid, are based on apparent displacements normal to the line of sight. Two computing methods are described which use directions information from the structural computer analysis to upgrade the readings in the pathlength errors sense. Comparative rms values of the 1/2 pathlength errors, after a paraboloid best fit, resulting from the field measurements, the analytical analysis, and the rms equivalences to RF radio star measurements, are overlayed on an rms surface tolerance versus elevation angle chart for the 64-m-diam antenna. Close rms agreements allow designation of an error tolerance of ± 0.08 mm (0.003 in.) for the field-measured rms values.

I. Introduction

The state-of-the-art method of measuring distortions of a large ground-based antenna uses an angle-measuring theodolite mounted on the axis of symmetry just above the vertex of the paraboloid. The only other dimension measured is the arc length from the vertex to the target located on the surface of the paraboloid (Fig. 1). Since the theodolite can only measure apparent deflections measured normal to its line of sight, the actual RF pathlength error may not be evaluated within useful precision when the Z components of the readings are input to the rms

computer program (Ref. 1). This anomaly was apparent since the first output of the three vector components from the analytical solutions.

One solution proposed by R. Levy (Ref. 2) uses analytically computed three-component distortions read by simulated field readings by the theodolite method. The difference in the two rms values can then be applied as corrections to the field-measurement values. This method, revised to use vector analysis, is described and is now

incorporated as subroutine ANAFLD as part of the rms package (Type D).

Another solution method, also described in this article, combines the single-dimension field measurement with direction vectors from the analytic solution to determine the correct rms value. Subroutine FIELD modifies the data before its input to the best fitting computation (Type C).

II. Process of Field Measurement

Normally, the surface panels are first installed and adjusted close to the center of the adjustment range with the edges faired from one panel to the next one at zenith look. Then, the target mounting holes are drilled to predetermined arc distances from the vertex of the paraboloid using a strap gage. The change in arc distances is assumed presently to be negligible for the different elevation angle positions.

Table 1 defines terms used in the discussion that follows.

At an elevation angle selected for the "perfect" paraboloid position (45-deg for the 64-m-diam antenna), each

Table 1. Definition of terms

Deflection vector	vector from the original position of the target point to its deflected position
Field reading QT	the projection of the deflection vector onto the line which passes through the target point and is perpendicular to the line of sight. The unit vector in the direction $QT/\ QT\ $ has components, denoted F_x, F_y, F_z . Explicitly: if the target point Q has coordinates X, Y, Z , then $F_x = \frac{-X \sin \psi}{(X^2 + Y^2)^{1/2}}, \quad F_y = \frac{-Y \sin \psi}{(X^2 + Y^2)^{1/2}},$ $F_z = \cos \psi$
Instrument angle reading ψ	the angle between the line of sight and its projection onto the zero-plane
Line-of-sight vector	vector from the point (0,0,38 cm) (0,0,15 in.) to the target point
Measuring-plane	plane determined by the Z-axis and the line of sight; field measurements are made in this plane
X-axis	line in XY-plane perpendicular to Y-axis; this line is parallel to the elevation axis of an az-el antenna
XY-plane	plane perpendicular to Z-axis, passing through the vertex
Y-axis	line which passes through the paraboloid vertex and points to zenith when elevation angle is 0 deg (to horizon)
Z-axis	axis of symmetry of undeflected paraboloid
Zero-plane	plane perpendicular to Z-axis, passing through the theodolite rotation axes and the datum targets; this is the reference plane for theodolite measurements

$\phi = \psi' - \psi = \text{ROTATION CORRECTION}$
 $R = \text{VERTICAL MOTION}$
 $Q'T = \text{ACTUAL FIELD READING}$
 $QT = \text{CORRECTED FIELD READING}$

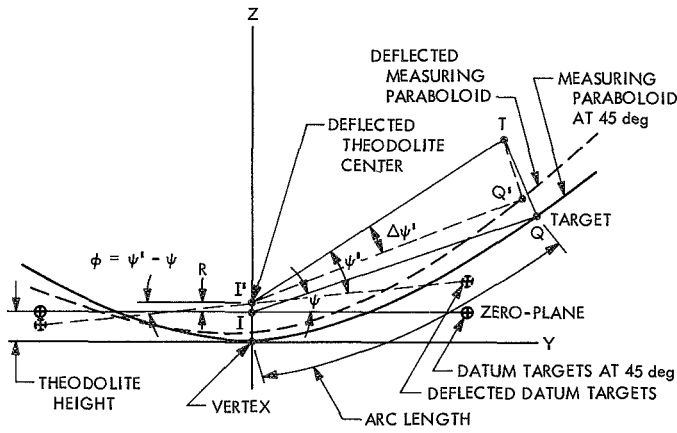


Fig. 1. Field measurement scheme

target is sighted with a theodolite located above the vertex and on the axis of symmetry, with the zero-plane aligned to the four datum reference targets located in the reflector structure. Two of the datum targets are located just above the elevation bearings along the X-axis and the other two are in the wheel girder of the 64-m-diam antenna reflector structure along the Y-axis. The angle ψ between the target and the zero-plane, calculated from the focal length and arc distances of the paraboloid, is used to set the targets of the panels for the "perfect" paraboloid case (Fig. 1).

After the reflector is rotated to another elevation angle, the reading process is repeated for the same target points. There will be a change in the theodolite's angle ψ , denoted as ψ' in Fig. 1. Thus, the apparent deflection of target Q will be a vector $Q'T$, which is normal to the line of sight.

III. Correction to Field Measurement from Motion of the Measuring Paraboloid (Type C)

Due to the change in direction of the gravity load for the different elevation angle positions, the datum targets themselves deflect in a manner (Fig. 1) which effectively:

- (1) Rotates the measuring paraboloid as determined by the datum plane about the X-axis by angle ϕ . Since ϕ is very small, we can make the approximation: $\phi \sim \sin \phi$.
- (2) Offsets the datum plane in the direction of the symmetry axis (Z-axis) by offset R.

It can thus be concluded that the field measurements, at elevation angles other than the perfect paraboloid angle, are made with respect to a rotated and translated coordinate system. Therefore, correction factors to $Q'T$ must be applied to obtain the true field readings (QT) as follows:

$$QT = Q'T + CO + CR$$

where the vector which represents the offset motion,

$$\begin{aligned}
 CO &= (0, 0, R) \cdot \frac{QT}{\|QT\|} \\
 &= R F_z \\
 &= R \cos \psi
 \end{aligned}$$

and the vector which represents the rotation motion,

$$\begin{aligned}
 CR &= (0, -\phi Z, \phi Y) \\
 &= (0, -\phi Z, \phi Y) \cdot \frac{QT}{\|QT\|} \\
 &= -\phi Z F_Y + \phi Y F_Z \\
 &= \phi Y \left\{ \left[\frac{\sin \psi (X^2 + Y^2)^{1/2}}{4F} \right] + \cos \psi \right\}
 \end{aligned}$$

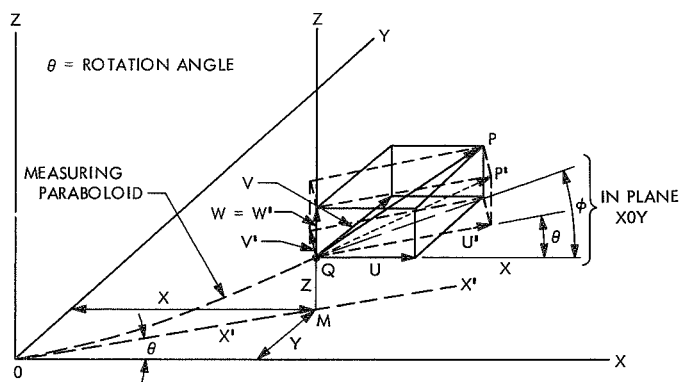
since

$$Z = \frac{(X^2 + Y^2)}{4F}$$

IV. Correction of Field Measurements By Adding Direction Sense from Analytical Structural Analysis (Type C)

Figure 2 shows a typical analytically computed distortion vector QP with its three components U, V, and W in the X, Y, Z coordinate system.

When this vector is field read, the theodolite's field measuring plane $X'OZ$ rotates about the symmetric axis OZ of the measuring paraboloid and picks up the change in angle ψ (Fig. 1) from point Q to P. Since the angle ψ measured by the theodolite to P and P' is essentially the same, the component QP' in the measuring plane is used in the calculations.



To compute \mathbf{QP}' , the distortion vector, \mathbf{QP} in the X, Y, Z coordinate system must be transformed to the measuring plane $X'OZ$ (Appendix A). The resulting components are U' , V' , and W .

Since the magnitude of the distortion vector is very small with respect to distance X' , the two lines of sight may be considered to be parallel for vector transformation calculations in the measuring plane. Of course, an optical micrometer used on the theodolite would conform exactly to the above assumption.

To upgrade the field-measured deflection $\mathbf{Q'T}$, the direction sense from the analytically computed deflection vector $\mathbf{QP'}$ may be combined (Fig. 3). The direction sense of $\mathbf{QP'}$ determined by $\mathbf{U'}$ and \mathbf{W} is combined with the magnitude and direction of the field measurement \mathbf{QT} to determine the magnitude of the theoretically true deflection vector $\mathbf{OP'}$ (Appendix B).

The vector QP' is then normalized, that is, projected to the normal vector at point Q as QN since the magnitude of the normal error is a direct function of the path-length error. A further conversion is made for compatibility to the rms analysis by dividing the normal by the tangent angle to result in a ΔZ deflection input (Appendix C).

There has arisen a problem connected with the accuracy tolerance of the field measurements when $\mathbf{QT} \cdot \mathbf{QP}'$ is near zero. This method requires more careful and accurate field readings at these target points. To eliminate the effect on the accuracy of the final rms number, any target reading for which $(\mathbf{QT} \cdot \mathbf{QP}') < 0.05$ rad is presently deleted from the least squares analysis.

V. Computation of Theoretical Field Measurements from Analytically Computed Distortion Vectors (Type D)

The object of this computation is to simulate the theodolite method of measuring the analytically computed three-component distortion vectors. Then, the resulting rms output from the best-fit program may be compared to the rms output from field measurements without corrections.

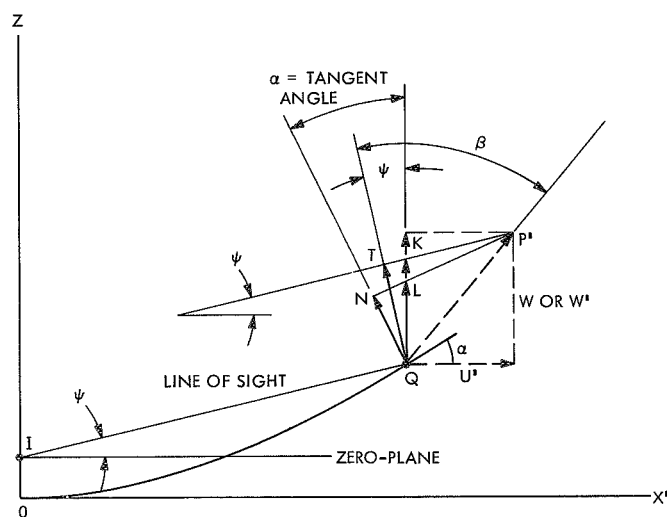
As described in *Section IV* with Figs. 2 and 3, the field measurement vector \mathbf{QT} subtends the “transposed to the measuring plane” vector \mathbf{QP}' . However, now the magnitude as well as the direction of vector \mathbf{QP}' are known. Therefore, vector \mathbf{QT} may be computed and input to the best-fitting program to output the rms figure.

In order to satisfy the data requirements of the rms program coding, the ΔZ component QK of vector QT is used with U and V set equal to 0.

VI. Standard Field and Assumed Normal Direction Computations (Types A and B)

For computing the standard field measurement rms value (Type A), the ΔZ component \mathbf{QK} of the apparent deflection vector \mathbf{QT} normal to the line of sight is computed by dividing by the cosine of the instrument angle ψ (Fig. 4).

Instead of assuming that the deflection vector is normal to the line of sight, one can assume that all deflections are



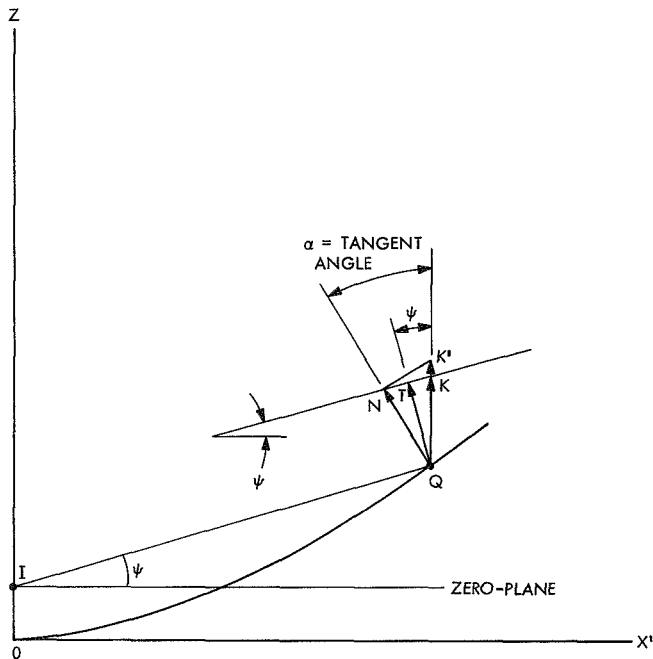


Fig. 4. Field measurement conversions for Type A or B analysis

in the line normal to the surface of the reflector (Type B). Using this assumption, QN equals QT divided by the cosine of $(\alpha - \psi)$ and it follows that QK' , the ΔZ component, is computed by dividing by the cosine of the tangent angle α . This results in the Type B rms answers.

VII. Results and Conclusions as Applied to the 64-m-diam Antenna Data

The different rms analysis methods for field measurements were typed from A to D and applied to the available 64-m-diam antenna data. Types E and F are from analytical computations. Since there was a large change (15,873 to 18,140 kg) (35,000 to 40,000 lb) in the weight of the cassegrain field cone assembly from the monocone to the tricone configuration, the systems were separately evaluated and the answers for reflector structure deflections exclusively are noted in Table 2.

At the present time, results from RF tests are available (Ref. 3) for only the monocone configuration; the answers projected from Table 2, with the addition of the surface panel rms distortions, etc., are overlayed on an upgraded curve from page 17 of Ref. 3 and reproduced here as

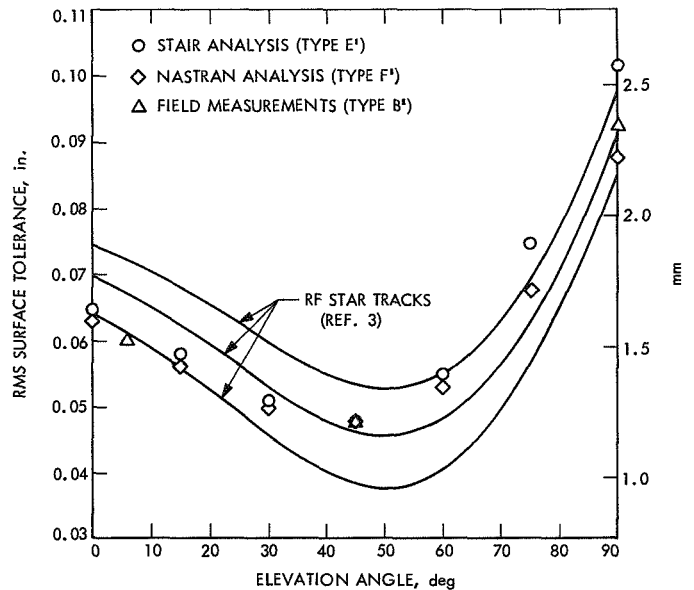


Fig. 5. RMS surface tolerance vs elevation angle (64-m-diam antenna, monocone cassegrain system; zenith attenuation = 0.06 dB)

Fig. 5. The upgrade of the curve is a change in the zenith attenuation from 0.036 to 0.060 dB.

The conclusions that can be made at the present time are:

- (1) The field rms distortion value, using the present theodolite system and Type B or Type (F - D + A) for the 64-m-diam antenna, should be within ± 0.08 mm (0.003 in.) of the true value.
- (2) For a practical answer, the Type B analysis method could be used for the present theodolite system. This is the method used to report the field rms distortion described in Ref. 4.
- (3) The Type C method requires very precise theodolite measurements, a condition marginally accomplished at the present time.
- (4) There is a definite need to improve the accuracy of the field measurement method, if the method is used for larger antennas.
- (5) The NASTRAN computer analysis, used for the structural model plates and rigid jointed bars in the tie truss and the rectangular girder, definitely improves the fit between the analytic results and field measurements.

Table 2. 64-m-diam antenna reflector structure rms distortions after best fit
(focal length change included)^a

Type	RMS analysis method	Horizon look rms value, mm (in.)	Zenith look rms value, mm (in.)
Tricone cassegrain system			
A	^b Standard field measurement	0.91 (0.036)	1.45 (0.057)
B	^b Assumed normal direction field measurement	0.97 (0.038)	1.57 (0.062)
C	^b Field reads + analytical directions (field subroutine)	1.09 (0.043)	1.63 (0.064)
D	Theoretical field reads (ANAFD subroutine)	0.94 (0.037)	1.40 (0.055)
F	Latest NASTRAN analysis 1/2 reflector model + some rigid joints	1.01 (0.040)	1.52 (0.060)
Monocone cassegrain system			
A'	^b Standard field measurement	0.81 (0.032)	1.45 (0.057)
B'	^b Assumed normal direction field measurement	0.86 (0.034)	1.60 (0.063)
E'	STAIR analysis 1/4 reflector model + pin joints	1.01 (0.040)	1.90 (0.075)
F'	Latest NASTRAN analysis 1/2 reflector model + some rigid joints	0.94 (0.037)	1.40 (0.055)
^a Surface panels were set at 45-deg elevatio...			
^b Horizon field measurements were made at 6-deg elevation.			

References

1. Katow, M. S., and Schmele, L. W., "Antenna Structures: Evaluation Techniques of Reflector Distortions," in *Supporting Research and Advanced Development*, Space Programs Summary 37-40, Vol. IV, pp. 176-184. Jet Propulsion Laboratory, Pasadena, Calif., Aug. 31, 1966.
2. Levy, R., "A Theoretical Consideration in the Comparison of Measured and Computed Reflector Distortions," in *The Deep Space Network*, Space Programs Summary 37-61, Vol. II, pp. 102-107. Jet Propulsion Laboratory, Pasadena, Calif., Jan. 31, 1970.
3. Bathker, D. A., *Radio Frequency Performance of a 210-Ft. Ground Antenna: X-Band*, Technical Report 32-1417. Jet Propulsion Laboratory, Pasadena, Calif., Dec. 15, 1969.
4. Katow, M. S., "Techniques Used to Evaluate the Performance of the NASA/JPL 210-Foot Reflector Structure Under Environmental Loads," in *Structures Technology for Large Radio and Radar Telescope Systems*. Edited by J. W. Mar and H. Liebowitz. The M.I.T. Press, Cambridge, Mass., 1969.

Appendix A

Coordinate Transformation of the Deflection Vectors to the Theodolite's Measuring Plane

With the measuring plane restricted to rotation θ only about axis OZ (Fig. 2), only X and Y components of deflection vectors are transformed.

Based on the basic coordinate system,

$$\left. \begin{aligned} U &= r \cos \phi \\ V &= r \sin \phi \end{aligned} \right\} \quad (A-1)$$

where

$$r = (U^2 + V^2)^{1/2}$$

Transformed to the measuring plane,

$$\left. \begin{aligned} U'' &= r \cos(\phi - \theta) = r \cos \phi \cos \theta + r \sin \phi \sin \theta \\ V'' &= r \sin(\phi - \theta) = r \sin \phi \cos \theta - r \cos \phi \sin \theta \end{aligned} \right\} \quad (A-2)$$

Substituting Eq. (A-1) into Eq. (A-2) results in

$$\left. \begin{aligned} U'' &= U \cos \theta + V \sin \theta \\ V'' &= V \cos \theta - U \sin \theta \\ W' &= W \end{aligned} \right\} \quad (A-3)$$

Also, for target point Q , if Q has components (X_q, Y_q, Z_q) ,

$$X'_q = (X_q^2 + Y_q^2)^{1/2}$$

$$Y'_q = 0$$

$$Z'_q = Z_q$$

$$\theta = \tan^{-1} \frac{Y}{X}$$

Also, in this coordinate system, the vector $QT/\|QT\|$ has components (F'_x, F'_y, F'_z) , where

$$F'_x = \sin \psi$$

$$F'_y = 0$$

$$F'_z = \cos \psi$$

Appendix B

Resolution of the Field Measurement Vectors with the Analytically Computed Directions

The magnitude of the theoretical deflection vector \mathbf{QP}' in Fig. 3 is computed as follows.

If the direction vectors of \mathbf{QP}' are $(\mathbf{U}', \mathbf{W}')$, then from

$$S = [(\mathbf{U}')^2 + (\mathbf{W}')^2]^{1/2}$$

vector

$$\mathbf{QP}' = \|\mathbf{QP}\| \left(\frac{\mathbf{U}'}{S}, \frac{\mathbf{W}'}{S} \right) = \|\mathbf{QP}\| (\mathbf{U}'', \mathbf{W}'')$$

where \mathbf{U}'' and \mathbf{W}'' are unit vector components of \mathbf{QP}' . If the unit vector of \mathbf{QT} has components (F'_x, F'_z) , the circle product of \mathbf{QP}' and the unit vector of \mathbf{QT} equal \mathbf{QT} when angle $\mathbf{QTP}' = 90$ deg (because we assume that the two lines of sight are parallel) or

$$(F'_x, F'_z) \cdot \|\mathbf{QP}\| (\mathbf{U}'', \mathbf{W}'') = \|\mathbf{QT}\|$$

Transposing,

$$\|\mathbf{QP}\| = \frac{\|\mathbf{QT}\|}{F'_x \mathbf{U}'' + F'_z \mathbf{W}''} \quad (\text{B-1})$$

To then compute for the magnitude of the normal error \mathbf{QN} , when angle $\mathbf{QNP} = 90$ deg:

$$\|\mathbf{QN}\| = \text{projection of } \mathbf{QP}' \text{ onto the unit normal}$$

When N_x and N_z are unit vector components of the normal,

$$\|\mathbf{QN}\| = (N_x, N_z) \cdot \|\mathbf{QP}\| (\mathbf{U}'', \mathbf{W}'') \quad (\text{B-2})$$

Substituting Eq. (B-1) into Eq. (B-2),

$$\|\mathbf{QN}\| = \frac{\|\mathbf{QT}\| (N_x \mathbf{U}'' + N_z \mathbf{W}'')}{(F'_x \mathbf{U}'' + F'_z \mathbf{W}'')}$$

To establish compatibility with the rms analysis, the normal distortion $\|\mathbf{QN}\|$ is converted to a ΔZ by

$$\mathbf{QL} = \frac{\|\mathbf{QN}\|}{\cos \psi} = \frac{\|\mathbf{QN}\|}{N_z}$$

Appendix C

Resolution in the Measuring Plane to Simulate Field Measurements

In Fig. 3, the circle product of the two vectors

which is equal to

$$\mathbf{QT} \text{ and } \mathbf{QP}' = \|\mathbf{QT}\| \times \|\mathbf{QP}\| \times \cos \theta$$

$$\|\mathbf{Q}\| = \mathbf{U}' \mathbf{U}'' + \mathbf{W} \mathbf{W}'$$

If vector \mathbf{QT}' is a unit vector in the direction of \mathbf{QT} , then

where

$$\|\mathbf{QT}\| = 1 \times \|\mathbf{QP}\| \cos \theta$$

$$\mathbf{U}'' = -1 \times \sin \psi$$

$$\mathbf{W}' = 1 \times \cos \psi$$

SFOF Cable Control

R. A. Paine

SFOF/GCF Development Section

Frequent reconfiguration of the Space Flight Operations Facility to meet changing mission requirements necessitates complex cable changes throughout the building. This article summarizes a detailed well-defined cabling plan which maintains discipline in the installation and removal of cabling.

I. Introduction

The SFOF experiences frequent reconfigurations both in its physical layout and functional capabilities. These changes are necessary in order to meet new requirements placed on it by the DSN and unmanned spaceflight programs. Without a detailed well-defined cabling plan, there would be problems with the installation of new cables, rerouting of existing cables, and disposition of unused cables. Such conditions would result in overly congested cable drops, cable ducts, and unruly cable lays.

This paper discusses the procedures developed to maintain cognizance and control of the cabling in the SFOF.

II. Establishing Cable Routes

There are cable drops and cable ducts that interconnect the floors of the building. The cable drops are cutouts in the floor that give access to the cable ducts, which are vertical enclosures between floors. The cable drops and cable ducts were located, identified and documented. Figure 1 is a typical example of the documentation of the cable drops and cable ducts for the four

floors. With the documentation of the cable drops and cable ducts, the vertical cable routes may be determined.

The horizontal cable runs, which are under computer flooring, may be determined from the same set of draw-

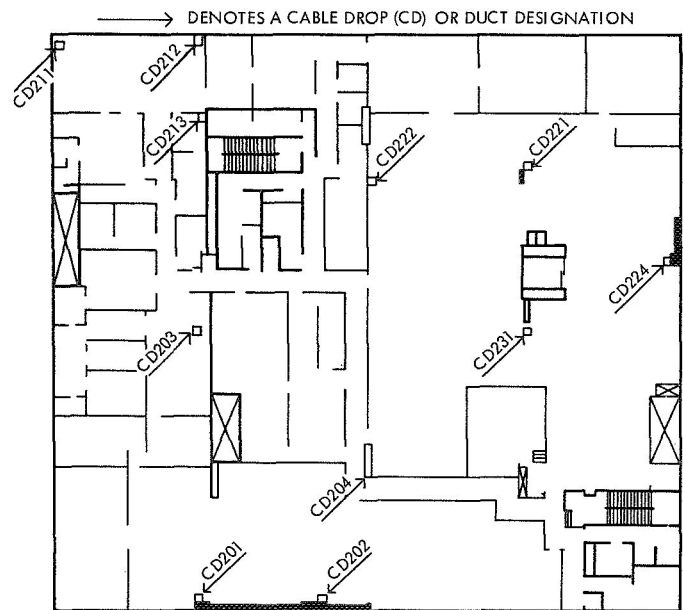


Fig. 1. Cable drops and cable ducts

- REPRESENTS INTERCONNECTING CABLE FOR LINE PRINTERS 1443 AND 2501.
CABLES W20100 THROUGH W20106.
- - - REPRESENTS INTERCONNECTING CABLE FOR 2260 CRT SWITCHER.
CABLES W20130 THROUGH W20140.
- REPRESENTS INTERCONNECTING CABLE FOR FORMAT REQUEST UNIT.
CABLES W20165 THROUGH W20169.

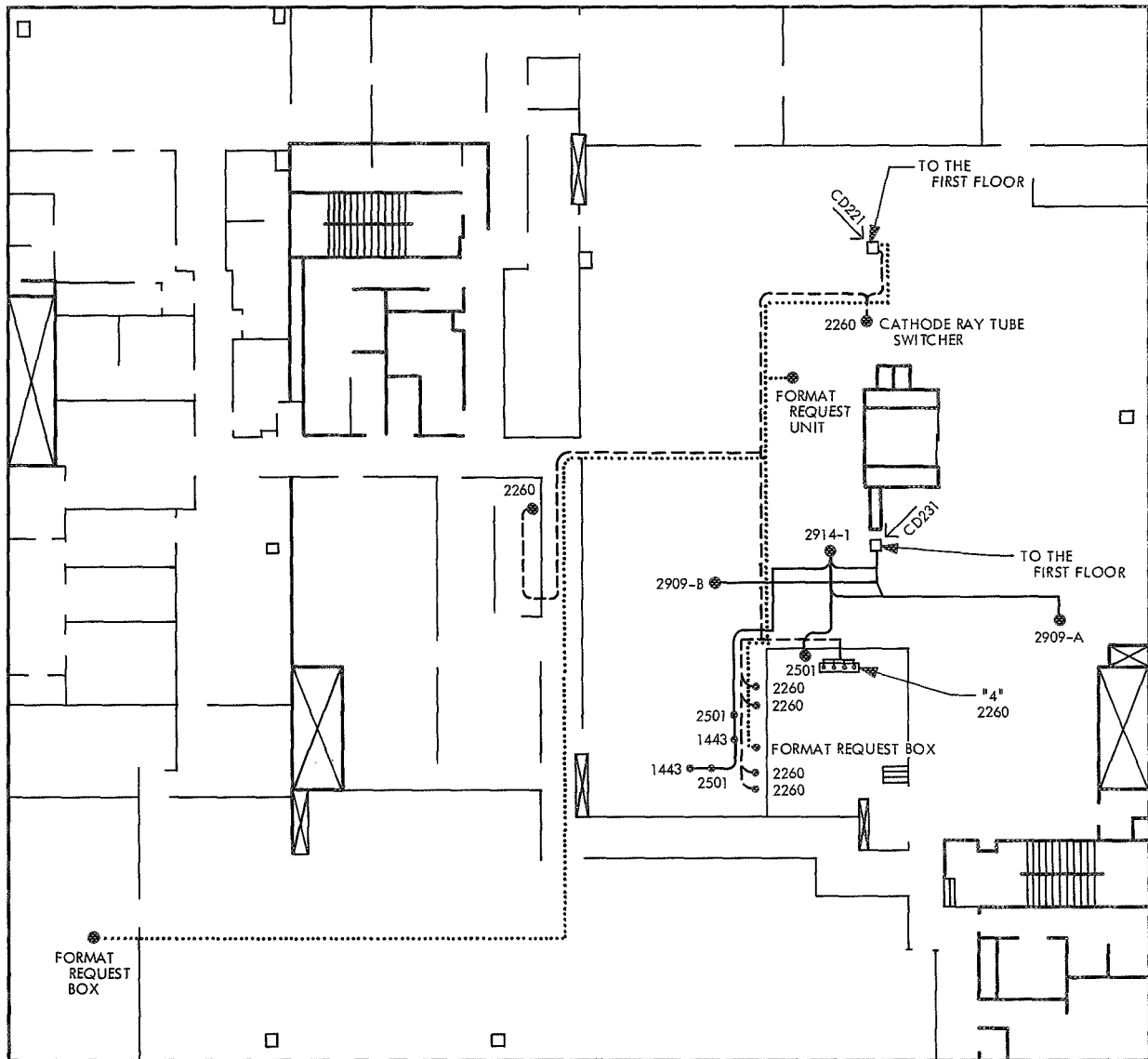


Fig. 2. Cable routing

ings (Fig. 1). The drawings are to scale, and the architectural configuration and the equipment layouts of the various floors are maintained on this set of drawings. Once the equipment layouts are complete for any given area, the cable routing may be determined. The cable routing will then be documented. Figure 2 is typical of this type of documentation. This, then, shall be the way in which the cables are installed. This method eliminates

the congestion in the cable drops, cable ducts, and horizontal cable lays.

When a system is removed or changed, the cable documentation shall be revised to indicate the modifications or deletions. This makes it possible to control the cable density in the cable drops, cable ducts, and cable lays.

III. Standardization of Cables

Figure 3 is representative of a standard cable drawing. As new cable requirements arise, an effort is made to use a cable drawing already in existence. This reduces the number of different types of connectors and wires in a system and also results in a cost savings. In the electromechanical design phase of a system, every effort is made to incorporate the standard cables by selecting interface connectors that will mate with a standard cable and still fulfill the interconnecting requirements.

IV. Cable Inventory

With the large quantity of cables that are used in the facility and the fact that cables normally do not wear out, it is advantageous to reuse the cables. This is accomplished by maintaining a cable inventory.

The cables are identified with a JPL part number. This part number consists of two parts: the basic drawing number and the number indicating the length of the cable in feet. The cable will have its part number attached to it by use of a self-adhering label.

Having identified the cables and documented their routing, maintaining an "in use" status on the cables can be accomplished. As a data processing system is revised or removed, the cables taken out of service may then be stored for future use.

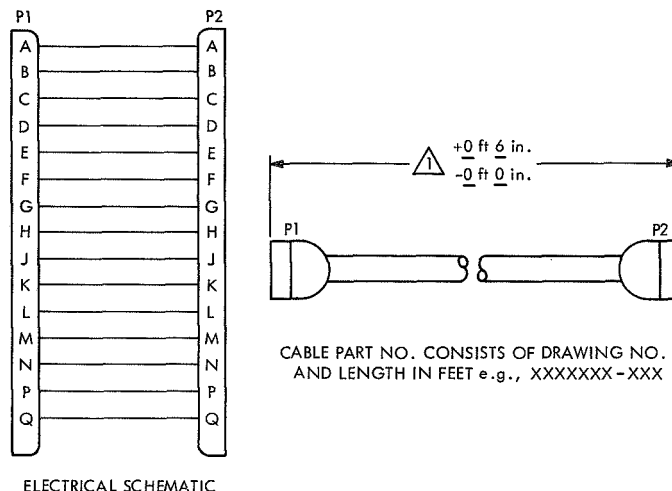


Fig. 3. Standard cable

V. Conclusion

Because of the complexity of the SFOF and the constant upgrading of its capabilities, it was important that a system for maintaining discipline in the installation and removal of the cabling be developed.

With the ability to predetermine cable routes, we can define the length of a cable, limit the density of cable drops and cable ducts, and using the standard cable inventory, determine if a cable is available, or if one will have to be made.

Diagnostics for the SFOF Mark IIIA Central Processing System: Pre-Mission CPS/Facility Checkout Procedures

R. A. Wells

SFOF/GCF Development Section

Prior to critical periods of mission processing, comprehensive diagnostic tests of the SFOF central processing system are conducted to detect and correct equipment deficiencies before they can affect the continuity of spaceflight data processing. The article describes the test methods employed in their relationships to the current dual IBM 360/75 computer configuration. By preparing a test "script" in advance, the hardware checkout process is formalized and the results documented.

I. Introduction

Prior to periods of critical mission data processing, it is worthwhile to conduct a comprehensive series of diagnostic tests to isolate and remedy equipment malfunctions. These diagnostics provide standard criteria and uniform methods for verifying the technical conditions of all critical computer-related hardware in the SFOF central processing system (CPS). In the past, such tests have been performed immediately prior to most launch, midcourse and encounter operations for *Mariner*, *Surveyor*, *Pioneer* and *Lunar Orbiter* missions. They are also planned in support of the *Mariner* Mars 1971 mission.

It has been the custom to prepare a detailed script for each checkout to reflect the mission-committed hardware configuration, the test durations and the procedural sequences. When completed, this itemized record can be used as the basis for system buyoff and a formal pre-mission transfer to the responsible operational organization.

The first two articles in this series (Refs. 1 and 2) have described the various types of diagnostic routines which presently exist for the IBM 360/75-related portion of the CPS. A full set of compatible diagnostics are currently operable under the diagnostic monitor (DIAMON) which supervises their execution under the overall control of the JPL operating system (JPLOS).

II. Objectives

CPS diagnostic checkouts serve the following purposes:

- (1) Verifying performance of newly installed equipment.
- (2) Certifying the condition of previously installed equipment.
- (3) Exercising hardware elements individually to expose suspected faults.

- (4) Training personnel in a "hands-on" environment.
- (5) Resolving many uncertainties concerning alleged hardware-versus-software problems.
- (6) Uncovering marginal performance.
- (7) Correcting system deficiencies.
- (8) Formalizing hardware acceptance.

III. Mark IIIA CPS Configuration

Figure 1 identifies the 360/75-related elements of the Mark IIIA CPS as they exist in SFOF at the present time (Ref. 3). Not shown are numerous user station devices which are installed in the various mission support areas, the DSN monitor area, and the DSN operations control area on the first floor of the SFOF. In substance, the two 360/75 central processing units (CPUs) may be considered identical and interchangeable, with input/output lines and user terminal and display (UTD) devices switchable between the two. Switching control is vested with the computer chief (or system controller) in the data processing control center (DPCC). Transfer is accomplished through two DPCC consoles: (1) a user device switching console, and (2) a GCF high-speed data/wideband data (HSD/WBD) switching console. DPCC personnel are also provided with monitoring and entry devices such as display stations, line printers, and a card reader.

Diagnostic testing involves all of the equipment elements shown in Fig. 1 plus:

- (1) The communications processor (CP) teletype (TTY) input/output (I/O) interface with GCF.
- (2) The HSD I/O interface with GCF.
- (3) The WBD input interface with GCF.
- (4) The Univac 1108A and 1108B I/O interface with the scientific computing facility (SCF).
- (5) The Control Data 3100 output interface for UTD DTV displays.
- (6) The mission display board (MDB) interface to the UTD Vigicon projectors.
- (7) The SFOF time reference interface for GMT displays and CPU timers.
- (8) Numerous 360/75-driven UTD user devices throughout the SFOF.

There are also 360/75-to-360/75 channels, not presently utilized, and additional peripherals for administrative computing section support. These are not part of the committed mission configuration and thus are not discussed here.

IV. Diagnostic Checkout Procedures

Prior to each checkout period, a plan or script is prepared to assure that testing will proceed in an orderly manner, will cover all committed equipment, and will be properly documented. The script:

- (1) Formalizes the sequence of testing.
- (2) Gives the required calls (2260 display station requests) for manual entry by the operator.
- (3) Specifies a suggested duration for each of the tests (number of data blocks, characters, transfers, etc.).
- (4) Fixes optimal data patterns.
- (5) Indicates the expected message responses and error printouts.
- (6) Identifies variations, or options, for each test.
- (7) Provides a checkoff column for logging test results.
- (8) Acts as a training aid for participating personnel.
- (9) Is a debriefing medium for post-test critiques.
- (10) Provides a basis for system buyoff and transfer.

At the outset of testing, the SFOF time reference and internal CPU timer registers are usually checked first as they are fundamental to all subsequent system testing. Since the test director usually operates from the data processing control center (Fig. 1), DPCC devices are generally tested next. Following this, other diagnostics may be initiated in parallel for concurrent execution. (The

present diagnostic implementation requires total dedication of the system elements being tested).

All DIAMON-related diagnostics are resident under JPLOS and are available for use by SFOF operations personnel as required.

V. Conclusion

In brief, these scheduled pre-mission checkouts are conducted periodically from published scripts. Diagnostic

requests are entered via 2260¹ display station keyboards, DIAMON messages are displayed on 2260 CRTs, and a hard-copy log is provided on the designated line printer(s).

Full-scale tests, such as described in this article, are scheduled upon request to assure optimum system performance in support of JPL's mission support commitments.

¹Also known as manual entry devices (MED).

References

1. Wells, R. A., "Diagnostics for the SFOF Mark IIIA Central Processing System: Standalone Acceptance and Maintenance Routines," in *The Deep Space Network*, Space Programs Summary 37-65, Vol. II, pp. 97-99. Jet Propulsion Laboratory, Pasadena, Calif., Sept. 30, 1970.
2. Wells, R. A., "Diagnostics for the SFOF Mark IIIA Central Processing System: 360/75 On-Line Test Routines," in *The Deep Space Network*, Technical Report 32-1526, Vol. I, pp. 103-106. Jet Propulsion Laboratory, Pasadena, Calif., Feb. 15, 1971.
3. Stiver, R. A., "Mark IIIA IBM 360/75 Computer Configuration," in *The Deep Space Network*, Space Programs Summary 37-66, Vol. II, pp. 71-75. Jet Propulsion Laboratory, Pasadena, Calif., Nov. 30, 1970.

GCF Reconfiguration of the Goldstone DSCC Microwave Terminals for 50-kbit Data Transmission

R. G. Hanselman
SFOF/GCF Development Section

This article covers the reconfiguration of the Goldstone Deep Space Communications Complex area microwave terminals at the Mars Deep Space Station and the Goldstone area communications terminal for the transmission of dual 50-kbit digital data streams between the two locations.

I. Introduction

This article describes the reconfiguration of the Goldstone DSCC microwave terminals required for the transmission of dual 50-kbit/s digital data streams between DSS 14 and the Goldstone area comm terminal (ACT) located adjacent to DSS 12. This article is an amplification of two earlier articles (Refs. 1 and 2).

Requirements for a 50-kbit/s data transmission capability of the GCF were derived from the GCF functional design for 1971–1972 (Ref. 3). The GCF functional design specifies two 50-kbit/s data streams between the SFOF and DSS 14, one stream being a backup to the other.

II. Background

The current microwave transmission capability between DSS 14 and the Goldstone area comm terminal is entirely JPL owned and operated. That portion of the overall DSS 14-to-SFOF transmission capability existing between

the Goldstone area comm terminal and the SFOF is owned and maintained by Western Union and leased to JPL. The problem of how to best use the available microwave baseband spectrum between DSS 14 and the area comm terminal for dual 50-kbit streams was thus a portion of the development effort.

There are five duplex microwave channels between DSS 14 and the area comm terminal. Each of these channels has a 10-MHz baseband bandwidth. The equipment manufactured by Collins Radio Corp. of Dallas, Texas, is an off-the-shelf system and is designed primarily for intercity telephony or broadcast quality television. This particular group of equipment has been installed at the Goldstone DSCC since 1966 and is used for numerous functions such as:

- (1) Multiple-mission support, wherein the DSS 14 antenna is used to track a spacecraft and the resultant DSS 14 data is forwarded to data reduction equipment at another station via the microwave channel.

- (2) GCF voice circuits between the two stations.
- (3) GCF teletype circuits and high-speed data circuits between the two stations.

Included as a portion of each terminal is a standard frequency division multiplex (also manufactured by Collins Radio). Prior to the requirement of 50-kbit data between DSS 14 and the ACT, this multiplex equipment was used to pass several operational voice channels. The GCF recognized the requirement to transmit the following information between the two stations, utilizing as few microwave channels as possible and still be guaranteed of high reliability:

- 9 Channels of voice
- 2 Channels of 4800-bit/s high-speed data
- 6 Channels of 75-bit/s teletype
- 2 Channels of 50-kbit/s wideband data
- 1 Channel of 1 pulse/s intersite timing

The frequency division multiplex (Collins MX-106) was originally purchased as a basic 60-channel (voice) system, wired for 24 channels and equipped with 12 channels. In the world of commercial communications, 12 voice channels can be multiplexed into a 48-kHz-wide signal, occupying the basic spectrum of 60 to 108 kHz. Channel modems perform the basic modulation of voice signals in the 0 to 4 kHz portion of the spectrum to 60 to 108 kHz portion of the spectrum. Four kHz is allocated for each of these modems, the twelve channels thus forming a "group" 48 kHz wide. As earlier stated, only one group initially existed (i.e., 12 voice channels) but the wiring, module space, power, etc., provided for future expansion of the multiplex.

The General Electric TDM420 modems used to translate the GCF 50-kbit conditioned signal to that portion of the baseband spectrum normally occupied by a group of 12 voice channels, generate and accept a vestigial sideband signal occupying 60 to 108 kHz in the baseband spectrum.

III. Implementation

Initially it was planned to place the vestigial sideband signal directly on the microwave baseband, thus dedi-

cating two 10-MHz-broad channels for carrying the two 48-kHz 50-kbit signals. Further analysis led to the conclusion that the available microwave channels would best be utilized by concentrating as many GCF signals onto one broadbanded channel as practicable.

Investigation of the available hardware at each terminal showed the following:

- (1) An existing baseband combiner which could automatically and instantly switch between two microwave receivers.
- (2) A radar multiplex which could be used to pass fast risetime pulses in the 4 to 6.5 MHz portion of the available baseband spectrum (such as 1-pulse/s timing).
- (3) Resistive splitters allowing a single source to drive two microwave transmitters simultaneously.
- (4) Available carrier source already installed in the MX-106 multiplex.

It was thus determined that the most economical and reliable usage of the microwave would be to stack all known circuits onto two microwave channels and arrange the receivers at each end to feed the GCF equipment via the baseband and combiner mentioned earlier. The net result of the diversity arrangement is one 10-MHz full duplex (both directions simultaneously) diversity video channel carrying the following signals:

Secondary 50 kbit	60 to 108 kHz
12 (each) voice circuits ¹	408 to 456 kHz
Prime 50 kbit	456 to 504 kHz
Continuity pilot carrier	6.2 MHz
Time pulse and time pulse verification	4 to 6.5 MHz

To obtain the additional 48-kHz-wide group for the second 50-kbit channel it was only necessary to purchase two each group modulators and demodulators and plug them into prewired mounting positions at each station.

Figure 1 shows the multiplex and diversity arrangement at both DSS 14 and the ACT. Both stations have

¹Each voice circuit can pass either voice, 4800-bps high-speed data, or as many as 18 teletypewriter circuits.

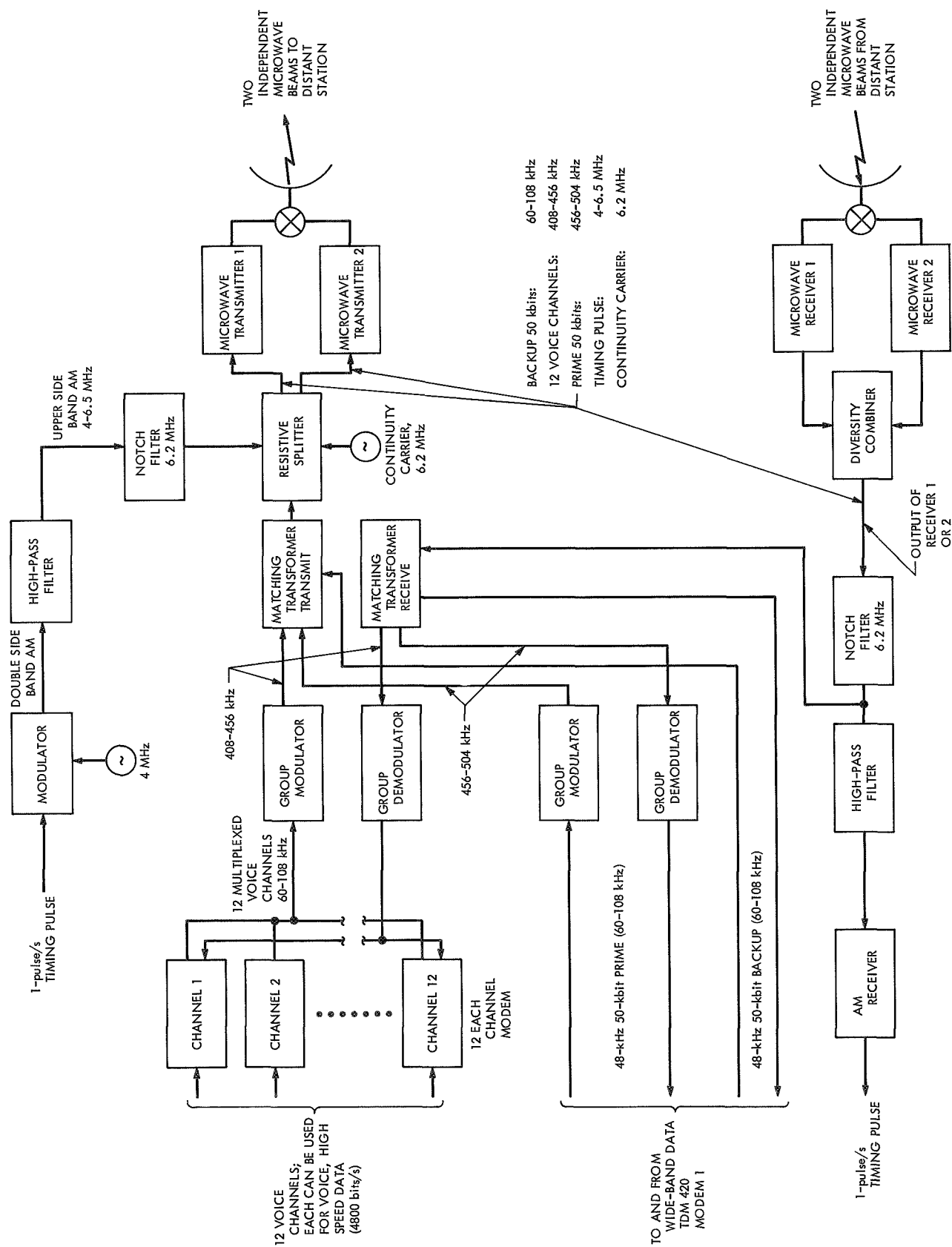


Fig. 1. Microwave terminal configuration block diagram, DSS 14 and area comm terminal

an identical arrangement, the only difference being the operating frequency of the microwave transmitters and receivers.

IV. Conclusion

In response to the requirements put forth in the 1971-1972 GCF functional design for the 1971-1972 wideband

system, certain rearrangements were made to the existing area microwave between DSS 14 and the ACT to take advantage of the wideband characteristics of the microwave channels. Signals from all GCF systems—voice, high speed, teletype, and wideband—may now be placed on a single diversity channel. Additionally, the GCF has ample bandwidth on this one channel for future expansion.

References

1. McClure, J. P., "GCF Wideband Digital Data System," in *The Deep Space Network*, Space Programs Summary 37-65, Vol. II, pp. 107-110. Jet Propulsion Laboratory, Pasadena, Calif., Sept. 30, 1970.
2. Hanselman, R., "Wideband Digital Data System Terminal Configuration," in *The Deep Space Network*, Space Programs Summary 37-66, Vol. II, pp. 107-110. Jet Propulsion Laboratory, Pasadena, Calif., Nov. 30, 1970.
3. McClure, J. P., "Ground Communications Facility Functional Design for 1971-1972," in *The Deep Space Network*, Space Programs Summary 37-66, Vol. II, pp. 99-102. Jet Propulsion Laboratory, Pasadena, Calif., Nov. 30, 1970.

Coherent Reference Generator for DSN Mark III Data System

R. B. Crow

RF Systems Development Section

A new frequency generator/distribution subsystem is being developed to meet the increasing complexity of the Deep Space Network Mark III data system. The coherent reference generator is an assembly that will accept the primary frequency standard from the hydrogen maser (or possible secondary standard from the rubidium, cesium, or remote standards) and furnish required reference frequencies for a deep space station.

A new frequency generator/distribution subsystem is being developed to meet the increasing complexity of the DSN Mark III data system.

The coherent reference generator is an assembly that will accept the primary frequency standard from the hydrogen maser (or possible secondary standard from the rubidium, cesium, or remote standards) and furnish the required reference frequencies for:

- (1) Receiver assembly (9 each).
- (2) Programmed exciter assembly (3 each).
- (3) Subcarrier demodulator assembly (8 each).
- (4) Ranging demodulator assembly (2 each).
- (5) Mark II frequency/timing system (1 each).

The basic design goals that have been stressed are (1) performance, (2) economy, (3) computer control/monitoring, and (4) minimum physical size.

A simplified block diagram of the Mark III frequency distribution and the coherent reference generator is shown in Fig. 1. All the inputs to the coherent reference generator will be simultaneously switched when a change in the input frequency standard source is made.

A simplified block diagram of the coherent reference generator is shown in Fig. 2. Note that the 1-MHz reference output will have a fail/safe power supply so that there will be no interruption to the station timing system should primary power fail.

A list of the preliminary detailed design specifications for the coherent reference generator is shown in Table 1.

Table 1. Coherent reference generator performance specifications^a

Parameter	Source of requirement	Requirement	Proposed specification														
Phase stability	DSN Mark III data system development plan [Document 803-1, Vol. III, p. 11.C (1)]	Charged particle calibration = 0.2 m; variation in electrical phase path = 0.2 m															
	Phase budget for Mark III receiver/exciter (based on differenced range versus integrated doppler technique)	Receiver $\leq \pm 0.06$ m which implies ± 330 deg at S-band	Receiver reference (0.1, 1, 10, 10.1, 45 MHz) = ± 33 deg at S-band														
		Exciter $\leq \pm 0.08$ m which implies ± 440 deg at S-band	Exciter reference (50 MHz) = ± 44 deg at S-band														
Power output	Accepted DSIF reference level		Range = +10 to +13 dBm; stability $\leq \pm 0.5$ db														
^b VSWR _{in}	Engineering judgment		1.1:1														
^b VSWR _{out}	Engineering judgment		1.5:1														
Harmonic distortion	Engineering judgment		$\leq 5\%$														
Non-harmonically related spurious output	Engineering judgment		Minimum of 70 dB below nominal output														
Isolation output to output	Engineering judgment		<table><tr><th>Frequency, MHz</th><th>Isolation, dB</th></tr><tr><td>0.1</td><td>≥ 120</td></tr><tr><td>1</td><td>≥ 120</td></tr><tr><td>5</td><td>≥ 120</td></tr><tr><td>10</td><td>≥ 110</td></tr><tr><td>45</td><td>≥ 90</td></tr><tr><td>100</td><td>≥ 70</td></tr></table>	Frequency, MHz	Isolation, dB	0.1	≥ 120	1	≥ 120	5	≥ 120	10	≥ 110	45	≥ 90	100	≥ 70
Frequency, MHz	Isolation, dB																
0.1	≥ 120																
1	≥ 120																
5	≥ 120																
10	≥ 110																
45	≥ 90																
100	≥ 70																

^aEnvironment: time = 12 h; temperature = control room temperature $\pm 217^{\circ}\text{C}$ ($\pm 5^{\circ}\text{F}$); power supply variations of 3%; elastic survival for temperature of 0 \rightarrow 50°C; dc power variation of $\pm 5\%$.

^bVSWR = voltage standing-wave ratio.

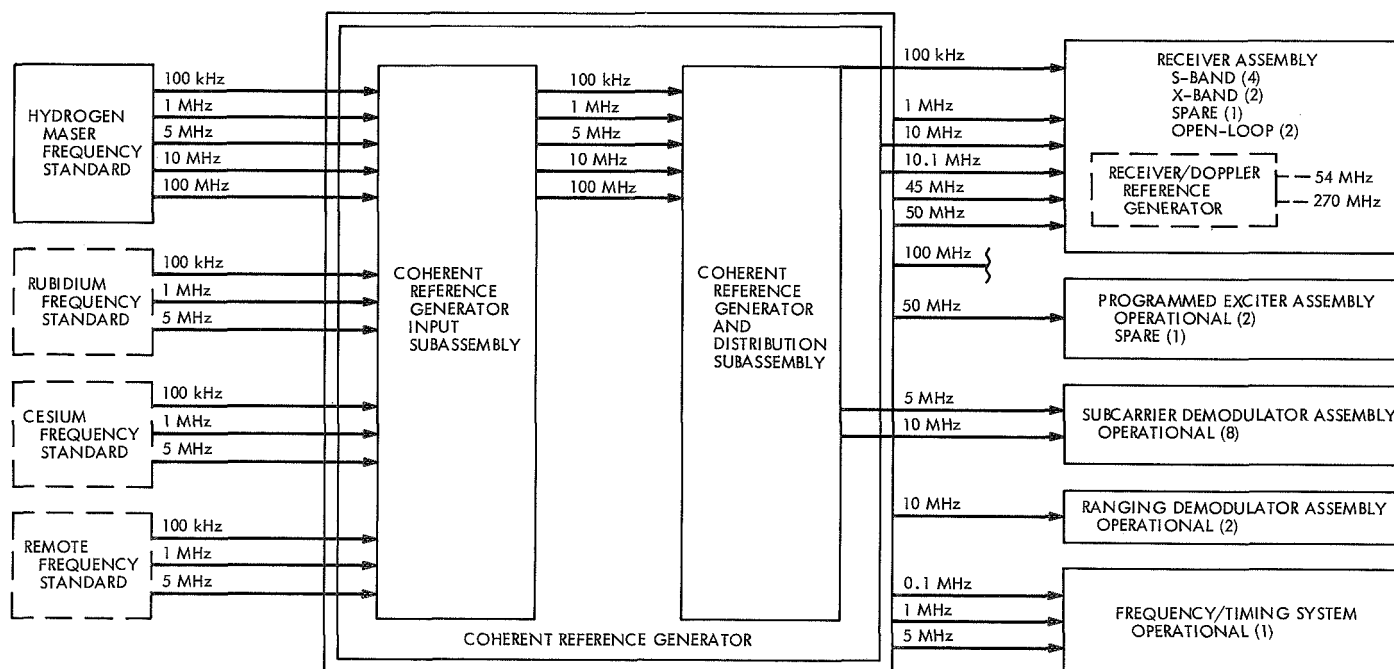


Fig. 1. Simplified block diagram of Mark III frequency distribution and coherent reference generator

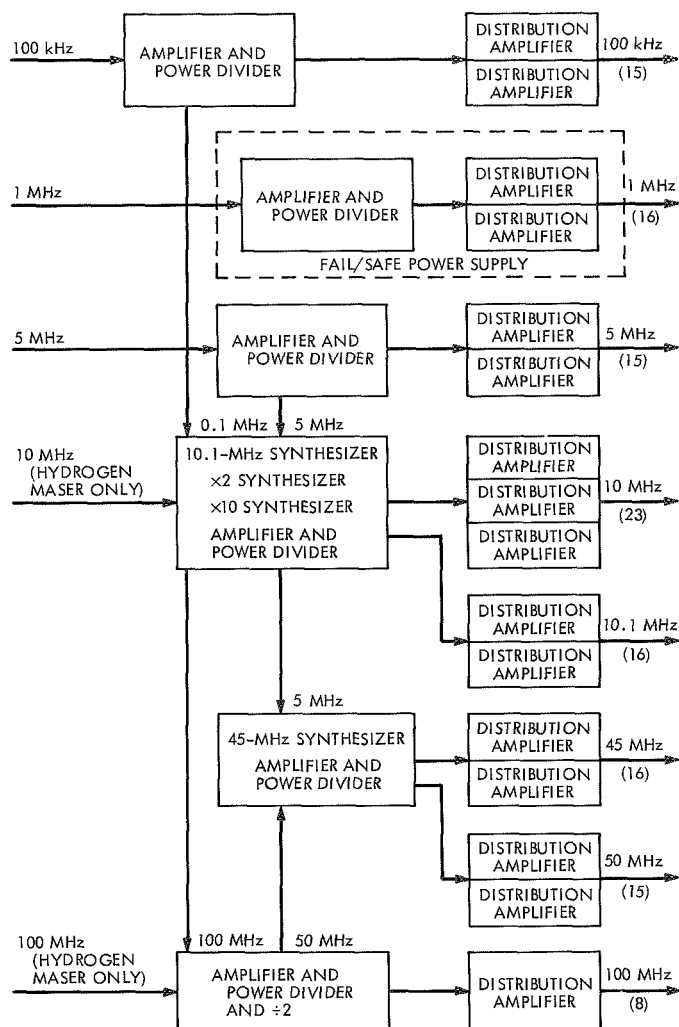


Fig. 2. Simplified block diagram of coherent reference generator

These specifications were developed to assure that the frequency distribution and synthesis of the coherent reference generator offer reference frequencies that allow the receiver/exciter subsystem to meet design requirements as dictated in the Mark III Data System Development Plan (Document 803-1, Vol. III).

A typical distribution amplifier that will be a basic building block in the coherent reference generator is shown in Fig. 3. Broadband circuits with internal feedback will be used to meet the phase and amplitude stability requirement. No intentional filtering or automatic gain control will be attempted in the distribution amplifier since these characteristics have already been defined either in the frequency standard or the reference generator.

Preliminary design of the coherent reference generator was started in the middle of January 1971. Present plans call for an engineering model to be completed in fiscal 1972.

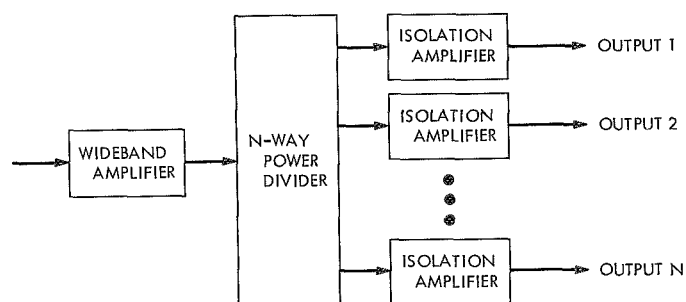


Fig. 3. Simplified block diagram of coherent reference generator distribution amplifier

Tracking and Data System Near-Earth Telemetry Automatic Switching Unit

L. Butcher
DSIF Operations Section

A hardware-software system is described that is capable of selecting the one from among as many as six incoming data streams which is best by an externally programmed criterion and switching it automatically to the Deep Space Instrumentation Facility (DSIF) Telemetry System. The system has been implemented at the Cape Kennedy Compatibility Test Station to provide the best spacecraft telemetry stream to the DSIF Telemetry System during the near-earth phase of a tracking mission, when as many as six Air Force Eastern Test Range stations are receiving spacecraft telemetry.

I. Introduction

The requirement of the Tracking and Data System for near-earth telemetry support is an important function in the unmanned spacecraft launch support. The requirement is placed upon the Air Force Eastern Test Range and Kennedy Space Center stations to provide spacecraft telemetry in a serial bit stream to DSS 71 after launch until DSN acquisition. The spacecraft telemetry serial bit stream is received at DSS 71 via 202 data modems. It is processed at DSS 71 by the DSIF Telemetry System and transmitted to the SFOF in real-time. There are as many as six near-earth stations receiving and, subsequently, transmitting telemetry data to DSS 71 during the launch phase. The automatic switching unit at DSS 71 provides

a means of selecting the best available data and performs automatic switching to select the station data source to output the data to the DSIF Telemetry System for processing. This is to be accomplished with a minimum loss of spacecraft data during the time of launch until loss of signal by the last near-earth supporting station. This data is to be processed at DSS 71 and transmitted to the SFOF in real-time via the GCF high-speed data system.

II. Technical Description

The automatic switching unit consists of an XDS CF-16 system controller and an interface buffer implemented with JPL Hi-Rel digital modules as utilized in the DSIF

Telemetry System. The CF-16 system controller is a packaged unit consisting of digital logic and stored programs with an 8k core memory. Peripheral equipment includes an ASR-33 teletype with paper tape reader and punch for input/output, and an FR-1200 magnetic tape recorder for recording all incoming data lines. A block diagram of the automatic switching unit is shown in Fig. 1.

The interface buffer logic consists of 15 digital Hi-Rel circuit modules mounted in a single chassis for input, output, and data switching to the CF-16 system controller. The telemetry data input from the 202 data modems is ± 6 -V amplitude. All six inputs are input to negative-to-positive modules for uni-polar output clamped at 5 V. All six lines are then fed to the CF-16 controller to be used for frame sync and line selection when in the automatic mode. Each input data line also is routed through another negative-to-positive circuit to the line selection logic, which has the capacity of selecting one data line whose data is sent to the DSIF Telemetry System for processing.

The data selection can be achieved by either manual or automatic modes. The manual or automatic mode is selectable by a toggle switch on the front panel. When the manual mode is selected, it enables the use of six front panel pushbutton switches to select the desired data source. When the automatic mode is selected, the CF-16 is utilized under program control to select the data source.

The output data is also present on an interrupt line and is used for bit sync detection.

A timing signal of 1 kHz is supplied to the CF-16 on an interrupt line. A lift-off pulse or first motion pulse is supplied to the CF-16 to provide time from lift-off for the automatic operation.

III. Functional Description

As presently implemented, the system has a capability of monitoring six input data lines and selecting one line for output data. Criteria for the selection of a data line are data quality, priority of the data, and tracking predict times for each data source.

Data quality is determined by checking for a frame sync pattern in the received data. Counts are kept of the number of good and bad frame syncs for each data line, and therefore a current frame sync status of each line is maintained.

Data line priorities are used to help determine which source to select if two or more lines have a good frame sync. Tracking predict times are used to select a data source if no lines have a recognizable frame sync pattern. Predict times are in seconds from first motion to acquisition of signal (AOS) and loss of signal (LOS) for each station and are counted with a 1-pps clock in the software.

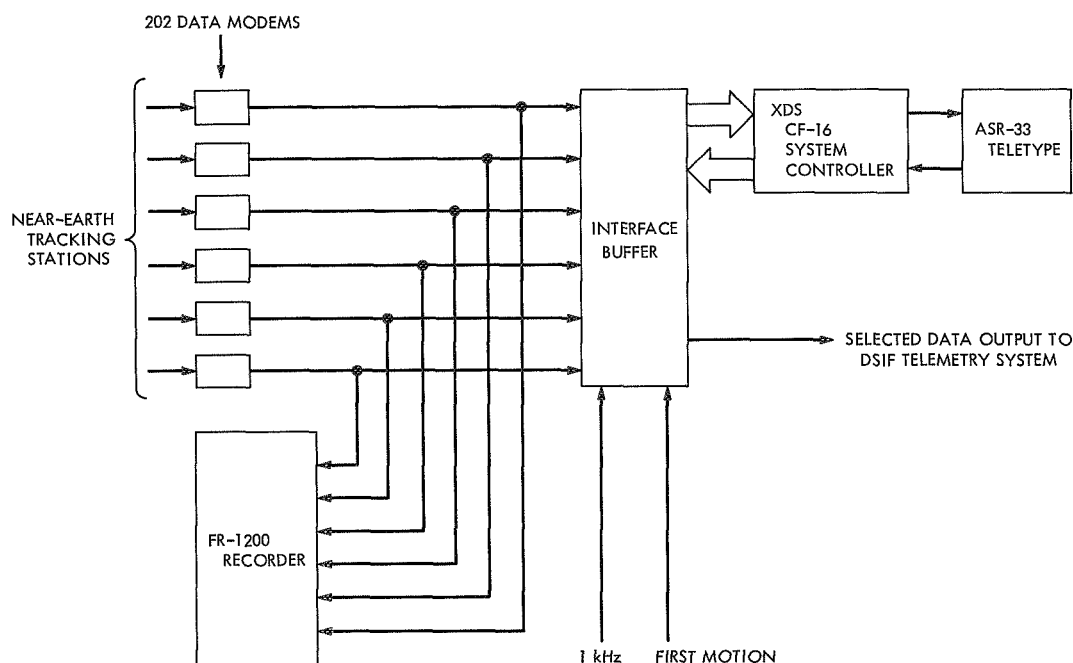


Fig. 1. Block diagram of near-earth telemetry switching unit

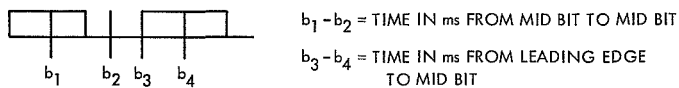


Fig. 2. Time references

The software for the system is written entirely in symbolic language and is divided into three sections: a main routine, and two interruptable subroutines. The main routine handles all inputs/outputs and, in addition, performs the line switching for the system. The 1-kHz interrupt subroutine controls all the timing functions for the system and maintains bit sync and frame sync status for each of the six input lines. By determining middle bit time, the data interrupt subroutine is used to help maintain bit synchronization for the 1-kHz subroutine (Fig. 2).

IV. Theory of Operation

A. Main Subroutine

The sequence of operations begins by first setting up the interface logic to accept data on line 1. This would normally be pre-launch and launch data. Then the processor enters an input routine whereby pertinent constants are accepted into storage through the ASR-33 teletype input. These constants are:

- (1) Bit rate of expected data.
- (2) Lead time in seconds before AOS to begin looking for data.
- (3) Number of sequential good sync codes to recognize before setting the frame sync flag.
- (4) Number of sequential bad syncs to have in order to reset the frame sync flag.
- (5) AOS times for each data line.
- (6) LOS times for each data line.
- (7) Priority number for the line.

The processor can handle bit rates of either 8½ or 33½ bps, and is initialized for 33½ bps. If 8½ bps is entered for the bit rate, the millisecond counts for middle bit time and total bit time are changed accordingly.

After the input routine is completed, the next step in operations is to initialize the message timeout routine and the count for the 1-pps timing. Then the two interrupt routines are enabled and the processor will go into a polling loop to check sync status, AOS, and LOS for each data line.

In the polling loop, the sync status for each line is checked. If only one frame sync is found, the processor will select the data line corresponding to the frame sync. If that line happens to be the one already selected, the re-selection does not affect anything. If more than one frame sync is found, the processor checks the priority of the lines. A line with frame sync and a priority of one takes precedence, but if no line had a priority of one, the first line found with frame sync status would be the selected line. If no lines had a frame sync, the AOS and LOS times would be examined for current time (X) to be in the range $\text{AOS}^{(N)} < X < \text{LOS}^{(N)}$ where N is the line number. The first data source to meet this condition would be the selected line.

After scanning the status of all the data lines, the next step in the polling loop is a check for launch vehicle first motion. This event, when it occurs, signifies the start of the 1-pps timing clock. The main routine outputs a message to show that first motion has occurred. Until the time of first motion, only a line with an AOS time of zero (normally the preselected line) could be selected and the processor would ignore all other lines.

After sensing for first motion, the main routine next enters a loop where it looks for a change in frame sync status on any line. If a data line has had a change of sync status, a message giving the new sync condition, the line number, and the current 1-pps time value will be typed out.

The 1-pps time value is unfortunately typed out as a hexadecimal number instead of a more readable decimal number. This is the result of a time constraint placed upon the main routine in that if it took the time to convert to decimal before typing out, the portion which has to make the line selection could not be executed often enough. When this loop has been completed for all lines, the main routine will return to the line selection where the cycle begins again.

B. 1-kHz Interrupt Subroutine

A 1-kHz timing pulse controls the execution of this routine so that the 1-pps count, data sampling, data bit sync, and total bit count per frame are all controlled by this timing reference.

The subroutine first checks for a first motion flag to have been set. If the first motion has been sensed, a count of 1000 is decremented to generate the 1-pps clock. If first motion had not occurred, the 1-pps clock would be bypassed. If a 1-pps count is generated, the AOS and

LOS times are decremented for each line so that these counts may be used by the main routine for line selection. No frame syncs will be set for any line not having $AOS \leq T < LOS$.

For each 1-kHz timing pulse, the subroutine decrements a count which determines the appropriate time to sample a data bit. It represents the time in milliseconds from middle bit time to middle bit time or from leading edge to middle bit time reference (Fig. 2). To aid in bit synchronization, this count is controlled by the data interrupt subroutine.

If the count for mid bit has reached zero, the routine will then sample the data lines simultaneously by inputting in parallel and then performing a parallel-to-serial conversion so that the input block is separated into separate lines. Then each stored word of 16 bits corresponding to each data line is shifted down and merged with the new data bit for each line.

After doing this segment, the subroutine will exit, and on the next 1-kHz count, it performs the portion of the subroutine which checks for frame sync. The reason for the two segments is that the total time required to execute the subroutine is greater than the 1-ms interval between interrupt pulses.

With the next 1-kHz pulse after the sampling pulse, the routine enters the segment to check for frame sync. First, it decrements a count representing the total number of bits in a frame for each line and then looks to see if there is frame sync for each line. If there is, the next check is to see if it is time to look for frame sync again. If it is, the routine then compares the stored input data word against the known frame sync pattern both normal and inverted. If it is a good code, the count for bad syncs is reset. If it is not a good code, the number of bad frame syncs for the line is incremented and the number of good counts is reset. The number of good or bad counts considered to be in or out of lock is a keyboard entry in the

main routine. If it were not time to look for the frame sync code, the routine would exit and await the next cycle. If the frame sync flag were not set for the line at the time to look for frame sync, the routine would then check AOS and LOS times. This would be the initial condition for any line before it had good data. If the current time (T) corresponded to $AOS < T < LOS$ for that line, then the routine would check the sync codes. If a sync code is matched with the data word, the number of good frame syncs is incremented. The proper number of consecutive good frame syncs would set the frame sync flag for that line.

Each data line has its own frame sync loop and good and bad count status so that input data lines with a time delay of a data bit time or more between corresponding data bits may be handled simultaneously.

C. Data Interrupt Subroutine

This routine is executed by an interrupt pulse caused by the positive-going edge of a data bit of the data source selected. The subroutine functions as a bit synchronizer by resetting a count which represents the time in milliseconds from leading edge of a data bit to middle bit time (Fig. 2). The priority of this interrupt is higher than that of the 1-kHz interrupt, thus always giving a correct mid-bit count for data sampling.

D. Power Fail/Safe Routine

In the event of a power failure, two high-priority interrupt locations are available to access the power fail/safe routine; one for power down, the other for power up. When entered from a power down interrupt, the routine saves the contents of the program accessible registers and the program counter register, stores the current selected line number, and then halts the processor. When power comes back on, the power up interrupt again accesses the subroutine, all registers are restored, the line is again selected, and the program returns to the point at which power failed.

DSN Discrepancy Reporting Subsystem

D. G. Tustin

DSN Engineering and Operations Office

The Deep Space Network discrepancy reporting subsystem and the results of the first year's discrepancy reporting operation using a computerized data management system are briefly described. The general problems encountered and the steps being taken to solve them are discussed.

The discrepancy reporting subsystem (DRS), as a part of the DSN Operations Control System, is responsible for collecting and cataloging all documented reports of operational discrepancies. These include hardware and software failures, as well as procedural problems that occur during any scheduled operation. The cataloged information must contain a description of the discrepancy, including (1) the facility(s), system(s), and equipment(s) involved, (2) the corrective action taken, (3) the personnel involved, and (4) the time of occurrences. This information should be cataloged in such a way as to facilitate rapid retrieval based on varied selection criteria.

Approximately one year ago, the DRS data files were placed in a computerized data management system using a prototype program. This system has since proved its worth many times over. It allows for the rapid retrieval of data in endless formats, using practically any available data parameter or parameters as selection criteria, and can be accomplished with a minimum of programming effort.

Although this new capability represented a major improvement in the DRS, several old, as well as some new deficiencies, were present. There are several new parameters very necessary for report sorting that were not

included in the computerized data base, and a definite ability to correlate discrepancy reports (DRs) with the network schedule is required. In addition, the forms used for reporting a discrepancy are not fully compatible with the computerized data base and are time-consuming.

Efforts are now underway to correct these known deficiencies and to make several other needed improvements. The data base is being expanded to include the needed missing data parameters. It is also being restructured in a manner that will facilitate the use of the DSN scheduling data base as a reference file during computer runs. Also, the reporting forms are undergoing a major revision. Working with the various facilities, the DR forms are being reviewed and redesigned in an effort to make them more comprehensive and easier to complete.

The method of reviewing corrective action taken, and closing out DRs, is also being investigated, and several methods of involving the facility and system engineers in this process are being considered.

These improvements should all be completed and placed in operation prior to the *Mariner* Mars 1971 launch in May 1971.

Optimal Frame Synchronization

W. Kizner

DSN Engineering and Operations Office

Optimal frame synchronization algorithms are developed which will reject bad data as well as provide high probabilities for obtaining correct frame synchronization with data which has an error rate consistent with project requirements. The exact analysis to obtain these probabilities is outlined. The amount of computation to obtain these quantities may be very large, hence easily computed approximations are also given.

I. Introduction

The aim of this study is to develop optimal frame synchronization algorithms under a very general set of assumptions. The definition of optimality can be specified to a large extent by the user. The problem of frame synchronization may be posed in the following way. Initially, data is received starting from some unknown part of the frame. The beginning of the frame is determined by recognizing a sync word, or a binary sequence of given length which is not likely to be confused with a string of information bits. When further identifications of sync words occur at intervals equal to integer multiples of a length of a frame, then a final determination can be made that frame synchronization has been attained.

The figure of merit of an algorithm depends on how reliably good data is frame-synched, and how few errors are made in labeling as synched data which is not properly synched or data which has a large number of errors. Another is the computation time involved. Here, the user can specify his own figure of merit consistent with his goals.

One optimal property of the present technique is that if the quality of the data should be seriously degraded after some point, then this algorithm insures that the good frames up to this point are kept and the bad frames after and including this point are rejected. This is in contrast to other algorithms which have a time lag. It also contrasts to the use of the computed signal-to-noise ratio, which also lags.

Definitions of terms used are given in Table 1.

II. Stages of the Algorithm

The method consists of three states:

- (1) *Search mode.* Initially, the information train is examined one bit at a time in a serial shift register, N bits in length, where N is the number of bits in the sync word. When the contents of the shift register match the sync word, allowing up to E_p error bits, the provisional lock mode is entered. A pattern with up to E_p errors is called good.

Table 1. Definition of terms

E_g	maximum number of bad patterns allowed in group
E_p	number of allowable bit errors in a pattern
N	number of bits in sync word
N_F	number of bits in frame
N_g	number of patterns in group, or number of representations of sync word that are used to determine mode of algorithm
p_b	probability of a bit error
p_c	probability that a sequence of N bits of the information train is confused as a pattern when starting in the wrong position
p_L	probability of a bad pattern (one which has more than E_p errors)
p_s	probability that a group of N_g sequences of N bits is mistaken for the condition that the system is in lock when starting in the wrong position
q_L	probability of a good pattern
Type I error	good data which should be in sync but is declared out of sync
Type II error	locking in at the wrong position in N_F or fewer tries of consecutive positions

(2) *Provisional lock mode.* The contents of the shift register are examined only once every N_F bits, where N_F is the length of the frame. Next, a sequence of patterns, or group, is tested as follows: N_g patterns at a time are examined. Thus, $N_g - 1$ new patterns are considered. If $N_g - E_g$ or more good patterns are observed, lock mode is entered. If not, search mode is entered again.

(3) *Lock mode.* Here, groups of N_g patterns, each spaced N_F bits apart, are examined. If $N_g - E_g$ or more good patterns are observed, the lock mode is continued. Here, a new pattern would be added to the group and the oldest one eliminated. If more than E_g bad patterns are observed, the lock mode is discontinued and the search mode is entered again at the approximate location of the next sync word. The frames up to the last good sync word are accepted and the others are rejected.

In the model used here, it is assumed that no bits are created or destroyed in error. Hence, the normal assumption is that loss of lock is due to bad data.

III. Approximate Calculation of the Possibilities of Some of the Errors

One type of error, called type I, is to declare good data as out of sync or bad. Another kind of error is to lock on data in the wrong position, which we call a type II error. Still another kind of error is to include as good data that data which has a high error rate. It will turn out that it is possible to calculate the probability of a type I error accurately, but the cost of computation may be high. Hence, a simple approximate formula is given here. It is not possible to calculate the probability of a type II error with any accuracy without a detailed knowledge of the kind of data transmitted, since this error consists of the possibility of confusing this data or part of this data with a sync word. However, some approximate optimistic estimates will be given.

Now to the calculation of the different types of errors: the criterion for labeling a pattern as good or bad may be generalized from what has been said before to take into account dependence of errors within a pattern. However, it is assumed that the probability that a pattern is bad p_L can be calculated, and that the probability that any pattern is good or bad is independent of the state of other patterns.

A heuristic method of computing the probability of a type I error can now be given. It consists of finding the probability of observing a group of N_g patterns with more than E_g errors, or

$$\text{prob (type I)} = 1 - \sum_{i=0}^{E_g} B(N_g; i, p_L) \quad (1)$$

where $B(n; k, p)$ is the probability of having k "successes" in n Bernoulli trials with probability p for "success,"

$$B(n; k, p) = \binom{n}{k} p^k (1 - p)^{n-k} \quad (2)$$

and

$$\binom{n}{k}$$

is the binomial coefficient.

A closer examination of the reasoning reveals many flaws. For instance, part of a bad group may be usable.

In addition, the algorithm may reject some good groups in the process of losing lock and reacquiring it. Later, an exact treatment will be given.

Consider next the probability of a type II error, or the probability of achieving lock at the wrong position. We assume that the probability that any particular pattern of N bits is 2^{-N} . If E_p errors are allowed, then the probability of confusion of a pattern on a single try when out of sync p_c is

$$p_c = \sum_{i=0}^{E_p} \binom{N}{i} 2^{-N} \quad (3)$$

The probability of a type II error on a single try when out of sync is the probability that the first pattern in the group is confused as good (to gain provisional lock) and that at least $N_g - 1 - E_g$ in $N_g - 1$ are also taken as good, or

$$P_s = p_c \sum_{i=N_g-1-E_g}^{N_g-1} B(N_g - 1; i, p_c) \quad (4)$$

The probability of a type II error in N_F tries is the probability of a type II error in at least one of the $N_F - 1$ bad positions with the correct position rejected. Hence,

$$\begin{aligned} \text{prob (type II)} &= [p_L + (1 - p_L) \sum_{i=E_g+1}^{N_g-1} B(N_g - 1; i, p_L)] \\ &\quad \times \sum_{j=1}^{N_F-1} B(N_F - 1; j, p_s) \\ &= [p_L + (1 - p_L) \sum_{i=E_g+1}^{N_g-1} B(N_g - 1; i, p_L)] \\ &\quad \times [1 - (1 - p_s)^{N_F-1}] \end{aligned} \quad (5)$$

IV. Exact Solution for Type I Error

The method for obtaining the exact estimate of the probability of a type I error will now be outlined. First, we recognize that loss of lock is a recurrent event. This means roughly that the initial situation is restored again after each loss of lock, or that the experiment starts all over again. Next, the experiment is divided into two phases: gaining and losing lock. The expectation of the number of frames that are lost before gaining lock and the number of frames that are accepted when in lock are calculated. Lastly, the expectation of the number of

frames that are lost when going out of lock before the process starts again is calculated.

To find the expectation of the number of frames lost before lock is achieved, one uses some results from the theory of Markov chains. A state is defined so as to specify the sequence of good and bad patterns in the group. The initial probability of each state is easily found, given the probability of a bad pattern p_L . The distribution of succeeding states is found by setting up the transition matrix, or the matrix which specifies the probability of the transition from state i to state j , given state i . States which are in lock are defined as absorbing, and the expectation of the time for absorption, or the expected number of frames lost, is calculated. The process is then reversed. Starting with a known distribution of states in lock, the expected number of frames that are accepted (before going out of lock) is calculated. Lastly, a correction is made for some additional frames lost.

V. Calculation of the Probability of Good or Bad Patterns

For uncoded data, the probability of a good pattern q_L is easily computed if it is assumed that the bit errors are independent.

$$q_L = 1 - p_L = \sum_{i=0}^{E_p} B(N; i, p_b) \quad (6)$$

where p_b is the probability of a bit error.

For coded data, the situation is different. For block coded data, for instance, one would like to try to determine the number of code words in error, rather than the number of bits in error in a sync word, because the number of wrong code words is a much better indicator of the status of the communications system. Also, although errors in code words are independent errors, the resulting bits are not. The problem of defining bad patterns for coded data is being pursued at present.

VI. Some Numerical Results

A few numerical results (Tables 2 and 3) will now be given to show the validity of the approximation for type I error and the possibility of obtaining algorithms which meet the objectives stated. First, a few results are given for establishing how accurate the approximation Eq. (1) is for the probability of type I error. These results and the others listed suggest that the approximation Eq. (1)

Table 2. Numerical results for $N_g = 5$, $E_g = 1$,
 $N = 15$, $N_F = 140$, and $E_p = 1$

Parameter	$p_b = 0.005$	$p_b = 0.05$
Probability of a bad pattern	0.2513×10^{-2}	0.1709
Expected number of consecutive frames lost	2.25	3.09
Expected number of consecutive frames in lock	40,081	18.09
Probability of type I error	0.5622×10^{-4}	0.1456
Approximation for probability of type I error, using Eq. (1)	0.6287×10^{-4}	0.2045
Probability of type II error	0.8061×10^{-13}	0.9014×10^{-11}

is good to within a factor of 2 and is increasingly accurate as the probability gets smaller.

Another conclusion that we can draw is that it is possible to meet the requirements of having small type I and II errors for bit error rates within project requirements and having a large type I error when the bit error

Table 3. Numerical results for $N_g = 7$, $E_g = 1$,
 $N = 15$, $N_F = 140$, and $E_p = 1$.

Parameter	$p_b = 0.005$	$p_b = 0.05$
Probability of a bad pattern	0.2514×10^{-2}	0.1709
Expected number of consecutive frames lost	2.17	4.09
Expected number of consecutive frames in lock	26,925	17.25
Probability of type I error	0.8061×10^{-4}	0.1916
Approximation for probability of type I error, using Eq. (1)	0.1316×10^{-3}	0.3422
Probability of type II error	0.2946×10^{-9}	0.4494×10^{-17}

rate exceeds this amount by, say a factor of 8. If $N_g = 15$, $E_g = 4$, $E_p = 0$, $p_b = 0.005$, and the other quantities are unchanged from those used in Tables 2 and 3, then Eq. (1) yields 0.0032 for the approximate type I error. If $p_b = 0.04$, then Eq. (1) becomes 0.89. In other words, there is a good chance that the poor data will be rejected. For this case, the probability of a type II error is essentially zero.

DSN Traceability and Reporting Program

J. A. Miccio

DSN Engineering and Operations Office

The Traceability and Reporting Program is a combination of three programs designed to coordinate and disseminate information to meet the needs of researchers, analysts, and managers for information concerning the DSN mission data record for a current and/or past mission. It also serves as a monitor or as an accounting device by providing status information relative to the generation of System, Master, and Experimenter Data Records. The program additionally functions as an index to the mission data captured on magnetic tape and microfilm retained in the DSN Operational Data Control Center.

I. Introduction

The Traceability and Reporting Program (TRP) is part of the DSN Operations and Analysis function; it is maintained and operated by the DSN Operational Data Control Center (ODC). The DSN ODC acts as the recipient and transfer point for DSN products, i.e., the System Data Record (SDR), Master Data Record (MDR), and the Experimenter Data Record (EDR). The ODC utilizes magnetic tape and microfilm as its principal information retention media; these media are also used for user reference and retrieval. The TRP supplements those retention media and functions as an information source to the DSN and its users, providing information concerning the mission data record.

Past mission operations have indicated a need for a system to provide information concerning the status and state of operational data once it has passed through real-time monitor and processing functions. The analyst or investigator of past missions, in order to determine what data had been received, its physical state (magnetic tape, disc, etc.), and its quantity and quality, would have to pursue many avenues to acquire the necessary information.

The monitor and data processing functions normally exercise direct influence over operational data from time of acquisition to 24 h after termination of a tracking

sequence. The TRP begins building its information base for a tracking period during that same period and displays status information within hours after the end of the tracking sequence. The information base is continually updated until all information concerning a data sequence has been acquired and fed into the TRP. The process of information acquisition encompasses the period from end of track up to 2 yr after the end of the mission.

The basic capability of the TRP is the coordination and abstraction of information from multiple sources into one source. The TRP delivers to the user decision making, analysis, and visibility support, covering a time period from near-real-time operational interest to long-term research analysis.

II. Function

The Traceability and Reporting Program, in three formats, provides the DSN, its users, and investigators information concerning the scientific and engineering data collected through the course of mission operations. The program provides information to effect the reconstruction or upgrading of a data record sequence for a past data day in terms of current demands.

In terms of the Information Sciences, the concept of TRP is oriented toward making more efficient use of documented data and its sources generated in the mission data record sequence.

The TRP applies discipline to the extraction of information from the real-time data stream. In essence, the TRP is based upon an eclectic principle of specifically choosing selected information elements from the data stream.

The selection criteria for specific element extraction are predetermined by analyzing the linguistic composition of an investigator's or user's subject matter with which he is concerned. The elements extracted from the data stream form the basic linguistic units which lend organization and/or structure to the investigator's subject matter.

The program has the flexibility to permit revision of its data base in light of newly reconstructed and/or upgraded data. Through its various elements, the TRP displays information for each mission in chronological sequence under each source for each data day. (A data day is defined as Goldstone set to Australia rise.)

Specifically, under format A, or the Basic User Information Catalog, all participating sources (ranging from DSIF stations to DSN system analysis areas) are represented. All types of material generated by each source are listed in alphabetical and chronological sequence.

Within the TRP, a mission sequence number is assigned to the spacecraft, source, and GMT combination. Since this combination is fixed, the TRP can list all information relative to that specific combination whenever it becomes available, thus representing a complete account of information for each source for a specific time period.

III. Elements

The Traceability and Reporting Program generates three reports: a Basic User Information Catalog, an SDR/MDR/EDR Status Report, and a Projected Sequence Report. The information content in each report is in relation to the nature of a user's request. In format A, or the basic catalog, the design criteria assumed a user would lack sufficient detailed information and therefore provides as complete as possible a representation of all available information concerning the data records for any given data day or portion thereof.

Figure 1 represents a sample page of the user catalog. It provides the user such information as mission, spacecraft identification, originating source for any data listed, GMT, data day, data processing classification (normal-critical, represented as 1-4), and data quality in actual percent. For example, in a configuration such as *Pioneer VIII*, DSS 12, GMT day 018, all information received by ODC is represented on one page. To the user, this catalog can, by any number of edit parameters, isolate a sequence of data for a specific station or for an entire data day.

In the SDR/MDR/EDR Status Report, or format B, detailed information is displayed pertaining to the status and state of each individual data record (see Fig. 2). This report will display data record status by spacecraft, GMT, percentage of good data, serial number, Original Data Record availability, reuse or degauss cycle, and data record availability, either magnetic tape or disc.

The TRP, while generating specific reports, continually updates its data base, allowing greater research and analysis of past operations. The program operates simultaneously on two levels: in operational or near-real-time and in an archival mode, defined as 48 h after the fact.

MAR 15, 1971		FLIGHT DATA CATALOG SYSTEM					PAGE 239	
TRACEABILITY INFORMATION REPORT								
FORMAT NO 1								
ENT-START	ENT-END	PASS	DOCUMENTS	C	CRIT	CONF	COMMENTS	KEY
DATA DAY 1133								
AR-DSS 12 GULSTONS CALIF ECFC SITE								
PF-PASS FOLDER								
710182220	710180400	1133	KDCA 0037-0046				CP RECALL INFO JBSC01A 19/2330Z-JH5002A 18/2335Z	PN8BAZ00543
TL-STATION REPORT								
710181745	710180400	1133	KDRP 0147-0157					PN8BAF01151
AI-DSS 41 WOLPERA AUSTRALIA								
PF-PASS FOLDER								
710180327	710180715	1133	KDPZ 0191-0199				NMT MODE 032701Z TO 071500Z	PN8BAZ00533
TL-STATION REPORT								
710180330	710181115	1133	KDRQ 0252-0325				PN6 PASS 1840	PN8BAFC12C8
AM-DSS 51 JOHANNESBURG SOUTH AFRICA								
PF-PASS FOLDER								
710181055	710181500	1133	KDPZ 0200-0209				CP RECALL INFO JBW001A 18/1100Z-JBW003A 18/1433Z	PN8BAZ00534
TL-STATION REPORT								
710180900	710181500	1133	KDRN 0207-0220					PN8BAFC1171

Fig. 1. Sample page of user catalog

DSN DATA RECORD STATUS REPORT			
STATION <u>14</u>			
S C	DATA DAY	AOS	LOS
81	262	194854	211843
SYSTEM			
TRACKING	TELEMETRY	COMMAND	MONITOR
	XXX		
DATA RECORD			
ODR	SDR	MDR	
DISC TAPE	DISC TAPE	DISC	TAPE
14762	13765	264	
14699			
DATA QUALITY			
ODR	SDR	MDR	
14762	90.5	13621	95.5
14699	77.9		

Fig. 2. Sample representation of format B

By operating the program on both levels, any past mission report may be entered into the data base and further complete the information bank for any particular mission phase. This process allows researchers, analysts, etc., to review a project and be able to reconstruct, via the information catalogs, entire phases of a mission 2 mo to 2 yr past.

IV. Conclusion

The Traceability and Reporting Program attempts to provide as broad a base as possible to allow for user inquiries that lack specific request information. It provides the user information concerning the status, state, quantity, and quality of the DSN data record in near-real-time and archival modes. The program is new and future design planning is presently working toward real-time access and display of data record information, and eventual data base integration with DSN Operations and Analysis programs.

The Teletype Discipline of Data Transfer Designed for Support of Mariner Mars 1971 Missions

F. E. Bond, Jr.

SFOF/GCF Operations Section

This article describes the overall teletype configuration that has been developed to support the ground communications requirements established for the Mariner Mars 1971 missions. Primary emphasis is placed on the worldwide distribution of mission traffic formatted in the teletype discipline, routed through the communications switching facilities, and provided to various analysis and control centers.

I. Introduction

Since the early *Ranger* missions, space flight projects supported by the DSN have used the teletype discipline of data transmission to send low bit-rate data between the various locations of the tracking network during all phases of each mission. In addition to this primary use of teletype, special multiple-distribution networks were developed within the Space Flight Operations Facility (SFOF) to use teletype as a means of internally displaying not only the data received from the tracking stations but also the formatted telemetry readouts of data processing computers receiving input data from higher bit-rate disciplines of communications data transfer. Although the *Mariner* Mars 1971 Project will make extensive use of high bit-rate techniques, such as the high-speed and wide-band systems, to effect transfer of the majority of their data, their use of teletype will be greater than any mission previously supported by the DSN. Current

communications planning for missions to follow *Mariner* Mars 1971 will place far greater emphasis on transmitting data using multiplexed high bit-rate techniques between the tracking stations and the SFOF. This, in addition to the planned use of specialized readout devices within the SFOF to display the outputs of the data processing computers rather than the use of teletype equipment, indicates that the teletype system developed for *Mariner* Mars 1971 may well represent the most complex and extensive application of teletype that the DSN has or will develop and employ.

In view of this, the following article has been prepared to document the overall teletype system to be used by the *Mariner* Mars 1971 Project. For purposes of clarity, certain omissions have been made intentionally, such as the use of teletype prior to the launch of the spacecraft for purposes of mission simulations, but in general the

following information reflects the total use of teletype by *Mariner* Mars 1971 from the launch phase throughout the entire mission.

II. Worldwide Teletype Network

Many separate activities located throughout the world, including tracking stations, control centers, launch activities, and communications switching centers, have requirements for the transfer of data or exchange of information between themselves using the teletype discipline in order to support the *Mariner* Mars 1971 missions. Many different types of teletype data will be generated by these activities destined in rare cases for a single recipient but far more often addressed to a multiplicity of receiving stations. Sufficient teletype circuits interconnecting these supporting activities (see Fig. 1) have been provided through the resources of the NASA Communications Network (NASCOM) in conjunction with those provided by the DSN Ground Communications Facility (DSN GCF). The teletype circuits routed to each supporting activity, regardless of its location, must always be interconnected to one of the four communications switching centers. Each of these centers has the required capability to receive input teletype traffic from the activities it is designated to support and to switch and forward such traffic to the desired recipients. The Canberra Switching Center supports DSSs 41 and 42 and the Madrid Switching Center supports DSSs 51 and 62 as well as the activities located at Tananarive (TAN) and Canary Island (CYI). The NASCOM Primary Switching Center at Greenbelt, Maryland supports the activities at Goddard Space Flight Center at Cape Kennedy, the MSFN tracking station at Ascension Island (ACN), and the activities at Bermuda (BDA) and *USNS Vanguard* (VAN). The West Coast Switching Center (WCSC) at the Jet Propulsion Laboratory supports the DSN tracking stations at Goldstone, California and provides a central communications switching center for all internal switching requirements of the SFOF. The quantity of teletype traffic, together with the complexity inherent in multiple recipients for such traffic, creates real-time switching functions at each of the switching centers which are performed by specially programmed computers, termed *Commprocessors*, that are programmed to read and react to addressing information furnished by the transmitting activity.

III. Teletype Conventions

Each teletype circuit, interconnecting the various network locations to the Commprocessors, is assigned a

teletype address, termed a *routing indicator*, consisting of four letters used by the originators of teletype traffic to indicate the desired distribution of their traffic. Table 1 lists the routing indicators assigned to the various activities supporting the *Mariner* Mars 1971 missions. In some cases, a particular routing indicator may be assigned to two circuits at a given activity, where incoming traffic will be routed to the second circuit by the Commprocessor in the event that the first circuit is busy with traffic sent at an earlier time. All switching elements of the teletype communications system carrying teletype traffic use these routing indicators, first, to direct traffic to the appropriate switching center using the first letter of the

Table 1. Routing indicators used in support of *Mariner* Mars 1971

Area	Activity	Location	Routing indicators
California	DSS 12	Goldstone	JECO, JELA, JEXC
	DSS 14	Goldstone	JMAR, JMLA, JMXA
	SFOF	Pasadena	JSFO ^a
	Operations Control	Pasadena	JOCC
	Net Control	Pasadena	JTNC, JNCC, JNDC, JNEC
	WCSC	Pasadena	JJPL, JCNF
Florida	DSS 71	Cape Kennedy	GKEN, GKXE
	RTCS	Cape Kennedy	GKAP
	Bldg AO	Cape Kennedy	GKYA
	Merritt Island (MILA)	Cape Kennedy	GMIL
Atlantic Ocean	MSFN-ACN	Ascension Island	GACN, GSXE
		Bermuda	GBDA
		Canary Island	LCYI
		USNS Vanguard	GVAN
Australia	DSS 41	Woomera	AOMJ, AOLA, AOXM
	DSS 42	Tidbinbilla	ANBE, ANLA, ANXB
Maryland	MSFN-OC	Greenbelt	GCEN, GUNV
	Goddard Real-Time System (GRTS)	Greenbelt	GCDF, GDCS
	NASCOM	Greenbelt	GSTS
Spain	DSS 62	Cebreros	LCEB, LCLA, LCXE
Africa	DSS 51	Johannesburg	LJOB, LJLA, LJXO
	TAN	Tananarive	LTAN
^a Must be used in conjunction with preambles.			

routing indicator and, secondly, to direct traffic to the circuits assigned to the recipient as determined and identified by the remaining letters of the routing indicator.

All teletype traffic is divided into messages, usually 15 min in duration. Each message is divided into three parts: the header, which contains among other things the addressing information (routing indicator); the body, which contains the data to be transferred; and the end-of-message, which instructs the Commprocessor to disconnect all circuits established by the header.

In the special case of the SFOF, incoming teletype messages are quite often simultaneously furnished to many areas and internal recipients. As a result, the addressing and the routing to achieve the overall teletype data flow becomes rather complex. Two separate methods of message addressing have been developed to simplify these routing problems, both basically controlled by the information provided within the messages themselves by the originators. The first of these methods, referred to as *direct addressing*, is used in those cases where the originator of teletype messages knows the desired distribution of his traffic and can therefore address his messages using the routing indicators assigned to the recipients. This is the standard method of addressing teletype traffic and is used throughout the majority of the NASCOM network. In the majority of cases, such as the transmission of tracking data to the SFOF from various tracking stations, the originator is not and cannot be aware of the real-time distribution of his data within the SFOF and thus cannot directly address his traffic to all recipients involved. In these cases, the second method of addressing is used, termed *indirect addressing*, where the originator of teletype messages addresses his traffic to a pseudo routing indicator, JSFO, which routes the traffic to the WCSC Commprocessor serving the SFOF, and additionally includes information in each message that identifies the source of the data, the spacecraft, and the type of data being sent. These three items of information, collectively, are termed a preamble, which is used by the Commprocessor to route incoming messages to any desired set of multiple recipients in the SFOF. The first part of the preamble consists of two numbers (station identifier), which indicate the source of the data. A listing of all station identifiers used in support of *Mariner Mars 1971* is given in Table 2. The second part of the preamble consists of two numbers (spacecraft identifier) which indicate the spacecraft to which the data applies. A listing of *Mariner Mars 1971* spacecraft identifiers is given in Table 3. The third part of the preamble consists of two numbers (message data

Table 2. *Mariner Mars 1971* station identifiers

Station	Identifiers	Location
DSS 12	12	Goldstone, Calif.
DSS 14	14	Goldstone, Calif.
SFOF	20	Pasadena, Calif.
DSS 41	41	Woomera, Australia
DSS 42	42	Tidbinbilla, Australia
DSS 51	51	Johannesburg, South Africa
DSS 62	62	Cebreros, Spain
DSS 71	71	Cape Kennedy, Florida
RTCS	70	Cape Kennedy, Florida
MSFN-ACN	75	Ascension Island

Table 3. *Mariner Mars 1971* spacecraft identifiers

Mission	Spacecraft identification	
	Actual	Simulated
A or H	74	84
B or I	75	85
Proof test model	76	86

type identifier), which indicate the type of data being transmitted. As an illustration, when DSS 12, having a station identifier of 12 (obtained from Table 2), sends a message pertaining to Mission A, having a spacecraft identifier of 84 (obtained from Table 3), containing tracking information with identifier 40 (obtained from Table 4), the preamble 12/84/40 would be entered after the routing indicator JSFO. Upon receipt of this message at the WCSC, it would be automatically routed to the data processing computers (for computation), to teleprinters (for page copy), and by means of teletype-television converters to television monitors (for viewing). The manner in which this is accomplished is discussed later in this article.

IV. Worldwide Teletype Data Flow

Use of the assigned routing indicators and preambles in conjunction with the message switching Commprocessors and the worldwide network of teletype circuits will collectively provide the necessary teletype capabilities required to properly support the *Mariner Mars 1971* Project. These capabilities, as provided, are necessary, but not, in themselves, sufficient to insure proper flow of teletype traffic, unless they are used in accordance

Table 4. Mariner Mars 1971 teletype traffic identification

Message/ data type	Name	Description	Message/ data type	Name	Description
10	Operations Control	Consists of computer formatted sequence of events and real-time schedules as well as manually formatted status and launch messages generated at the SFOF intended for transmission to tracking stations.	44	SFOF predicts	for transmission to applicable tracking stations. Consists of third set of predicts generated by SFOF intended for transmission to applicable tracking stations.
20	OPS-X	Consists of manually formatted messages sent between the SFOF Net Control and tracking stations containing information and instructions relative to a spacecraft tracking pass.	45	Pseudo residuals	Consists of first set of pseudo residuals generated by SFOF intended for SFOF internal distribution.
21	Trajectory	Consists of inter-range vector, state vector, <i>I</i> -matrix, orbital elements and liftoff data generated by either SFOF or RTCS intended for transmission to tracking stations.	46	Pseudo residuals	Consists of second set of pseudo residuals generated by SFOF intended for SFOF internal distribution.
22	RTCS predicts	Consists of predicts generated by Air Force Eastern Test Range (AFETR) RTCS intended for transmission to tracking station at Ascension Island and furnished to SFOF and MSFN-OC.	47	Pseudo residuals	Consists of third set of pseudo residuals generated by SFOF for SFOF internal distribution.
23	RTCS predicts	Consists of predicts generated by AFETR RTCS intended for transmission to DSS 51 and furnished to SFOF.	50	Telemetry	Consists of 8 1/3-bit/s engineering telemetry data generated by the tracking stations intended for transmission to SFOF in event prime method of telemetry transmission (high-speed data) becomes inoperative.
24	RTCS predicts	Consists of predicts generated by AFETR RTCS intended for transmission to DSS 62 and furnished to SFOF; generated only when requested by SFOF in real time.	51	Telemetry	Consists of 33 1/3-bit/s engineering telemetry data generated by tracking stations intended for transmission to SFOF in event prime method of telemetry transmission (high-speed data) becomes inoperative.
28	Conference	Consists of manually prepared real-time messages between SFOF and DSN tracking stations; used only when normal voice circuits become inoperative.	55	Telemetry	Consists of 8 1/3-bit/s engineering telemetry data and edited 50-bit/s science telemetry data generated by tracking stations intended for transmission to SFOF in event prime method of telemetry transmission (high-speed data) becomes inoperative.
40	Tracking	Consists of tracking data generated by all tracking stations (including Ascension and excluding DSS 71) intended for transmission to SFOF.	70	Command	Consists of spacecraft commands generated by SFOF intended for transmission to tracking stations, and of verification of receipt of these commands generated by tracking stations intended for transmission to SFOF.
42	SFOF predicts	Consists of first set of predicts generated by SFOF intended for transmission to applicable tracking stations.		Formats	Consists of various types of telemetry formats generated by SFOF (360-75) for SFOF internal distribution only.
43	SFOF predicts	Consists of second set of predicts generated by SFOF intended			

with preplanned instructions as developed and provided by the DSN GCF to all locations transmitting teletype data during the launch and subsequent phases of the *Mariner* Mars 1971 missions. Table 5 is a worldwide teletype data flow plan that reflects the overall planning furnished to participating locations. Those locations transmitting teletype data are listed in the left column of this table together with the types of data to be transmitted by them on each routing indicator assigned to each transmitting circuit. The remaining part of this table illustrates receipt of the transmitted data by all other locations and indicates not only the activity receiving the data but the routing indicator of that activity to be used by the transmitting location for the transfer of his traffic. All traffic intended for locations other than the SFOF is directly addressed to the recipient, while traffic intended for the SFOF may be either indirectly addressed, by use of the routing indicator JSFO and the preamble as previously discussed, or directly addressed as indicated. Thus, Table 5 reflects both the source and the recipient of all teletype data for the *Mariner* Mars 1971 missions except for the detailed distribution of teletype data within the SFOF and the backup teletype capabilities, both of which are discussed later.

V. Teletype Message Switching

The computer programs residing in the Commprocessors, shown in Fig. 1, have been designed so as to automatically route any message, properly addressed, from any location in the network to any other location. This technique, termed *message switching*, is used throughout the teletype system and may be roughly compared to direct dialing techniques used over commercial telephone networks in that the user provides the addressing information to equipment capable of interpreting such addressing and establishing the required circuit interconnections to connect the originator to the addressed location. Thus the *routing indicator* of the teletype system is analogous to the *telephone number* of the commercial telephone network. Continuing this analogy, the first letter of the routing indicator, either A, G, L, or J for each of the four switching centers, may be compared with the telephone area codes, since the Commprocessor at each switching center provides a central switching point in the various geographical areas where tracking stations are concentrated. These stations transmit and receive teletype data from the switching centers at 100 words/min, which roughly corresponds to 50 bits/s. At each switching center, data are forwarded to other switching centers in blocks via 2400-bit/s data lines.

By inserting a routing indicator in the header of a message, a transmitting location instructs the receiving Commprocessor to route the message to the desired recipient over the teletype circuit corresponding to the chosen routing indicator. For the duration of this message, this circuit is not available to teletype traffic transmitted from other sources directed to the same routing indicator. Such traffic is held at the Commprocessor and automatically forwarded when the circuit is released upon completion of transmission of the previous message. Release of the circuit is made by the Commprocessor upon receipt of the end-of-message indicator sent by the transmitting location at the end of his message. If provisions were not otherwise made, non-transmission or non-receipt of this end-of-message indicator would result in permanent denial of the circuit to all subsequent traffic addressed to it. To prevent this from occurring, the Commprocessors are programmed to count the time intervals experienced between successive teletype characters as received from all transmitting locations. Should a time interval greater than 16 s occur, the Commprocessor interprets this as an end-of-message indicator and releases the circuit. Normally, transmitting locations are capable of formatting their output teletype traffic such that 16-s pauses between successive characters do not occur; thus, this timeout feature does not interrupt traffic. Certain types of data formats, however, are such that pauses between characters greater than 16 s will occur and additional provisions have been made to accommodate these exceptions. In these cases, the transmitting locations enter the code AA in the header of the messages and the receiving Commprocessor automatically substitutes a 30-min timeout in place of the 16-s limit. Should a transmitting location format traffic having pauses between characters greater than 30 min, then they must transmit an end-of-message indicator subsequent to such a break and a new header prior to resuming traffic transmission.

In addition to having the same capabilities as the other Commprocessors, the Commprocessor at the WCSC is specially programmed to multiple route received messages to many internal SFOF locations depending upon the preamble assigned to each message. Upon receipt of all messages addressed to JSFO, the WCSC Commprocessor reads the preamble and by referring to a previously entered preamble table, which cross-references preambles to multiple internal routing indicators, receives instructions to route such traffic to all such addresses. Since these preamble tables can be changed in real time by the operators of the WCSC Commprocessor, the capability exists to internally route incoming messages in any

Table 5. Mariner Mars 1971 worldwide teletype data flow

Receiving stations																																	
Transmitting stations			Space Flight Operations Facility															Deep Space Instrumentation Facility															
			Indirect address (JSFO)										Direct address					Tracking stations															
			CPS	Comm	TTY	Opera-tions	NAT	DSIF	Discrete	Telem-etry	Opera-tions	NAT	DSIF	Discrete	Telem-etry	DSS 12	DSS 14	DSS 41	DSS 42	DSS 51	DSS 62	DSS 71	ACN	OC	GRTS	Comm	Building AO	RTCS	TAN	CYI	VAN	BDA	MILA
SFOF		JDPS JJPL JDPS JCNF JDPS JDPS JDPS JDPS JJPL JDPS		JJPL	JDES JBOS JDFS JBQS JBZS JDAS JDBS JDDS	JOCE JZED JZED JZED JZED JZED JZED JZED	JZED JZED JZED JZED JZED JZED JZED JZED	JTNC JTNC JNEC JNCC JNDC JNEC							JELA JEXC JELA JEXC JELA JELA JELA	JMLA JMXA JMLA JMXA JMLA JMLA JMLA	AOXA AOXM AOXA AOXM AOXA AOXA AOXA	ANXB ANXB ANLA ANXB ANLA ANLA ANLA	LJLA LJXO LJLA LJXO LJLA LJLA LJLA	LCXA LCXE LCXA LCXE LCXA LCXA LCXA	GKXE GKXE GKXE GKXE GKXE GKXE GKXE	GSXE GSXE GSXE GSXE GSXE GSXE GSXE	GUNV GUNV GUNV GUNV GUNV GUNV GUNV	GSTS	GKYA GKYA GKYA	GKAP							
DSS 12		JEXC JEXC JELA JECO JEXC		JCNF	JBNS JBPS JBSS JDDS		JZED JZED JZED JZED	JTNC JTNC JTNC								JMXA	AOXA	ANXB	LJXO	LCXE	GKXE												
DSS 14		JMXA JMXA JMLA JMAR JMXA		JCNF	JBNS JBPS JBTS JDDS		JZED JZED JZED JZED	JTNC JTNC JTNC							JEXC	AOXA	ANXB	LJXO	LCXE	GKXE													
DSS 41		AOXM AOXM AOXA AOMJ AOXM		JCNF	JBNS JBPS JBUS JDDS		JZED JZED JZED JZED	JTNC JTNC JTNC							JEXC	JMXA	ANXB	LJXO	LCXE	GKXE													
DSS 42		ANXB ANXB ANLA ANBE ANXB		JCNF	JBNS JBPS JBVS JDDS		JZED JZED JZED JZED	JTNC JTNC JTNC							JEXC	JMXA	AOXA	LJXO	LCXE	GKXE													
DSS 51		LJXO LJXO LJLA LJOB LJXO		JCNF	JBNS JBPS JBWS JDDS		JDED JDED JZED JZED	JTNC JTNC JTNC							JEXC	JMXA	AOXA	ANXB	LCXE	GKXE								GKAP					

Table 5 (cont'd)

Transmitting stations			Receiving stations																														
			Space Flight Operations Facility												Deep Space Instrumentation Facility																		
			Indirect address (JSFO)						Direct address						Tracking stations																		
			CPS	Comm	TTY	Opera- tions	NAT	DSIF	Discrete	Telem- etry	Opera- tions	NAT	DSIF	Discrete	Telem- etry	DSS 12	DSS 14	DSS 41	DSS 42	DSS 51	DSS 62	DSS 71	MSFN		GRTS	Comm	Building AO	RTCS	TAN	CYI	VAN	BDA	MILA
Station	Data	Routing indicator	CPS	Comm	TTY	Opera- tions	NAT	DSIF	Discrete	Telem- etry	Opera- tions	NAT	DSIF	Discrete	Telem- etry	DSS 12	DSS 14	DSS 41	DSS 42	DSS 51	DSS 62	DSS 71	ACN	OC	GRTS	Comm	Building AO	RTCS	TAN	CYI	VAN	BDA	MILA
DSS 62	20 28 40 50/51/55/60 70	LCXE LCXE LCLA LCEB LCXE	JDP5	JCNF	JBNS JBPS JBYS		JZED	JTNC				JK(1)M	JOCC			JEXC	JMXA	AOXM	ANXB	LJXO		GKXE											
DSS 71	20 28 50/51/55/60 70	GKXE GKXE GKEN GKXE		JCNF	JBNS JBPS		JZED	JTNC			JOCC		JZED	JTNC	JFBM		JEXC	JMXA	AOXM	ANXB	LJXO	LCXE					GKYA						
MSFN-ACN	20 28 40	GSXE GSXE GACN	JDP5	JCNF	JBNS JBPS JDGS		JZED	JTNC			JOCC		JZED	JTNC	JFBM																		
RTCS	20 21 22 23 24 Predicts	GKAP GKAP GKAP GKAP GKAP			JBNS JDGS JDGS JDHS JDHS		JZED	JTNC JNEC JNCC JNDC JNDC					JZED	JTNC JNEC JNCC JNDC JNDC						LJXO LJOB	LCXE LCEB		GSXE GSXE	GUNV GUNV GUNV	GDCS		GKYA GKYA		LCYI	GVAN			
GRTS	Predicts	GDCS																											LTAN	LCYI	GVAN	GBDA	GMIL
MSFN-OC	20	GCEN									JOCC															GKYA							
VAN BDA MILA CYI TAN		GVAN GBDA GMIL LCYI LTAN																								GKYA GKYA GKYA GKYA GKYA							

^aJZ(1)D indicates any 1 of 15 routing indicators.

^bJF(1)M indicates any 1 of 14 routing indicators (see Fig. 5).

^cJK(2)M indicates any 1 of 14 routing indicators (see Fig. 5).

^dJK(1)M indicates any 1 of 12 routing indicators (see Fig. 5).

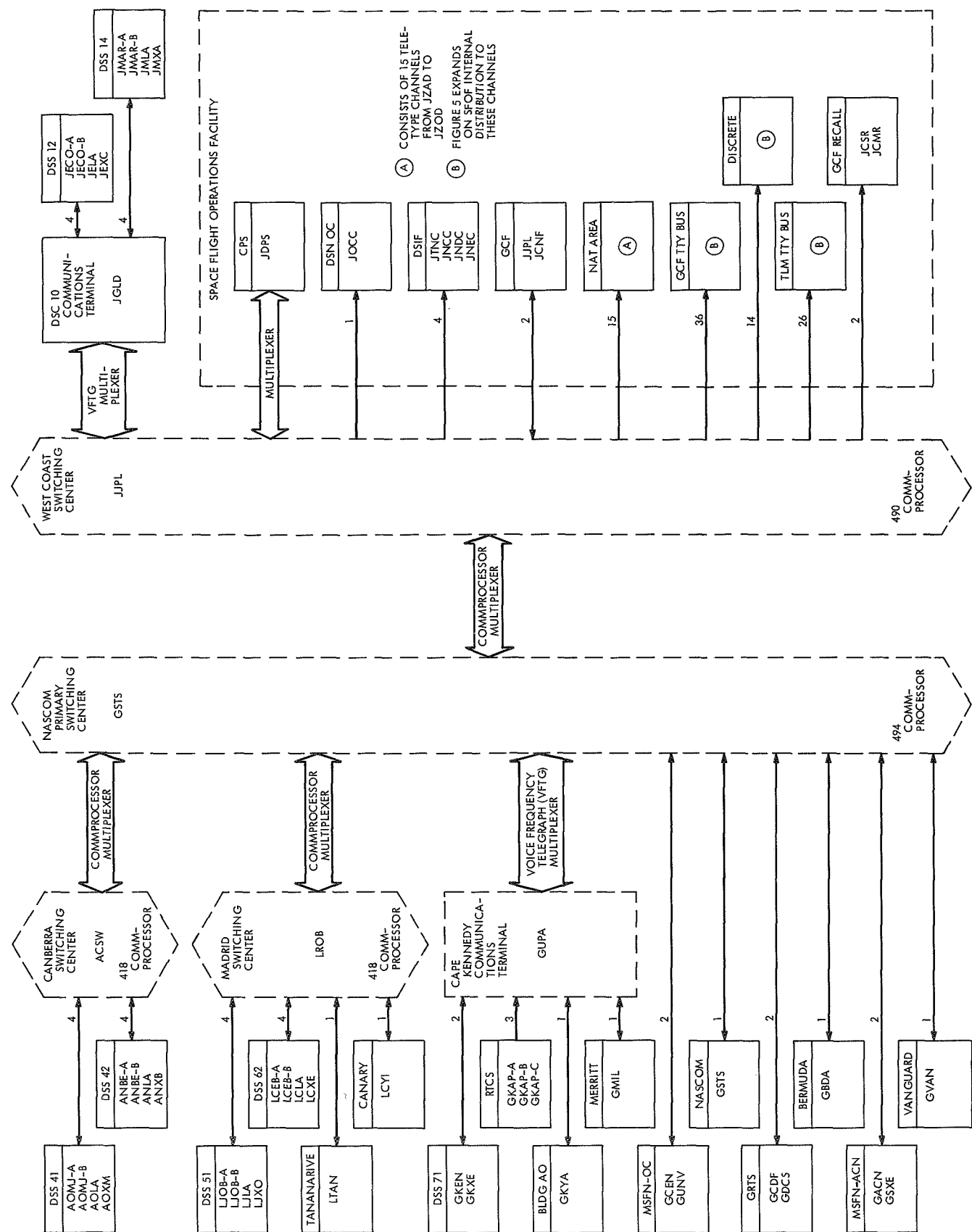


Fig. 1. Mariner Mars 1971 worldwide teletype network



Fig. 2. West Coast Switching Center Univac 490 Commprocessors

manner desired by *Mariner* Mars 1971 personnel. Figure 2 is a photograph of the WCSC Commprocessor. Two Univac 490 computers are used to provide necessary redundancy.

It would perhaps be informative to illustrate, by example, the end-to-end flow of a specific type of data from the originator multiple addressed to the recipients, illustrating the use of routing indicators, using both direct and indirect addressing techniques. Table 5 reflects that DSS 51 in South Africa must send spacecraft tracking data to the SFOF in Pasadena and to the Real-Time Computing System (RTCS) in Florida. At the SFOF, these data must be supplied not only to the Central Processing System (CPS) but to users in page copy form as well as visually presented on television monitors. The time sequence of this data flow is shown in Table 6.

VI. SFOF Teletype Data Distribution

During the launch and subsequent phases of the *Mariner* Mars 1971 mission, personnel located within the SFOF must receive, monitor, and analyze various types of teletype data. Such streams of traffic may be sent to the SFOF from external locations, or sent from the SFOF to external locations or generated within the SFOF intended solely for distribution to internal areas. Each operating position having requirements for page copy of teletype data is equipped with one or more teleprinters, each of which is driven by the WCSC Commprocessor since all streams of teletype traffic, regardless of origin or destination, must be routed through this computer. Three methods of distribution from the Commprocessor to user teleprinter equipment have been developed. The first method interconnects 36 teletype output channels to numerous selector boxes capable of selecting any one of the channels for connection to an

Table 6. Time sequence of data flow from DSS 51 to external addressees

Item	Location	Action
1	DSS 51	<ul style="list-style-type: none"> a. Originates tracking data in TTY format. b. Multiple addresses TTY messages to GKAP and JSFO adding preamble 51/84/40. c. Transmits TTY messages to Madrid Switching Center using circuit LJLA at 100-word/min rate.
2	Madrid Switching Center	<ul style="list-style-type: none"> a. Receives TTY messages from DSS 51. b. Multiplexes messages and transmits to NASCOM Primary Switching Center at 2400 bits/s.
3	NASCOM Primary Switching Center	<ul style="list-style-type: none"> a. Receives TTY messages from Madrid Switching Center. b. Demultiplexes messages. c. Reads routing indicator GKAP and transmits messages to RTCS at Cape Kennedy at 100-word/min rate. d. Reads routing indicator JSFO and multiplexes messages to WCSC at 2400-bit/s rate.
4	RTCS	<ul style="list-style-type: none"> a. Receives messages from NASCOM Primary Switching Center.
5	West Coast Switching Center	<ul style="list-style-type: none"> a. Receives messages from NASCOM Primary Switching Center. b. Demultiplexes messages. c. Reads routing indicator JSFO which instructs Commprocessor to read 51/84/40 preamble. d. Accesses preamble table and determines local routing indicators (JDPS and JBWS) to which traffic is to be routed. e. Transmits messages to JDPS at 40.8 kbits/s. This provides data to CPS. f. Transmits messages to JBWS at 100 words/min. This provides data to GCF TTY BUS for page copy and to associated TTY-TV converter for TV viewing.
6	Central Processing System	<ul style="list-style-type: none"> a. Receives messages from WCSC.
7	SFOF <i>Mariner Mars 1971</i> users	<ul style="list-style-type: none"> a. Selects messages by depressing button 10 on TTY selector box of GCF TTY BUS (JBWS) for page copy printout. b. Selects messages by depressing button 10 on TV selector switch for visual presentation.

associated teleprinter. This 36-channel bus arrangement is termed the GCF TTY BUS and is illustrated in Fig. 3. Teletype traffic fed to any of these channels may consist of any of the various types of data except telemetry. The second method interconnects 26 teletype output channels to numerous selector boxes capable of selecting any one of the channels for connection to an associated teleprinter in a manner similar to the first method. This 26-channel bus arrangement is termed the TLM TTY BUS and is illustrated in Fig. 4. The first 12 channels of this bus are allocated for displaying teletype telemetry data incoming from tracking stations (data types 50, 51, 55, and 60). The remaining 14 channels of this bus are allocated for displaying teletype telemetry formats generated by the Central Processing System of the SFOF (360-75 computers). These 14 channels on the bus are not sufficient to display all of the CPS formats. As a result, a third method of distribution has been developed which consists of 14 teleprinters directly connected (no selector box) to the Commprocessor, located within the *Mariner Mars 1971* operational areas. Figure 5 shows all three of these methods for internal distribution. It should be noted that 24 channels of the GCF TTY BUS and 12 channels of the TLM TTY BUS are connected to TTY-TV converters which provide visual display via television monitors of the traffic carried on these channels. Two additional TTY-TV converters are so configured as to permit *Mariner Mars 1971* operations

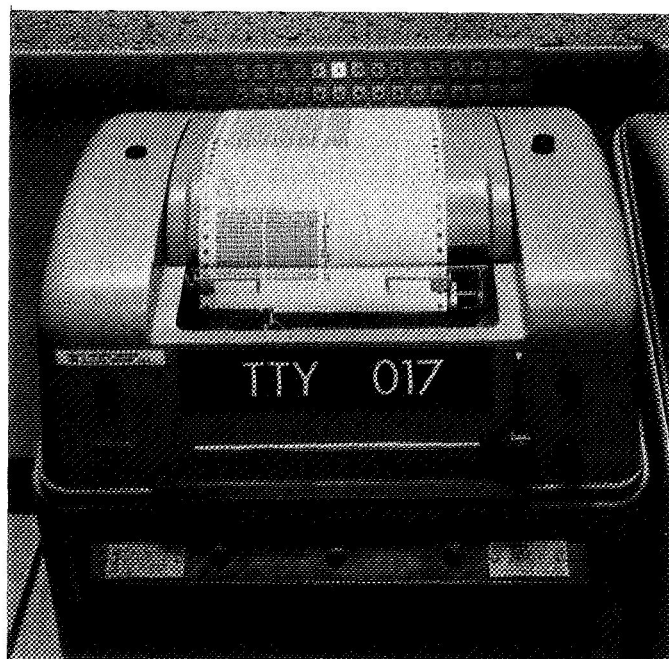


Fig. 3. Receive only teleprinter with 36-button selector box (GCF TTY BUS)

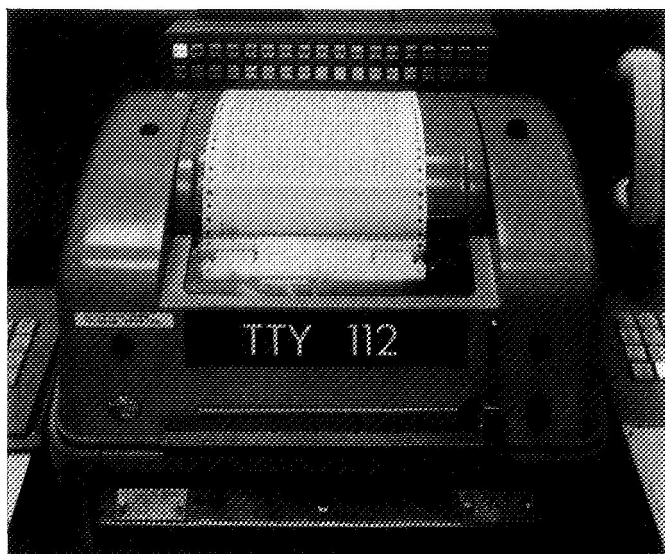


Fig. 4. Receive only teleprinter with 36-button selector box (TLM TTY BUS)

personnel to drive them with any desired output teletype format generated by the 360-75 computers so that these outputs may be viewed on television monitors capable of selecting the video outputs of these two converters.

To illustrate, by example, the manner of distributing teletype data incoming to the SFOF, when the tracking station DSS 12 is tracking the first *Mariner* Mars 1971 spacecraft and desires to send tracking data to the SFOF, such traffic will be indirectly addressed by DSS 12 to JSFO followed by the preamble 12/74/40. The selection of the identifiers in this preamble follows the outlines given previously. Table 5 indicates that this indirectly addressed traffic when received at the WCSC Commprocessor will be routed to JDPS (the Central Processing System) and to JBSS on the GCF TTY BUS. Figure 5 reflects that JBSS may be selected for page copy printout by depressing the sixth button on the GCF TTY BUS selector box and may be viewed on television monitors. To illustrate, again by example, the manner of distributing teletype data outgoing from the SFOF, when a message is sent pertaining to the first *Mariner* Mars 1971 spacecraft, containing instructions to DSS 14, such traffic would be directly addressed to JMXA and indirectly addressed to JSFO followed by the preamble 20/74/20. Table 5 indicates that the JMXA routing indicator permits the WCSC Commprocessor to route the traffic to DSS 14 and the JSFO routing indicator together with the preamble is used to internally route the traffic to JBOS on the GCF TTY BUS, to JZED in the Network Analysis Team (NAT) Area, and to JTNC in the DSIF

Control Area. Figure 5 reflects that JBOS may be selected for page copy printout by depressing the second button on the GCF TTY BUS selector box and may be viewed on television monitors.

The teletype system used for *Mariner* Mars 1971 message traffic has the capability to receive, transmit, and print out on page copy a multiplicity of symbols which can be divided into three categories: 26 symbols representing the alphabetical characters from A to Z (upper case and lower case), 10 symbols representing the numbers from 0 to 9, and 14 symbols representing punctuation and other meanings as follows:

Symbol	Meaning
-	Dash, hyphen, or minus sign
#	Number
.	Period, full stop, or decimal point
/	Slash
?	Question mark
;	Semicolon
"	Quotation or ditto marks
:	Colon
\$	Dollar sign
'	Apostrophe
,	Comma
(Open parenthesis
&	Ampersand
)	Close parenthesis

Many receiving teleprinters in the SFOF are equipped with standard type-boxes which, upon receipt of the teletype codes assigned to all of the possible symbols, convert these codes and print out the corresponding symbols. Transmission of plain-text *Mariner* Mars 1971 teletype messages uses all of these symbols in the normal conduct of routine operations traffic. Certain types of *Mariner* Mars 1971 teletype messages require that receiving teleprinters have the capability of printing 11 special symbols not normally available in the standard type-boxes. As a result, special modified type-boxes have been developed and installed in appropriate teleprinters

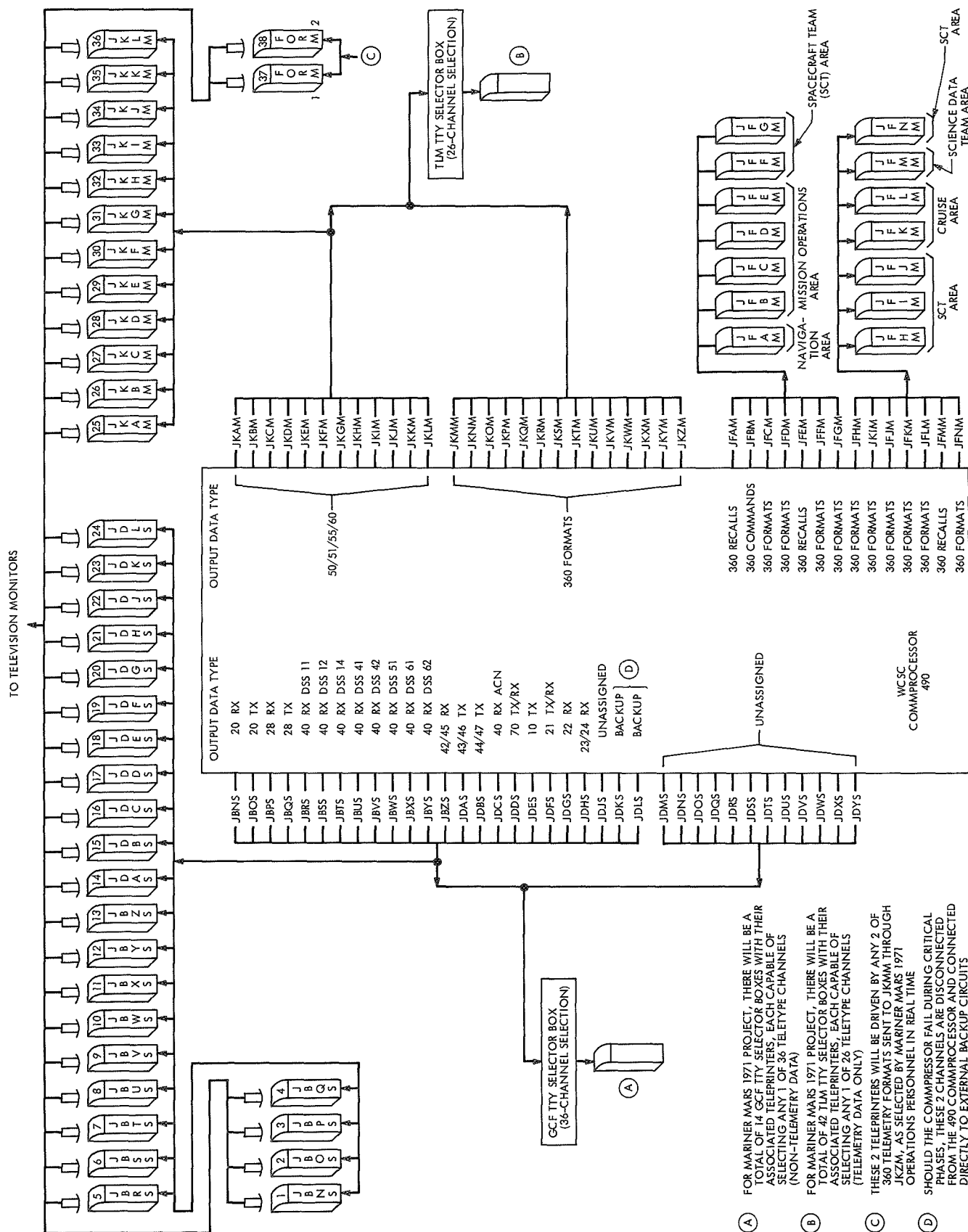


Fig. 5. Distribution of teletype data to Mariner Mars 1971 areas of SFOF

which delete certain standard symbols and replace them with the special symbols listed below:

Standard symbol	Converted to	Pronounced	Meaning
?	+	Plus	Addition
;	*	Asterisk	Alarm
"	=	Equal	Equal
:	<u>0</u>	Bar zero	Ten
\$	<u>1</u>	Bar one	Eleven
'	<u>2</u>	Bar two	Twelve
,	<u>3</u>	Bar three	Thirteen
Open	<u>4</u>	Bar four	Fourteen
(<u>5</u>	Bar five	Fifteen
&	<u>6</u>	Bar six	Sixteen
)	<u>7</u>	Bar seven	Seventeen

Thus, a transmitting station desiring to transmit the *bar one* symbol, meaning eleven, would transmit the teletype code corresponding to the \$ and the modified type-boxes on the receiving teleprinters would print the symbol 1.

Occasions will arise during the *Mariner* Mars 1971 missions where any of the recipients of teletype messages in the SFOF may require that certain messages be retransmitted to them a second time. To eliminate the obvious disadvantages of requiring the originator of such traffic to retransmit these messages, provisions have been made in the WCSC Commprocessor that permit the operators of this computer, upon request for such retransmission, to recall the desired messages from the Commprocessor and route these recalls to any teletype channel in the SFOF. It is possible, of course, to route recalled messages to the teletype channel to which the original messages were transmitted, but if this were done, real-time traffic addressed to this channel would be interrupted or delayed by the recalled traffic. To prevent this, two special teletype recall channels, JCSR and JCMR, have been established with associated teleprinters located throughout the SFOF to which recall traffic is routed by the operators of the Commprocessor, thus producing page copy for the requesting user. These two channels are illustrated in Fig. 1. Teleprinters connected to channel JCSR are equipped with standard teletype type-boxes while those connected to channel JCMR are equipped with *Mariner* Mars 1971 modified teletype type-boxes in order to display special *Mariner* Mars 1971 formats.

It is entirely possible during a lengthy tracking pass that streams of teletype traffic sent to the SFOF by several tracking stations may arrive at the WCSC Commprocessor at a higher total bit rate than the teleprinter on the output channel can operate. This is especially true in those cases where a particular type of data coming from several tracking stations is routed to a single-output teletype channel using stacking techniques. As a result, incoming messages may be queued in the Commprocessor awaiting available output time for transmission and, as a result, the data displayed on the output teleprinter will be delayed. To overcome the obvious disadvantages of this, user personnel in the SFOF may request that the operators of the Commprocessor initiate input instructions to this computer which result in the skipping of one or all messages on queue and routing the latest incoming message to the output channel teleprinter, thus providing real-time data to using personnel. All messages skipped in this manner are not automatically forwarded to the user but may be recalled using the methods previously described for recalled traffic.

VII. Television Distribution of Teletype Data

Within the operational areas of the SFOF, numerous consoles and positions have been equipped with television monitors, each having an associated selector box permitting the user to select many channels of television displays. These television channels display various types of data including equipment status, configurations, mission times, area surveillance, and 360-75 computer outputs. In addition, 38 different channels of both incoming and outgoing teletype traffic may be viewed on these television monitors. Figure 5 identifies these 38 channels, each of which is derived from an output channel of the WCSC Commprocessor and fed to 38 teletype teleprinters individually viewed by the same number of television cameras as shown in Fig. 6. The outputs of these cameras are provided to the selector boxes of each television monitor. Thus, project personnel may select any incoming or outgoing teletype channel for direct viewing on any of numerous television monitors. Figure 7 illustrates a typical *Mariner* Mars 1971 operations console showing two television monitors with their associated selector boxes, and Fig. 8 illustrates a typical desk type television monitor. It should be noted that the first 24 of these teletype-television channels are associated with all types of teletype traffic, such as predicts and tracking data, except telemetry, while the remaining 14 channels are associated with telemetry and commands only. Of these 14 channels, 12 are assigned for viewing



Fig. 6. Teletype to television converters

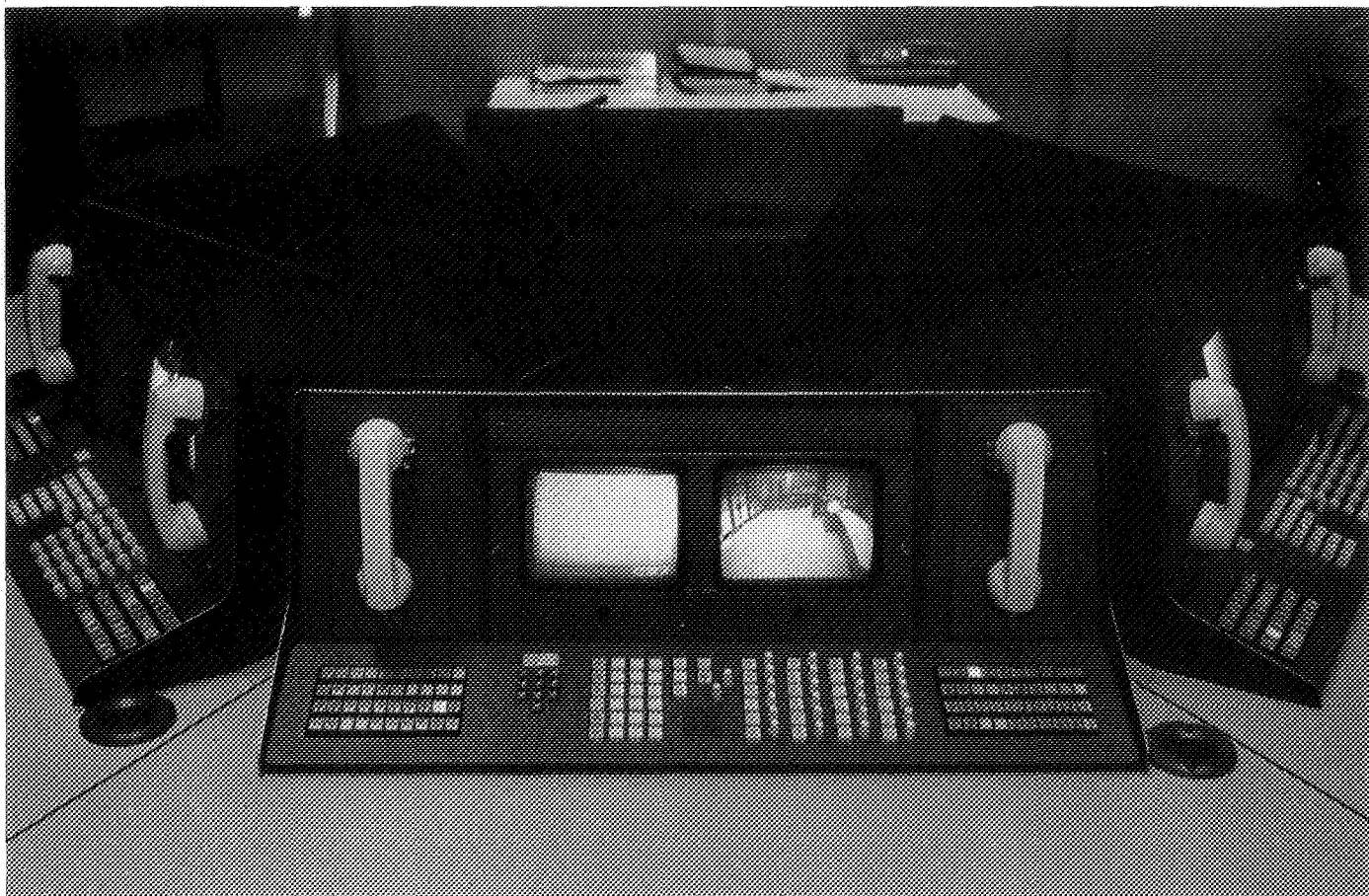


Fig. 7. *Mariner Mars 1971 operations console*

incoming raw teletype telemetry from the tracking stations while the remaining 2 channels are user selectable for viewing any of the teletype-formatted telemetry outputs of the 360-75 computers as derived from the telemetry data furnished to these computers by the inbound high-speed data circuits.

VIII. Teletype Backup Circuits

The overall design and mission configuration of the entire teletype system provided for the *Mariner Mars 1971* Project, by the DSN GCF and NASCOM, requires that all agencies and stations transmitting or receiving teletype traffic be directly connected to one of the four Commprocessors at one of the switching centers. Certain streams of teletype data may pass only through a single Commprocessor, such as traffic originating at DSS 12 at Goldstone, California destined for transmission to the SFOF, while other streams may pass through as many as three Commprocessors, such as traffic originated by DSS 51 in South Africa destined for transmission to the SFOF. In all cases, however, since all teletype traffic

must pass through at least one Commprocessor, a failure of any one of the four during critical phases of the *Mariner Mars 1971* mission could result in non-receipt at the SFOF of data that could have critical importance to mission personnel.

NASCOM, in conjunction with the DSN GCF, has developed limited capabilities which, when activated, will permit certain selected streams of teletype traffic inbound to the SFOF from any of nine supporting locations to be bypassed around the Commprocessors and provided in raw form to mission personnel as illustrated by Fig. 9. Since the interface between any two of the Commprocessors is dependent upon the proper operation of both, then a failure experienced by one necessitates that all Commprocessors in the teletype stream must be bypassed from the originating station to display devices in the SFOF. Although nine different locations are supported by these bypass capabilities, only combinations of two stations can be used simultaneously and combinations of DSS 41 with DSS 42 and DSS 51 and DSS 62

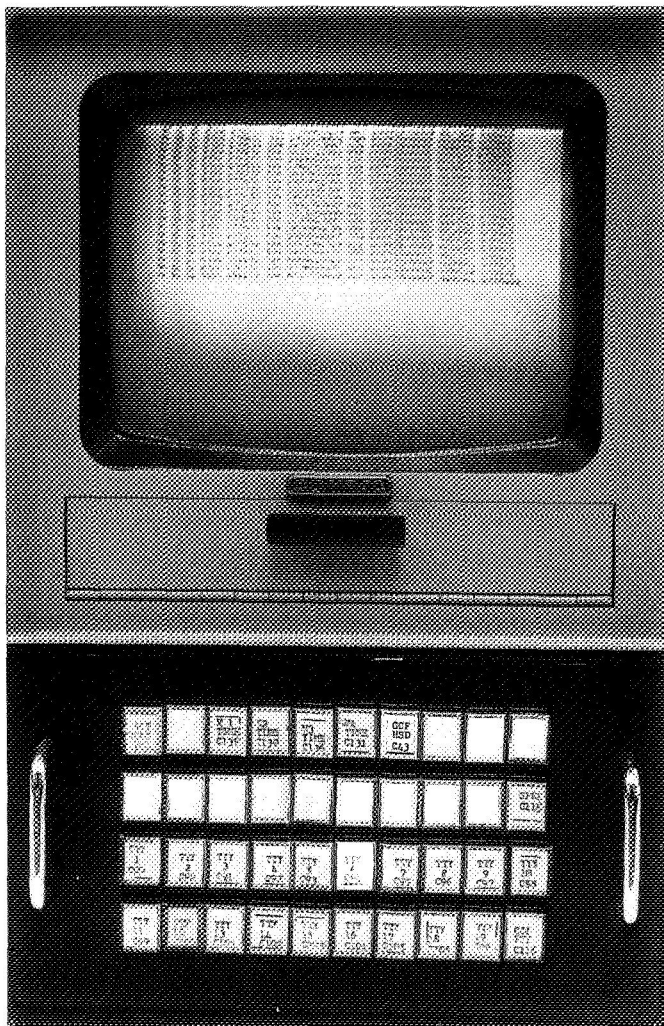


Fig. 8. Television monitor and selector box

are not possible. These restrictions are a result of the availability of only a few discrete teletype circuits to the overseas switching centers and only two display channels in the SFOF. Upon receipt of the two bypass

teletype streams, the WCSC connects these to output channels 23 and 24 on the GCF TTY BUS, which may be selected by mission personnel for page copy printout or for television viewing.

During the two launches scheduled for *Mariner* Mars 1971, certain portions of the total bypass capability illustrated in Fig. 9 will be pre-scheduled and activated by communications personnel. Certain streams of teletype traffic, such as that originated by the MSFN tracking stations at Ascension Island, will be transmitted to the SFOF not only by the normal Commprocessor route but also by the bypass circuits activated for this purpose until loss of signal by the tracking stations. In the event of a Commprocessor failure resulting in interruption of the normal streams, the data arriving via the bypass circuits will immediately be available for use. During subsequent cruise phases of the mission, activation of bypass circuits to DSN tracking stations will be made only as required by either spacecraft maneuvers or spacecraft emergencies when receipt of teletype data is vital to operations. Since the prime method of telemetry transmission is over the high-speed data system and since this system is independent of Commprocessor failures, it is not anticipated that these bypass circuits will be used for transmission of telemetry data.

IX. Conclusion

A considerable amount of advanced planning has been accomplished for all types of communications support for the two *Mariner* Mars 1971 missions, not only by personnel of the *Mariner* Mars 1971 Project and the DSN GCF but by elements of the DSIF, SFOF, MSFN, and NASCOM as well. As a result, the teletype system developed for the support of the *Mariner* Mars 1971 missions undoubtedly represents the highest development of this communications discipline used for any mission supported by the DSN.

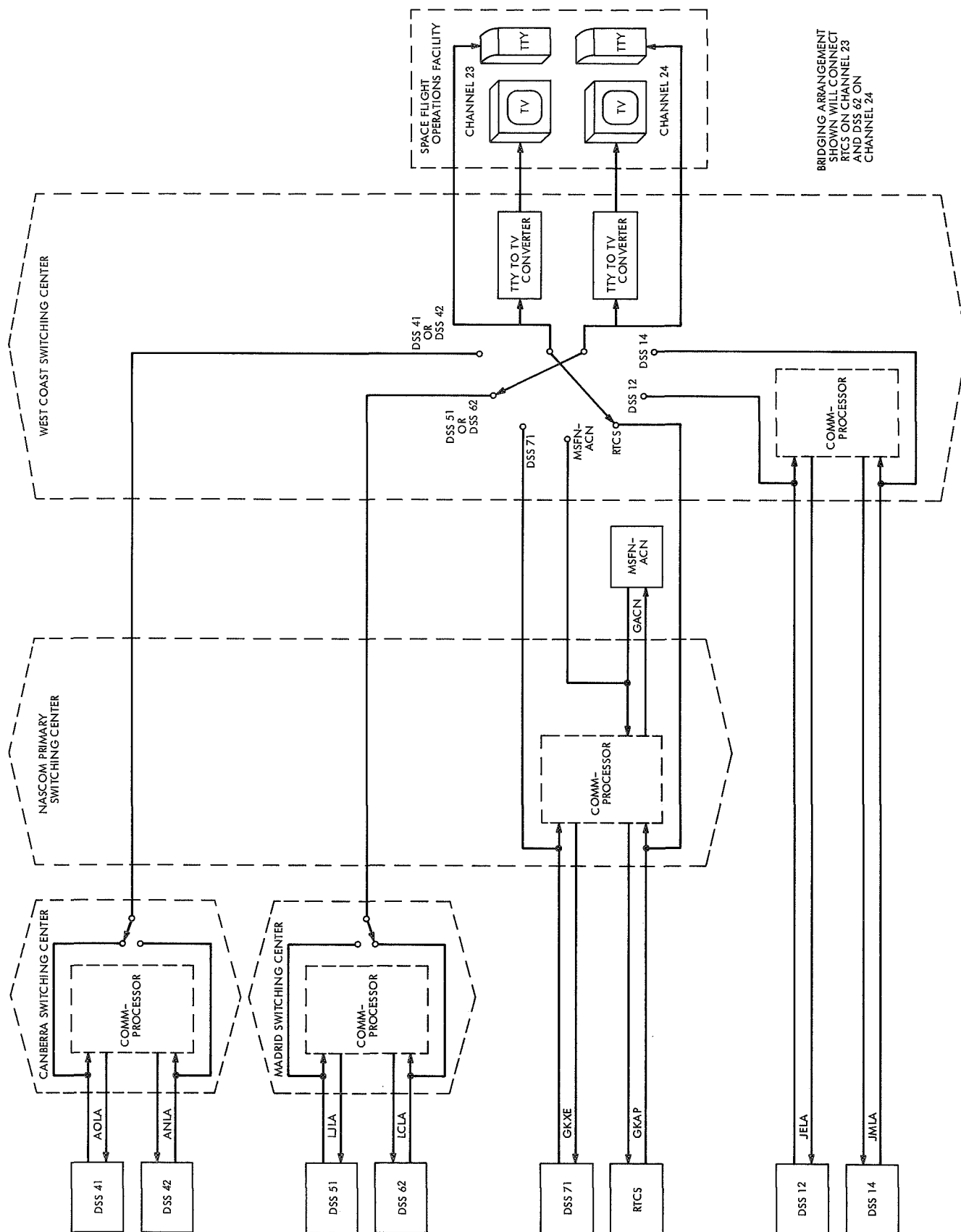


Fig. 9. Mariner Mars 1971 teletype backup circuits

DSIF Uplink Amplitude Instability Measurement

A. Bryan and G. Osborn
DSIF Operations Section

A simple and inexpensive upper bound technique for the measurement of DSIF effective radiated power is described. Test results verify the theoretical model and imply that DSIF uplink stability can satisfy Pioneer F/G attitude control requirements.

I. Introduction

The spin-stabilized *Pioneer F/G* spacecraft will utilize an automatic attitude control system (CONSCAN) based upon RF conical scanning techniques. The uplink RF signal radiated by the DSIF is the reference for the spacecraft attitude control system. The CONSCAN processor cannot distinguish between RF amplitude variations due to spacecraft aiming errors and those due to fluctuations in the DSIF effective radiated power (ERP). This usage of the uplink signal as a beacon required the DSIF to reevaluate its ERP variations. The variations are due to two uncorrelated sources, uplink antenna pointing errors and power variations in the transmitter.

Instability in the transmitter power was monitored with a crystal detector and, with the aid of the frequency translator, the DSIF S-band receiver. The antenna pointing error was evaluated from the ground receiver automatic gain control (AGC) while tracking ALSEP 1, the lunar scientific package. Instability in the uplink due to antenna pointing errors is assumed to be nearly the same as in the downlink signal.

ERP variations detected by the synchronous AGC detector are recorded on digital tape and analyzed off-line. In addition to frequency analysis (i.e., a power spectrum), a chart recorder provides a time domain record for comparison.

II. Validation and Analysis

Software development and validation of the use of the receiver AGC to measure power spectra was done at DSS 71. The spectrum is obtained from the squared magnitude of the discrete Fourier transform in an ensemble averaging mode, wherein many spectra are averaged to reduce the variance of the final estimate. The Fourier transform has a dynamic range of approximately 80 dB, and is adequate for analysis of very small stationary and random signals so long as the thermal noise is not too great.

Figure 1 is the program output for 0.406% rms (0.1 dB peak-to-peak) sinusoidal carrier modulation at 0.08

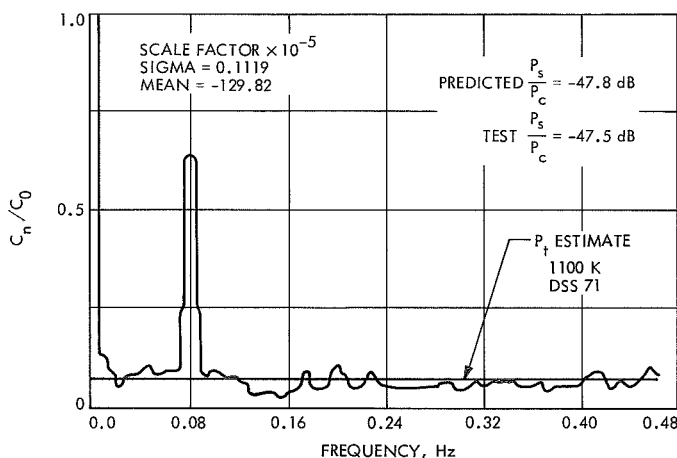


Fig. 1. Fourier transform of 0.1 dB peak-to-peak sine wave modulation at 0.08 Hz

Hz. The signal was generated by modulating the station test transmitter, and was detected from the receiver AGC. To estimate the sideband power P_s , it is noted that the instantaneous power $P(t)$ can be expressed as

$$P(t) = P_c(1 + 2m(t))$$

with $\langle m(t) \rangle = 0$ and $\langle m^2(t) \rangle \ll 1$. The ratio of sideband to carrier power is just

$$\frac{P_s}{P_c} = \langle m^2(t) \rangle$$

For the test case, $\langle m^2(t) \rangle = (4.06 \times 10^{-8})^2 = 1.65 \times 10^{-5}$, or -47.8 dB. To compare this value to the data graphed in Fig. 1, the program output must be interpreted.

The program provides the power density spectrum as a function of frequency (at 0.004 Hz intervals) in the form of the coefficients

$$C_0, C_1, C_2 \cdots C_n$$

C_0 is the carrier term, which is normalized to one. The program returns coefficients representing positive frequencies only, while an equal amount of power is contained in negative frequencies. Each coefficient other than C_0 must therefore be doubled to get the total power.

In order to improve the spectral response, a gaussian time window truncated at the three sigma points was used, but this technique smears the power in the C_0 term. This effect requires the C_0 term to be multiplied by a constant of 2.39¹ or

$$P_c = 2.39 C_0$$

The gaussian window does not affect the amplitude of a flat spectrum, and has little effect on the power contained in a window spanning many coefficients. The power contained in such a window (with no strong signals near the end points) is then

$$\frac{P_s}{P_c} = \frac{2 \sum_{k=i}^j C_k}{2.39 C_0} - \frac{P_t}{P_c} \quad (1)$$

P_t is the thermal noise power. When Eq. (1) is applied to the test data of the 0.1 dB modulation, the sideband power is -47.5 dB, which compares favorably with the -47.8 dB computed above.

A prediction of thermal noise power with respect to carrier power, considering that the receiver coherent detector enhances carrier power by a factor of two relative to thermal noise, is

$$\frac{P_t}{P_c} = \frac{kT \Delta F}{10^{(\text{dBmW} - 30)/10}}$$

The signal level in dBmW is obtained from the receiver AGC, k is Boltzmann's constant, T is the system temperature, and ΔF is the bandwidth. Note that the predicted thermal noise level agrees closely with the observed level in Fig. 1.

III. Preliminary Test Results

Using the validated test techniques, preliminary tests of the antenna pointing error were performed at DSS 12. This station tracked ALSEP 1 in both autotrack and APS modes. Figure 2 is a block diagram of the hardware configuration. Results of the APS track are shown in Fig. 3. Note how easily detectable is the 1.6-Hz ALSEP

¹Determined from the transform of a constant.

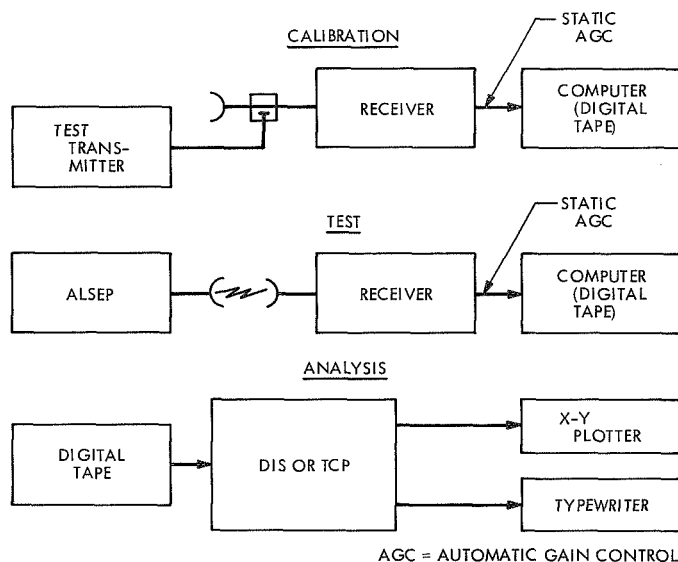


Fig. 2. Station configuration for antenna-pointing error test

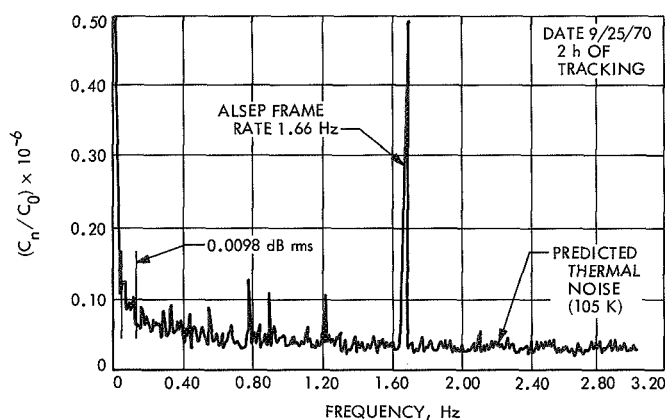


Fig. 3. ALSEP power spectrum (antenna in APS mode)

frame rate as an amplitude modulation. Also clearly evident (at 1.2 Hz) is the effect of the maser amplitude modulation. The thermal noise level is consistent with the predicted thermal noise level. Within the CONSCAN frequency response band, Eq. (1) yields $P_s/P_c = 1.28 \times 10^{-6}$, which is equivalent to 0.0098 dB rms amplitude

variation. There is no evidence of a periodic component in this region.

Tests were performed at DSS 11 on the 20-kW transmitter operated at 250 W, 1 kW, and 20 kW. Operation at 250 W was required in order to satisfy an uplink power requirement of the *Pioneer F* and *G* spacecraft during initial maneuvers after launch. Essentially the same technique is used as in the antenna pointing error measurement, as shown in Fig. 4.

Figure 5 shows the results of these three tests. The 20-kW transmitter operating at 250 W revealed the most instability, as expected. Note that the result, 0.0035 dB rms in the CONSCAN frequency band of 0.04 to 0.12 Hz, is strictly an upper bound as the receiver noise is also included in this measurement. To obtain a spectrum of the transmitter amplitude instability without the receiver noise, a crystal detector operating in its linear range was used to detect power variations at 1 and 20 kW.

With the assumption of no correlation between the antenna pointing error and transmitter instability at 250 W, a vector sum result is 0.0135 dB rms. This figure is to be compared to a project suggested value for the DSIF ERP variation of 0.0355 dB rms centered at the maximum response of the CONSCAN attitude control system.

IV. Conclusion

A relatively simple and inexpensive upper bound² measurement technique for ERP amplitude variations has been developed and verified. Preliminary tests imply that the DSIF uplink amplitude stability can satisfy *Pioneer F/G* attitude control requirements. The technique will be implemented at all stations supporting *Pioneers F* and *G*, as RF amplitude stability tests will probably be required periodically, as well as following maintenance of subsystems that affect antenna pointing or transmitter stability.

²The real part of the cross power spectrum of two receiver outputs would also provide the desired power spectrum, and would reduce the receiver contribution to the measurement.

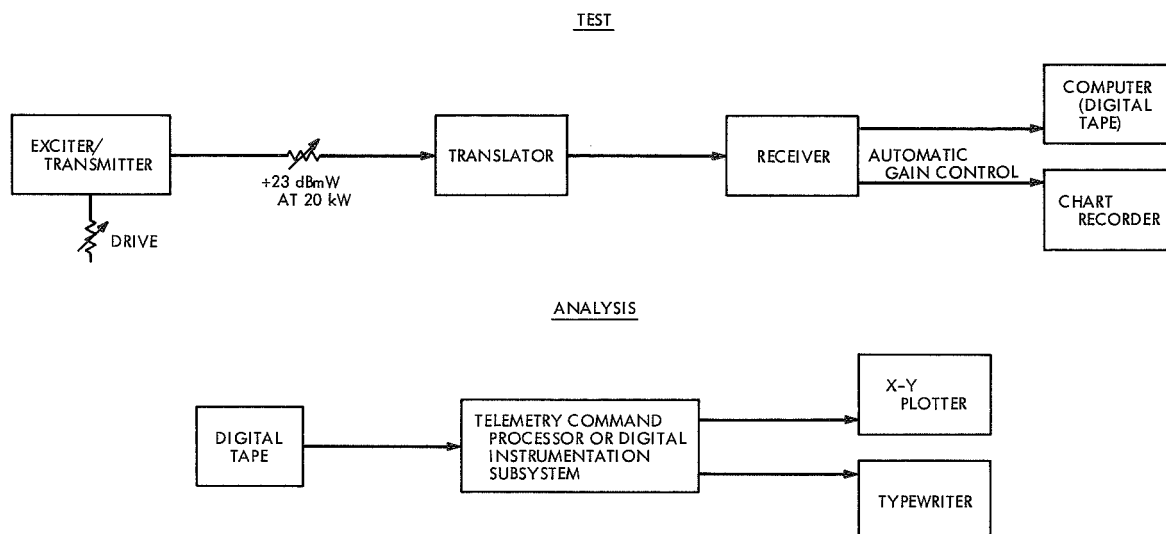
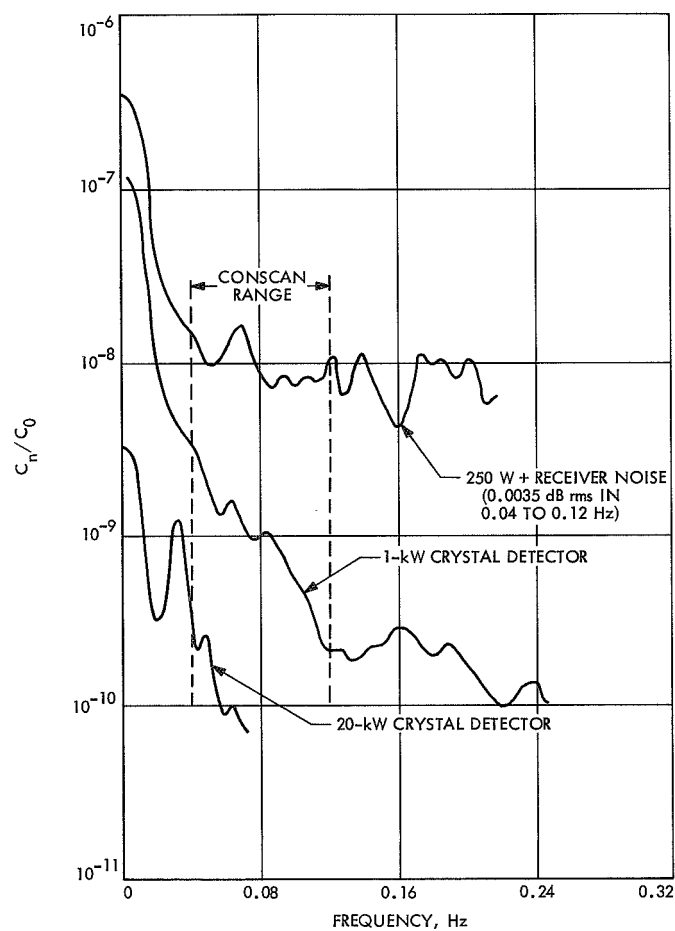


Fig. 4. Transmitter amplitude stability test



**Fig. 5. Power spectra of klystron
(antenna moving at sidereal rate)**

Processed Data Combination for Telemetry Improvement—DSS 62

J. M. Urech
DSIF Operations Section

This article documents the continuation of the study described in JPL Space Programs Summary 37-63, Vol. II, pp. 116–120, "Telemetry Improvement Proposal for the 85-Foot Antenna Network." Four methods of improving telemetry bit error rate performance by combining data with common time tags from two stations are described in the referenced article. This article discusses the method of a posteriori combination of processed telemetry data. The theory is presented and the results of a scheduled test with a Pioneer spacecraft are shown to be in good agreement. The computer program description is included as an appendix.

I. Introduction

This article is a follow-up to the original report (Ref. 1) which presented method 4, "processed data combination," as a potential telemetry improvement procedure.

The method suggested the sending of the two data streams via teletype or high-speed data line (already processed by the telemetry and command processor) from the different stations to a central computer located at either of the stations or at the SFOF. This computer will compare both information streams and select the best data. It is obvious that the process is only applicable to projects using some kind of error detection technique (such as parity error for *Pioneer*) which will allow the computer to detect erroneous words in either channel and select the corresponding good word from the other

channel. Thus, the probability of having an error after combination is the joint probability of having the same word in error in both channels. This, due to the independent noise contributions, is equal to the product of error probabilities for each channel.

The processed data combination method is not affected by the time delay between the two stations, since the computer may employ a high-capacity telemetry buffer. This method may also be used by any pair of stations sharing a common view period (DSS 11/12, DSS 41/42, DSS 51/61/62).

Although the method is ideally applicable to two stations with the same configuration (two ground operational equipment [GOE] or two multiple-mission telemetry [MMT] stations), the computer program has been

developed at DSS 62 for its peculiar configuration—DSS 61 using GOE and DSS 62 the MMT. This configuration further complicates the computer program as it intends to make the formats used by GOE (DOI-5021-OP) and by MMT (DOI-5020-OP) compatible. The program description is given in the appendix.¹

II. Basic Theory

In the case of uncoded telemetry for the *Pioneer* Project, we may use the following definitions and approximations:

P_{EL} = probability for a bit level in error (NRZ-L)

$P_{EM} = 2P_{EL}(1 - P_{EL}) \simeq 2P_{EL}$ if P_{EL} is very small, P_{EM} being the probability for a bit error (NRZ-M)

P_W = probability of a word in parity error, where $P_W \simeq 8P_{EL}(1 - P_{EL})^2$ and if $P_{EL} < 10^{-2}$ then $P_W \simeq 8P_{EL}$

P_U = probability of having an undetected word in error, where

$$P_U \simeq \frac{8!}{6!2!} P_{EL}^2 (1 - P_{EL})^6 \\ \simeq 28P_{EL}^2 \simeq 0.437P_{EL}^2, \text{ if } P_{EL} < 10^{-2}$$

This is computed for the case of having two bit levels in error per word, although any even number of bit levels in error per word will be undetected by the parity bit; however, the probability of having more than two errors is much smaller.

For the general development of a combining program, two different criteria may be selected:

A. First Criterion

A word tagged in error is outputted only when that word contains a detected error in both channels. In the case of two corresponding words being different (due to a word with an undetected error), select as the output word the one coming from the channel with the most favorable signal-to-noise ratio (SNR), which also has the highest probability of being correct.

Then, the theoretical improvement may be easily computed by making a few valid approximations of the normal operating values of SNR (the exact calculations

would be much longer, but for our purpose would not add any useful information).

If the subscripts 1 and 2 are used for each channel, under the assumption that channel 1 has a greater SNR, we will have:

1. Probability of an output word with a detected error

$P'_W = P_{W1} \cdot P_{W2}$ (due to independent noise contribution from both channels)

as $P_W < 1$ this always means an improvement.

2. Probability of an undetected word in error at the output

$$P'_U = P_{W1} \cdot P_{U2} + P_{W2} \cdot P_{U1} + P_{U1}(1 - P_{W2}) \\ = P_{U1} + P_{U2} \cdot P_{W1}$$

which means a small increment in the undetected word error rate.

These results are shown in Figs. 1 and 2 for the particular case of two channels having the same SNR and therefore,

$$P'_W = P_W^2 \quad \text{and} \quad P'_U = P_U(1 + P_W)$$

B. Second Criterion

A word tagged in error is outputted when both channels contain a detected error, and also if two corresponding words are different.

Then, using the same notation as before, we will have:

1. Probability of having an output word with a detected error

$$P''_W = P_{W1} \cdot P_{W2} + (1 - P_{W1})P_{U2} + (1 - P_{W2})P_{U1} - P_{U1} \cdot P_{U2}$$

2. Probability of having an undetected word error at the output

$$P''_U = P_{W1} \cdot P_{U2} + P_{W2} \cdot P_{U1}$$

These results are also shown in Figs. 1 and 2 for comparison with previous ones and for two channels having the same SNR, in which case:

$$P''_W = P_W^2 + 2P_U(1 - P_W) - P_U^2$$

and

$$P''_U = 2P_W \cdot P_U$$

¹The assembly language listing is available by request to author.

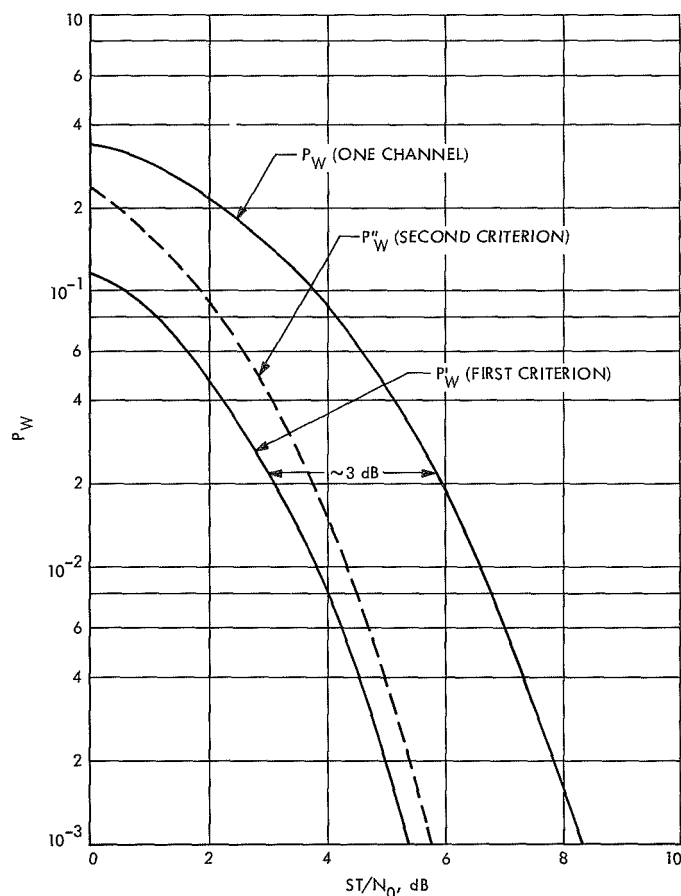


Fig. 1. Probability of a detected word error for a single channel and for the two criteria of combination

By examining both sets of curves (Figs. 1 and 2), one can see that the first procedure yields an almost *constant improvement of 3 dB* (for the operating SNR range) if the detected word error rate is considered. However, the undetected word error rate is not improved with respect to only one channel; furthermore, this rate slightly increases for very low signal-to-noise ratios. For the second criterion, the results are different. The detected word error rate shows an improvement smaller than 3 dB, but still greater than 2 dB in the normal operating range; also, the undetected word error rate is smaller having an equivalent improvement of 1 to 1.5 dB.

C. Criterion Selected for Demonstration Program

Based on the above theory, the selection of the criteria to be employed should be made by the *Pioneer* Project, which should specify the relative importance of decreasing the detected word error rate and the undetected word error rate. Nevertheless, the first criterion has been selected at DSS 62, since this computer program is not

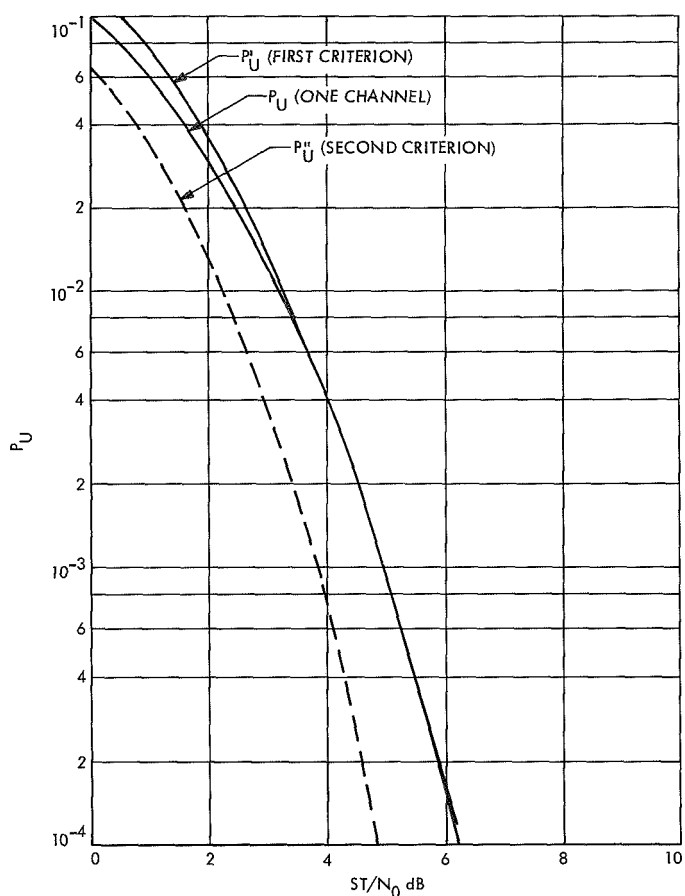


Fig. 2. Probability of an undetected word in error for a single channel and both criteria of combination

intended to be an exhaustive and definite one, but rather has been developed mainly for feasibility demonstration and testing.

III. Conclusion

The "merging" program was checked out internally at the station, and a DSN scheduled test was conducted on day 260 from 16:00 Z to 18:00 Z at DSS 61/62. The results were satisfactory and in close agreement with the basic theory, although the statistics obtained for such a short period (1.5 h) cannot be very accurate. The estimation obtained was:

Station	Percentage of error (avg)	ST/N_0 (avg), dB
DSS 61 (GOE)	0.0215	5.8
DSS 62 (MMT)	0.0114	6.4
DSS 61/62 (Merging)	0.00014	9.3

This shows a telemetry improvement close to the theoretical 3 dB.

Further tests will be conducted when both stations are available at the same time; but if this method of telem-

etry combination is considered useful to the DSN, the demonstration program will be modified in order to have more capabilities, such as: GOE/GOE combination and/or MMT/MMT combination, or to use the second criterion if required.

Reference

1. Urech, J. M., "Telemetry Improvement Proposal for the 85-ft Antenna Network," in *The Deep Space Network*, Space Programs Summary 37-63, Vol. II, pp. 116-120. Jet Propulsion Laboratory, Pasadena, Calif., May 31, 1970.

Appendix

Processed Data Program Description

Identification

Demonstration program for *Pioneer* science data merging

Author

Miguel A. Urech, DSS 62.

Configuration

Any TCP Phase II-C.

Purpose

Program has been written to demonstrate Method Number 4, *Processed Data Combination* of "Telemetry Improvement Proposal for the 85-ft Net" by Jose M. Urech, DSS 62, dated 11 March, 1970.

Programmed Operators

None.

Storage

Program requires locations 00200 to 00202 and 00300 to 22037.

Timing

N/A.

Source Language

SDS Meta-Symbol.

I. Program Description

The purpose of the program is to improve telemetry by means of combining two data streams already processed by TCP.

The two data streams used for this combination are:

- (1) Science TTY output of program DOI-5021-OP at a GOE station, and
- (2) Science TTY output of program DOI-5020-OP at a MMT station.

These two streams are first fed into the "merging computer," through R1 and R0 of the communications buffer,

where they are compared word by word and the combined data outputted through T3 of the buffer with the same format as used by DOI-5021-OP.

The program has two modes of operation:

A. Merging Mode

In this mode the two data streams are compared word by word employing the following criteria:

- (1) If both words are the same and different from dollar signs (\$\$), anyone of the two is outputted and no error is counted.
- (2) If each word is dollar signs (\$\$), these signs are outputted and the error counter is incremented by one.
- (3) If the two words are different, and one of them is dollar signs, the word not being the dollar signs is outputted and no error is counted.
- (4) If the two words are different and neither is dollar signs, the word coming from the stream with the most favorable SNR is outputted, and no error is counted.

The program does not calculate the SNR of the two data streams, but this can be introduced by an input through typewriter.

The above-mentioned criteria apply only to words 4 to 16 and 19 to 32 of the data frame. Words 3, 20, and 21 (except in the case of extended frame count for word no. 3) are parity checked in both streams, and the following criteria are then used for comparison:

- (1) If the two words are the same and have correct parity, anyone of them is outputted and no error is counted.
- (2) If the two words are the same and both have incorrect parity, any one of them is outputted and the error counter is incremented.
- (3) If the two words are different and only one has correct parity, the one with the correct parity is outputted and no error is counted.

- (4) If the two words are different and both have correct parity, the word from the prime stream (that of most favorable SNR) is outputted and no error is counted.
- (5) If the two words are different and both have incorrect parity, the word from prime stream is outputted and the error counter is incremented.

B. Count Error Only Mode

This mode of operation is used upon operator request or when one of the two data streams is not available for comparing in the merging mode (i.e., out-of-lock conditions, which mean that no science TTY data is available from the GOE station, nor is there frame synchronization data from MMT).

In this mode of operation the program's only function is to count errors in the available data stream as it *copies* each word.

The program determines that the DOI-5021-OP data stream is out-of-lock by means of the time tags on each frame. When the time difference between one frame and the next is not the expected one (± 2 s), the program assumes that there is missing data caused by an out-of-lock condition in the GOE computer. This means that the program will not go into a "count error only mode" until this data stream is back in lock, and time gap is determined.

The out-of-lock condition in the DOI-5020-OP data stream is easily detected by means of non-frame synchronization data.

The other most important features of the program are:

- (1) The program outputs percentage of error (PE) messages every 10 min through the TTY and also on the console typewriter. The PE is calculated by the simple algorithm:

$$PE = \frac{\text{number of words in error}}{\text{number of words processed}}$$

- (2) The program monitors ground receiver AGC and SPE, either from the TTY data coming from the GOE station, or directly through the analog-to-digital converter at the MMT station.
- (3) The program copies any command messages appearing in the TTY data from GOE station.

II. Operation Instructions

A. Preoperational Procedures

Ensure that the TCP-II-C computer is configured as follows:

- (1) MMT TTY data stream is patched to "R0."
- (2) GOE TTY data stream is patched to "R1."
- (3) Batteries are on "T3," which is the SCP used for output.

Ensure that the following patches are made on the interrupt patch panel:

- BLUE 6 TO GREEN 5 (100 pps)
- ORANGE 21 TO GREEN 6 (TTY OUT)
- BLUE 11 TO GREEN 7 (1 pps)
- BLUE 19 TO BLUE 20 (ADC CONVERT)

B. Operational Procedures

Load program from paper tape with "standard fill" procedure.

Once loaded, the program requests initialization parameters, (mainly header information) which are the following:

- (1) STATION ID =
Type the two digit number of the station.
Example: STATION ID = 62\$
- (2) SPACECRAFT ID =
Type the two digit S/C number
Example: SPACECRAFT ID = 20\$
- (3) DAY OF MONTH =
Type the two digit day of month
Example: DAY OF MONTH = 09\$
- (4) BIT RATE IS =
Type one of the two legal entries, either 08 or 16.
Example: BIT RATE IS = 08\$
- (5) CHANNEL DESIGNATOR =
Type the three-letter designator.
Example: CHANNEL DESIGNATOR = CEB\$

- (6) MESSAGE COUNT =
Type a three-digit number for the first header
Example: MESSAGE COUNT = 003\$
- (7) CHANNEL INDICATOR =
Type a one-letter channel indicator
Example: CHANNEL INDICATOR = B\$
- (8) PRECEDENCE =
Type a two-letter precedence code
Example: PRECEDENCE = SS\$
- (9) ROUTING 1 =
Type a four-letter routing indicator or a 0 (zero) if it is not required.
Examples:
ROUTING 1 = JSFO\$
ROUTING 1 = O\$
- (10) ROUTING 2 =
Same as item 9.
- (11) ROUTING 3 =
Same as item 10
Thus, up to three routing indicators may be requested.
- (12) STATION INDICATOR =
Type the four-letter station indicator.
Example: STATION INDICATOR = LCEB\$
- (13) TYPE 1 IF MMT IS PRIME, OR 0 IF 5021 IS PRIME
Type 0 or 1 to indicate which stream has the most favorable SNR.
- (14) TYPE 1 TO MONITOR MMT AGC, or 0 FOR 5021.
Type 0 or 1, depending on which stream (GOE station or MMT station) is desired to monitor the ground receiver AGC and SPE.
As soon as the last input is entered the program types:
PROGRAM READY
DOY HHMMSS
This indicates that the program is ready and will try to go to the "merging mode" unless forced into a "count error only mode" by breakpoint setting.

C. Breakpoint Options

Breakpoint 1 Set: Requests typewriter input in the case of operator wanting to make any real-time requests.

Breakpoint 2 Set: Go to "count error only mode" with GOE data.

Breakpoint 3 Set: Go to "count error only mode" with MMT data.

Breakpoint 4 Set: Request new Nascom header.

D. Run-Time Typewriter Inputs

- (1) RO1/, RO2/, and RO3/ are used to request, change, or delete a routing indicator.
Examples: RO2/JAER\$
RO2/0\$ (to delete)
- (2) MCT/, followed by a three digit number, is used to change the Nascom header sequence number.
Example: MCT/008\$
- (3) EOM/\$
Put an EOM on the TTY line and terminate the program.
- (4) AGC/
Type either 0 or 1, depending on which AGC and SPE is desired to monitor.
- (5) RSP/\$
In the event of garbled characters appearing in the GOE data stream, synchronization of this stream could be lost for comparison purposes. Under these circumstances this message would serve to resynchronize the stream.
- (6) RSM/\$
Same as item (5) but for the MMT data stream.
- (7) BRT/
Is used to change the nominal bit rate, either 08 or 16.
- (8) MMT/\$
Is used to indicate that the prime stream is now that of the MMT station.
- (9) PNN/\$
Same as item (8), but GOE station is the prime.
- (10) STR/YYYYY/XXXXXXXXX\$
Used to alter the contents of a memory location (YYYYY).

- (11) EXM/XXXXX\$
Used to display the contents of a memory location (XXXXX) on the console typewriter.

A sample printout is shown in Fig. A-1.

E. Operation Notes

The program should not be initiated in merging mode until the MMT stream has achieved frame synchroniza-

tion and has typed at least ten frames. This is to avoid wrong time tag on the frames.

Since storage buffers are capable of holding only 50 data frames (about 10 min of data at 16 bps), any out-of-lock condition detected on one of the two streams and lasting more than 10 min will cause some data from the other stream to be lost. Therefore, the operator should set either B.P. 2 or 3 to force a "count error only mode."

```
*** PN SCIENCE DATA MERGING PROGRAM ***

STATION ID = 62$
SPACECRAFT ID = 20$
DAY OF MONTH = 18$
BIT RATE IS = 08$
CHANNEL DESIGNATOR = CEB$
MESSAGE COUNT = 001$
CHANNEL INDICATOR = B$
PRECEDENCE = SS$
ROUTING 1 = JSFO$
ROUTING 2 = 0$
ROUTING 3 = JACR$
STATION INDICATOR = LCEB$
TYPE 1 IF MMT IS PRIME
OR 0 IF 5021 IS
1$
TYPE 1 TO MONITOR MMT AGC
OR 0 FOR 5021
1$
PROGRAM READY
261 114833
261 115000 PE 0000
261 120000 PE 0658
.
.
.
261 160000 PE 0016
261 161000 PE 0344
261 162000 PE 0049
RSP/$
261 162612
RSM/$
261 162754
261 163000 PE 0076
261 164000 PE 0015
.
.
.
```

Fig. A-1. Sample printout of typewriter initialization and periodic output

Overseas DSIF 64-m Antenna Project Status

F. D. McLaughlin
DSIF Engineering Section

The status of construction of two 64-m-diameter steerable paraboloid tracking antennas being installed near Canberra, Australia and Madrid, Spain is presented for the January/February 1971 reporting period. The antennas are being constructed by the Collins Radio Company, Dallas, Texas, under JPL contract.

I. Introduction

Two existing 26-m-diameter antenna stations at overseas locations are being upgraded to 64-m antenna stations. This effort includes the construction of two 64-m antenna instruments and requisite support facilities. (See Refs. 1 and 2 for earlier reports on the upgrading effort.)

A fixed-price contract was effected with the Collins Radio Company, Dallas, Texas, on August 14, 1969. The contractual period for construction of the Spanish antenna is 40 mo and that for the Australian instrument is 31 mo. The contract is presently in its eighteenth month.

Figure 1 shows a cross section of the 64-m antenna and identifies the major components. Figure 2 lists the sub-

contractors to the Collins Radio Company who are responsible for the fabrication of these components and gives the status of the components through the January/February reporting period.

II. Construction at Australian Site

As a structural support element, the Australian antenna pedestal (Fig. 3) is essentially complete. However, the architectural and engineering portions of the pedestal interior and placement of facility equipment within the pedestal have yet to be completed.

Atop the pedestal, the azimuth radial bearing runner and the azimuth bull gear have been installed and the hydrostatic thrust bearing runner has been positioned in

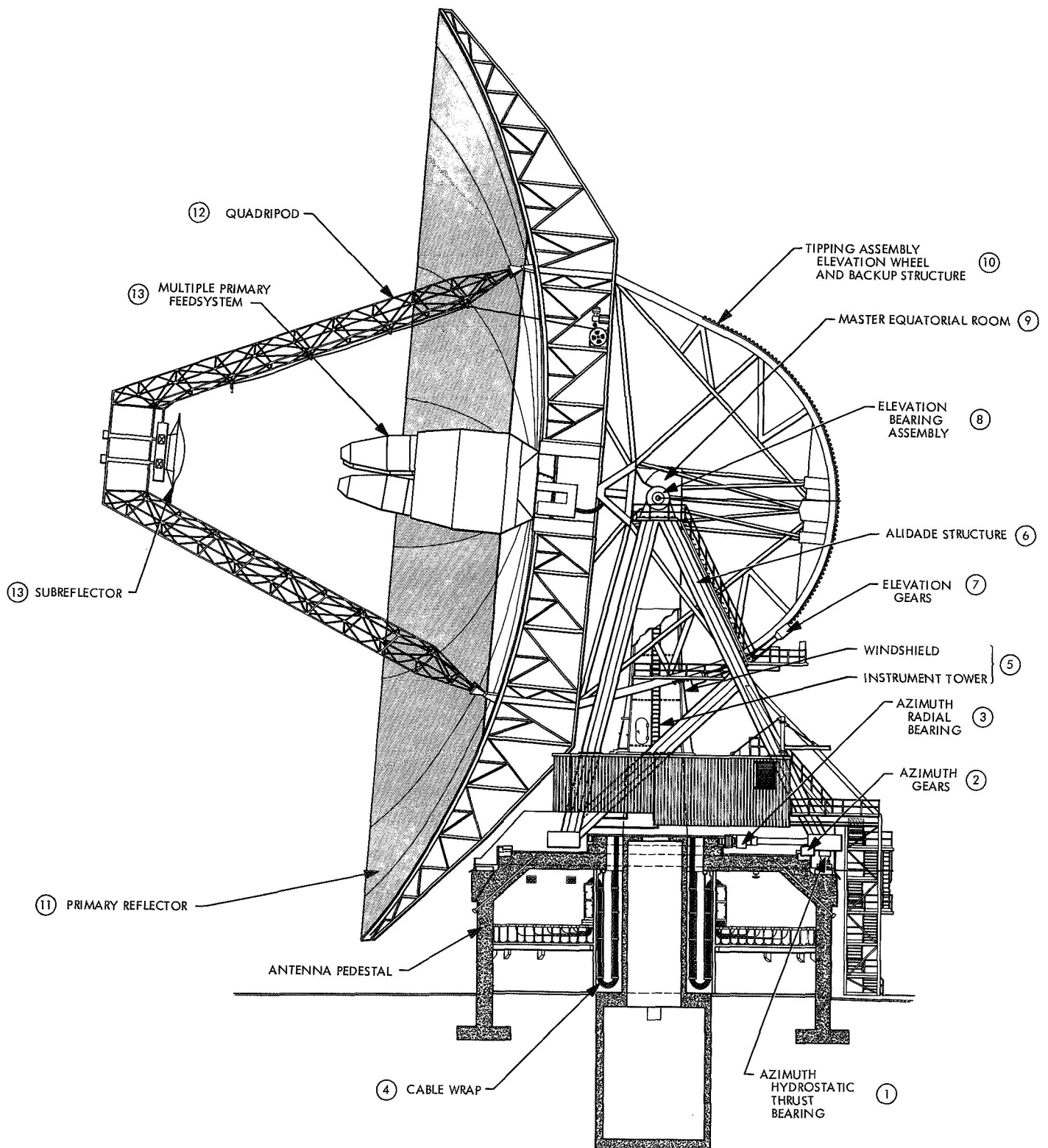


Fig. 1. Cross section of antenna

ITEM (FIG. 1)	COMPONENT	SUBCONTRACTOR	AUSTRALIAN SITE						SPANISH SITE									
①	HYDROSTATIC BEARING																	
	RUNNER	WESTERN GEAR	■	▲	▽	○				■	▲	▽		○				
	PADS	WESTERN GEAR	■	▲	▽	○				■	▲	▽		○				
	HYDRAULICS	HYDRANAMICS	■	▲	▽	○					□		▲	▽	○			
②	AZIMUTH GEARS																	
	BULL GEAR	PHILADELPHIA GEAR	■	▲	▽	○				■	▲	▽		○				
	REDUCERS	PHILADELPHIA GEAR		■		▲	▽	○		■	▲			▽	○			
③	AZIMUTH RADIAL BEARING																	
	RUNNER	WESTINGHOUSE	■	▽			○				■	▲	▽		○			
	TRUCKS	WESTERN GEAR		■	▲	▽	○				■	▲		▽	○			
④	CABLE WRAP	CAPITAL WESTWARD		■		▲	▽	○			■		▲	▽	○			
⑤	INSTRUMENT TOWER/WIND SHIELD	PRECISION FABRICATORS	■	▲		▽					■		▲	▽				
⑥	ALIDADE																	
	STRUCTURE	PRECISION FABRICATORS		■	▲		▽	○			■	▲		▽				
	BUILDING	PRECISION FABRICATORS	■	▲			▽			■	▲			▽				
⑦	ELEVATION GEARS																	
	BULL GEAR	PHILADELPHIA GEAR			□	▲	▽	○				□		▲	▽	○		
	REDUCERS	PHILADELPHIA GEAR			□	▲	▽	○				□		▲	▽	○		
⑧	ELEVATION BEARING	NATIONAL STEEL & SHIP BUILDING	■	▲		▽		○		■	▲		▽		○			
⑨	MASTER EQUATORIAL ROOM	LECKEMBY CO.			□	▲	▽					□		▲	▽			
⑩	TIPPING ASSEMBLY																	
	ELEVATION WHEEL	COEUR D'ALENES		■		▲	▽	○				□		▲	▽	○		
	BACKUP STRUCTURE	COEUR D'ALENES		■		▲	▽	○				□		▲	▽	○		
⑪	REFLECTOR PANELS	RADIATION SYSTEMS INC			□		▲	▽				□			▲	▽		
⑫	QUADRIPOD	PRECISION FABRICATORS			□		▲	▽	○			□			▲	▽	○	
⑬	TRICONE ^a																	
	SERVO ^b																	
	ELECTRONICS	COLLINS			□	▲	▽		○				□		▲	▽	○	
	HYDRAULICS	HYDRANAMICS		■				▲	▽	○			□			▲	▽	○
^a SEPARATE CONTRACT WITH PHILCO FORD; FOLLOWS COLLINS EFFORT.			JUL/AUG	SEP/OCT	NOV/DEC	JAN/FEB	MAR/APR	MAY/JUN	JUL/AUG	SEP/OCT	NOV/DEC	JAN/FEB	MAR/APR	MAY/JUN	JUL/AUG	SEP/OCT	NOV/DEC	
^b NOT ILLUSTRATED																		
	SCHEDULED	COMPLETED	□	■														
			▲	▲														
			▽	▽														
			○	●														
		FABRICATION																
		DELIVERY TO SITE																
		INSTALL																
		TEST																
			1970		1971		1972			1970		1971		1972				

Fig. 2. Major components and status of antenna

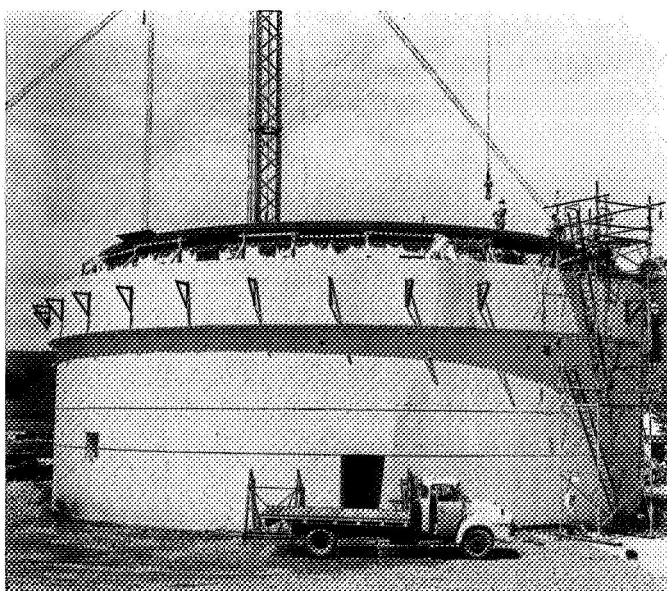


Fig. 3. Antenna pedestal at Australian site

preparation for final alignment and grouting. The remainder of the runner sole plates, the last items required for completion of installation of this critical path element, was received at the site on February 16. Grouting is expected to begin near the end of this reporting period. During the next reporting period, the hydrostatic bearing runner grouting will be completed and erection of the alidade structure will begin.

III. Construction at Spanish Site

Construction at the Spanish site began on June 22, 1970. Figure 4 shows the status of the pedestal construction. Lift number 8 was completed on February 10, 1971.

Figure 5 shows an overall view of the construction site. During excavation, granite outcroppings were encountered which required considerable blasting and slowed progress. The site construction, however, is well ahead of schedule.

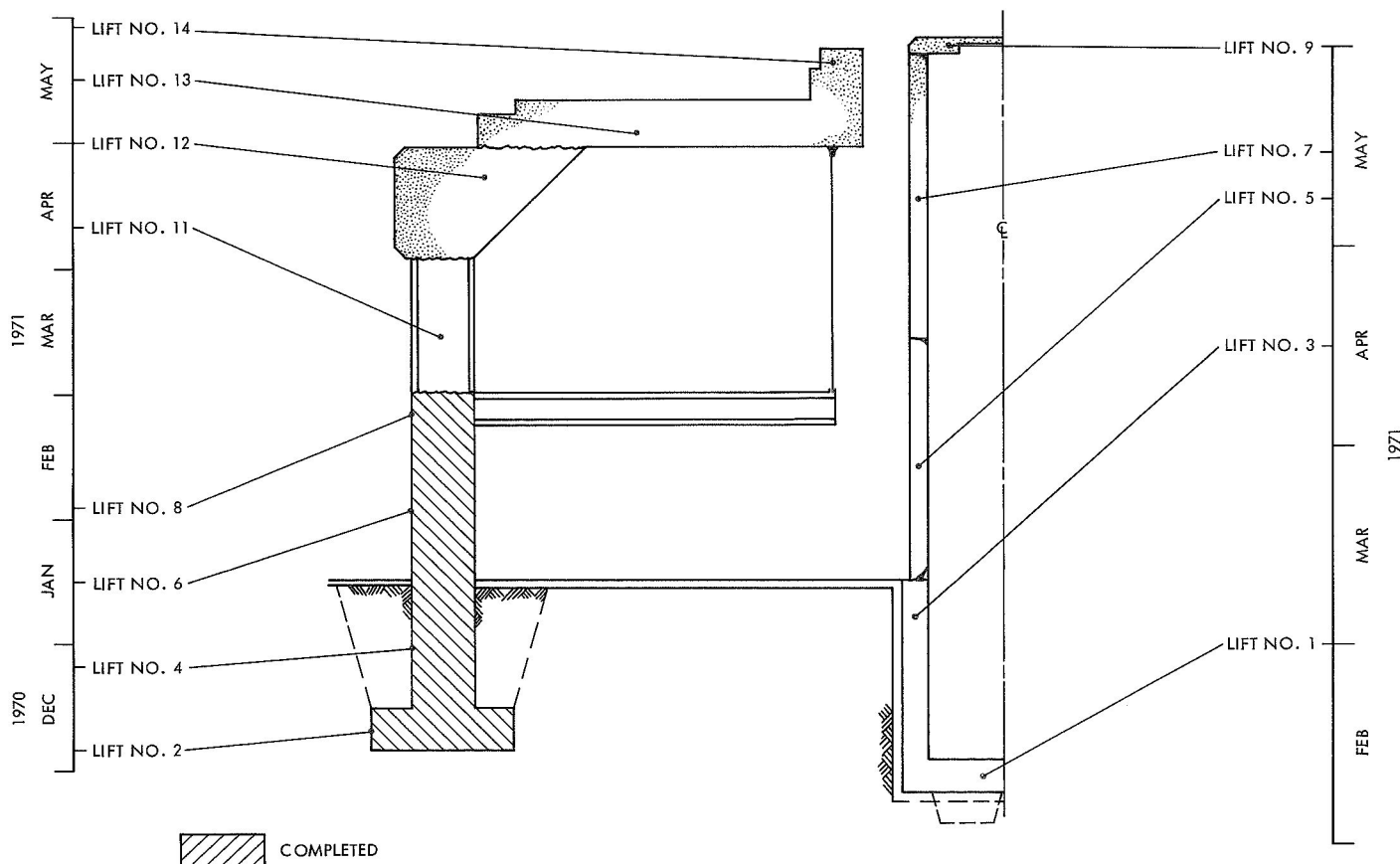


Fig. 4. Status of pedestal construction at Spanish site

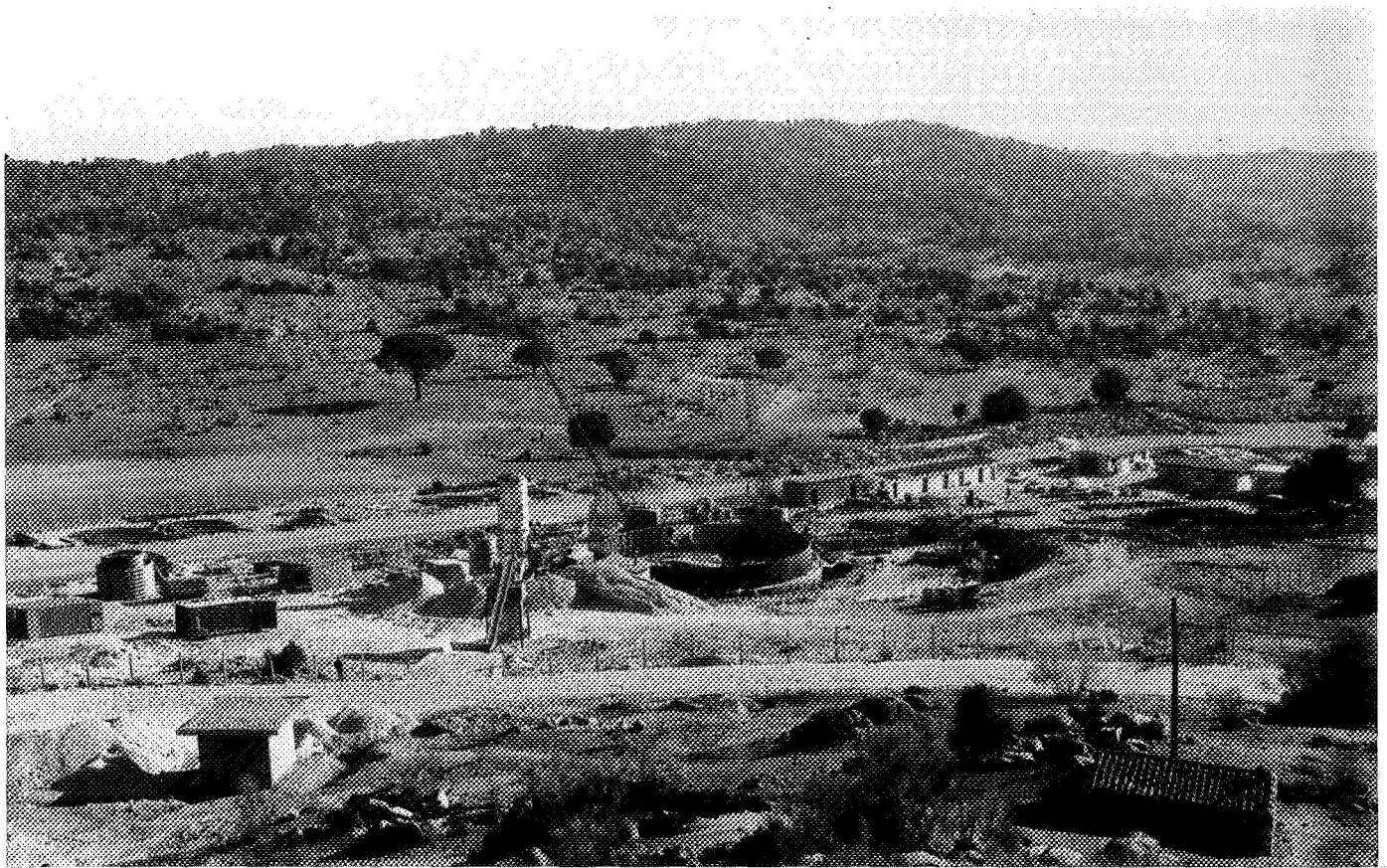


Fig. 5. View of Spanish construction site

References

1. Casperson, R. D., and Lord, W. W., "Overseas 210-ft-diam Antenna Project," in *The Deep Space Network*, Space Programs Summary 37-65, Vol. II, pp. 154-158. Jet Propulsion Laboratory, Pasadena, Calif., Sept. 30, 1970.
2. Casperson, R., Kroll, G., and Kushner, L., "DSS 61/63 Facility Modifications and Construction," in *The Deep Space Network*, Space Programs Summary 37-66, Vol. II, pp. 154-158. Jet Propulsion Laboratory, Pasadena, Calif., Nov. 30, 1970.